

PROCESSING—THERMAL CONDUCTIVITY RELATIONSHIPS IN MGO—PYROCHLORE
COMPOSITE INERT MATRIX MATERIALS

By

SAMANTHA J. YATES

A DISSERTATION PRESENTED TO THE GRADUATE SCHOOL
OF THE UNIVERSITY OF FLORIDA IN PARTIAL FULFILLMENT
OF THE REQUIREMENTS FOR THE DEGREE OF
DOCTOR OF PHILOSOPHY

UNIVERSITY OF FLORIDA

2009

© 2009 Samantha J. Yates

ACKNOWLEDGMENTS

I need to first acknowledge Dr. Juan C. Nino for his guidance and unconditional support. He has shown unwavering faith in my abilities and has constantly pushed me to reach my potential. I also need to recognize Dr. Ken McClellan for nurturing me at LANL. He taught me to look at the problem from a different perspective and gave me the opportunity to take my research in any direction I chose to pursue. I would also like to thank the rest of my committee members Dr. Phillipot, Dr. Baney, Dr. Sigmund, and Prof. Tulenko for their comments, both personal and scientific in nature, that helped me become a better scientist. I also need to thank Dr. Ebrahimi for her gentle push to enter graduate school and for both her academic and emotional support as I have pursued both of my graduate degrees.

I also need to thank all of the current and former members of Dr. Nino's research group. I have to give even more credit to the members who know me best: Shobit Omar, Lu Cai, Peng Xu, Wei, Qiu, Louis Perez, Laurel Wucherer, and Kevin Tierney for suffering through my idiosyncrasies and nagging with good humor and grace as I managed many of the day-to-day details of the group. I would also like to thank Donald Moore and Christina Chang for their help on some last minute details as I have prepared this dissertation.

I would like to thank all of the people at LANL that made it possible for me to perform my research. Some people at LANL that deserve special acknowledgement include Darrin Byler and John Dunwoody, for their help as I learned how to use the equipment and for being my first line of inquiry as I learned how to work through the LANL beaucrocity. Dr. Chris Stanek and Dr. Kurt Sickafus who were always available to answer a question or two; and Beverly Basey-Jones, for being the one person who suffered through most of my questions on paperwork and other tedious details. Dr. Luis Morales and Bob Houlton, for their assistance and support with the laser flash; Dr. Rob Dickerson, for his patience for those two months when I asked at least twice a week when the new SEM would be installed; and Dr. Pedro Peralta, for his introduction to orientation imaging microscopy.

I also need to thank a few people that made my internship at Idaho National Laboratory possible. Jon Carmack for mentoring me, Andrew Maddison for his help performing thermal diffusivity measurements, and Dr. Rory Kennedy for his technical expertise.

My family has supported me with their love and affection throughout my lengthy scholastic career. I need to acknowledge Randy, who has given me his love and unconditional support for the last nine years. I know he did not have any idea when I began working on this PhD four years ago that I would be gone for half of it, but he was still there even when I was 1700 miles away.

TABLE OF CONTENTS

	<u>page</u>
ACKNOWLEDGMENTS	3
LIST OF TABLES.....	9
LIST OF FIGURES	11
LIST OF ABBREVIATIONS AND TERMS	15
ABSTRACT.....	16
CHAPTER	
1 INTRODUCTION.....	18
1.1 Problem Statement and Motivation.....	18
1.2 Scientific Approach	20
1.3 Organization of the Dissertation.....	22
1.4 Contributions to the Field.....	24
2 BACKGROUND.....	25
2.1 Inert Matrix Materials	25
2.2 Particulate Composites	27
2.2.1 Constituents.....	27
2.2.1.1 MgO	27
2.2.1.2 Pyrochlores	29
2.2.2 Processing	31
2.2.3 Grain Growth	33
2.2.4 Microstructure	35
2.2.5 Characterization.....	36
2.3 Thermal Conductivity	37
2.3.1 Physics	37
2.3.2 Phonon Scattering	40
2.3.3 Effective Conductivity of Composites.....	42
3 COMPOSITE SELECTION AND PROCESSING.....	46
3.1 Pyrochlore Selection.....	46
3.2 Composite Composition.....	50
3.3 Experimental Procedures.....	51
3.3.1 Optical Microscopy	51
3.3.2 Scanning Electron Microscopy.....	51
3.3.3 Particle Size Analysis.....	52
3.3.4 X-ray Diffraction	52
3.4 Constituent Preparation and Processing	52
3.4.1 MgO.....	52
3.4.2 Nd ₂ Zr ₂ O ₇	54

3.5 Composite Processing	59
3.5.1 Dry vs. Aqueous Processes.....	61
3.5.2 Composite Processing Methods	62
3.5.2.1 Mortar and pestle	62
3.5.2.2 Spex blending	64
3.5.2.3 Magnetic bar stirring.....	66
3.5.2.4 Ball milling	68
3.6 Composite Pellet Fabrication	70
3.7 Conclusions	72
4 COMPOSITE CHARACTERIZATION	74
4.1 Introduction	74
4.2 Description of the Composite.....	74
4.3 Composite Characterization Methods.....	76
4.3.1 Heterogeneity Quantification.....	76
4.3.2 Homogeneity.....	77
4.3.3 Grain Size Measurements	78
4.3.4 Contiguity.....	79
4.4 Composite Characterization.....	79
4.4.1 Characterization of the Macrostructure.....	79
4.4.2 Characterization of the Microstructure	83
4.4.2.1 Homogeneity	85
4.4.2.2 Grain Size	86
4.4.2.3 Contiguity	87
4.4.3 Processing Defects	88
4.5 Conclusions	90
5 MACROSTRUCTURE—THERMAL DIFFUSIVITY RELATIONSHIP	93
5.1 Introduction	93
5.2 Laser Flash Thermal Diffusivity.....	93
5.3 Results and Discussion.....	97
5.4 Conclusions	102
6 MICROSTRUCTURE—THERMAL CONDUCTIVITY RELATIONSHIP	104
6.1 Introduction	104
6.2 Thermal Conductivity Calculation	104
6.3 Results and Discussion.....	105
6.4 Conclusions	115
7 BALL MILLING BATCH-TO-BATCH VARIATION ANALYSIS	117
7.1 Introduction	117
7.2 Process Selection	117
7.3 Batch Processing.....	119
7.4 Composite Characterization.....	120
7.4.1 Macrostructure Characterization.....	120
7.4.2 Microstructure Characterization	121
7.5 Composite Thermal Diffusivity and Thermal Conductivity	123

7.5.1 Thermal Diffusivity	123
7.5.2 Thermal Conductivity	124
7.6 Conclusions	127
8 SUMMARY AND FUTURE WORK.....	128
8.1 Summary.....	128
8.2 Future Work	133
8.2.1 Controlling the Agglomerates.....	133
8.2.2 Sintering Kinetics	134
8.2.3 Circumferential Crack Characterization	135
APPENDIX	
A DETAILS OF QUANTITATIVE STEREOLOGY	136
A.1 Details on the Characterization of the Macrostructure	136
A.2 Details on the Characterization of the Microstructure.....	138
B TABLES OF THERMAL CONDUCTIVITY VALUES	141
C SPECIFIC HEAT CAPACITY	143
C.1 Introduction.....	143
C.2 Differential Scanning Calorimetry	143
C.3 Results	145
D THERMAL EXPANSION MEASUREMENTS.....	148
D.1 Introduction.....	148
D.2 Dilatometry	148
D.3 Results.	150
E COMPOSITE GRAIN GROWTH AT 1550°C	154
E.1 Introduction.....	154
E.2 Experimental Procedure	154
E.3 Results.....	154
E.3.1 Microstructure Characterization.....	154
E.3.2 Grain Growth Kinetics.....	156
E.3.3 Thermal Conductivity	161
F COMPOSITE GRAIN GROWTH AT 1650°C	162
F.1 Introduction	162
F.2 Experimental Procedure	162
F.3 Results.....	162
F.3.1 Microstructure Characterization.....	162
F.3.2 Grain Growth Kinetics.....	164
F.3.3 Thermal Conductivity	169

LIST OF REFERENCES.....	171
BIOGRAPHICAL SKETCH	178

LIST OF TABLES

<u>Table</u>	<u>page</u>
2-1 Rock salt structure data.....	28
2-2 Pyrochlore ($A_2B_2O_6O'$) structure data with the origin at the B site. ³⁰	29
4-1 Quantitative stereology results for the MgO and $Nd_2Zr_2O_7$ heterogeneities	82
4-2 Homogeneity of the MgO and $Nd_2Zr_2O_7$ constituent phases in the interpenetrating matrix.....	85
4-3 Grain size of the MgO and $Nd_2Zr_2O_7$ constituent phases in the interpenetrating matrix.....	87
4-4 Contiguity of the MgO and $Nd_2Zr_2O_7$ constituent phases in the interpenetrating matrix.....	88
7-1 Quantitative stereology results for the heterogeneities in the ball milled composites.	121
7-2 Contiguity results for the microstructure in the ball milled composites.	122
A-1 Example of the Excel spreadsheet used to calculate the V_V and N_L for the composite constituents. This particular spreadsheet is for the magnetic bar stirred composites.	137
A-2 Example of an Excel spreadsheet with the intercept data and the grain size and contiguity calculations. This spreadsheet is for the Spex blended composites.	139
A-2 Continued	140
B-1 Thermal conductivity and corresponding error for composites processed by the four processing methods. The data was corrected to 0% porosity using Equation 6.2.....	141
B-2 Thermal conductivity and corresponding error for the ball milled composites. The data was corrected to 0% porosity using Equation 6.2.....	141
B-3 Thermal conductivity and corresponding error for the ball milled composites isothermally soaked at 1550 °C. The data was corrected to 0% porosity using Equation 6.2.	142
B-4 Thermal conductivity and corresponding error for the ball milled composites isothermally soaked at 1650 °C. The data was corrected to 0% porosity using Equation 6.2.	142
E-1 Grain sizes of the MgO and $Nd_2Zr_2O_7$ in the microstructure of the ball milled composites isothermally held for the given amount of time.....	156
E-2 Contiguity of the MgO and $Nd_2Zr_2O_7$ in the microstructure of the ball milled composites isothermally held for the given amount of time.....	156
E-3 Grain growth exponents, constants, and the correlation coefficient from the best fit to the grain growth equation. The activation energy of the grain growth is also included.	160
F-1 Grain sizes of the MgO and $Nd_2Zr_2O_7$ in the microstructure of the ball milled composites isothermally held for the given amount of time.....	164

F-2	Contiguity of the MgO and Nd ₂ Zr ₂ O ₇ in the microstructure of the ball milled composites isothermally held for the given amount of time.....	164
F-3	Grain growth exponents, constants, and the correlation coefficient from the best fit to the grain growth equation for the initial stage. The activation energy of grain growth is also included.	169
F-4	Grain growth exponents, constants, and the correlation coefficient from the best fit to the grain growth equation for the second stage. The activation energy of grain growth is also included.	169

LIST OF FIGURES

<u>Figure</u>	<u>page</u>
1-1 Inert matrix fuel loading in a light water reactor.....	19
1-2 The processing—microstructure—properties—performance interrelationships that form the basis for materials science and engineering.	21
2-1 Diagram showing the reprocessing strategy for IMF.....	25
2-2 Rock salt structure.....	28
2-3 Structure of pyrochlore.....	30
2-4 Pyrochlore structure.....	31
2-5 Processing defects related to the presence of inhomogeneities in the composite powder.....	32
2-6 Composite grain growth methods.....	34
2-7 The ten geometrically distinct patterns for two-phase composite connectivity.....	35
2-8 Schematic of the connectivity of the α phase in a composite with α and β phases as the contiguity of the α phase changes.....	36
2-9 Diagram of heat flow in a cylinder across a distance Δx with a temperature difference ΔT	38
2-10 The relationship between frequency and wave number for lattice vibrations of a linear chain of atoms alternating between masses m and M	39
2-11 Regions of thermal conductivity in a solid.....	40
2-12 Phonon scattering processes.....	41
2-13 Collision processes in a two-dimensional square lattice. The square represents the first Brillouin zone in the phonon k space.....	42
2-14 Schematic of the extreme cases of phase arrangement in composites.....	43
2-15 Comparison between the predicted effective thermal conductivity of the composites using arbitrary values of $\kappa_\alpha = 20$ and $\kappa_\beta = 1$	45
3-1 Cation anti-site defect formation energy for pyrochlores where the open diamonds are known pyrochlore compositions and the cross-hatched diamonds are compositions known to form defect fluorites.....	47
3-2 Contour map of the thermal conductivity at $T = 1473$ K of rare earth pyrochlores calculated from molecular dynamics simulations.	49
3-3 Equivalent burnup data for $\text{MgO—Nd}_2\text{Zr}_2\text{O}_7$ composite fuel compositions containing 8 vol% weapons grade PuO_2	50
3-4 SEM image of the calcined Cerac MgO.....	53
3-5 Particle size distribution of the calcined Cerac MgO.....	54
3-6 Flow chart for the solid state synthesis of $\text{Nd}_2\text{Zr}_2\text{O}_7$	55
3-7 XRD profile for synthesized $\text{Nd}_2\text{Zr}_2\text{O}_7$ calcined at 1350°C for 12 hours.....	56

3-8	Lattice parameter calculation for the synthesized $\text{Nd}_2\text{Zr}_2\text{O}_7$ where the data is fit to the given equation.	57
3-9	SEM image of the synthesized $\text{Nd}_2\text{Zr}_2\text{O}_7$	58
3-10	Particle size distribution of the synthesized $\text{Nd}_2\text{Zr}_2\text{O}_7$	59
3-11	Flow chart for the different composite synthesis methods.	60
3-12	XRD profiles of mixed, calcined, and sintered composites. In the aqueous processing methods the MgO transforms into $\text{Mg}(\text{OH})_2$ during mixing and requires an extra calcination step to transform the $\text{Mg}(\text{OH})_2$ back into MgO before sintering.	61
3-13	SEM images of the mixed composite powder for the mortar and pestle mixed composite powder.	62
3-14	Particle size distribution of the $\text{Nd}_2\text{Zr}_2\text{O}_7$ and MgO feed stock and synthesized composite powder for the mortar and pestle method.	63
3-15	SEM images of the mixed composite powder for the Spex blending method.	64
3-16	Particle size distribution of the $\text{Nd}_2\text{Zr}_2\text{O}_7$ and MgO feed stock and synthesized composite powder for the Spex blending method.	65
3-17	SEM images of the mixed composite powder for the magnetic bar stirring method.	66
3-18	Particle size distribution of the $\text{Nd}_2\text{Zr}_2\text{O}_7$ and MgO feed stock and synthesized composite powder for the magnetic bar stirring method.	67
3-19	SEM image of the mixed composite powder for the ball milling process.	69
3-20	Particle size distribution of the $\text{Nd}_2\text{Zr}_2\text{O}_7$ and MgO feed stock and synthesized composite powder for the ball milling method.	70
3-21	Furnace temperature profile for composite sintering.	71
4-1	Optical image of the composite macrostructure showing MgO and $\text{Nd}_2\text{Zr}_2\text{O}_7$ heterogeneities surrounded by the interpenetrating matrix.	75
4-2	Flow chart for the composite characterization methods.	76
4-3	Optical images of composite pellets synthesized by the four processing methods.	80
4-4	Composite of optical images from pellets processed by the four processing methods.	81
4-5	SEM images of the interpenetrating matrix for composites synthesized by the four processing methods.	84
4-6	SEM images of $\text{Nd}_2\text{Zr}_2\text{O}_7$ heterogeneities showing the interface between the heterogeneity and the interpenetrating matrix.	89
5-1	Schematic of a Netzsch LFA sample holder.	93
5-2	Cutaway schematic of a Netzsch LFA 457 laser flash analyzer.	94
5-3	Diagram of the laser pulse and measurement in laser flash thermal diffusivity.	95
5-4	Thermogram signal from the graphite standard showing the calculation of $t_{1/2}$	96
5-5	Temperature profile for laser flash thermal diffusivity measurements.	97
5-6	Corrected thermal diffusivity of pellets processed by the four processing methods.	99

6-1	Corrected thermal conductivity and corresponding error of the composites processed by the four processing methods.....	107
6-2	Comparison of the thermal conductivity of the composites between the different processing methods.	108
6-3	The contiguity—thermal conductivity relationship at 300 K and 1300 K.....	111
6-4	Thermal conductivity of the composites compared to the thermal conductivity of MgO ⁹³ , Nd ₂ Zr ₂ O ₇ ³² , and UO ₂	113
6-5	The thermal conductivity of the Spex blended and ball milled composites compared to the thermal conductivity of the composites calculated from the thermal conductivity of the constituents using Equations 2.5 through 2.9.....	114
7-1	Composite optical images of pellets processed from the three batches of ball milled composite powder	119
7-2	Optical images of the composites from the three batches of ball milled composite powder.....	120
7-3	SEM images of the composites from the three batches of ball milled composite powder.....	122
7-4	Compiled thermal diffusivity measurements of the ball milled composites.....	124
7-5	Thermal conductivity compilation for the three ball milling batches.....	125
7-6	The thermal conductivity and corresponding error of ball milled composites.....	126
A-2	Example of an optical image showing how N _i and P, and P _P were counted.....	136
A-3	Example of a SEM image with examples of both N _{αα} and N _{αβ} intercepts.....	138
C-1	Sample holder for the DSC 404C showing the two Pt alloy pans on the sample head.....	143
C-2	Cross-section of the Netzsch DSC 404C.	144
C-3	Furnace temperature profile for specific heat capacity measurements with a ramp rate of 20 °C/min.....	145
C-4	The measured specific heat capacity of the 70 vol% MgO—30 vol% Nd ₂ Zr ₂ O ₇ composite and the specific heat capacity of the composite calculated from the rule of mixtures and specific heat capacity	146
D-1	Netzsch DIL 402C dilatometer showing the measuring head and the sample furnace.....	148
D-2	Sample and spacer setup in the sample tube for thermal expansion measurements.....	149
D-3	Furnace profile for thermal expansion measurements with a ramp rate of 10°C/min.....	150
D-4	Thermal expansion of a mortar and pestle composite.....	151
D-5	Thermal expansion of a magnetic bar stirred composite.....	151
D-6	The thermal expansion of a Spex blended composite.....	152
D-7	Thermal expansion of a ball milled composite.....	152

E-1	Microstructures of ball milled composites isothermally held at 1550°C.....	155
E-2	Grain growth of MgO and Nd ₂ Zr ₂ O ₇ in ball milled composites.....	157
E-3	The grain size of the MgO compared to the grain size of the Nd ₂ Zr ₂ O ₇ showing a constant grain size ratio during grain growth.....	157
E-4	Determination of the grain growth exponent by calculating K for n = 2, n = 3, and n = 4. The line with the correct grain growth exponent has a slope that equals 1.....	158
E-5	Composite showing grain boundary diffusion of the Nd ₂ Zr ₂ O ₇ between the MgO—MgO grain boundary.....	159
E-6	Calculation of the activation energy for grain growth in the ball milled composites for the given grain growth exponents.	160
E-7	Thermal conductivity of the composites isothermally held for the given time at 1550°C.....	161
F-1	Microstructures of ball milled composites isothermally held at 1650°C.....	163
F-2	Grain size of ball milled composites isothermally held at 1650°C.	165
F-3	The grain diameter of the MgO vs. the grain diameter of the Nd ₂ Zr ₂ O ₇ showing the constant grain size ratio as the isothermal time increases.....	165
F-4	A log-log plot of the grain size vs. time showing the change in slope.	166
E-5	Calculation of the grain growth exponent for the initial stage of grain growth in the composites isothermally held at 1650°C.....	167
F-6	Calculation of the grain growth exponent for the second stage of grain growth in the composites isothermally held at 1650°C.....	167
F-7	The calculation of the activation energy for the initial stage of grain growth in the ball milled composites isothermally held at 1650°C.....	168
F-8	The calculation of the activation energy for the second stage of grain growth in the ball milled composites isothermally held at 1650°C.....	168
F-9	Thermal conductivity of composites isothermally held at 1650°C for the given time.	170

LIST OF ABBREVIATIONS AND TERMS

IM	Inert Matrix
IMF	Inert Matrix Fuel
CTE	Coefficient of Thermal Expansion
MOX	Mixed Oxide Fuel
EOL	End of Life
LWR	Light Water Reactor
Centerline Fuel Temperature	The temperature of the fuel at the center of the pellet during the operation of a nuclear reactor.
Spent Nuclear Fuel	Nuclear fuel that has been irradiated in a reactor to the point at which it can no longer help sustain a nuclear reaction.
Neutron Multiplication Factor (k_{eff})	The average number of neutrons that are released from the fission of one atom that can be absorbed by another atom. If $k < 1$ the mass is sub-critical and the system cannot sustain the critical reaction. When $k = 1$ the system is at critical mass. If $k > 1$ the mass is super-critical and the number of fission reactions will increase exponentially.
Minor Actinides	The actinides present in spent nuclear fuel other than uranium and plutonium. The minor actinides are responsible for a significant percentage of the radiotoxicity of spent nuclear fuel.
Mixed Oxide Fuel	Nuclear fuel consisting of plutonia dispersed in a urania matrix. Currently used to dispose of weapons grade plutonium by burning it in light water reactors.
Light Water Reactor	A nuclear reactor that uses water as a moderator to reduce the speed of neutrons to the lower velocity thermal neutrons. The most common types include boiling water reactors and pressurized water reactors.
Contiguity	Average fraction of surface area shared by a single phase with all of the neighboring grains of the same phase.

Abstract of Dissertation Presented to the Graduate School
of the University of Florida in Partial Fulfillment of the
Requirements for the Degree of Doctor of Philosophy

PROCESSING—THERMAL CONDUCTIVITY RELATIONSHIPS IN MgO—PYROCHLORE
COMPOSITE INERT MATRIX MATERIALS

By

Samantha J. Yates

May 2009

Chair: Juan C. Nino

Major: Materials Science and Engineering

Inert matrix (IM) materials are proposed to act as non-fertile matrices to burn excess plutonium and minor actinides in nuclear reactors. MgO is a good IM candidate because of its high thermal conductivity, good radiation resistance, and high temperature stability, but its hot water corrosion resistance is poor limiting its use in light water reactors. A composite approach has been suggested to improve the hydration resistance of the MgO by adding a pyrochlore phase to act as a hydration barrier while maximizing the effective thermal conductivity of the composite. In this work, MgO—Nd₂Zr₂O₇ composites are fabricated using four different processing methods to deliberately vary the microstructure thus enabling the investigation of processing—microstructure—thermal conductivity relationships in the composites.

The first processing—microstructure—property relationship that is developed is the effect of the composite processing method on the sample-to-sample variation in the thermal diffusivity. The processing method affects the formation of agglomerates in the mixed composite powders, and these agglomerates are the source of MgO and Nd₂Zr₂O₇ heterogeneities in the sintered composites. Differential sintering occurs in some of the agglomerates, resulting in the formation of circumferential cracks between the heterogeneity and the matrix. The presence of the circumferential cracks cause sample-to-sample variations of up to $\pm 2 \text{ Wm}^{-1}\text{K}^{-1}$ in the thermal conductivity between composites fabricated from the same

batch of mixed composite powder. This variation makes it more difficult to accurately and reliably predict the thermal conductivity of the composites.

The second processing—microstructure—property relationship developed describes the effect of the contiguity of the MgO on the average thermal conductivity of the composites. The processing method is found to affect the contiguity of the MgO in the composites. Lower MgO contiguity values cause the average thermal conductivity to decrease from $23 \text{ Wm}^{-1}\text{K}^{-1}$ to $20 \text{ Wm}^{-1}\text{K}^{-1}$ at 373 K. However, the thermal conductivity of the composites is found to be independent of microstructure after $\sim 1000 \text{ K}$. The thermal conductivity of the 70 vol% MgO—30 vol% $\text{Nd}_2\text{Zr}_2\text{O}_7$ composites is $\sim 7 \text{ Wm}^{-1}\text{K}^{-1}$ at 1273 K, which is virtually the same thermal conductivity as pure MgO at 1273 K.

Quantification of the amount of batch-to-batch variation in the thermal conductivity is investigated on one of the four composite processing methods since the processing method is found to affect the sample-to-sample variation between composites from the same batch of powder. Ball milling produces the most consistent microstructures with the highest average thermal conductivity, therefore two additional batches of ball milled composite powder are synthesized and composites are fabricated. Composite characterization shows that there is little variation between the microstructures of the composites fabricated from each batch of the ball milled composite powder, resulting in a combined average thermal conductivity of $24.0 \pm 0.6 \text{ Wm}^{-1}\text{K}^{-1}$ at 373 K and $6.8 \pm 0.2 \text{ Wm}^{-1}\text{K}^{-1}$ at 1273 K. Thus, ball milling is shown to produce IM composites with a consistent and predictable thermal conductivity.

CHAPTER 1 INTRODUCTION

1.1 Problem Statement and Motivation

Stockpiles of plutonium from dismantled nuclear weapons and spent nuclear fuel is considered to be a threat to national and international security. As of 1996, approximately 2000 metric tons (MT) of plutonium was estimated to exist in various stockpiles around the world.¹ Another 70 to 80 MT of new plutonium is generated every year and stored on-site at the 439 nuclear power plants in 30 different countries.² Along with the production of plutonium, the other minor actinides ^{237}Np , ^{241}Am + ^{243}Am , and ^{244}Cm are by-products of nuclear power. Minor actinides are of particular concern because in the case of ^{237}Np , the half-life is 2.1 million years. Long-term disposal of these actinides to manage their radiotoxicity is a complicated problem, and the disposal of the actinides from the spent nuclear fuel is a critical aspect of the fuel cycle.

There are main three strategies for the disposal of plutonium and the other minor actinides.³⁻⁸ The first one involves the use of nuclear reactors or accelerator driven systems to burn or transmute the plutonium and the other minor actinides. This approach involves reprocessing the spent nuclear fuel to recover the fissile material and the actinides to subsequently fabricate fuels or targets. The second approach is the direct disposal of the spent nuclear fuel into a repository. Unfortunately, this strategy would require a greater number of repositories to be built and monitored. The third option is a burn-and-bury hybrid approach where the spent nuclear fuel would be recycled, burned in a reactor, and disposed directly into a repository. However, calculations have shown that recycling a fuel or target multiple times maximizes the quantity of actinides burned or transmuted and minimizes the amount of waste that must be sent to a repository.⁹

The transmutation and burn-and-bury strategies require an inert matrix material to act as a stable non-fertile matrix to burn the plutonium or act as transmutation targets for the other minor actinides in light water reactors. Fuel rods containing the inert matrix fuel would replace a

fraction of the UO_2 in a light water reactor. Figure 1.1 is a schematic of a light water reactor core showing two inert matrix fuel types and possible variations in the packing of both the fuel assemblies and the fuel rods to maximize the transmutation of the plutonium and minor actinides in the inert matrix fuel. The first of the two fuel types being considered is a heterogeneous composite where inclusions of the fissile phase are suspended in the inert matrix material. The second is a homogeneous single-phase material that incorporates the fissile atoms into the crystal structure of the inert matrix material.

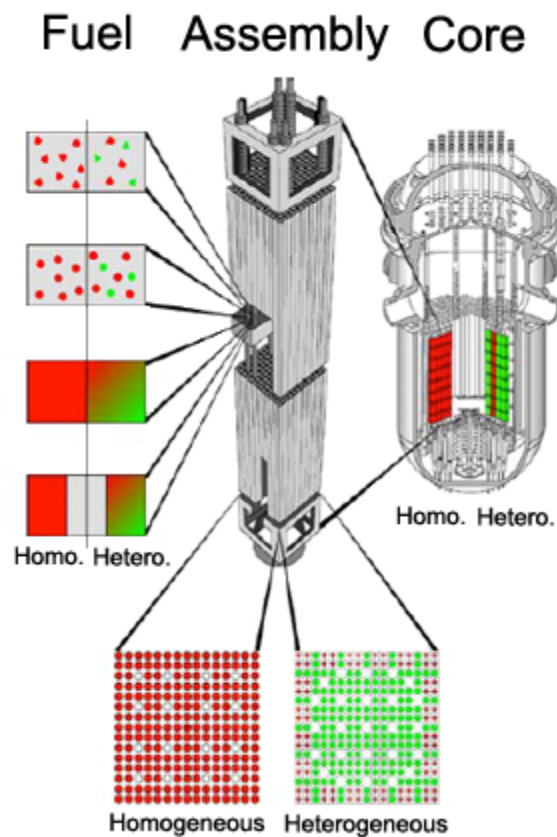


Figure 1-1: Inert matrix fuel loading in a light water reactor.⁵

A few of the properties a potential inert matrix material must possess include high temperature stability, good irradiation behavior, high thermal conductivity and reactor coolant compatibility.^{10;11} Although oxides adequately address most of these requirements, their primary disadvantage is their inherently low thermal conductivity when compared to other fuel types.¹²⁻¹⁵

The formation of defects and fission products during the irradiation of the fuel further decreases the thermal conductivity.¹⁶ A low thermal conductivity will result in an increase in the centerline fuel temperature of the fuel, making it more difficult to maintain a safe thermal margin between the centerline fuel temperature and the liquidus temperature of the fuel. Since inert matrix fuels (IMF) are intended to be used in current reactor design and operation, a potential IMF must possess a thermal conductivity to melting point ratio that meets or exceeds that of UO_2 .¹¹

Candidate composite IMFs have been investigated by multiple researchers around the world, but there is no consistency among these researchers in how the composites were processed.¹⁷⁻²² The inconsistencies in composite processing has produced considerable variations in the composite microstructures. Little, if any, attention has been given to analyzing the composite microstructures resulting from these composite processing methods. Furthermore, there is also very little work that has been done to determine the effect of the microstructures on the effective thermal conductivity of the composites. Thus, a clear relationship between composite processing and the effective thermal conductivity of the composites does not exist. This work focuses on maximizing the thermal conductivity of oxide IM composites by investigating the processing—microstructure—property relationships.

1.2 Scientific Approach

Oxides that have attracted the most attention as potential inert matrix materials include yttria-stabilized zirconia (YSZ), MgAl_2O_4 , and MgO . YSZ has many of the desired properties of an inert matrix material, but its thermal conductivity is poor and it is very difficult to reprocess.²³ MgAl_2O_4 has excellent thermal conductivity and hot water corrosion resistance, but its resistance to fission fragments during irradiation induces unacceptable amounts of swelling in the fuel.²⁴ MgO is an excellent IM candidate due to its high thermal conductivity, high melting point, good radiation tolerance, and its ability to be reprocessed in nitric acid, however, its hot water corrosion resistance is poor, limiting its use in light water reactors.

MgO—ZrO₂ composites attempt to improve the hot water corrosion resistance of MgO by adding ZrO₂ to act as a hydration barrier, and the composite exhibits an adequate thermal conductivity of ~6-9 Wm⁻¹K⁻¹ at 1273 K.²⁵ Zirconate pyrochlores are a promising composite constituent and evolutionary extension of the work on MgO—ZrO₂ composites because they allow a wide substitution of rare earth elements and some actinides, the structure is radiation tolerant, and molecular dynamics simulations have predicted slightly higher thermal conductivities than that of ZrO₂.²⁶⁻³¹ Lutique et al.³² reported thermal conductivities of ~5-7 Wm⁻¹K⁻¹ for MgO—Nd₂Zr₂O₇ composites at 1273 K.

Figure 1.2 illustrates the materials science paradigm where the processing—microstructure—property interrelationships affects the performance of the IMF. Establishing the processing—microstructure—thermal conductivity relationships is fundamental to being able to predict the performance of an IM. This work focuses on developing these interrelationships in MgO—pyrochlore composites in order to optimize the design and fabrication of the candidate IM.

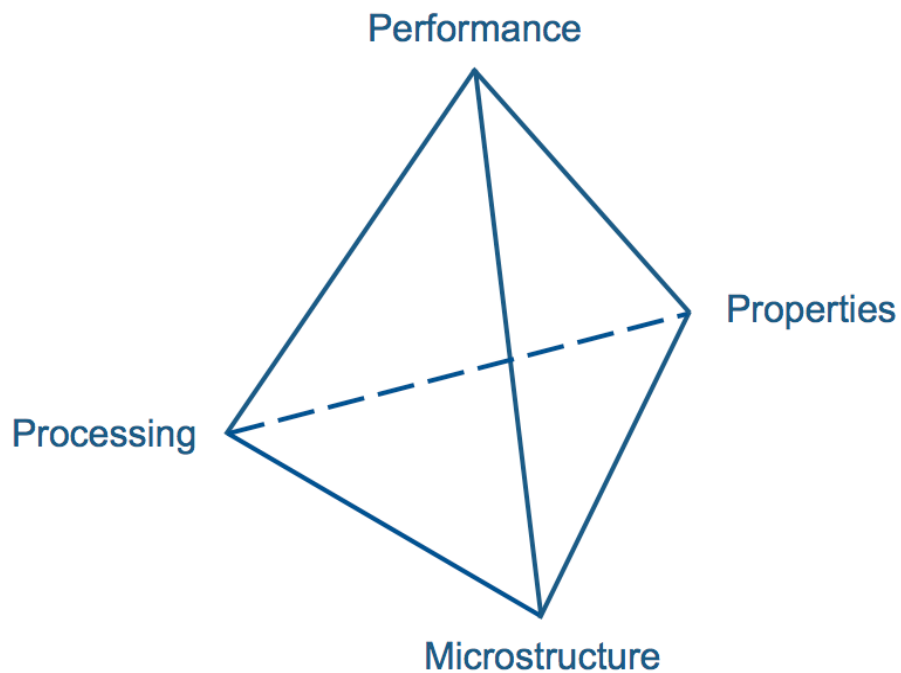


Figure 1-2: The processing—microstructure—properties—performance interrelationships that form the basis for materials science and engineering.³³

In this work, the investigation of the processing—microstructure relationship will begin by fabricating MgO—pyrochlore composites using a variety of composite processing methods intended to deliberately vary the microstructure of the composites. The mixed composite powders and resulting composite microstructures from the different processing methods are characterized to determine the effect of processing on the microstructure of the composites.

The investigation of the interrelationships continues by measuring the thermal diffusivity of the MgO—pyrochlore composites fabricated by the different processing methods. The thermal diffusivity results are analyzed and compared to the microstructures of the composites to establish the processing—thermal diffusivity relationship.

The thermal conductivity of the composites are then calculated from specific heat capacity, thermal expansion, and thermal diffusivity measurements. The thermal conductivity is compared to the results of the characterization of the composites to determine the microstructure—property relationship.

Finally, one of the processing methods is selected and two more batches of MgO—pyrochlore composite powder is synthesized. The composite microstructure is characterized and thermal diffusivity measured on the composites fabricated from the additional batches of composite powder. The grain growth kinetics of the composites processed by the selected processing method are then studied. The processing—microstructure—thermal conductivity relationships that emerge from the analysis of the characterization and measurements are used to predict the performance of the composite as an IM.

1.3 Organization of the Dissertation

Following this introduction, a brief background of topics pertinent to the analysis and discussion of the research in the following chapters is presented. Subjects covered in the background include an introduction to the thermal conductivity of non-metallic solids and the structure of the MgO and pyrochlores. The processing and structure of particulate composites

is also introduced, and the effect of the composite structure on the effective conductivity is briefly reviewed.

Chapter 3 begins with a discussion on the selection of the pyrochlore composition using neutronics, predicted radiation tolerance, and estimated thermal conductivities of zirconate pyrochlores. Following the selection of the pyrochlore composition through fuel burn-up simulations, the synthesis of the composite powder by four different processing method is described and the composite powder is characterized. The macrostructure and microstructure of the composites that are fabricated from the composite powder in Chapter 3 are characterized in Chapter 4 using quantitative stereology techniques. The processing—microstructure relationships are then analyzed.

Chapter 5 begins by describing the laser flash thermal diffusivity technique. The thermal diffusivity is then measured on the composites fabricated in Chapter 3 and characterized in Chapter 4. Chapter 5 concludes with the development of the macrostructure—thermal diffusivity relationship. Chapter 6 calculates the thermal conductivity of the composites using the thermal diffusivity measurements from Chapter 5. The microstructure—thermal conductivity relationship is then discussed.

Chapter 7 begins by selecting the best composite processing method based on the macrostructure, microstructure, and thermal conductivity of the composites. The chapter continues by describing the synthesis and characterization of two more batches of composites using the selected composite processing method. The thermal diffusivity of the two more batches was measured, and the three batches were analyzed for batch-to-batch consistency. The results of the processing, composite characterization, and thermal diffusivity can then be used to make a prediction about the performance of the IMF. The dissertation is summarized in Chapter 8 and a proposal for future work is presented. The grain growth kinetics of the composites is discussed in the appendices along with details of the quantitative stereology techniques and the experimental procedure and results for the specific heat capacity and

thermal expansion measurements. Tables of the thermal diffusivity and thermal conductivity values are also given.

1.4 Contributions to the Field

This work investigates the processing—microstructure—property relationships in 70 vol% MgO—30 vol% Nd₂Zr₂O₇ composites. The contributions of this investigation to the field of materials science and engineering are summarized below.

- Hard agglomerates in the mixed composite powders synthesized by the different processing methods causes circumferential cracks to form between the Nd₂Zr₂O₇ heterogeneities and the interpenetrating matrix. Variations in the density of the circumferential cracks are the source of sample-to-sample deviations in the effective thermal diffusivity of composite pellets fabricated from the same batch of mixed composite powder.
- The composite processing method affects the contiguity of the MgO in the composites. A decrease in the contiguity of the MgO within the composite microstructure results in a decrease in the effective thermal conductivity of the composite. This is the first time it has been shown that the contiguity of the thermally conductive phase directly affects the effective thermal conductivity of the composite, even as the volume fraction of the thermally conductive phase is held constant.
- Ball milled composites isothermally soaked at 1550°C exhibit normal grain growth controlled by grain boundary diffusion. Although the grain size increases as the isothermal soaking time increases, the contiguity of the MgO and Nd₂Zr₂O₇ remains the same. The effective thermal conductivity of the composites was independent of the isothermal soaking time. This indicates that the contiguity of the thermally conductive MgO determines the effective thermal conductivity of the composite, irrespective of grain size.

CHAPTER 2 BACKGROUND

A brief review of pertinent topics is presented to build a foundation for the fundamental understanding of the principles and relationships developed in this thesis. The following background is not intended to be the sum of knowledge for the particular topic, merely an introduction to the concepts that will be employed to analyze and discuss the results of this research.

2.1 Inert Matrix Materials

There has been a considerable amount of effort by several national and international research organizations to develop inert matrix materials that will incinerate plutonium and other minor actinides in thermal reactors, fast reactors, and accelerator driven systems. Inert matrix materials have the potential to utilize the plutonium for power generation, reduce the current stockpiles of plutonium, and manage the long-term radiotoxicity of spent nuclear fuel. A composite inert matrix fuel consists of a neutron-transparent inert matrix and the fissile phase.

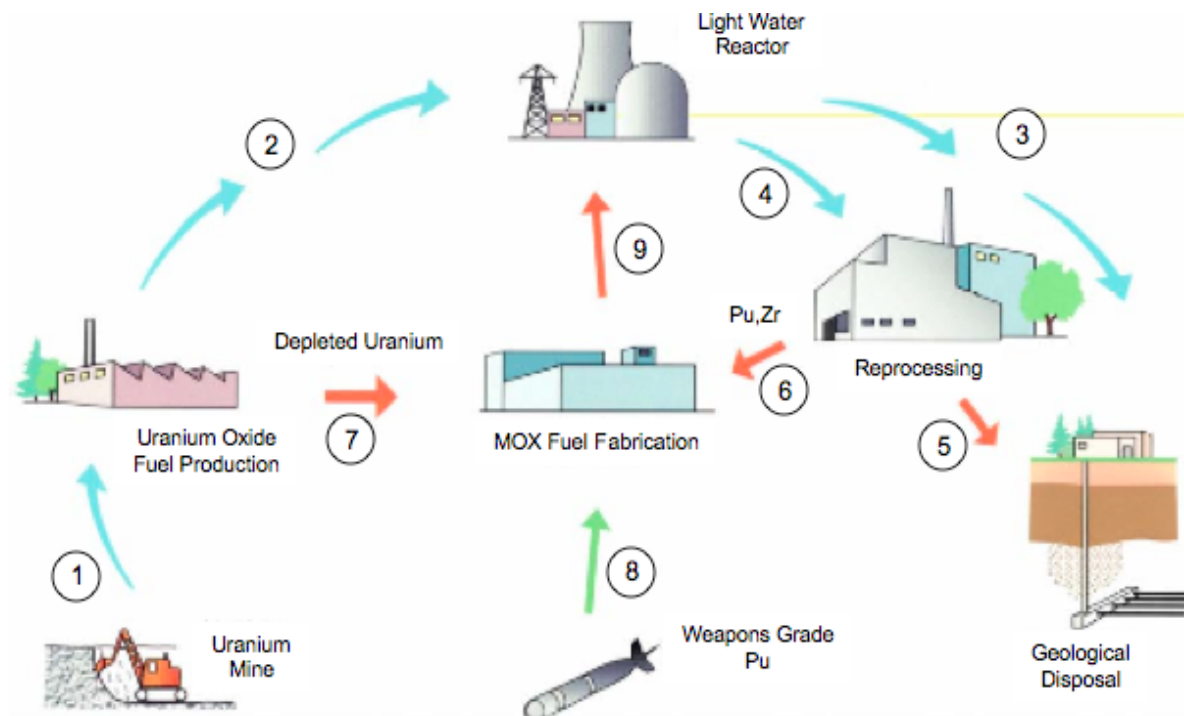


Figure 2-1: Diagram showing the reprocessing strategy for IMF.¹

Figure 2.1 shows the nuclear fuel cycle with different options to manage the spent nuclear fuel. The first is the once-through cycle shown by the arrows labeled 1, 2, and 3. The addition of a reprocessing step to extract the plutonium from the spent nuclear fuel is shown by the arrows 4 and 5. The fuel cycle is extended to accommodate mixed oxide (MOX) or IM fuels in steps 6-9. MOX fuels are currently being utilized in the world's commercial nuclear reactors to burn plutonium. Unfortunately, MOX fuels are not effective in quickly reducing the plutonium stockpiles because the MOX fuel produces more plutonium from the depleted uranium matrix as the plutonium incorporated into the fuel is incinerated. Therefore, IMs are being investigated because they will accelerate the burning and transmutation of plutonium because they will not generate more plutonium as the plutonium originally incorporated into the fuel is burned.

Neutronics, particularly the transparency of the potential IM to neutrons, is complemented by the physical properties of the candidate IM in order to select the most promising compositions for investigation. Desirable properties for an IM include high melting point, good thermal conductivity, limited swelling from neutron damage or fission products, good compatibility with the cladding, low solubility in the reactor coolant, good mechanical properties, and high density. Screening of the literature for candidate IM oxides has yielded multiple candidates, but YSZ and MgO have attracted the most attention. YSZ is an excellent candidate for a once-through fuel cycle, while MgO is an excellent candidate for a fuel cycle based on multi-recycling. Heterogeneous IMF composites have been investigated by multiple researchers, but there is a great deal of variation in the microstructures because there is no consistency in the processing method.^{19;21;34-37} In addition, microstructure defects such as interfacial de-bonding and differential sintering have been observed in these composites.^{36;37}

MgO composites have attracted the most attention as possible transmutation targets for the minor actinides. In fact, irradiation experiments performed by the Commissariat à l'Énergie Atomique (CEA) in the Phénix reactor has confirmed that MgO has passed its first set of tests for technical feasibility at the pin scale.³⁸ This work is being expanded by the CEA to include

the irradiation of MgO composites with microdispersed and macrodispersed fissile phases to determine the effect of the fissile particle size on the behavior of the IMF. Post-irradiation examination of these fuels is expected to begin in 2009.

Ronchi et al.³⁹ synthesized MgO—16 wt% Am_{2-x} composites, and the resulting composites had a thermal conductivity between ~6-9 Wm⁻¹K⁻¹ at 1273 K. MgO—UO₂ composites were tested as part of a study on the in-pile irradiation of potential IMF compositions and composites.⁴⁰ The images of the microstructures showed that the composites were heavily populated by UO₂ heterogeneities dispersed within the MgO matrix. Medvedev et al.^{25;37;41} investigated MgO—ZrO₂ composites to be used as a possible IM for light water reactors. Medvedev et al.²⁵ reported the thermal conductivity to be ~6-9 Wm⁻¹K⁻¹ at 1273 K on the MgO—ZrO₂ IM composite. Medvedev et al.³⁷ also synthesized MgO—ZrO₂—PuO₂ IMF composites. However, the SEM image of the microstructure shows interfacial de-bonding between the MgO—ZrO₂ matrix and the PuO₂ inclusions.

2.2 Particulate Composites

The following section is a summary of the processing and structure of particulate composites. The effective conduction of two-phase composites will also be discussed.

2.2.1 Constituents

The following section is a brief review of the structure of the MgO and pyrochlore composite constituents.

2.2.1.1 MgO

The Mg and O atoms in MgO are arranged in a rock salt NaCl structure. The symmetry of rock salt is $Fm\bar{3}m$ and is characterized by a 1:1 ratio of cations to anions. The Mg atoms are located in the corners and faces of the unit cell at the Wyckoff position 4a and the O atoms are located in the center of the cell edges and the center of the unit cell at the Wyckoff position 4b. The Mg atoms are surrounded by 6 O atoms and the O atoms are surrounded by 6 Mg atoms.

Table 2-1: Rock salt structure data.

Ion	Location	Coordinates
M	4a	0,0,0; 0,1/2,1/2; 1/2,0,1/2; 1/2,1/2,0
O	4b	1/2,1/2,1/2; 1/2,0,0; 0,1/2,0; 0,0,1/2

The lattice parameter of MgO is 4.2112 Å and the density is 3.58 gcm⁻³ according to the JCPDS 77-2179. A representation of the rock salt structure is shown below in Figure 2.2.

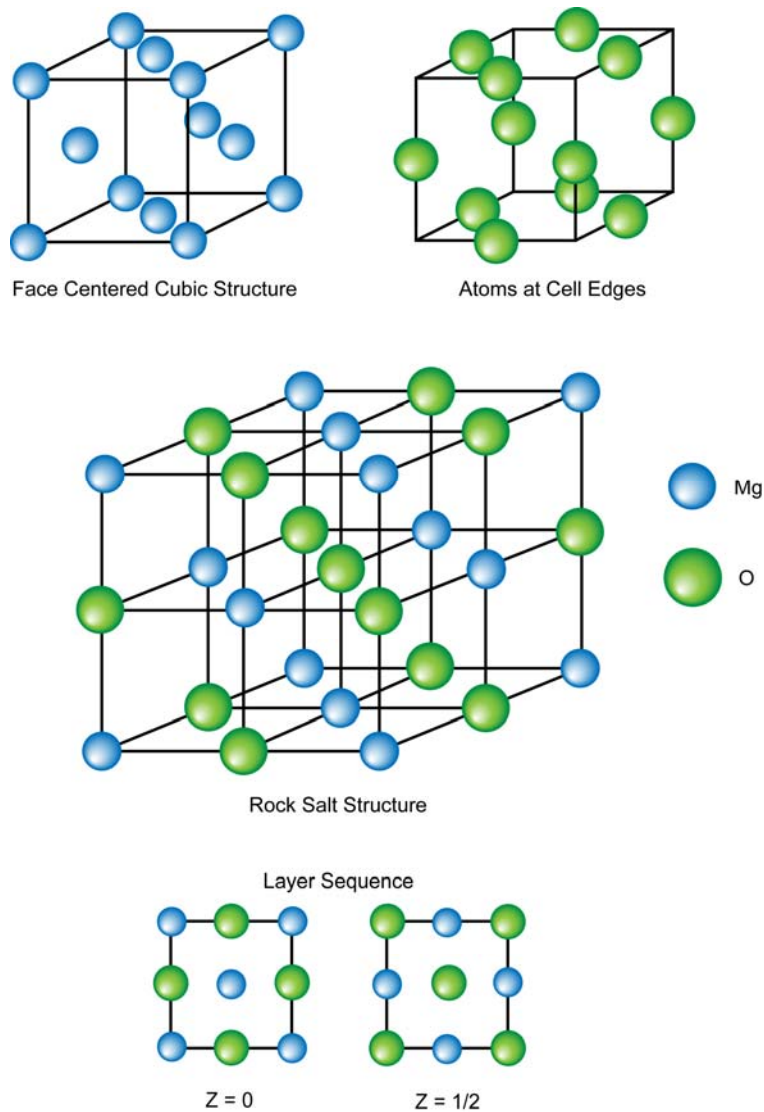


Figure 2-2: Rock salt structure.⁴²

2.2.1.2 Pyrochlores

The pyrochlore $A_2B_2O_6O'$ is cubic and possesses $Fd\bar{3}m$ symmetry with the larger A^{3+} ions in 8-fold coordination and the smaller B^{4+} ions in 6-fold coordination. There are 8 molecules per unit cell in the pyrochlore structure. The location of the atoms, site symmetry, and atomic coordinates of the unit cell are given in Table 2.1.

Table 2-2: Pyrochlore ($A_2B_2O_6O'$) structure data with the origin at the B site.³⁰

Ion	Location	Site Symmetry	Coordinates
			(0,0,0; 0,1/2,1/2; 1/2,0,1/2; 1/2,1/2,0) +
16A	16d	D_{3d}	1/2,1/2,1/2; 1/2,1/4,1/4; 1/4,1/2,1/4; 1/4,1/4,1/2
16B	16c	D_{3d}	0,0,0; 0,1/4,1/4; 1/4,0,1/4; 1/4,1/4,0
48O	48f	C_{2v}	x,1/8,1/8; -x,7/8,7/8; 1/4-x,1/8,1/8; 3/4+x,7/8,7/8 1/8,x,1/8; 7/8,-x,7/8; 1/8,1/4-x,1/8; 7/8,3/4+x,7/8 1/8,1/8,x; 7/8,7/8,-x; 1/8,1/8,1/4-x; 7/8,7/8,3/4+x
8O'	8b	T_d	3/8,3/8,3/8; 5/8,5/8,5/8
			x for regular octahedra: 0.3125 (5/16) x for regular cube: 0.3125 (3/8)

An elegant description of the pyrochlore structure is given by Galasso⁴². It is a anion deficient fluorite-derivative structure with a lattice parameter twice that of the fluorite unit cell. The unit cell of the pyrochlore can be divided into eight smaller cubes, half of which are type I and the other half of which are type II. The type I and type II cubes are shown in Figure 2.3 along with their positions in the unit cell. The A^{3+} and B^{4+} ions are located at the corner and in the faces of the cube and the O^{2-} ions are located in the tetrahedral spaces. In the Type I cube the A^{3+} ions are located on the face diagonals originating from the low left-hand corner and in the Type II cube the A^{3+} ions are located on the face diagonals originating from the upper right-hand corner of the cube.

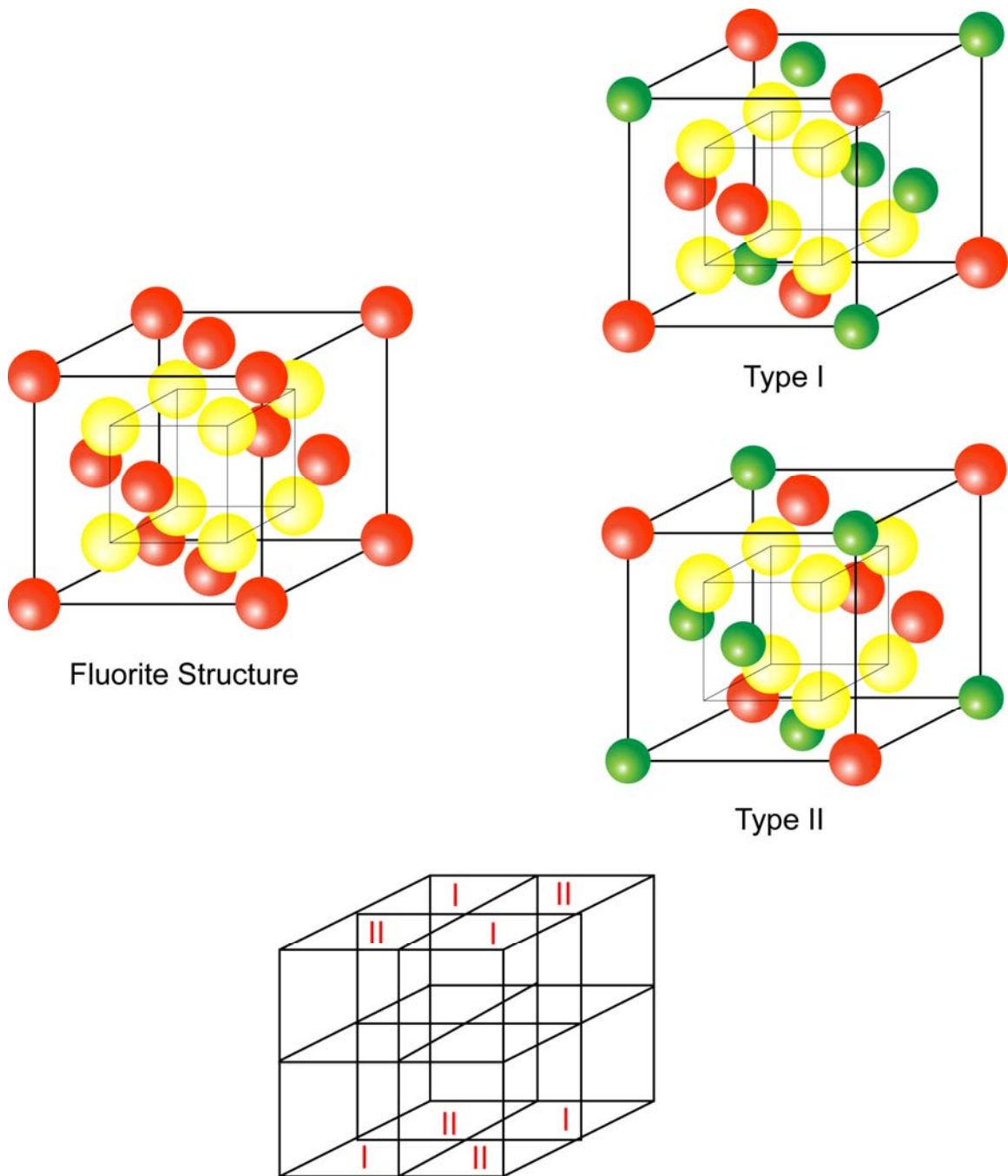


Figure 2-3: Structure of pyrochlore. ⁴²

A type I and type II cube has been placed diagonally across from each other in Figure 2.4 to show the arrangement of the A^{3+} and B^{4+} ions in the unit cell. The A^{3+} ions lie on the face diagonals of the unit cell starting at the upper right-hand and lower left-hand corner of the unit cell. However, the origin of the unit cell is conventionally located at the B-site.

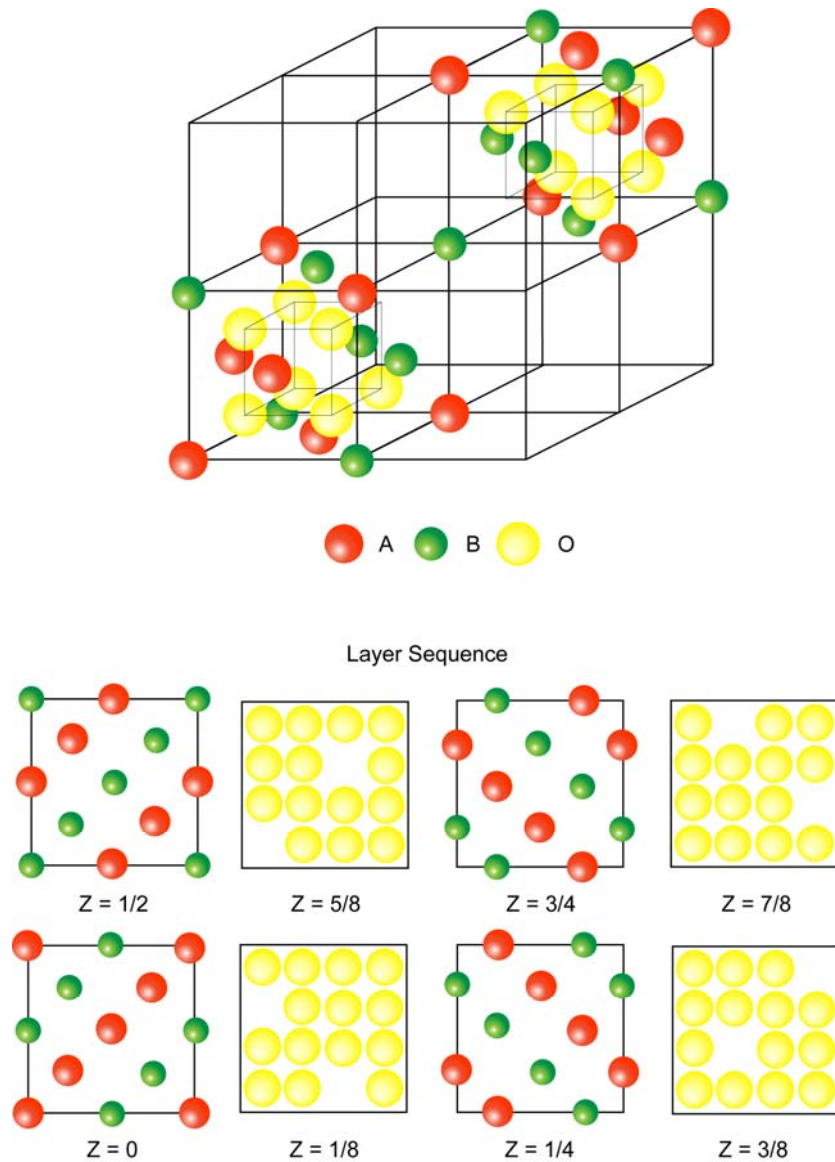


Figure 2-4: Pyrochlore structure.⁴²

2.2.2 Processing

Powder compacts are never homogeneous since they contain variations in packing density, distributions in pore sizes, and distributions in particle sizes. The presence of such inhomogeneities is concerning because they can become exaggerated during sintering, leading to a reduction in the densification rate and to the development of large pores and cracks during densification. Differential densification occurs when particular regions of a powder compact

densify at a different rate than the bulk. There is interaction between the different regions densifying at different rates, and this interaction causes transient stresses to develop during sintering. These stresses are transient because they rapidly shrink when densification is complete or when the temperature of the sample falls below temperatures at which sintering can take place.

Transient stresses are similar to the thermal stresses that develop in materials with different thermal expansion coefficients. This similarity will allow the internal stresses caused by the inhomogeneity to be modeled as a spherical core surrounded by a cladding with a different thermal expansion. If the rigid inhomogeneity shrinks slower than the surrounding matrix as in Figure 2.5a, a hydrostatic backstress is generated in the matrix that opposes the sintering stress and leads to a reduction in the densification rate of the composite. In Figure 2.5b slower shrinking inhomogeneities create circumferential or hoop stresses within the matrix, leading to radial cracking. When the inhomogeneity shrinks faster than the surrounding matrix, it can pull away from the matrix forming a circumferential crack as in Figure 2.5c.

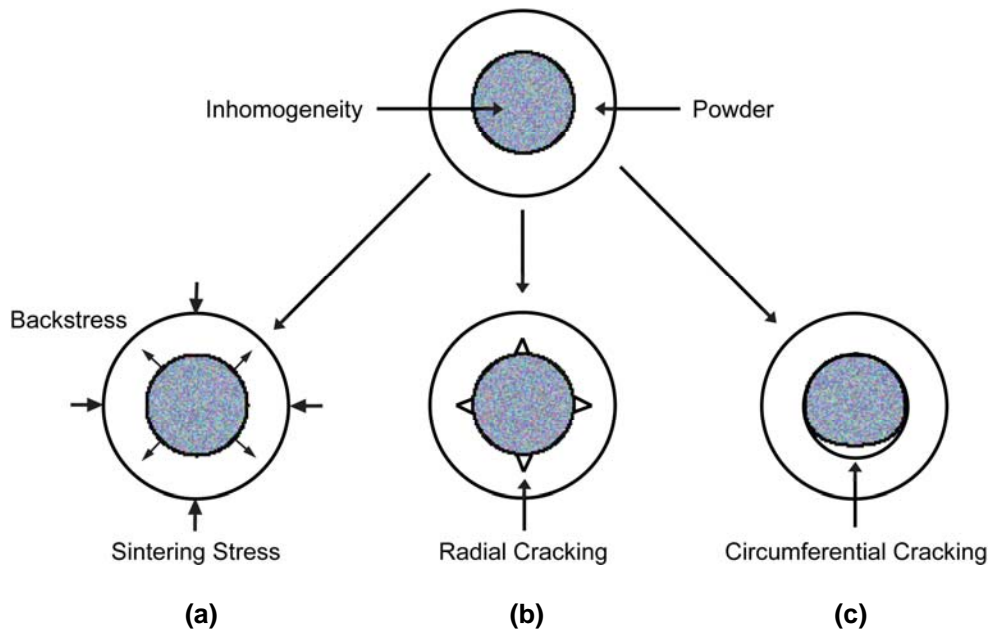


Figure 2-5: Processing defects related to the presence of inhomogeneities in the composite powder.⁴³

The number of inhomogeneities in the green compacts must be controlled in order to avoid the deleterious effects of differential sintering. Control of the inhomogeneities begins with controlling the powder quality and the pellet formation. Methods to manage inhomogeneities in powder compacts include the quantification of the inhomogeneities, the reduction of inhomogeneities, and mechanisms to reverse the structural damage that inhomogeneities create.

2.2.3 Grain Growth

The properties of the composite are controlled by the size and distribution of the phases in the microstructure. The grain growth kinetics for normal grain growth obeys Equation 2.1

$$D^n - D_0^n = Kt \quad (2.1)$$

where D is the grain diameter, D_0 is the grain diameter at t_0 , K is the grain growth constant, and n is the grain growth exponent. In two-phase composites the grain growth is inhibited because long range diffusion is limited. The grain growth of both phases is coupled since the constituents mutually constrain each other. The grain size ratio of the two phases will remain constant as the microstructure evolves.⁴⁴ The character of the microstructure will also remain constant as the scale of the microstructure increases.⁴⁵

The kinetics of grain growth in two-phase systems with coupled grain growth differ from single phase systems because of the presence of two simultaneously coarsening phases, contiguous minor phases, and high volume fractions of the minor phase. The interactions between the phases, the grain boundaries, and the inter-phase boundaries are topologically related, and can all serve as diffusion paths so the individual effects cannot be separated.^{44;46} Changes in the topology of the grains as the grains of both phases shrink, move, and grow alters the grain growth kinetics of the composite.

The topology of a two-phase composite can change by either mechanism depicted in Figure 2.6. In Figure 2.6a the second phase grows by an Ostwald ripening type of process

where the larger grains of the second phase will grow at the expense of the smaller grains. Figure 2.6b shows the second phase growing by coalescence. Since grain growth in a two phase composite is coupled, grain growth of both phases in the composite is constrained by the coarsening or coalescence of the slowest growing phase.

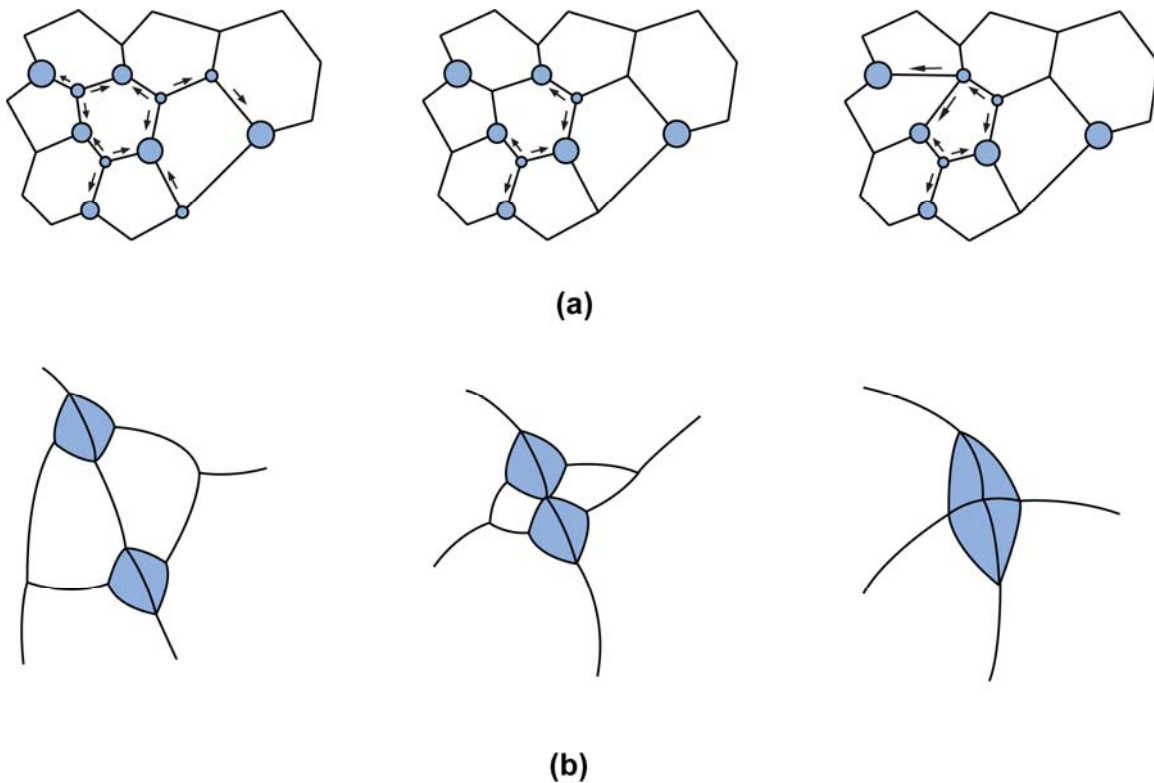


Figure 2-6: Composite grain growth methods.⁴⁷ A) Ostwald ripening B) coalescence

The grain growth exponent n predicts the grain growth mechanism in the composites. If the growth is controlled by the incorporation of the diffusing species into the interface of the growing grain then $n = 2$. Coupled grain growth by bulk diffusion has been reported to have a grain growth exponent of $n = 3$. An example of a system with this type of grain growth is α/β titanium alloys.^{48;49} Grain growth by grain boundary diffusion is expected to have a grain growth exponent of $n = 4$.^{44;50} In many systems, however, the grain growth is a mixture of these two mechanisms, and the grain growth exponent will fall between $n = 3$ and $n = 4$.^{47;51}

2.2.4 Microstructure

Two phase composites can be classified by their connectivity. The connectivity is the number of dimensions the phases in the composite are self-connected.⁵² Convention labels the active phase first and the inactive or inert phase last. Ten geometrically distinct composite connectivities are possible in two-phase composites: 0-0, 1-0, 2-0, 3-0, 1-1, 2-1, 3-1, 2-2, 3-2, 3-3, 0-1, 0-2, 0-3, 1-2, 1-3, and 2-3. Schematics of these composite connectivities are shown in Figure 2.11. The integers (0,1,2,3) indicate the dimensionality of the constituent phase. For example, a 2-1 composite connectivity means that the active phase is connected in two dimensions and the inactive phase is connected in one dimension. Dispersed composites have 0-1, 0-2, or 0-3 connectivity, while a 3-3 composite connectivity corresponds to a dual-phase interpenetrating microstructure.

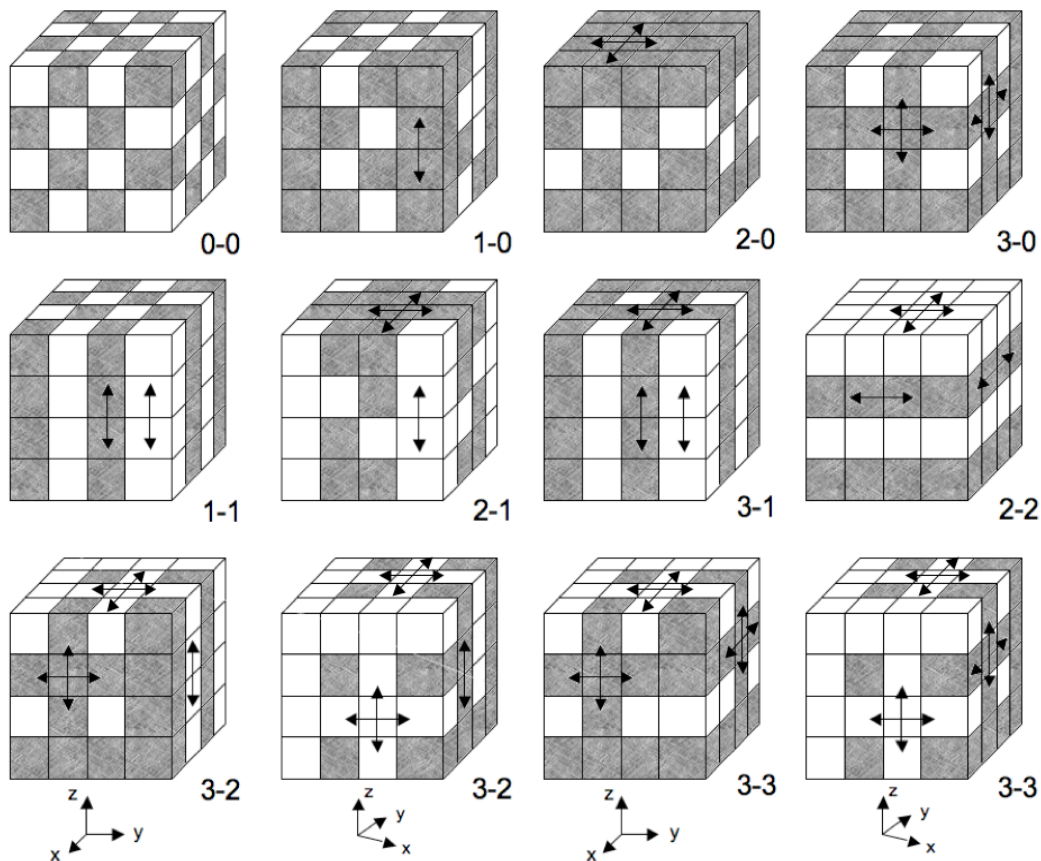


Figure 2-7: The ten geometrically distinct patterns for two-phase composite connectivity.⁵²

The connectivity of the composite will influence the effective properties. To maximize the conductivity of a two-phase composite, the active phase should have a connectivity of 3 to ensure the energy can flow throughout the composite in three dimensions. To minimize the effect of the low conductivity phase on the effective conductivity of the composite the inert or inactive phase should have a connectivity of 0. The best composite connectivity is 3-0 to maximize the conductivity of a two-phase composite where one phase has a high conductivity and the second phase has a low conductivity.

2.2.5 Characterization

The quantitative characterization of the geometric and topological parameters in a microstructure can be performed in a two-phase composite using well established techniques that have been extensively reviewed by Underwood.^{53;54} Key geometric features such as volume fraction, particle separation, and grain size can be quantitatively analyzed to accurately describe the microstructure of two-phase composites.

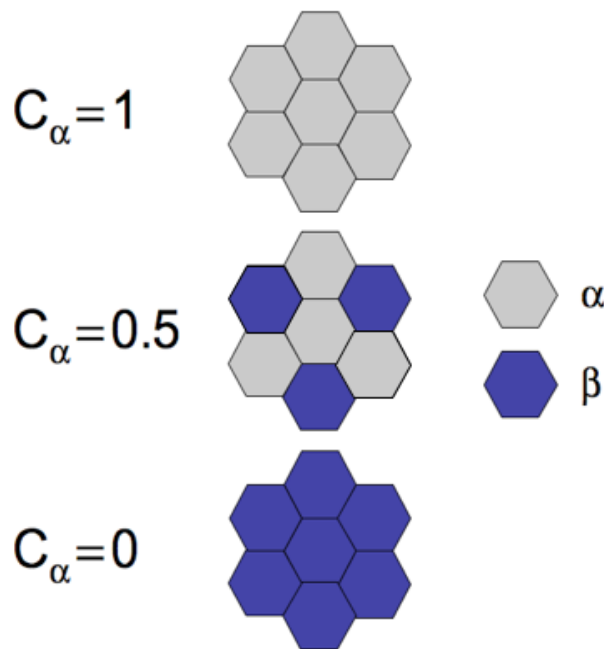


Figure 2-8: Schematic of the connectivity of the α phase in a composite with α and β phases as the contiguity of the α phase changes.

The topological parameter contiguity is useful to describe the amount of connectivity of the two phases in the composites. Gurland^{55,56} defines the contiguity as the average fraction of surface area shared by a grain of a particular phase with all of the neighboring grains of the same phase. The contiguity C_α of a material ranges from 0 to 1, where 1 is a material composed entirely of the α phase and 0 is a material composite of entirely the β phase. A schematic of composites with a range of C_α values is shown in Figure 2.8 to demonstrate the change in the connectivity of the α phase as function of C_α . Details of the procedure to calculate the contiguity of the α phase are given in Chapter 4 and Appendix A.

2.3 Thermal Conductivity

The following section is a brief review on the thermal conductivity in non-metallic solids.

2.3.1 Physics

When heat flows through a crystalline solid, in most cases the flow of heat per unit time is directly proportional to the temperature gradient and the cross-sectional area through which the heat is flowing. The constant that relates these two variables is the thermal conductivity of the material. In a situation such as the one shown below in Figure 2.9, the heat flows in the x -direction and the relationship can be described by Equation 2.2

$$\frac{\Delta Q}{\Delta t} = -\kappa A \frac{\Delta T}{\Delta x} \quad (2.2)$$

where κ is the thermal conductivity and A is the area. The expression is negative because positive $\Delta T/\Delta x$ would cause the heat to flow from the colder region to the hotter region. The thermal conductivity of a material is a second rank tensor and varies with crystallographic direction in anisotropic materials. The properties of polycrystalline composites are isotropic, therefore, the directional dependence of the thermal conductivity does not have to be addressed in this discussion.

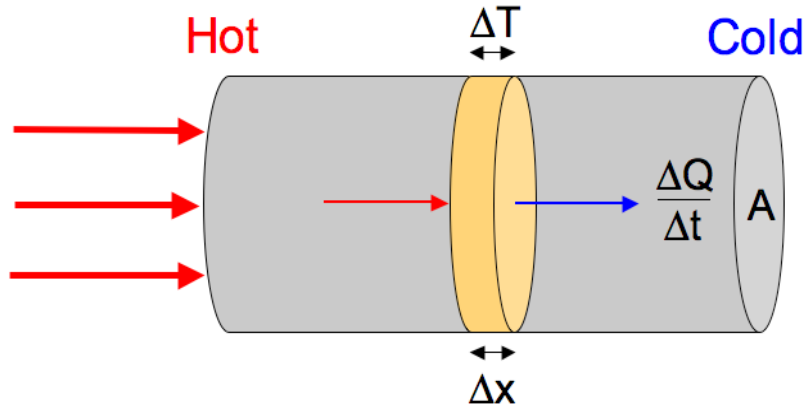


Figure 2-9: Diagram of heat flow in a cylinder across a distance Δx with a temperature difference ΔT .

Heat is conducted through the lattice of non-metallic solids by phonons. Two types of phonons carry thermal energy in materials that have two or more types of atoms in the unit cell. If you consider a simple diatomic lattice that contains two types of atoms with masses m and M , the relationship between the frequency and the wave number can be described by Equation 2.3

$$\omega^2 = \beta \left(\frac{1}{m} + \frac{1}{M} \right) \pm \beta \sqrt{\left(\frac{1}{m} + \frac{1}{M} \right)^2 - \frac{4 \sin^2 ka}{Mm}} \quad (2.3)$$

where β is the harmonic force constant and k is the wave number. This relationship is also represented graphically in Figure 2.10. The acoustic phonons carry the majority of the thermal energy, and they are characterized by lower frequencies compared to that of the optical phonons. The displacement of the two atoms in an acoustic wave at the long wavelength limit has the same amplitude, direction, and phase. In optical waves, the displacement of the two atoms in the unit cell at the long wavelength limit move opposite to one another with the atom with the lighter mass having a larger amplitude than the atom with the greater mass. Optical phonons are not efficient carriers of thermal energy, but they will affect the heat flow by interacting with the acoustic phonons.

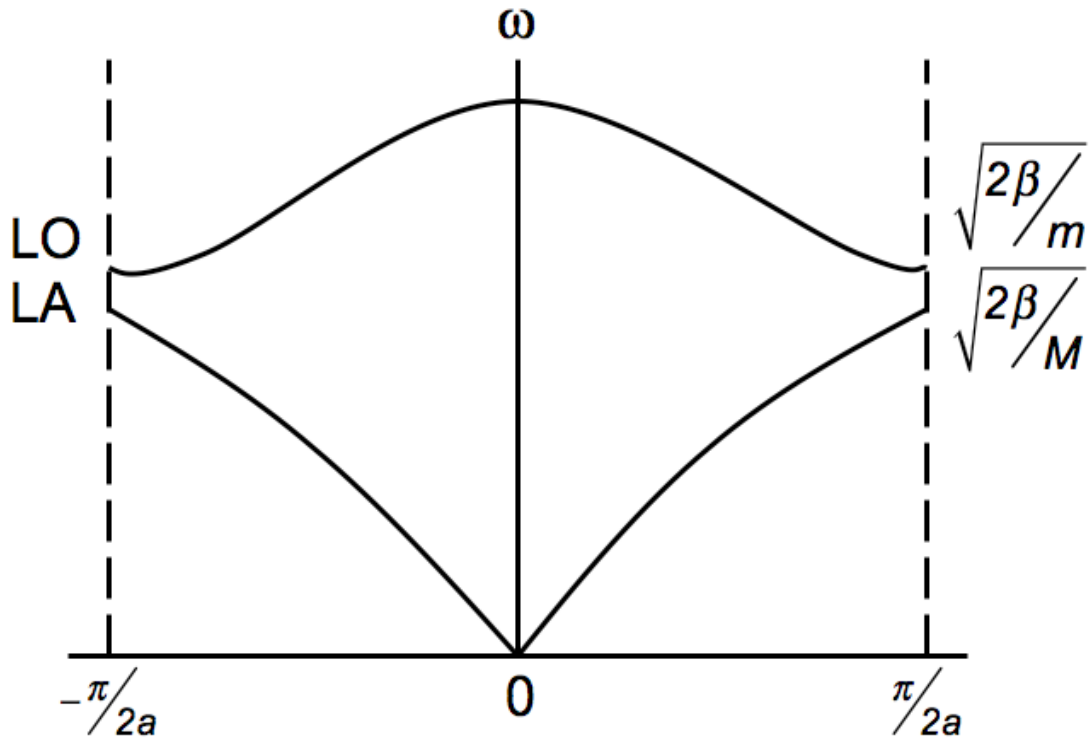


Figure 2-10: The relationship between frequency and wave number for lattice vibrations of a linear chain of atoms alternating between masses m and M .

The lattice conductivity is not infinite. The phonon mean free path is limited by collisions between phonons and lattice imperfections where energy and momentum is not conserved. The thermal conductivity of a material can be described by Equation 2.4

$$\kappa = \frac{1}{3} v_0 C_V \lambda \quad (2.4)$$

where v_0 is the velocity, C_V is the specific heat, and λ is the mean free path. Every scattering mechanism has a characteristic mean free path that reduces the thermal conductivity of the material.

The scattering mechanisms are additive, but the concept is simplified in Figure 2.11. In Region A there are only a few phonons that are excited at such low temperatures, therefore the collision processes between them are rare. The thermal conductivity is limited in this regime by the quantum T^3 dependence of the specific heat and yields a relationship where $\kappa \sim T^3$. The

maximum thermal conductivity occurs in Region B when mean free path for phonon—phonon scattering approximately equals the mean free path for phonon—defect scattering and follows a relationship where $\kappa \sim T^{-3/2}$. When the temperature exceeds the Debye temperature θ_D in Region C, the phonon—phonon scattering processes dominate. In Region D the thermal conductivity decreases less rapidly than the phonon—phonon scattering processes predict. There appears to be a saturation related to the fact that the mean free path cannot be shorter than the distance between two neighboring atoms. The next section will address the phonon—phonon scattering processes in Region C in more detail.

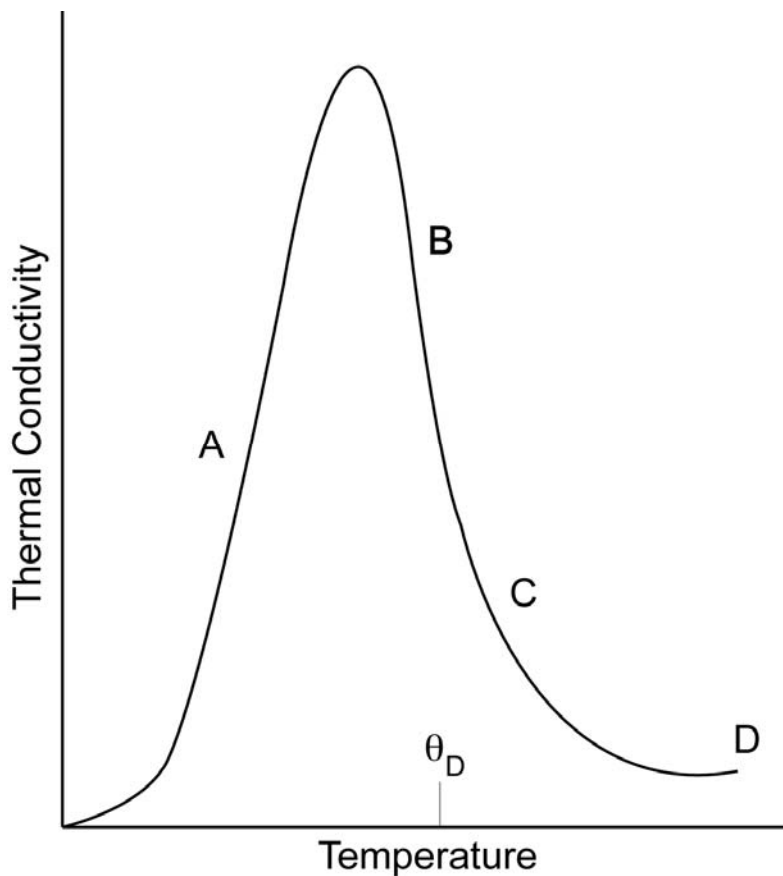


Figure 2-11: Regions of thermal conductivity in a solid.⁵⁷

2.3.2 Phonon Scattering

Phonon collisions that limit the thermal conductivity must involve three or more phonons.

Figure 2.12 has examples of simple three-phonon and four-phonon scattering processes. Four-

phonon scattering processes lead to a relationship where $\kappa \sim T^{-2}$. The phonon—phonon scattering at high temperatures is usually dominated by three-phonon processes, however, and in this case $\kappa \sim T^{-1}$ because the number of excited phonons is proportional to the temperature.

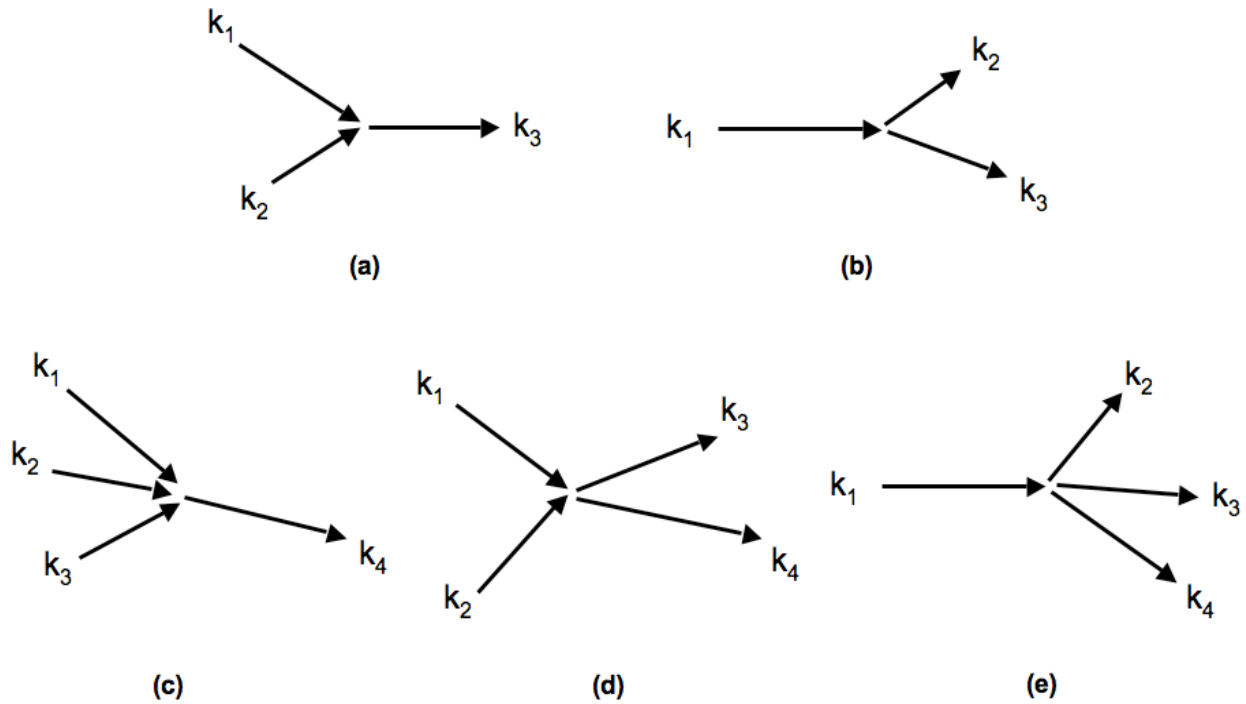


Figure 2-12: Phonon scattering processes. A-B) three-phonon C-E) four-phonon.⁵⁷

The three-phonon processes have the form $k_1 + k_2 = k_3 + nG$ where G is the reciprocal lattice vector and n is an integer. In normal processes energy is conserved and $n = 0$. Umklapp process occur when the energy is not conserved and $n \neq 0$. Figure 2.13 schematically shows the difference between normal processes where k is conserved and Umklapp processes where k is not conserved. In Figure 2.13a the vector k_3 does not exit the first Brillouin zone, therefore the momentum is conserved. However, in Figure 2.13b the vector $k_1 + k_2$ is emitted from the first Brillouin zone. The addition of the reciprocal lattice vector G will bring k_3 back to the first Brillouin zone. The resulting vector k_3 opposes the directional flow of the phonons, increasing the likelihood of phonon scattering and contributing to the thermal resistivity of the material.

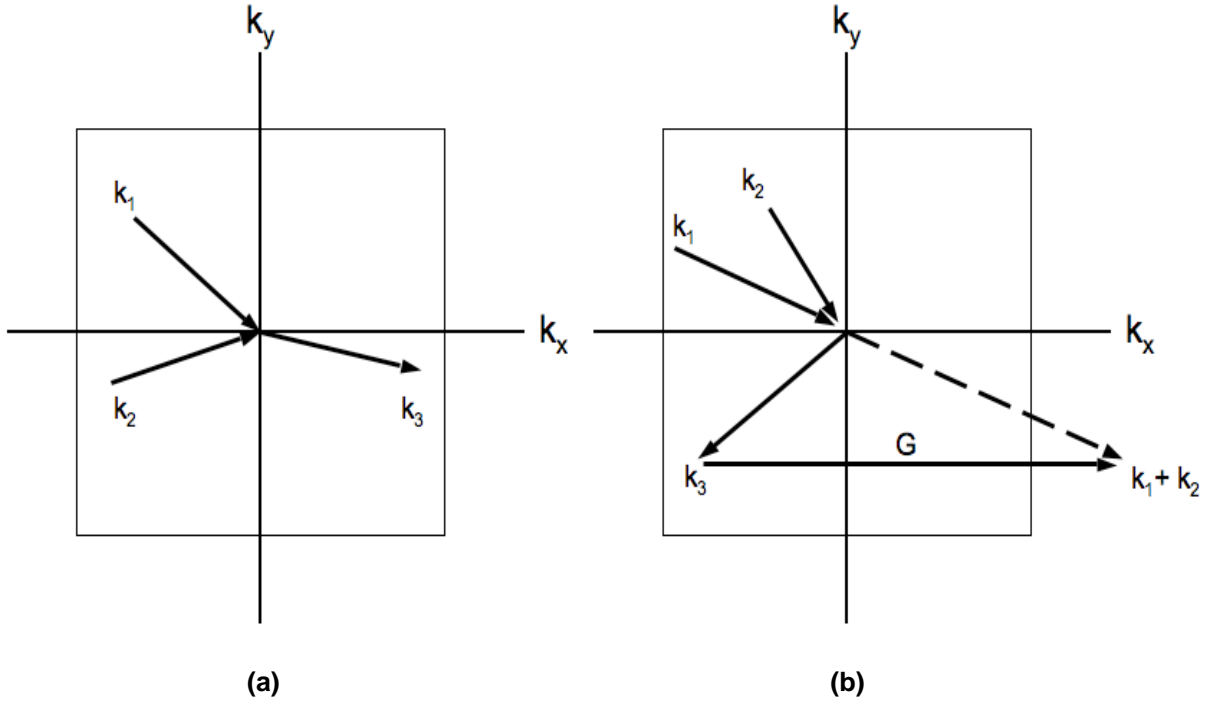


Figure 2-13: Collision processes in a two-dimensional square lattice. The square represents the first Brillouin zone in the phonon k space. A) normal B) Umklapp⁵⁸

2.3.3 Effective Conductivity of Composites

This is a brief introduction to the effective conductivity of composites and includes only a few of the basic models. To begin, there are two extreme arrangements of the phases in two-phase composites. The first is shown in Figure 2.14a where the phases are arranged parallel to the thermal flux. This arrangement of the phases produces the minimum thermal resistance and results in the maximum effective thermal conductivity according to Equation 2.5.

$$\kappa_e = \kappa_\alpha V_\alpha + \kappa_\beta V_\beta \quad (2.5)$$

where κ_e is the effective thermal conductivity of the composite, κ_α and κ_β are the thermal conductivities of the constituents, and V_α and V_β are the volume fractions of the constituents. If the phases are arranged perpendicular to the thermal flux as in Figure 2.14b the maximum thermal resistance occurs and the minimum effective thermal conductivity is calculated using Equation 2.6.

$$\kappa_e = \frac{\kappa_\alpha \kappa_\beta}{\kappa_\alpha V_\alpha + \kappa_\beta V_\beta} \quad (2.6)$$

Equations 2.5 and 2.6 are based on the rule of mixtures and form the highest upper bound (HUB) and lowest lower bound (LLB) of the effective conductivity of a composite.

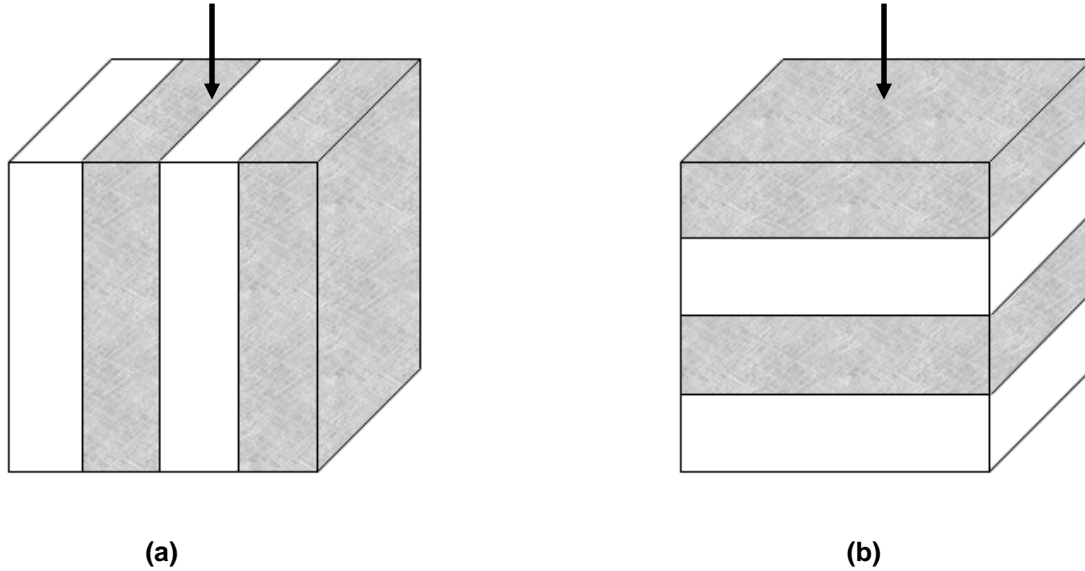


Figure 2-14: Schematic of the extreme cases of phase arrangement in composites. A) the phases are in series with the thermal flux yielding the maximum thermal conductivity B) the phases are in parallel with the thermal flux yielding the minimum thermal conductivity

Hashin and Shtrikman⁵⁹ narrowed the highest upper bound and lowest lower bound of composites by deriving another set of equations using the variational theory. Equation 2.7 corresponds to the highest upper bound of the Hashin—Shtrikman relationship and Equation 2.8 corresponds to the lowest lower bound of the Hashin—Shtrikman relationship.

$$\kappa_e^{UHS} = \kappa_\alpha + \frac{V_\beta}{1/(\kappa_\beta - \kappa_\alpha) + V_\alpha/3\kappa_\alpha} \quad (2.7)$$

$$\kappa_e^{LHS} = \kappa_\beta + \frac{V_\alpha}{1/(\kappa_\alpha - \kappa_\beta) + V_\beta/3\kappa_\beta} \quad (2.8)$$

where κ_e^{UHS} is the highest upper bound and κ_e^{LHS} is the lowest upper bound of the Hashin—Shtrikman relationship. The Hashin—Shtrikman equations have been shown to be the best estimates for the transport properties of macroscopically homogeneous and isotropic two-phase composites in terms of the transport properties and volume fraction of the constituents. However, their use is limited when there is a large difference between κ_α and κ_β because the difference between the upper and lower bounds becomes wider as the ratio between κ_α and κ_β increases making it more difficult to predict the effective conductivity of the composite.

The Maxwell—Eucken^{60;61} model assumes that the second phase is dispersed within a continuous matrix. The model assumes that the dispersed spheres are far enough apart that the local temperature distortions around each sphere do not interfere with each other. There are two forms of the Maxwell—Eucken model, depending on which phase is continuous and which phase is dispersed. If the continuous phase has a thermal conductivity of κ_α and the dispersed phase has a thermally conductivity of κ_β , then the effective conductivity of the composite can be calculated by Equation 2.9.

$$\kappa_e = \frac{\kappa_\alpha V_\alpha + \kappa_\beta V_\beta \frac{3\kappa_\alpha}{2\kappa_\alpha + \kappa_\beta}}{V_\alpha + V_\beta \frac{3\kappa_\alpha}{2\kappa_\alpha + \kappa_\beta}} \quad (2.9)$$

The effective conductivities calculated from Equations 2.5 through 2.9 for a composite with arbitrarily selected κ_α and κ_β values of 20 Wm⁻¹K⁻¹ and 1 Wm⁻¹K⁻¹ respectively, are plotted in Figure 2.15 as a function of the volume fraction of the dispersed β phase. The highest upper bound (HUB) and lowest lower bound (LLB) of the composite defines the maximum and minimum possible effective thermal conductivity. The Hashin—Strikman relationship narrows the HUB and LLB, improving the effective thermal conductivity predictions. The Maxwell—Eucken relationship predicts that the effective thermal conductivity of the composite is in between the upper Hashin—Strikman (UHS) and lower Hashin—Strikman (LHS) bounds.

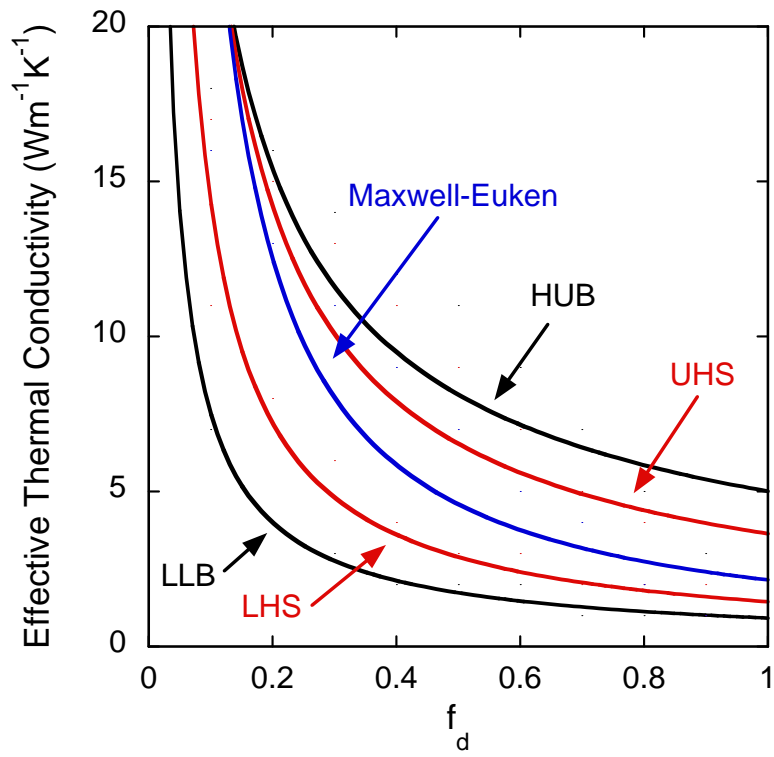


Figure 2-15: Comparison between the predicted effective thermal conductivity of the composites using arbitrary values of $\kappa_\alpha = 20$ and $\kappa_\beta = 1$.

CHAPTER 3 COMPOSITE SELECTION AND PROCESSING

3.1 Pyrochlore Selection

The specific pyrochlore used in the fabrication of the MgO composites was selected based on the composition with the best combination of neutronics, radiation tolerance, and thermal conductivity. The search was confined to the zirconate pyrochlores because of the interest ZrO_2 has generated as a possible inert matrix.⁶² This section describes the winnowing of the zirconate pyrochlores using thermal neutron absorption cross-sections, the predicted radiation tolerance, and simulated thermal conductivities of the candidate compositions. The final composition $Nd_2Zr_2O_7$ was then chosen from the candidate compositions based on its better combination of properties over that of the other candidates.

A number of the rare earth oxides are known neutron poisons, therefore, a table of thermal neutron absorption cross-sections was consulted in order to eliminate unsuitable rare earth zirconate pyrochlores as candidates.⁶³ Nuclear science and engineering collaborators set the threshold for the thermal neutron absorption cross-section of the rare earth oxides at approximately 50 barns.⁶⁴ A survey of the rare earth elements resulted in a list of rare earth oxides with adequately low thermal neutron absorption cross-sections that are also known to form zirconate pyrochlores. The list of candidate zirconate pyrochlores that satisfied the criteria includes $La_2Zr_2O_7$, $Pr_2Zr_2O_7$, and $Nd_2Zr_2O_7$.

The next property examined was the predicted radiation tolerance of the candidate pyrochlore compositions. Radiation tolerance is defined as the ability of a particular crystal structure to withstand irradiation without amorphization. The radiation tolerance of candidate rare earth pyrochlore compositions has been predicted by Sickafus et al.²⁷ through the calculation of cation anti-site defect energies. The cation anti-site defect energy is defined as the energy required to switch the A^{3+} and B^{4+} cations on the pyrochlore lattice. The pyrochlore compositions that are more willing to accommodate such defects have lower cation anti-site

defect energies than those compositions with higher cation anti-site defect energies, and are therefore considered to be more radiation tolerant. When the cation anti-site defects in a pyrochlore structure are allowed to accumulate, it will cause the pyrochlore to degenerate into a disordered fluorite, but it will not be amorphized. Therefore, by applying the criterion that pyrochlores with lower cation anti-site defect energies are more radiation tolerant than pyrochlores with higher cation anti-site defect energies, $\text{La}_2\text{Zr}_2\text{O}_7$ is the least radiation tolerant of the candidate pyrochlores and $\text{Nd}_2\text{Zr}_2\text{O}_7$ is the most radiation tolerant of the candidate pyrochlore compositions.

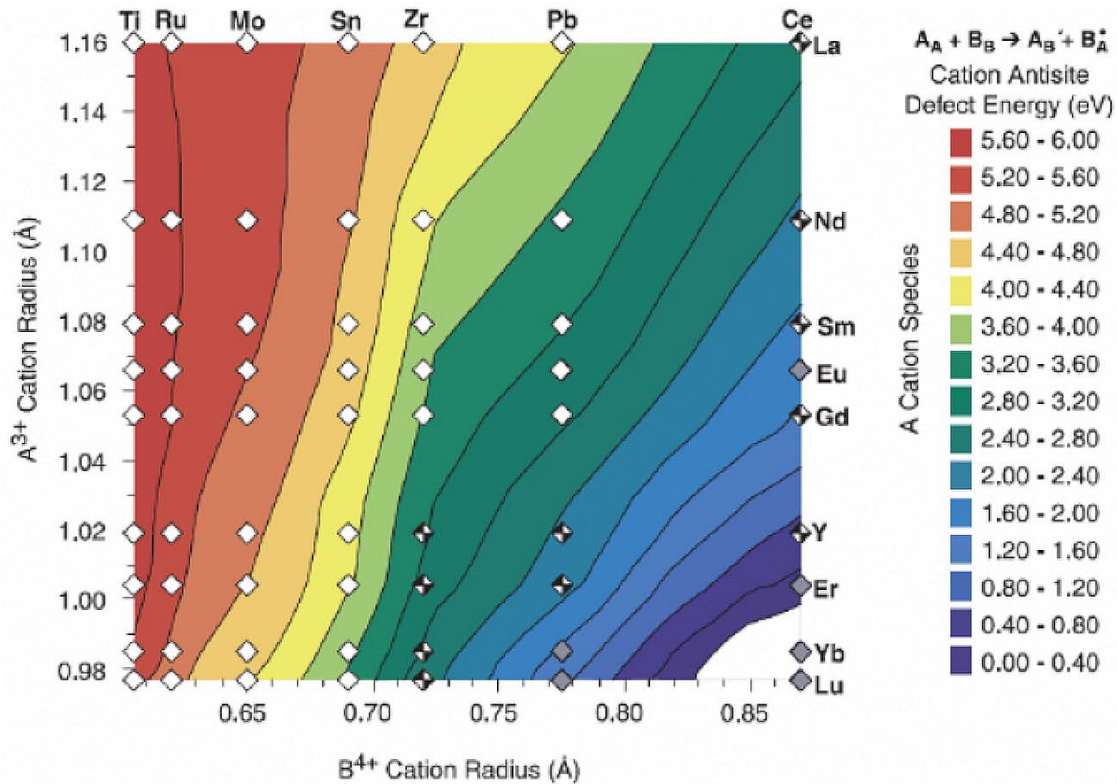


Figure 3-1: Cation anti-site defect formation energy for pyrochlores where the open diamonds are known pyrochlore compositions and the cross-hatched diamonds are compositions known to form defect fluorites. Compositions in grey are not known to exist.²⁷

The predicted cation anti-site defect energies are summarized in Figure 3.1 for a range of rare earth pyrochlore compositions. Focusing on the three candidate compositions of

$\text{La}_2\text{Zr}_2\text{O}_7$, $\text{Pr}_2\text{Zr}_2\text{O}_7$, and $\text{Nd}_2\text{Zr}_2\text{O}_7$, it is observed that the cation anti-site defect energy decreases with increasing rare earth cation radius from La^{3+} to Nd^{3+} . This trend agrees with the conclusion made by Sickafus et al. that the cation anti-site defect energy is lower in compositions where there is a smaller size difference between the A^{3+} and B^{4+} ions than in compositions where there is a larger size difference between the A^{3+} and B^{4+} ions.

The third criterion for the final selection of the pyrochlore composition from the candidates is the predicted thermal conductivity of the pyrochlore candidates. A contour map showing the thermal conductivity of rare earth pyrochlores predicted by Schelling et al.²⁶ through molecular dynamics simulations is shown in Figure 3.2. Focusing in again on the three candidate compositions $\text{La}_2\text{Zr}_2\text{O}_7$, $\text{Pr}_2\text{Zr}_2\text{O}_7$, and $\text{Nd}_2\text{Zr}_2\text{O}_7$, the simulated thermal conductivity of $\text{Pr}_2\text{Zr}_2\text{O}_7$ of $\sim 2 \text{ Wm}^{-1}\text{K}^{-1}$ is slightly higher than that of $\text{La}_2\text{Zr}_2\text{O}_7$ and $\text{Nd}_2\text{Zr}_2\text{O}_7$ at $1.98 \text{ Wm}^{-1}\text{K}^{-1}$ and $1.83 \text{ Wm}^{-1}\text{K}^{-1}$, respectively. These predictions indicate that in terms of thermal conductivity, $\text{Pr}_2\text{Zr}_2\text{O}_7$ has a slight advantage over the other candidate pyrochlore compositions $\text{La}_2\text{Zr}_2\text{O}_7$ and $\text{Nd}_2\text{Zr}_2\text{O}_7$.

Schelling et al. also compiled experimental thermal conductivities for the zirconate pyrochlores to compare to the simulated thermal conductivities. The experimental thermal conductivity for $\text{La}_2\text{Zr}_2\text{O}_7$ has been measured to be $\sim 1.5 \text{ Wm}^{-1}\text{K}^{-1}$ by Vassen et al.⁶⁵ and Suresh et al.⁶⁶ and the thermal conductivity for $\text{Nd}_2\text{Zr}_2\text{O}_7$ has been measured to be $1.33 \text{ Wm}^{-1}\text{K}^{-1}$ and $1.6 \text{ Wm}^{-1}\text{K}^{-1}$ by Lutique et al.³² and Wu et al.⁶⁷. Although $\text{Pr}_2\text{Zr}_2\text{O}_7$ has not been experimentally measured, the difference between the predicted and experimentally measured thermal conductivity of $\text{Sm}_2\text{Zr}_2\text{O}_7$ can be used to infer the relationship between the predicted and experimentally measured thermal conductivity of $\text{Pr}_2\text{Zr}_2\text{O}_7$. The simulation for $\text{Sm}_2\text{Zr}_2\text{O}_7$ predicts the thermal conductivity of the pyrochlore to be $2.09 \text{ Wm}^{-1}\text{K}^{-1}$, however, experimentally the thermal conductivity has been shown to be $1.5 \text{ Wm}^{-1}\text{K}^{-1}$ by Wu et al.⁶⁷ and Suresh et al.⁶⁶. The difference between the experimental and simulated thermal conductivity is most likely due to the presence of defects, impurities, and grain boundaries in the bulk ceramic that are not

present in the molecular dynamics simulations. This suggests that although the thermal conductivity of $\text{Pr}_2\text{Zr}_2\text{O}_7$ is predicted to be higher than that of $\text{La}_2\text{Zr}_2\text{O}_7$ and $\text{Nd}_2\text{Zr}_2\text{O}_7$, it is likely that experimentally there is little to no difference in the thermal conductivity between the three candidate pyrochlore compositions.

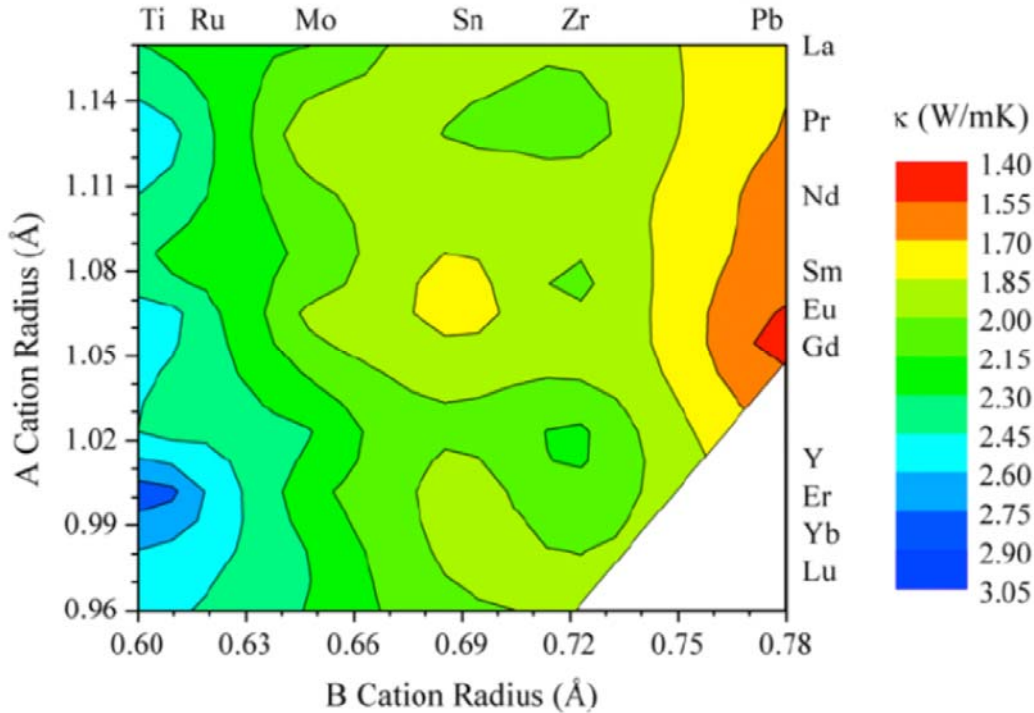


Figure 3-2: Contour map of the thermal conductivity at $T = 1473$ K of rare earth pyrochlores calculated from molecular dynamics simulations.²⁶

In summary, analysis of the thermal neutron absorption cross-sections, predicted radiation tolerance, and simulated thermal conductivities of zirconate pyrochlores does not yield a pyrochlore composition that has significant advantages over the other pyrochlore candidates. Examination of the thermal neutron absorption cross-sections narrowed the candidate pyrochlore compositions to $\text{La}_2\text{Zr}_2\text{O}_7$, $\text{Pr}_2\text{Zr}_2\text{O}_7$, and $\text{Nd}_2\text{Zr}_2\text{O}_7$. The predicted radiation tolerance of the candidate pyrochlore compositions indicates radiation tolerance increases with increasing Ln^{3+} radius with $\text{La}_2\text{Zr}_2\text{O}_7$ being the least radiation tolerant and $\text{Nd}_2\text{Zr}_2\text{O}_7$ being the most radiation tolerant. However, there does not appear to be a candidate pyrochlore composition with a clear advantage over the other candidates in terms of thermal conductivity. Radiation

tolerance was the only criteria that resulted in a distinguishable difference in the predicted behavior of the candidate pyrochlore compositions, therefore, the pyrochlore composition $\text{Nd}_2\text{Zr}_2\text{O}_7$ was chosen because it is predicted to be more radiation tolerant than $\text{La}_2\text{Zr}_2\text{O}_7$ and $\text{Pr}_2\text{Zr}_2\text{O}_7$.

3.2 Composite Composition

The ratio of the $\text{Nd}_2\text{Zr}_2\text{O}_7$ to MgO in the composite was chosen using equivalent burn-up data calculated using MONTEBURNS⁶⁸ and MCNP⁶⁹ by J. Wang based on a fuel cycle of 2000 full power days, or the equivalent of 60 MWdkg^{-1} . Simulations were performed on three different ratios of the constituents and compared to the equivalent burn-up for mixed oxide fuel (MOX) using 8 vol% weapons grade PuO_2 as the fissile phase.

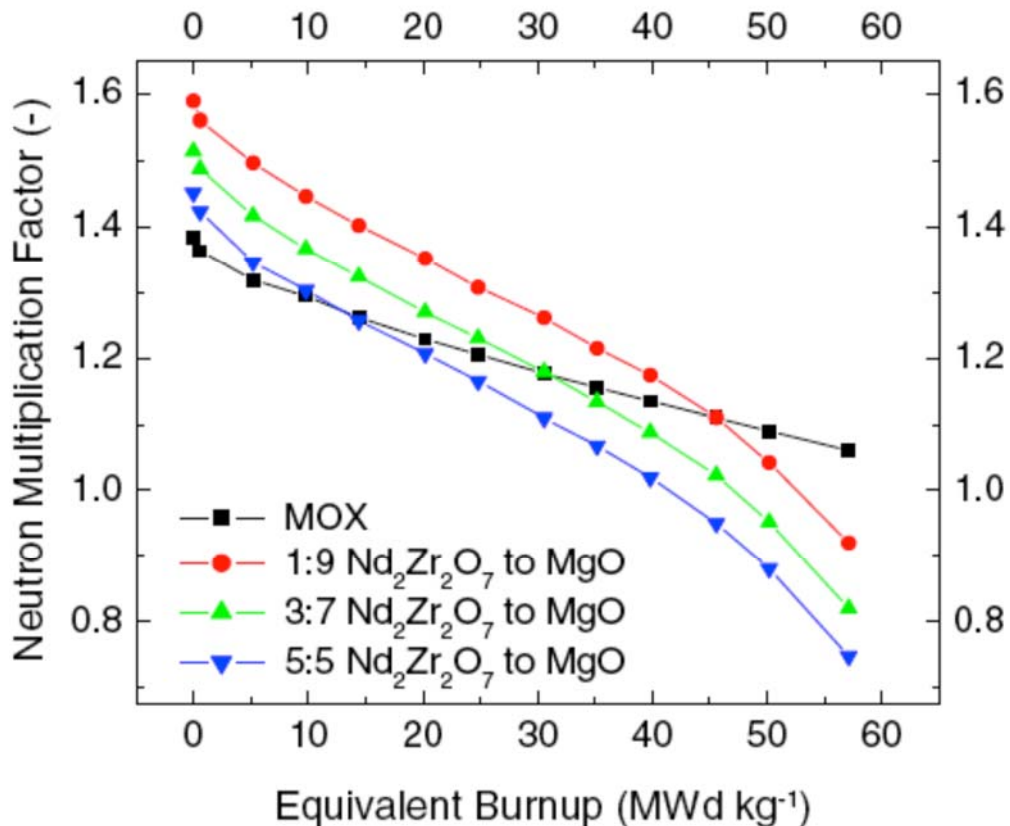


Figure 3-3: Equivalent burnup data for $\text{MgO}-\text{Nd}_2\text{Zr}_2\text{O}_7$ composite fuel compositions containing 8 vol% weapons grade PuO_2 .

The results in Figure 3.3 show that the neutron multiplication factor, k_{eff} , of the composite IMFs is higher than MOX at the beginning of life (BOL) and lower than MOX at the end of life (EOL). The k_{eff} also decreases as the content of $Nd_2Zr_2O_7$ increases because the thermal neutron absorption cross-section of natural Nd is higher than that of natural Mg. The calculations show the best ratio of $Nd_2Zr_2O_7$ to MgO is 3:7 because it can provide better EOL reactivity compared to that of the 5:5 ratio and does not require a neutron poison unlike the 1:9 $Nd_2Zr_2O_7$ to MgO ratio. In addition, a composite with a 3:7 $Nd_2Zr_2O_7$ to MgO ratio will have a continuous MgO phase according to percolation theory.⁷⁰ Therefore, the composite composition used throughout this work was 3:7 $Nd_2Zr_2O_7$ to MgO.

3.3 Experimental Procedures

This section describes the techniques used to analyze both the composite powders and composite microstructures.

3.3.1 Optical Microscopy

One side of a fabricated pellet was polished to 9 μm with diamond polishing suspensions on a Struers polishing wheel. The microstructure from the polished pellet was analyzed with an Olympus BX60 optical microscope (Center Valley, PA) using polarized light. Since polarized reflected light was used, the two phases could be differentiated in the optical images due to the difference in their refractive indices, where the dark phase is MgO and the light phase is $Nd_2Zr_2O_7$.

3.3.2 Scanning Electron Microscopy

One face of the pellet was polished to 1 μm with diamond polishing suspensions and finished with 0.5 μm colloidal silica on the Struers polishing wheel. The polished pellets were placed in an alumina setter, covered, and thermally etched in air for 30 minutes at 1450 °C. The thermally etched pellets were coated with carbon to make the sample conductive before being

inserted into a JEOL 6300FXV scanning electron microscope (Peabody, MA). The scanning electron microscope (SEM) was operated at 8 kV at a working distance of 15 mm.

3.3.3 Particle Size Analysis

The mixed composite powder synthesized by each of the processing methods was spin-riffled to separate a representative sample. The sample was added to DI water and placed in an ultrasonic for 1 minute to disperse any soft agglomerates. The dispersed powder was then added to a Beckman Coulter LS13320 (Fullerton, CA) and the particle size distribution was measured using laser light scattering. Since the average particle size of the powders is expected to be greater than 1 μm , the Fraunhofer model was used to analyze the particle size distribution.

3.3.4 X-ray Diffraction

An alumina mortar and pestle was used to crush the sintered pellets into powder. The powder was then compacted in a shallow depression on a glass slide. The sample was placed into a Phillips 3720 diffractometer (Westborough, MA) and data was collected from a 2θ angle of 10° to 70° with a 0.06° step size.

3.4 Constituent Preparation and Processing

This section describes the preparation and processing of the composite constituents MgO and $\text{Nd}_2\text{Zr}_2\text{O}_7$.

3.4.1 MgO

Commercially received MgO (Cerac 99.95%) was placed in an alumina crucible and calcined in air for 2 hours at 1000°C . The SEM image of the MgO powder in Figure 3.4 shows a combination of acicular, angular, and agglomerated particles. Laser light scattering particle size analysis was performed to determine the particle size distribution of the MgO powder. The resulting particle size distribution shown in Figure 3.5 is bimodal with the two modes at 0.3 μm and 5.9 μm .

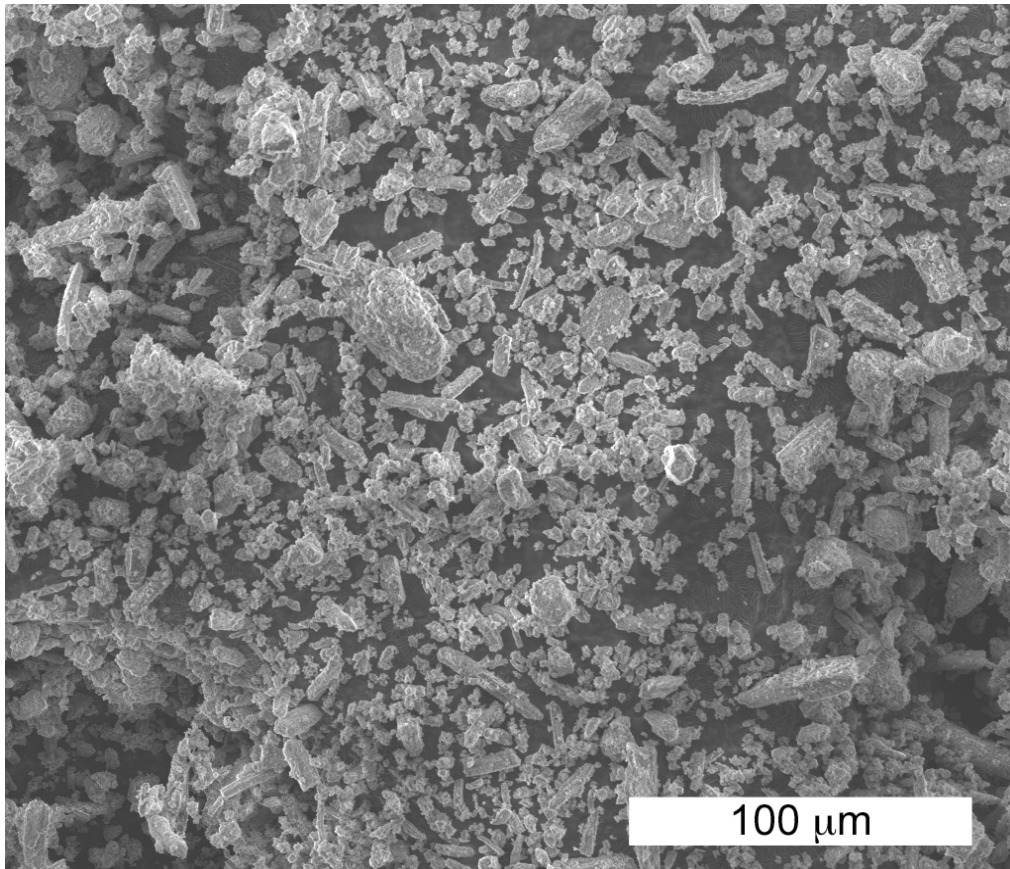


Figure 3-4: SEM image of the calcined Cerac MgO.

The general size of the MgO powder particles from the SEM in Figure 3.4 and the results of the particle size distribution in Figure 3.5 correspond reasonably well, with most of the particles appearing in the SEM image to measure between 1-10 μm and a small fraction appearing to measure between 10-20 μm . These rough visual measurements correlate with the particle size distribution results where the majority of particles in the primary peak range between 1 and 10 μm and there is a slight increase in the right tail of the distribution around 20 μm . Therefore, based on Figures 3.4 and 3.5, it can be inferred that the MgO powder is not heavily populated with soft agglomerates since there does not appear to be a clear difference between the size of the dry MgO powder and the sonicated suspension.

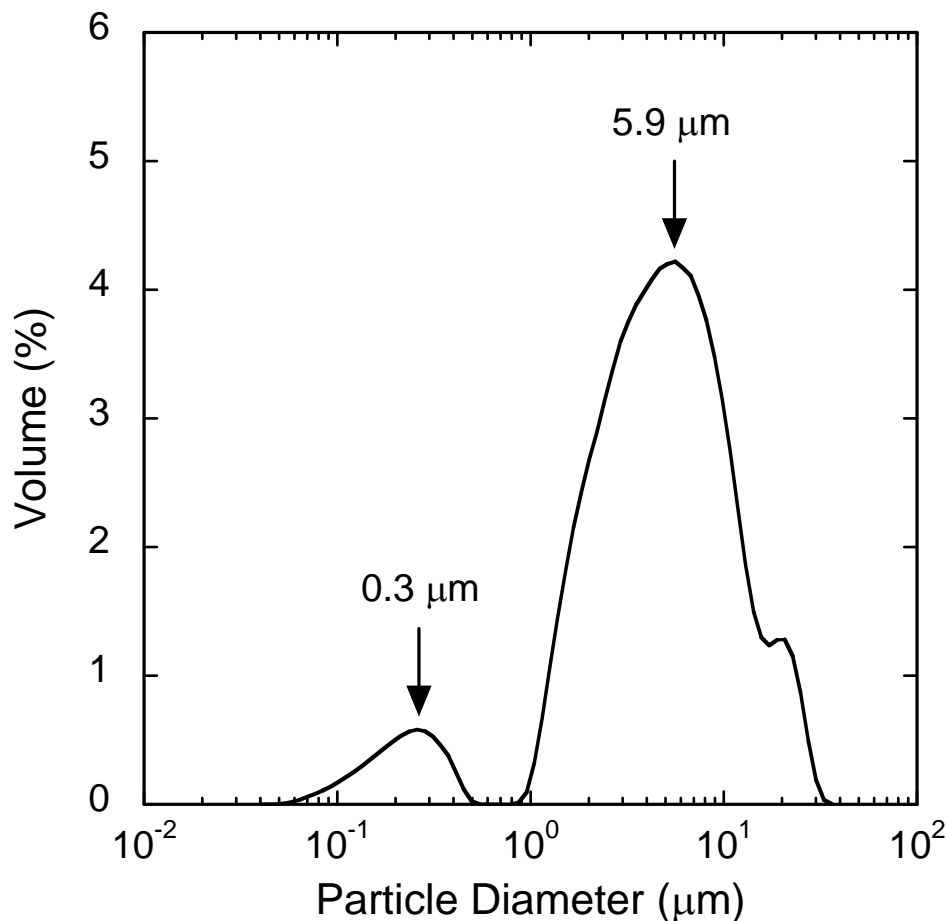


Figure 3-5: Particle size distribution of the calcined Cerac MgO.

3.4.2 Nd₂Zr₂O₇

The Nd₂Zr₂O₇ was prepared by adding stoichiometric ratios of Nd₂O₃ (Alfa Aesar 99.9%) and ZrO₂ (Alfa Aesar 99.7%) to spherical 3 mm and 10 mm YSZ (yttria stabilized zirconia) milling media in a 6 in diameter PTFE (polytetrafluoroethylene) ball mill jar with 100 ml of deionized water and 3 ml of ammonium polyacrylate dispersant (Darvan 821A). The slurry was milled for 24 hours on the ball mill at 85 rpm and dried overnight in an oven at 120°C. The dried powder was ground with a porcelain mortar and pestle and sieved through a 212 μm stainless steel mesh. A flow chart of the solid state synthesis of the Nd₂Zr₂O₇ is shown below in Figure 3.6.

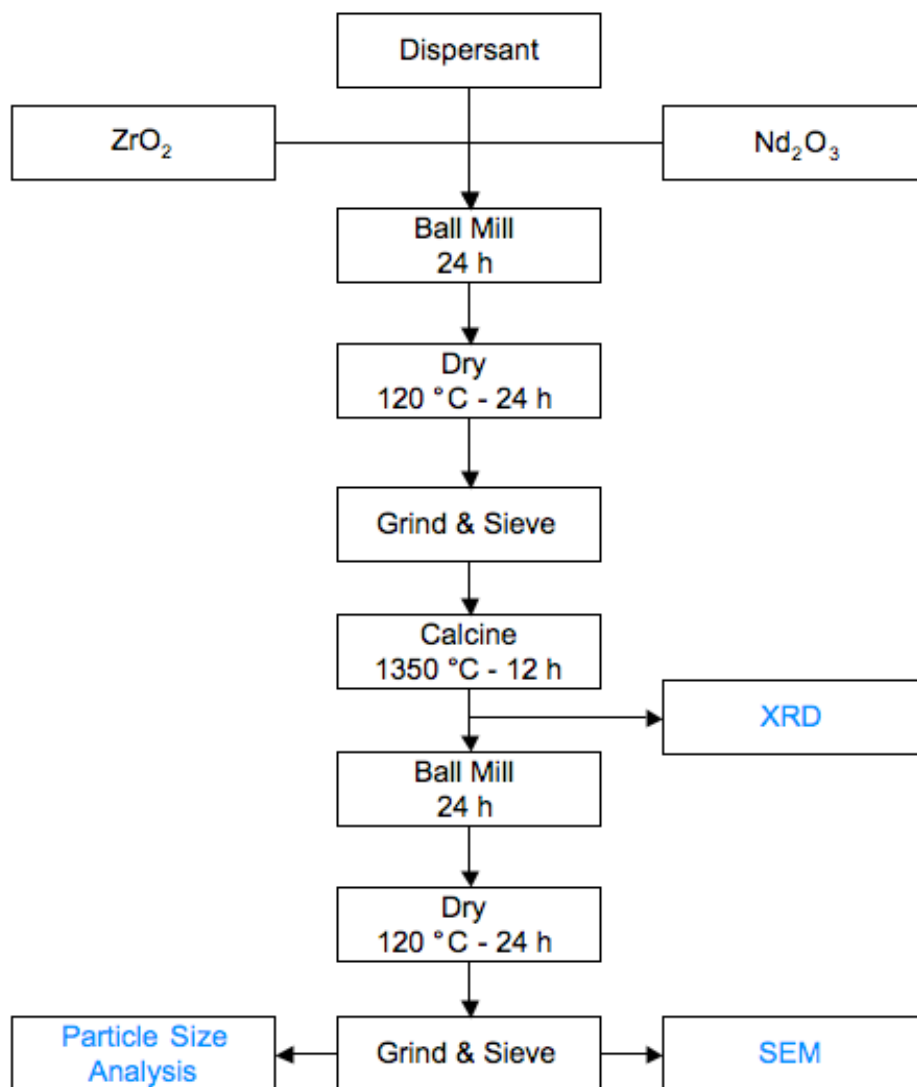


Figure 3-6: Flow chart for the solid state synthesis of $\text{Nd}_2\text{Zr}_2\text{O}_7$.

Optimization of the calcination temperature was performed on the synthesized pyrochlore to determine the most efficient time and temperature profile to achieve the pure pyrochlore phase. Samples of the ball milled Nd_2O_3 and ZrO_2 were calcined at 1300°C , 1350°C , 1400°C , 1500°C , and 1600°C for 12 hours. Phase pure $\text{Nd}_2\text{Zr}_2\text{O}_7$ formed at all temperatures except 1300°C . The x-ray diffraction pattern for the synthesized $\text{Nd}_2\text{Zr}_2\text{O}_7$ is shown below in Figure 3.7 and was compared to JCPDS file 17-0458.

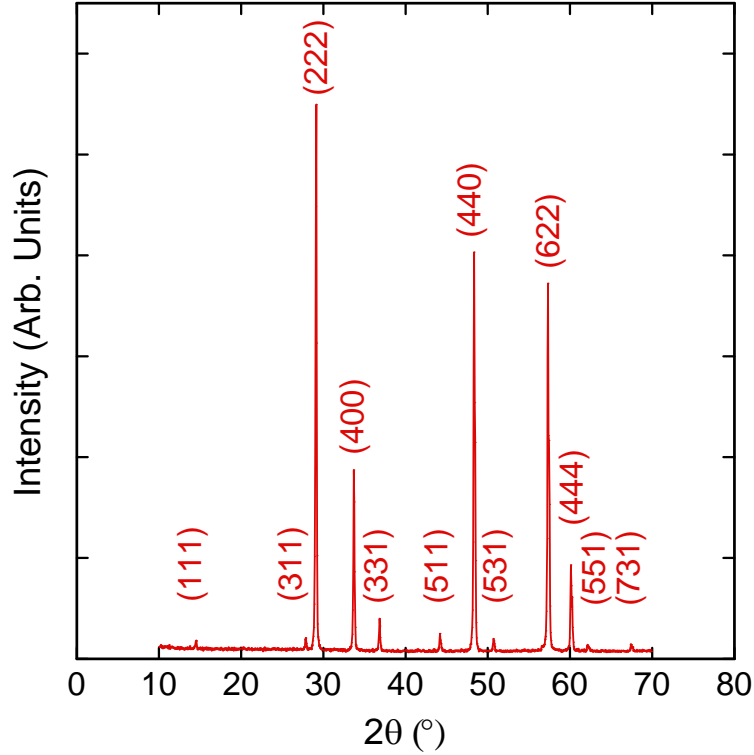


Figure 3-7: XRD profile for synthesized $\text{Nd}_2\text{Zr}_2\text{O}_7$ calcined at 1350°C for 12 hours.

The lattice parameter of the $\text{Nd}_2\text{Zr}_2\text{O}_7$ was determined using the Nelson-Riley function.⁷¹ The Nelson-Riley function is calculated in two parts by extracting the generated 2θ values and the corresponding diffraction planes from the X-ray pattern and inserting them into the following equations:

$$a(\theta) = \frac{\lambda \sqrt{(h^2 + k^2 + l^2)}}{2 \sin(\theta)} \quad (3.1)$$

$$a = a_0 - b \left(\frac{\cos^2(\theta)}{\sin(\theta)} + \frac{\cos^2(\theta)}{\theta} \right) \quad (3.2)$$

where θ is the X-ray phase angle in radians, λ is the X-ray wavelength of 1.54056 \AA , and (hkl) are the indices of the diffraction plane corresponding to the given angle θ . The extracted information from each diffraction peak was inserted into Equations 3.1 and 3.2, and the results are plotted as a vs. $f(\theta)$ below in Figure 3.8.

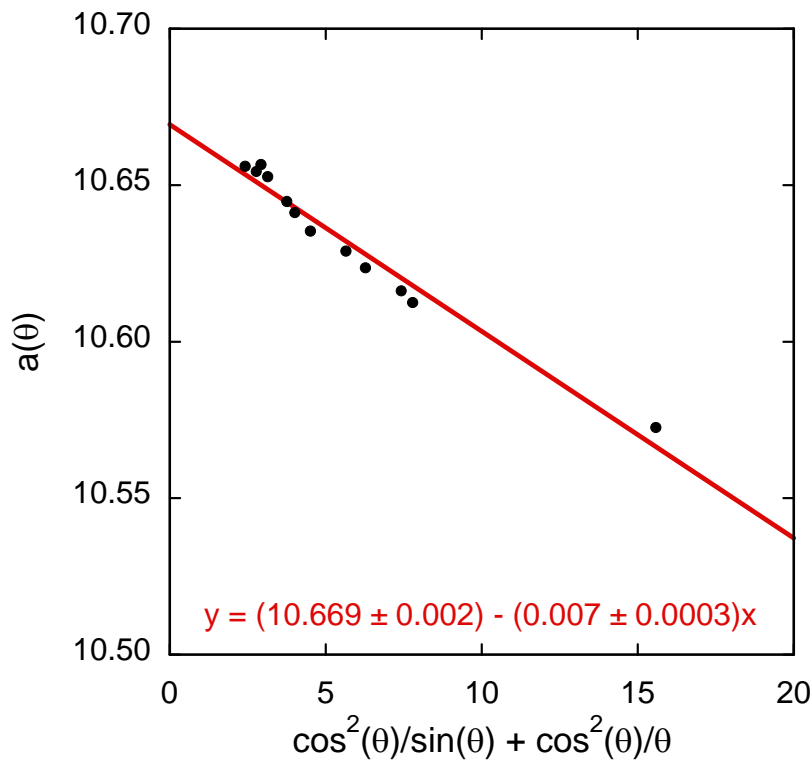


Figure 3-8: Lattice parameter calculation for the synthesized $\text{Nd}_2\text{Zr}_2\text{O}_7$ where the data is fit to the given equation.

The lattice parameter calculation for the synthesized $\text{Nd}_2\text{Zr}_2\text{O}_7$ using the Nelson-Riley function gives a lattice parameter of $10.669 \pm 0.002 \text{ \AA}$ and a theoretical density of $6.360 \pm 0.001 \text{ gcm}^{-3}$. The lattice parameter for the $\text{Nd}_2\text{Zr}_2\text{O}_7$ is similar to the data provided by Subramanian³⁰ and close to the experimental values Lutique et al.³² reported. After phase purity was confirmed, the $\text{Nd}_2\text{Zr}_2\text{O}_7$ powder was re-milled to a monomodal particle size distribution using the procedure described for ball milling in Figure 3.6.

In the SEM image of the synthesized $\text{Nd}_2\text{Zr}_2\text{O}_7$ powder in Figure 3.9 the re-milled $\text{Nd}_2\text{Zr}_2\text{O}_7$ particles appear to be approximately the same size, but they also seem to be agglomerated. Particle size analysis was performed and the resulting particle size distribution in Figure 3.10 shows that the $\text{Nd}_2\text{Zr}_2\text{O}_7$ is monomodal with a mode of $2.8 \text{ }\mu\text{m}$. The individual particles in the SEM image appear much smaller than $2.8 \text{ }\mu\text{m}$, indicating that the individual

$\text{Nd}_2\text{Zr}_2\text{O}_7$ particles are actually incorporated into hard agglomerates that remain intact after ultrasonic agitation.

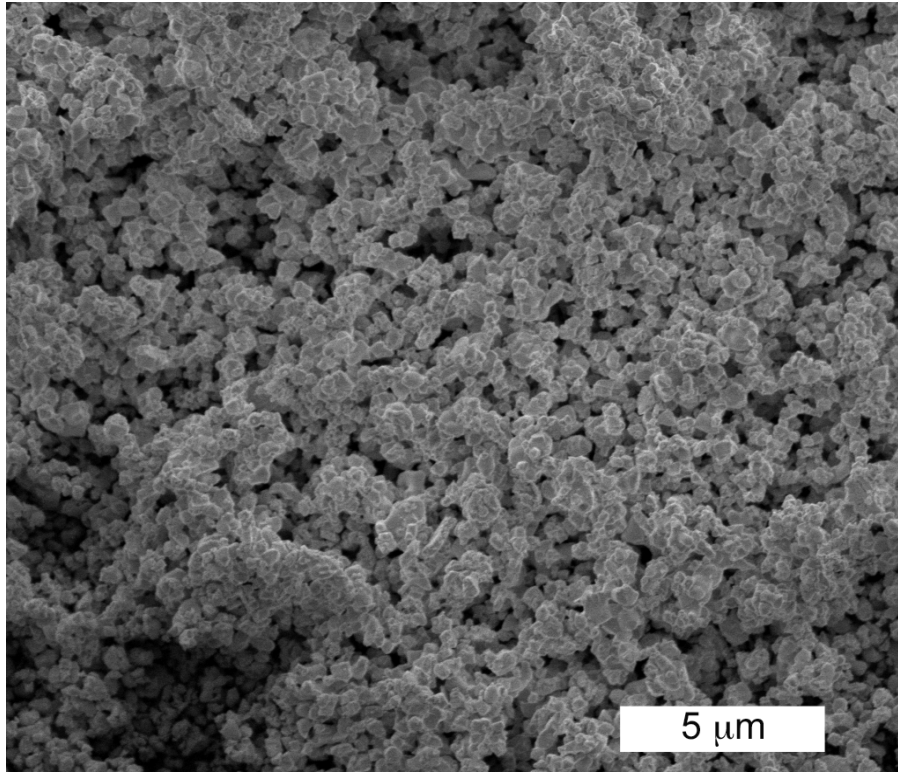


Figure 3-9: SEM image of the synthesized $\text{Nd}_2\text{Zr}_2\text{O}_7$.

The shape and narrowness of the particle size distribution is indicative of an optimized ball milling process. The average particle size of the $\text{Nd}_2\text{Zr}_2\text{O}_7$ is $2.80 \pm 1.40 \mu\text{m}$ and is calculated based on a Gaussian distribution since the particle size of the $\text{Nd}_2\text{Zr}_2\text{O}_7$ is normally distributed. In an optimized ball milling process the average particle size should be around $1 \mu\text{m}$ for sinterability.⁴³ The explanation for the larger average particle size is in how the particle size distribution is reported in Figure 3.10. The particle size distribution is measured in volume, which emphasizes the larger particles over the smaller particles.

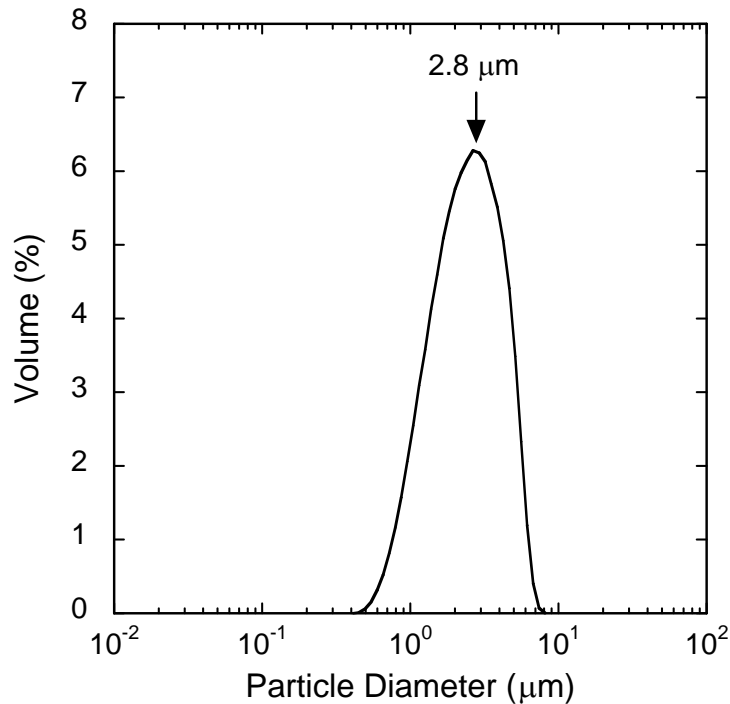


Figure 3-10: Particle size distribution of the synthesized Nd₂Zr₂O₇.

3.5 Composite Processing

Four processing methods were investigated to synthesize MgO—Nd₂Zr₂O₇ composites. The four processing methods include the crude, but simple mortar and pestle mixing of the constituents and an optimized ball milling process. A magnetic bar stirring process was included because of similar work performed on the processing of MgO—ZrO₂ candidate IMF composites.³⁷ Spex blending was added because of its popularity in laboratory scale studies of surrogate and IM fuels. The processing methods can be separated into two distinct categories of dry and aqueous processes, based on whether the process utilizes an aqueous slurry to combine the constituents. Mortar and pestle and Spex blending are dry processing methods, and magnetic bar stirring and ball milling are aqueous processing methods. A flow chart outlining the steps in each of the synthesis methods is shown below in Figure 3.11. Each of the processing methods has been designated with a specific color that will be kept constant throughout this work.

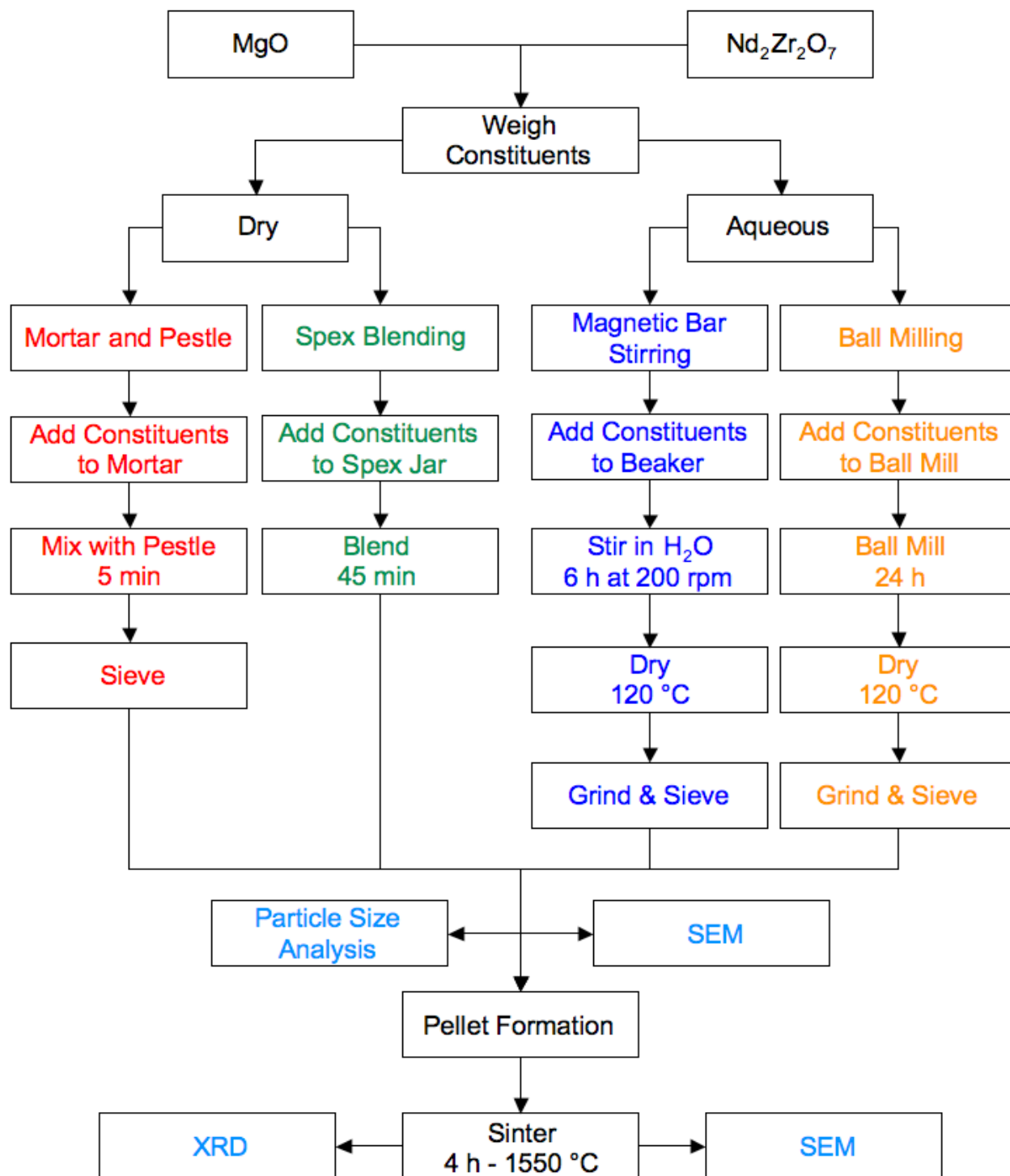


Figure 3-11: Flow chart for the different composite synthesis methods.

3.5.1 Dry vs. Aqueous Processes

The XRD profile of the mixed composite powder in Figure 3.12a for the dry processing methods mortar and pestle and Spex blending shows that the composite powder is composed of only the constituent phases of MgO and Nd₂Zr₂O₇ after mixing. However, the XRD profile in Figure 3.12b of the mixed composite powder for the aqueous processing methods magnetic bar stirring and ball milling shows that some of the MgO has transformed into Mg(OH)₂ during mixing according to JCPDS 07-0239.

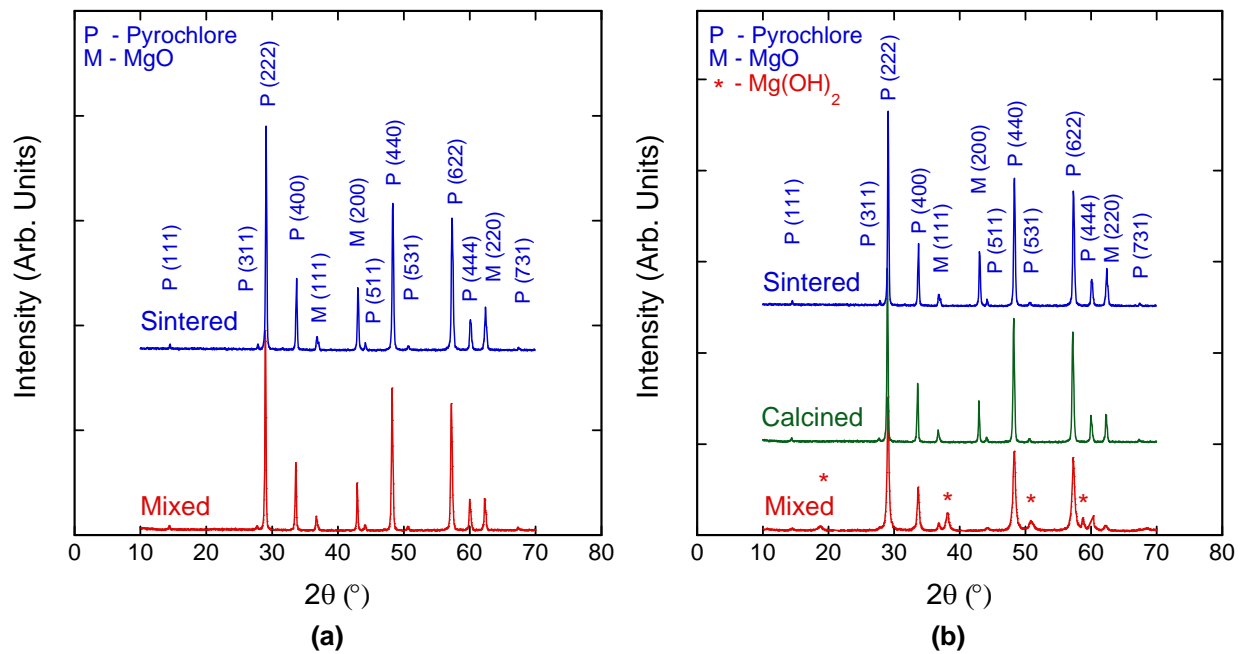


Figure 3-12: XRD profiles of mixed, calcined, and sintered composites. In the aqueous processing methods the MgO transforms into Mg(OH)₂ during mixing and requires an extra calcination step to transform the Mg(OH)₂ back into MgO before sintering. A) dry processing methods and B) aqueous processing methods

This result is expected because MgO hydrates into Mg(OH)₂ when the oxide is exposed to an excess of water, water vapor, or moisture.⁷² In an attempt to avoid the formation of Mg(OH)₂ the deionized water was replaced with acetone or ethanol. However, in both cases the XRD for the mixed composite powder showed that the MgO still transformed into Mg(OH)₂. Since replacing deionized water with acetone or ethanol did not circumvent the formation of

Mg(OH)₂, the solvent for the aqueous processes was reverted back to deionized water for all subsequent batches. An extra calcination step of 2 hours at 1000°C transforms the Mg(OH)₂ back into MgO before sintering.

3.5.2 Composite Processing Methods

The following section describes each of the composite processing methods used to combine the composite constituents MgO and Nd₂Zr₂O₇ and the powder characterization of the mixed composite powders.

3.5.2.1 Mortar and pestle

The weighed ratios of MgO (Cerac 99.95%) and Nd₂Zr₂O₇ were added to an alumina mortar and pestle and ground for 5 minutes to combine the oxide constituents. The mixed composite powder was then sieved through a 212 μm stainless steel mesh.

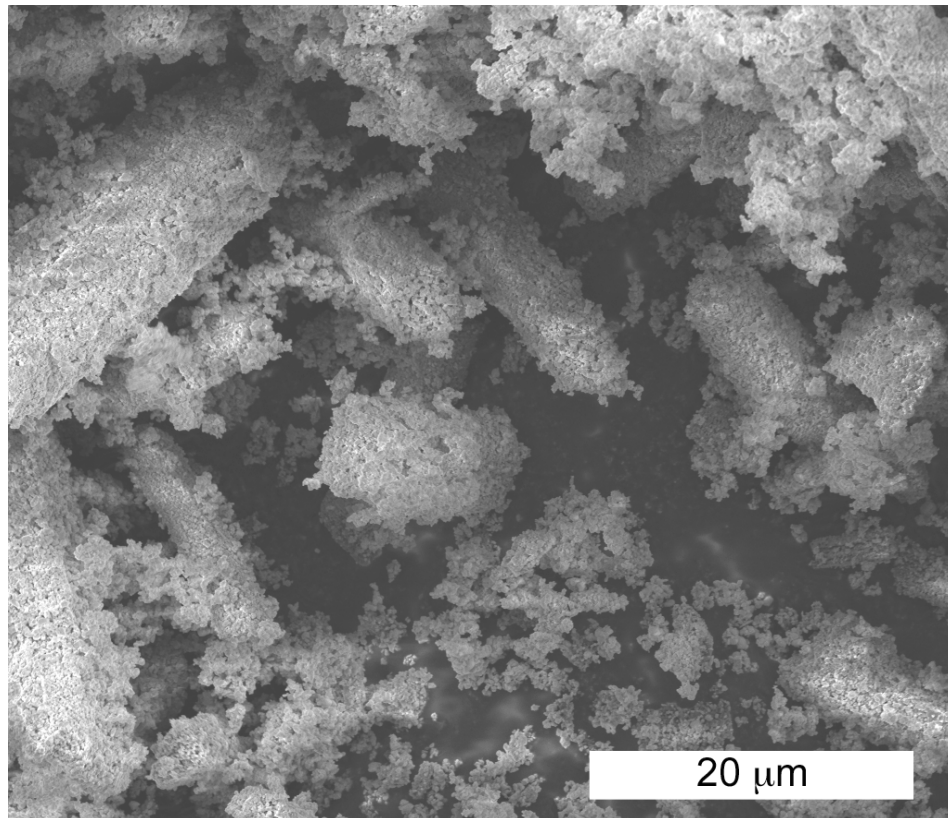


Figure 3-13: SEM images of the mixed composite powder for the mortar and pestle mixed composite powder.

The SEM image of the sieved composite powder in Figure 3.13 shows the mortar and pestle composite powder is composed mostly of acicular agglomerates ranging in size from 10-50 μm . The particle size distribution for the mortar and pestle composite powder is shown in Figure 3.14. The particle size distribution is slightly skewed toward the larger particle sizes and has mode of 10.2 μm .

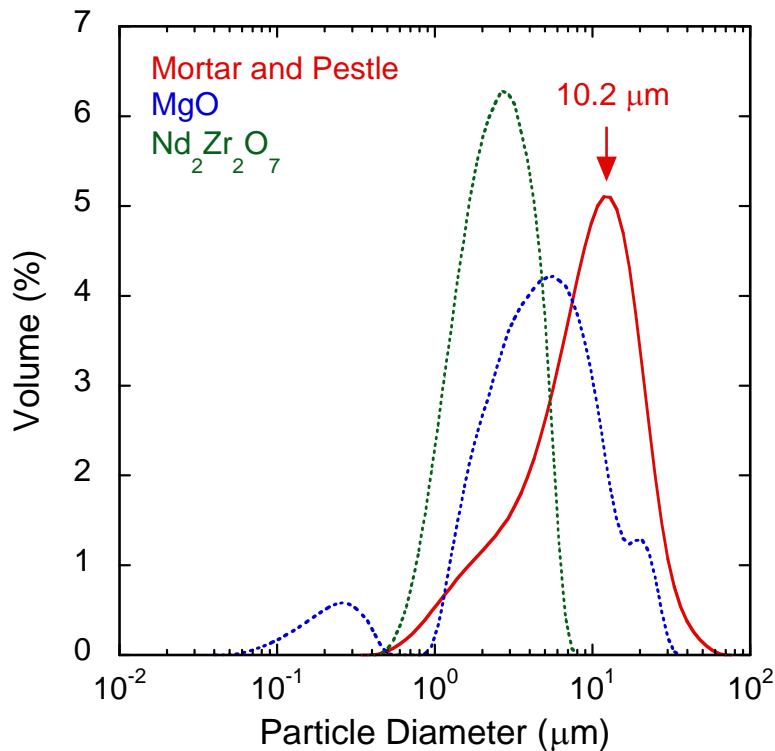


Figure 3-14: Particle size distribution of the $\text{Nd}_2\text{Zr}_2\text{O}_7$ and MgO feed stock and synthesized composite powder for the mortar and pestle method.

Comparing the particle size distribution in Figure 3.14 and the SEM image of the mixed powder in Figure 3.13 proves that the mortar and pestle powder agglomerated during mixing. In the SEM image the mortar and pestle powder is mostly composed of large acicular agglomerates over 20 μm , but the majority of the particles according to the particle size distribution are less than 20 μm . Therefore, most of the agglomerates observed with SEM are partially weak in character, and were broken up into smaller agglomerates during the sonication

of the suspension before particle size analysis. Since the mode of the mixed composite powder is larger than either of the constituent modes, the remaining agglomerates are most likely composed of random ratios of both MgO and Nd₂Zr₂O₇.

3.5.2.2 Spex blending

MgO and Nd₂Zr₂O₇ were weighed and added to a polystyrene Spex container with two 10 mm PMMA (polymethyl methacrylate) milling media. The Spex container was positioned into the Spex mill (SPEX 8000M Mixer/Mill) and the constituents were blended for 45 minutes. The SEM image of the Spex blended powder in Figure 3.15 shows that the particles are fairly uniform, although some agglomeration appears to be present. Unlike the mortar and pestle powder, there is no evidence of the acicular agglomerates that were observed in Figure 3.13.

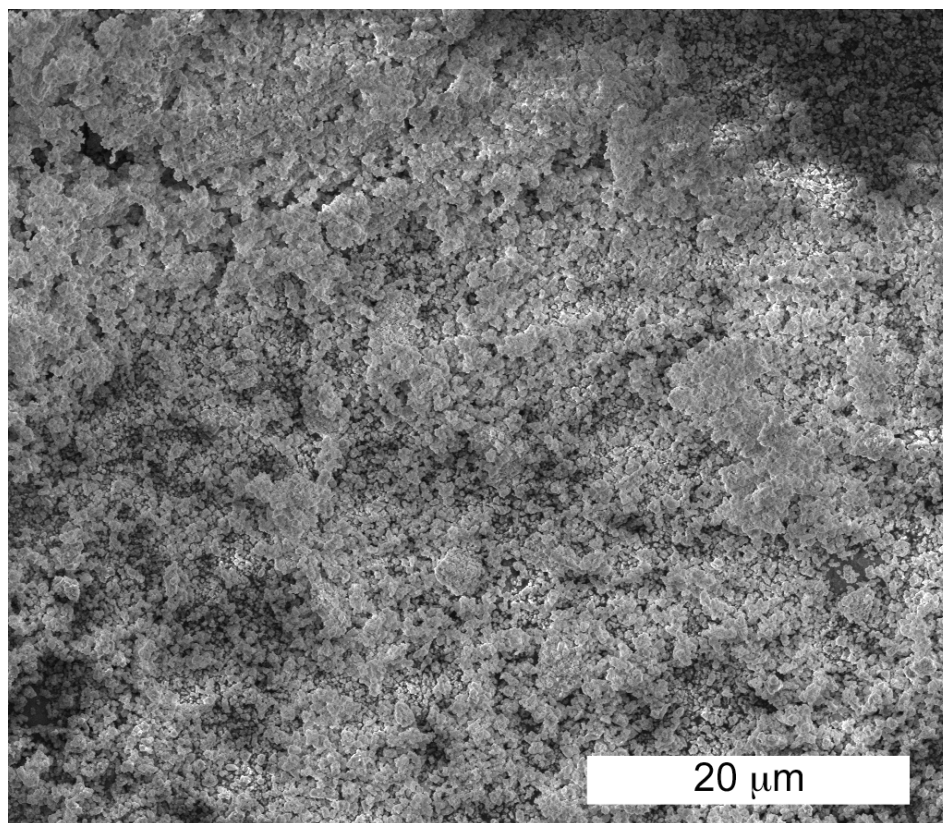


Figure 3-15: SEM images of the mixed composite powder for the Spex blending method.

Particle size analysis was performed and the resulting particle size distribution in Figure 3.16 for the Spex blended powder is monomodal with a mode of 5.1 μm . The mode of the Spex blended powder is close to that of the MgO, supporting the observation from Figure 3.15 that Spex blending avoided the formation of large agglomerates of the constituent phases. There also appears to be a reduced number of the 20 μm agglomerates observed in the right tail of the MgO particle size distribution, suggesting that Spex blending imparted enough energy from the PMMA milling media on the constituent powders during mixing to break up agglomerates present in the MgO powder.

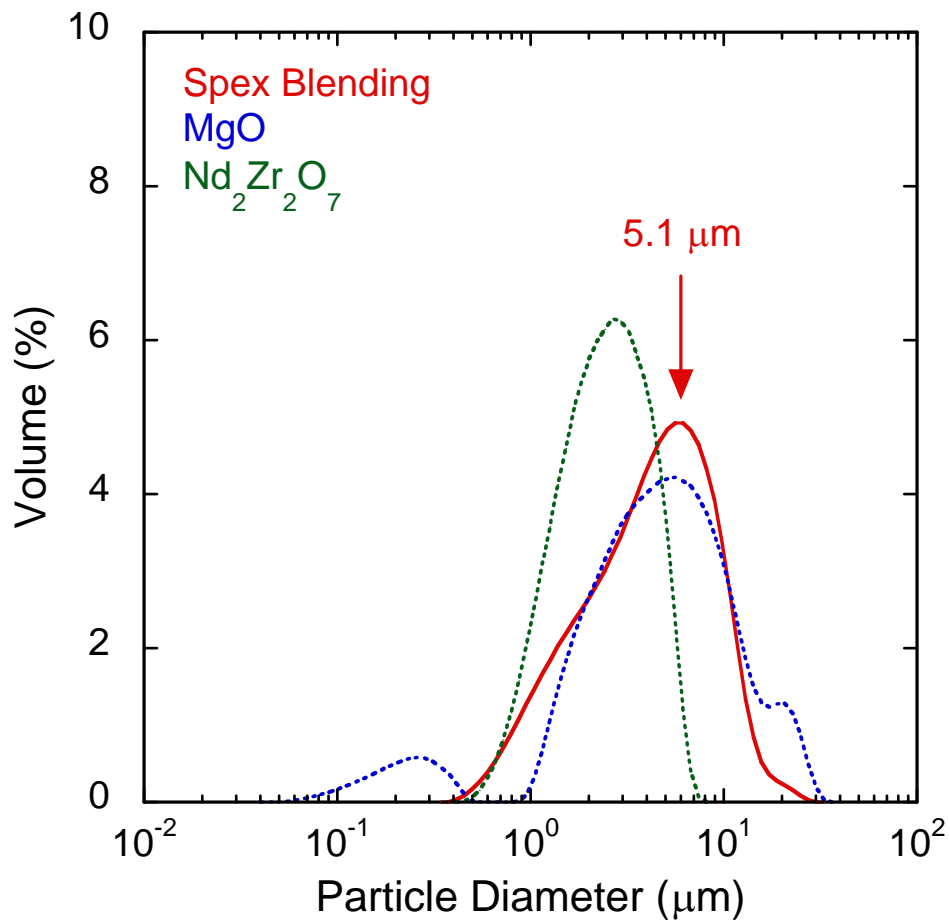


Figure 3-16: Particle size distribution of the Nd₂Zr₂O₇ and MgO feed stock and synthesized composite powder for the Spex blending method.

3.5.2.3 Magnetic bar stirring

MgO and $\text{Nd}_2\text{Zr}_2\text{O}_7$ were weighed and added to a beaker filled with 100 ml of deionized water and 3 ml of ammonium polyacrylate dispersant. The slurry was stirred using a 2 in magnetic bar for 6 hours at 200 rpm. The mixed slurry was dried in an oven overnight at 120°C , then ground and sieved through a $212\ \mu\text{m}$ stainless steel mesh. The powder was then calcined at 1000°C in air for 2 hours. The SEM image of the mixed composite powder in Figure 3.17 shows that the magnetic bar stirred powder is characterized by acicular agglomerates similar to those observed in the mortar and pestle powder in Figure 3.13.

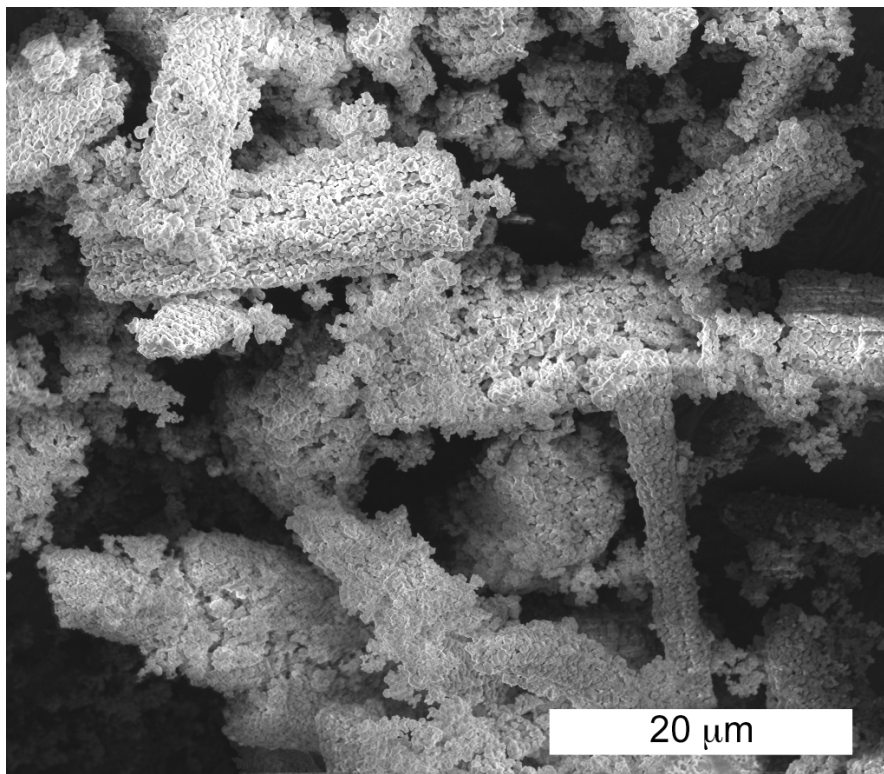


Figure 3-17: SEM images of the mixed composite powder for the magnetic bar stirring method.

The particle size distribution for the magnetic bar stirred composite powder shown in Figure 3.18 is monomodal and has a mode of $10.5\ \mu\text{m}$. As with the mortar and pestle composite powder, the mode of the magnetic bar stirred powder is larger than the modes of either constituent phase, indicating that agglomerates of the constituents were formed during

mixing. The skew of the distribution toward the larger particle sizes is more pronounced in the magnetic bar stirred composite powder than in the mortar and pestle powder, and in particular, there is a rather prominent shoulder in the magnetic bar stirred particle size distribution around 20 μm . This suggests that the agglomerates are harder in character in the magnetic bar stirred composite powder than the agglomerates in the mortar and pestle powder since the sonication was less effective at breaking the large acicular agglomerates up into smaller agglomerates.

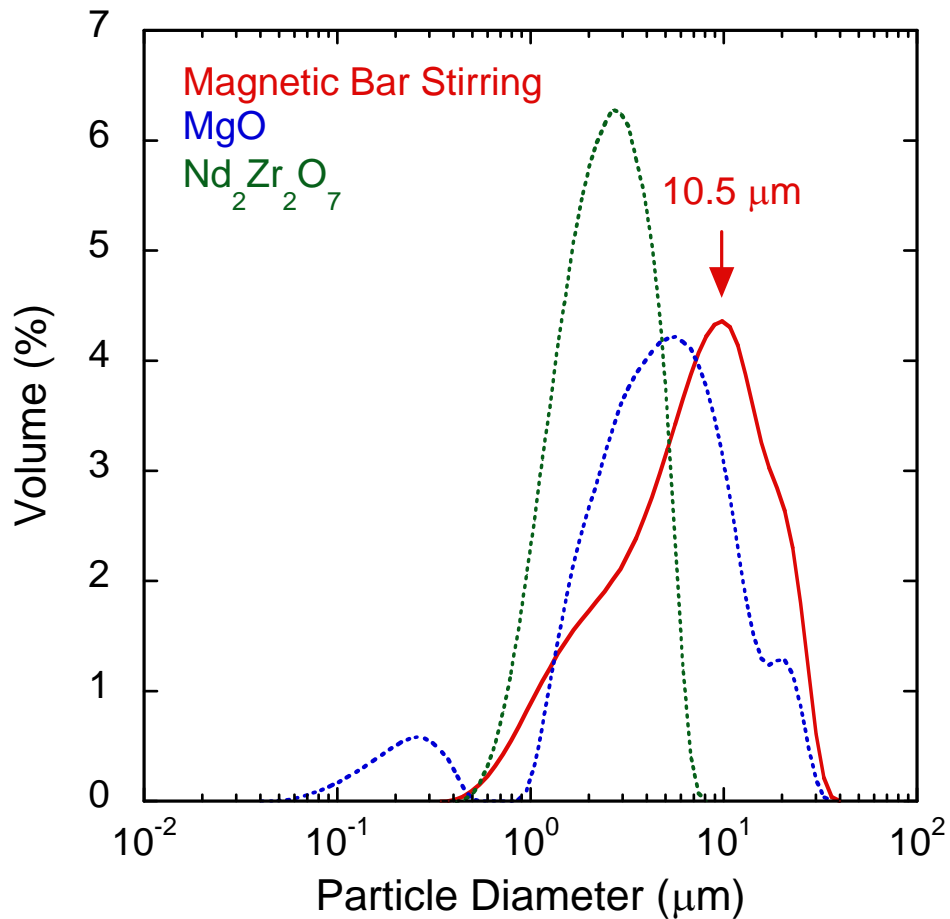


Figure 3-18: Particle size distribution of the $\text{Nd}_2\text{Zr}_2\text{O}_7$ and MgO feed stock and synthesized composite powder for the magnetic bar stirring method.

The prevalence of hard agglomerates is likely due to the formation of surface charges on the particles when the composite powder was introduced into the aqueous solution.⁴³ The surface charges cause the powders to flocculate in solution and strongly bonded agglomerates

to remain after the composite powder is dried. As shown in Section 3.4.2.1, grinding and sieving the composite powder is ineffective at breaking up agglomerates. Therefore, the agglomerates are intact and the primary particles in close contact during the calcination of the composite powder. Calcination provides enough energy to cause surface diffusion of the constituents to occur, creating solid bridges between the primary particles that prevent the agglomerates from breaking down into primary particles during sonication.

3.5.2.4 Ball milling

MgO and Nd₂Zr₂O₇ were added to a PTFE ball milling jar containing YSZ milling media with 100 ml of deionized water and 3 ml of ammonium polyacrylate dispersant. The slurry was milled for 24 hours before being dried overnight in an oven at 120°C. The dried powder was ground with a porcelain mortar and pestle and sieved through a 212 μm stainless steel mesh. The sieved powder was calcined at 1000°C in air for 2 hours. The SEM image of the ball milled composite powder in Figure 3.19 shows the powder is composed of uniformly sized particles. The particles appear to be somewhat agglomerated, but the agglomerates are smaller and do not assume the acicular shape characteristic of the mortar and pestle and magnetic bar stirred composite powders. The resulting particle size distribution for the mixed composite powder in Figure 3.20 is monomodal with a mode of 3.8 μm.

The particle size distribution for the ball milled composite powder is normally distributed with a mean of 4.2 ± 2.7 μm. Of the four processing methods, ball milling produces the smallest mode, average particle size, and is the most normally distributed. These characteristics are not unexpected, since these results are the products of an optimized ball milling process. In fact, the particle size distribution for the ball milled composite powder is nearly centered in between the particle size distributions for the constituent phases MgO and Nd₂Zr₂O₇ and all of the 20-50 μm MgO agglomerates have disappeared. This establishes that ball milling the constituent

powders together provided enough mechanical energy to break up the hard MgO agglomerates present in the constituent MgO powder into smaller particles.

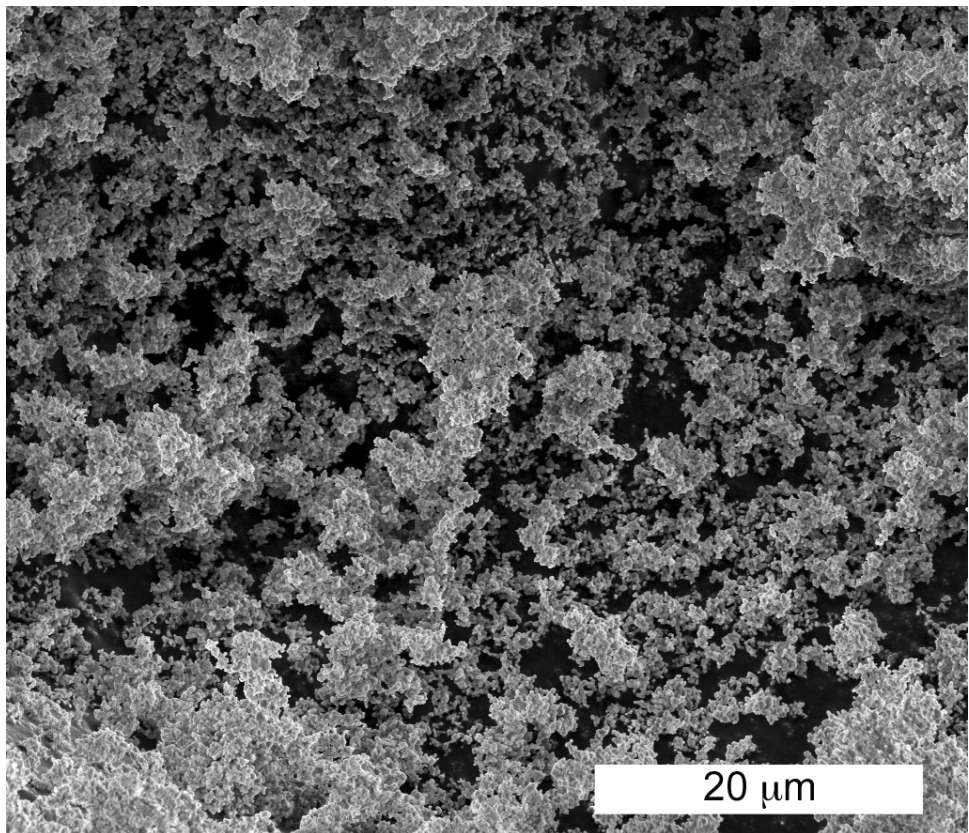


Figure 3-19: SEM image of the mixed composite powder for the ball milling process.

Hard agglomerates do not form in the ball milled composite powder as they do in the magnetic bar stirred composite powder. Although dispersant was added to both the magnetic bar stirring and ball milling slurries, the dispersant was only effective in the ball milling slurry. In the case of the magnetic bar stirring, there was not enough mechanical energy available to break up the agglomerates and the dispersant only succeeded at coating the surface of the agglomerates, not the individual particles. Ball milling provided enough energy to break up the agglomerates into smaller particles so the dispersant could coat the individual particles and keep them suspended in the slurry. As the ball milling slurry dried, the steric interaction of the polymer chains that coated the surface of the particles kept the particles from agglomerating.

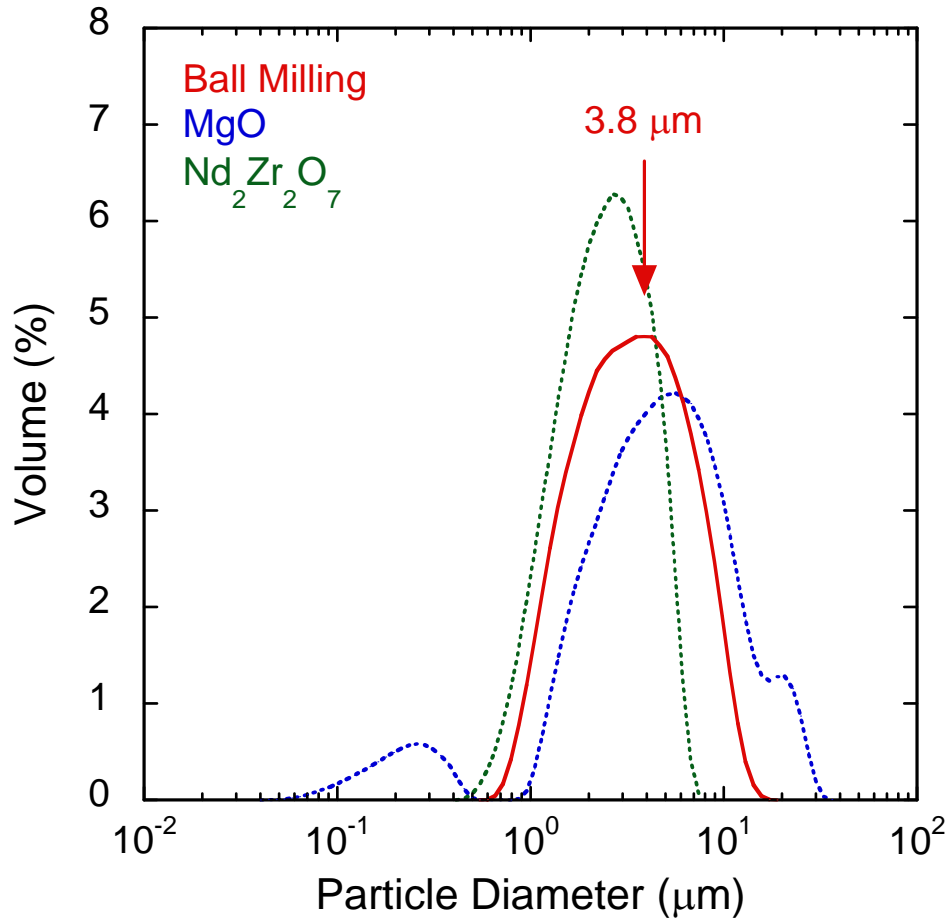


Figure 3-20: Particle size distribution of the Nd₂Zr₂O₇ and MgO feed stock and synthesized composite powder for the ball milling method.

3.6 Composite Pellet Fabrication

Cylindrical pellets were fabricated from the mixed composite powders to characterize the microstructure and thermal properties. The powders were combined with 2 wt% of binder (20 vol% Celvol 103 Polyvinyl Alcohol in deionized water) and ground with an alumina mortar and pestle until the powder sieved through a 300 μm brass mesh. The sieved powder was dried in a 120°C oven for 5 minutes to evaporate the water before being added to a 13 mm diameter punch and die set lubricated with 10W-30 motor oil and pressed with 68 MPa on a Carver press. The pellet was removed from the die and checked for cracks and surface finish.

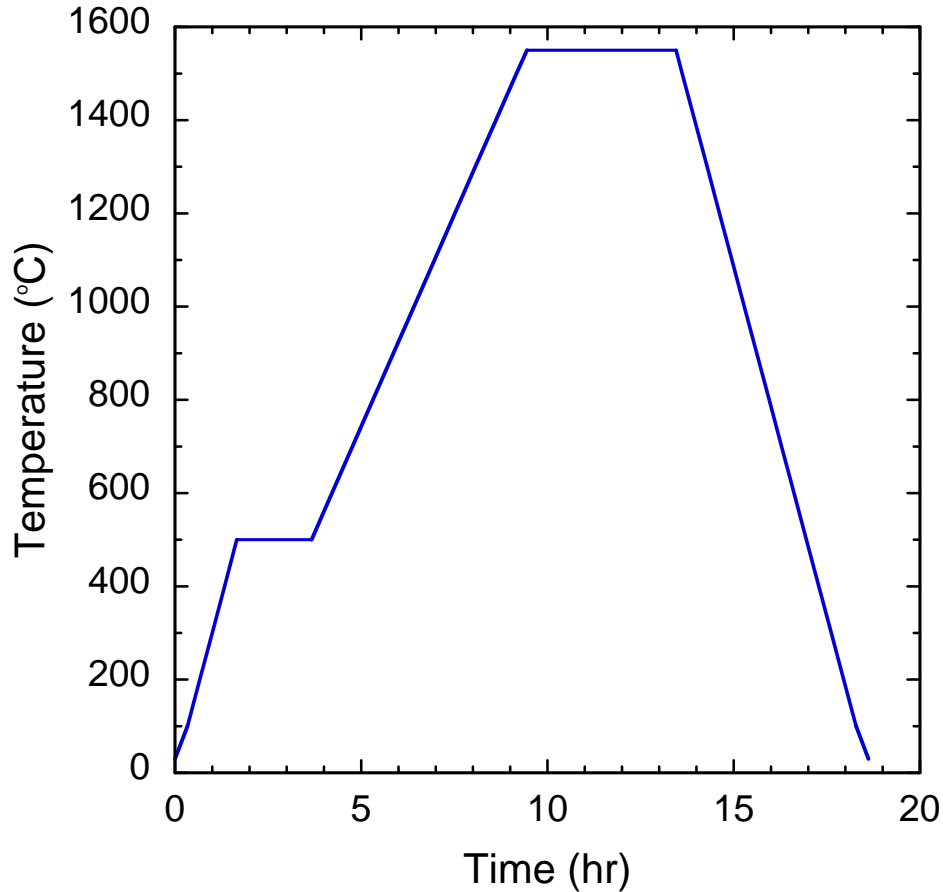


Figure 3-21: Furnace temperature profile for composite sintering.

The geometric green density was calculated and compared to the theoretical composite density of 4.4142 gcm^{-3} . The composite theoretical density was calculated based on a rule of mixtures using the theoretical density of MgO from literature and the theoretical density of the $\text{Nd}_2\text{Zr}_2\text{O}_7$ calculated in Section 3.3.2. The pellets that exceeded 50% of the theoretical density were sintered in air at 1550°C for 4 hours according to the thermal profile shown in Figure 3.21 and the pellets that were less than 50% of the theoretical density were discarded. The 2 hr step at 500°C is for binder burnout. The sintered pellets were checked for cracks and their geometric densities were calculated. If the geometric density exceeded 90% of the theoretical density of the composite, the density was then measured using the Archimedes method.

The geometric density for the magnetic bar stirred composites was calculated to be 90% of the theoretical density. The Archimedes density of the composites synthesized by mortar and pestle was 97% of the theoretical density, the Spex blended composites was 98%, and ball milled composites was 97% of the theoretical density. The decrease in density in the magnetic bar stirred composites can be attributed to the prevalence of the large agglomerates in the magnetic bar stirred composite powder compared to the mortar and pestle composite powder that would affect the packing arrangement of the agglomerates within the green ceramic. The difference in the packing arrangement of the large agglomerates adversely affects pore evolution during sintering resulting in a decrease in composite density.⁷³

3.7 Conclusions

MgO—pyrochlore composites are being investigated as possible candidate inert matrix materials for actinide incineration. The pyrochlore $\text{Nd}_2\text{Zr}_2\text{O}_7$ was chosen from the pool of known zirconate pyrochlores because it had the best combination of neutronics, radiation tolerance, and predicted thermal conductivity. The composite composition was selected after burn-up simulations were performed on various ratios of $\text{Nd}_2\text{Zr}_2\text{O}_7$ to MgO and compared to the k_{eff} of MOX. The composite composition with the best balance of beginning and end of life reactivity had a 3:7 ratio of $\text{Nd}_2\text{Zr}_2\text{O}_7$ to MgO.

Four methods were investigated to synthesize the 70 vol% MgO—30 vol% $\text{Nd}_2\text{Zr}_2\text{O}_7$ composite. Two of the methods, mortar and pestle and magnetic bar stirring, produced composite powders heavily populated with agglomerates and the other two methods, Spex blending and ball milling, produced composite powder that were uniform and monodisperse. Of the two methods that produced agglomerated powders, the magnetic bar stirring formed more hard agglomerates than mortar and pestle mixing. The hard agglomerates inhibited densification in the magnetic bar stirred composites, causing a decrease in the sintered density from 97% in the mortar and pestle composites to 90% in the magnetic bar stirred composites.

The effect of processing on the resulting microstructures of the composites will be discussed in Chapter 4.

CHAPTER 4 COMPOSITE CHARACTERIZATION

4.1 Introduction

This chapter characterizes the macrostructure and microstructure of the composites synthesized by the four processing methods described in Chapter 3 to provide a base to discuss the macrostructure—thermal diffusivity relationship in Chapter 5 and the microstructure—thermal conductivity relationship in Chapter 6. Following the characterization is discussion on the effect of processing on the macrostructure and microstructure. For the purpose of this discussion the macrostructure is defined as the features observed with optical microscopy and the composite microstructure is defined as the features that are observed with SEM.

4.2 Description of the Composite

Optical microscopy was performed according to the procedure described in Section 3.3.1 to analyze the composite macrostructure. In the optical image below in Figure 4.1 of a mortar and pestle composite the different features of the macrostructure can be identified. Due to the difference in the refractive indices of MgO and Nd₂Zr₂O₇ the two phases can be differentiated. The solid dark regions are MgO heterogeneities and the solid light regions are Nd₂Zr₂O₇ heterogeneities.

Between the MgO and Nd₂Zr₂O₇ heterogeneities is the mottled gray interpenetrating matrix which is composed of a homogeneous distribution of MgO and Nd₂Zr₂O₇ grains arranged in single-phase clusters. Porosity also appears dark in optical microscopy and could be mistaken for MgO heterogeneities, but SEM of the microstructure shows that the porosity has an average diameter of ~1 μm. Due to the resolution limits of the optical microscope, the solid dark regions observed in the optical images are MgO heterogeneities and dark regions arising from residual porosity are incorporated into the interpenetrating matrix. SEM images of the microstructure and the MgO and Nd₂Zr₂O₇ heterogeneities corroborated these observations.

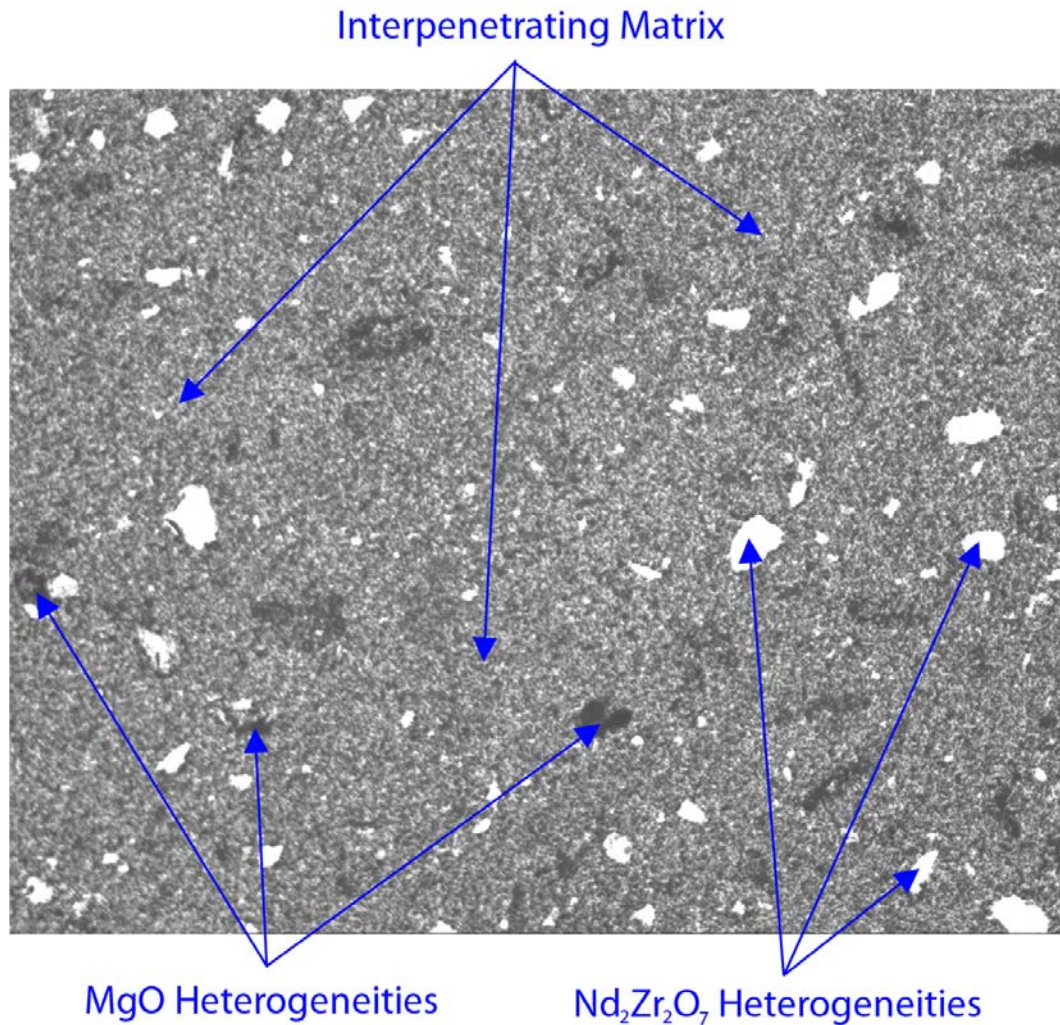


Figure 4-1: Optical image of the composite macrostructure showing MgO and Nd₂Zr₂O₇ heterogeneities surrounded by the interpenetrating matrix.

The crystal structure of MgO and Nd₂Zr₂O₇ are very dissimilar, therefore, limited solubility of the MgO in the Nd₂Zr₂O₇ and Nd₂Zr₂O₇ in the MgO is expected. Energy dispersive spectroscopy (EDS) was performed on both the MgO and Nd₂Zr₂O₇ heterogeneities to confirm this hypothesis. It was determined that there was solubility of the Nd₂Zr₂O₇ into the MgO and solubility of the MgO in the Nd₂Zr₂O₇. The solubility of the MgO in the Nd₂Zr₂O₇ was 3× greater than the solubility of the Nd₂Zr₂O₇ in the MgO. This is reasonable, given that the larger pyrochlore lattice can more easily accommodate the smaller Mg ions than the MgO lattice can accommodate the larger Nd and Zr ions.

4.3 Composite Characterization Methods

This section describes the quantitative stereology techniques used to characterize the heterogeneities and the interpenetrating matrix. Although the techniques are summarized below, see Appendix A for more details pertaining to how the measurements were performed. The flow chart in Figure 4.3 associates the characterization technique with the macrostructure or microstructure characterization method.

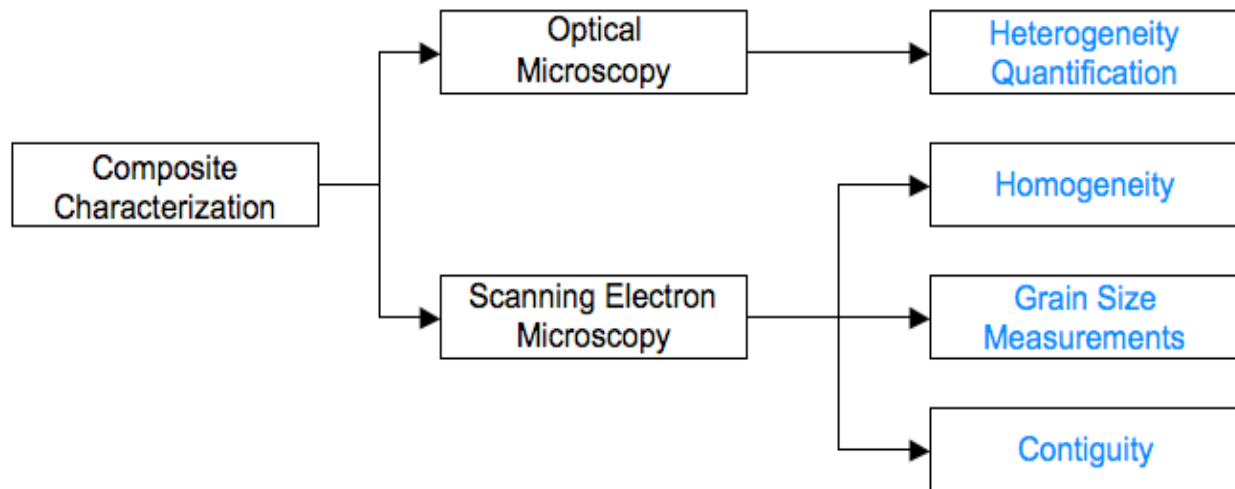


Figure 4-2: Flow chart for the composite characterization methods.

4.3.1 Heterogeneity Quantification

Quantitative stereology techniques described by Underwood^{53;54} were used to analyze the MgO and Nd₂Zr₂O₇ heterogeneities for each processing method by treating the heterogeneities as second phase particles dispersed in a homogeneous matrix phase. A regular grid of ten vertical and eight horizontal lines was randomly superimposed 3 times on 10 optical images collected at 50X from three pellets synthesized from each processing method using Image J software. The total lineal line length, L , of the 540 lines from the 30 analyzed grids was calculated to be 1.107 m and the total number of points P formed by the intersection of the vertical and horizontal lines totaled 2400.

The volume fraction V_V of the MgO and Nd₂Zr₂O₇ heterogeneities was determined for each phase by counting the number of points that laid on heterogeneities of the phase of interest and dividing it by the total number of points according to the equation

$$V_V = \frac{P_p}{P} \quad (4.1)$$

where P_p is the number of points that fell on the phase and P is the total number of points.

The frequency of the heterogeneities is described by the number of heterogeneity interceptions per unit length N_L , and is calculated according to

$$N_L = \frac{N_i}{L} \quad (4.2)$$

where N_i is the total number of interceptions of the phase of interest and L is the total lineal length of the grid. Larger N_L values correspond to a higher frequency of heterogeneities.

4.3.2 Homogeneity

The homogeneity of the interpenetrating matrix is determined through an approach used by Heijman et al.⁷⁴ to quantify the homogeneity of Voronoi polygons that were derived from cercer microstructures using a dimensionless parameter HP_q , but modified to use the variation in the area fraction of the Nd₂Zr₂O₇. The HP_q is defined as the standard deviation σ_q of the variation in area fraction of Nd₂Zr₂O₇ normalized with respect to its average value μ_q according to

$$HP_q = \frac{\sigma_q}{\mu_q} \quad (4.3)$$

where

$$\mu_q = \frac{1}{N} \sum_{i=1}^N q_i \quad (4.4)$$

and

$$\sigma_q = \sqrt{\frac{\sum_{i=1}^N (q_i - \mu_q)^2}{N-1}}. \quad (4.5)$$

Smaller values of the HP_q parameter indicate that the respective microstructure is more homogeneous than a microstructure with a larger value of HP_q .

Three random SEM images collected at 2000X from each processing method were partitioned into 64 equal sized sections using Image Cutter. Eighty sections were randomly selected from the 192 sections for statistical analysis. A binary threshold was applied to each of the sections using Image J and the area fraction of the $\text{Nd}_2\text{Zr}_2\text{O}_7$ phase was measured. The average area fraction and its corresponding standard deviation for each processing method was calculated and the HP_q was determined.

4.3.3 Grain Size Measurements

Random SEM images of the interpenetrating matrix were collected from pellets synthesized from each processing method. A grid of 9 horizontal and 9 vertical lines was applied to three SEM images using Image J software and the intercepts were manually counted. The grain size of the MgO and $\text{Nd}_2\text{Zr}_2\text{O}_7$ phases was determined using the method described by Wurst and Nelson⁷⁵ for two-phase polycrystalline ceramics. The method begins with a correction for the effective length of the test line C_{eff} using the relationship

$$C_{eff} = C(1-\nu) \quad (4.6)$$

where ν is the volume fraction of the second phase and C is the total length of the test line. Since two types of intercepts exist in a composite with a primary phase α and a secondary phase β , the equation for the effective number of line intercepts N_{eff} is modified using the equation

$$N_{eff} = N_{\alpha\alpha} + \frac{1}{2}N_{\alpha\beta} \quad (4.7)$$

where $N_{\alpha\alpha}$ is the number of intercepts of contiguous grains and $N_{\alpha\beta}$ is the number of intercepts between the primary and secondary phases.

The equation that calculated the average grain size of the primary phase is given by

$$\bar{D} = 1.56 \frac{C_{eff}}{MN_{eff}} \quad (4.8)$$

where M is the magnification of the micrograph.

4.3.4 Contiguity

Gurland^{55,56} defines contiguity as the average fraction of surface area shared by a grain of a particular phase with all of the neighboring grains of the same phase and is given by the equation

$$c_{\alpha} = \frac{2N_{\alpha\alpha}}{N_{\alpha\beta} + 2N_{\alpha\alpha}} \quad (4.9)$$

where $N_{\alpha\alpha}$ is the number of interfaces between α - α grains intersected per unit length of line and $N_{\alpha\beta}$ is the number of interfaces between α - β grains intersected per unit length of line. A grid of 9 horizontal and 9 vertical lines was applied to SEM images of the interpenetrating matrix using Image J software and the intercepts per unit line length were manually counted. Contiguity values range from 0 to 1, where 0 represents a 100% α microstructure and 1 represents a 100% β microstructure.

4.4 Composite Characterization

In the following section the macrostructure and microstructure matrix of the composites are characterized by analyzing the heterogeneities and the interpenetrating matrix.

4.4.1 Characterization of the Macrostructure

The four processing methods result in two distinct macrostructures. The first type of macrostructure from pellets synthesized from the mortar and pestle and magnetic bar stirred composite powders is observed in Figures 4.3a and 4.3b, and it is characterized by a higher quantity and density of MgO and Nd₂Zr₂O₇ heterogeneities than the composites in Figures 4.3c

and 4.3d of pellets synthesized from Spex blended and ball milled composite powders. It was shown in Chapter 3 that mortar and pestle and magnetic bar stirring produced composite powders populated by agglomerates of the constituents while Spex blending and ball milling produced relatively uniform and monodisperse particle size distributions. Therefore, the agglomerates are the likely source of the MgO and Nd₂Zr₂O₇ heterogeneities in the sintered composites.

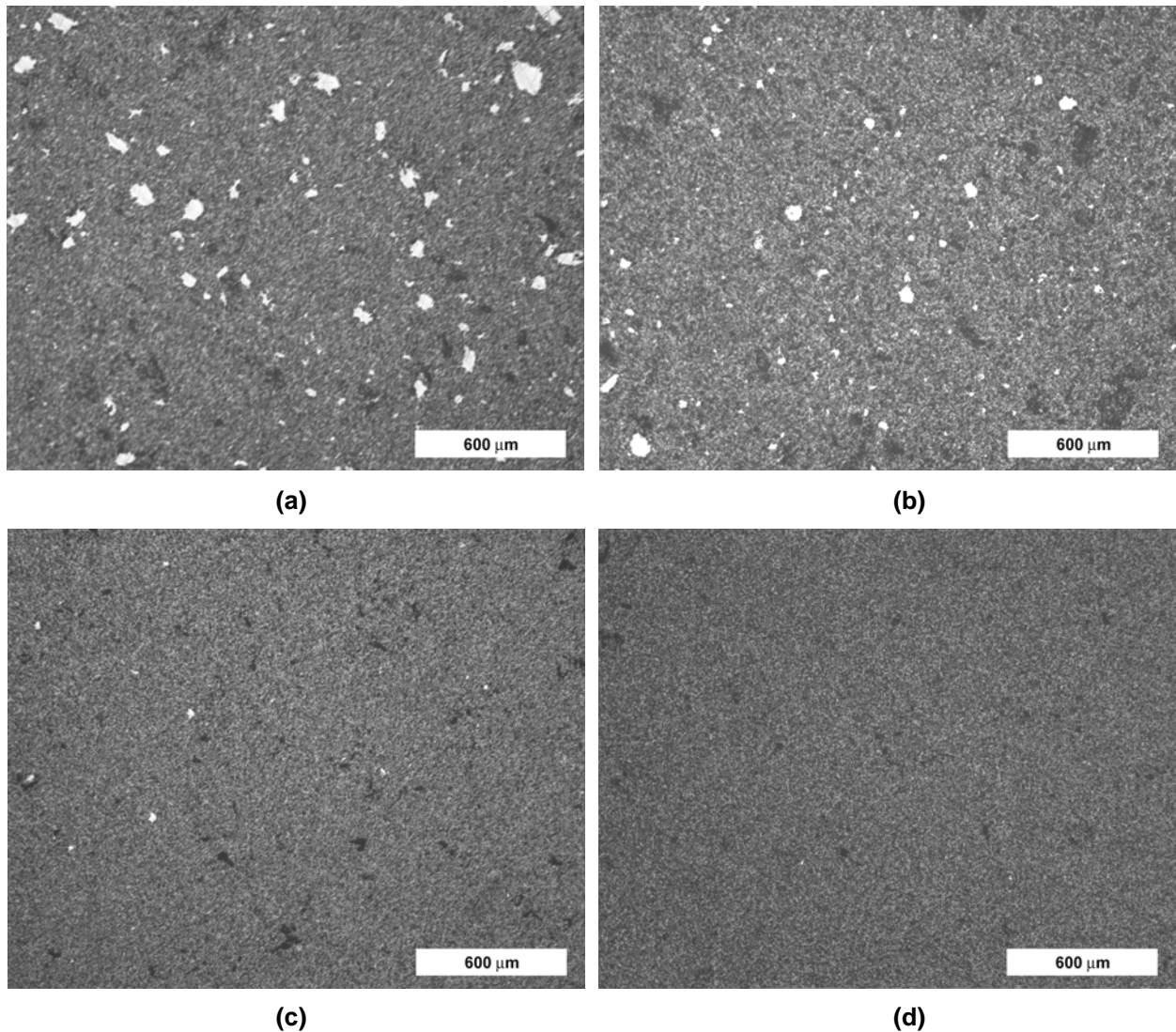


Figure 4-3: Optical images of composite pellets synthesized by the four processing methods. A) mortar and pestle B) magnetic bar stirring C) Spex blending D) ball milling

Optical images were fitted together in Figure 4.4 to form a composite image of an entire pellet from each processing method to look at the distribution of heterogeneities within the composites. In the mortar and pestle and magnetic bar stirring composites shown in Figures 4.4a and 4.4b the heterogeneities appear to be uniformly distributed with no obvious depletion regions within or around the edges of the composite.

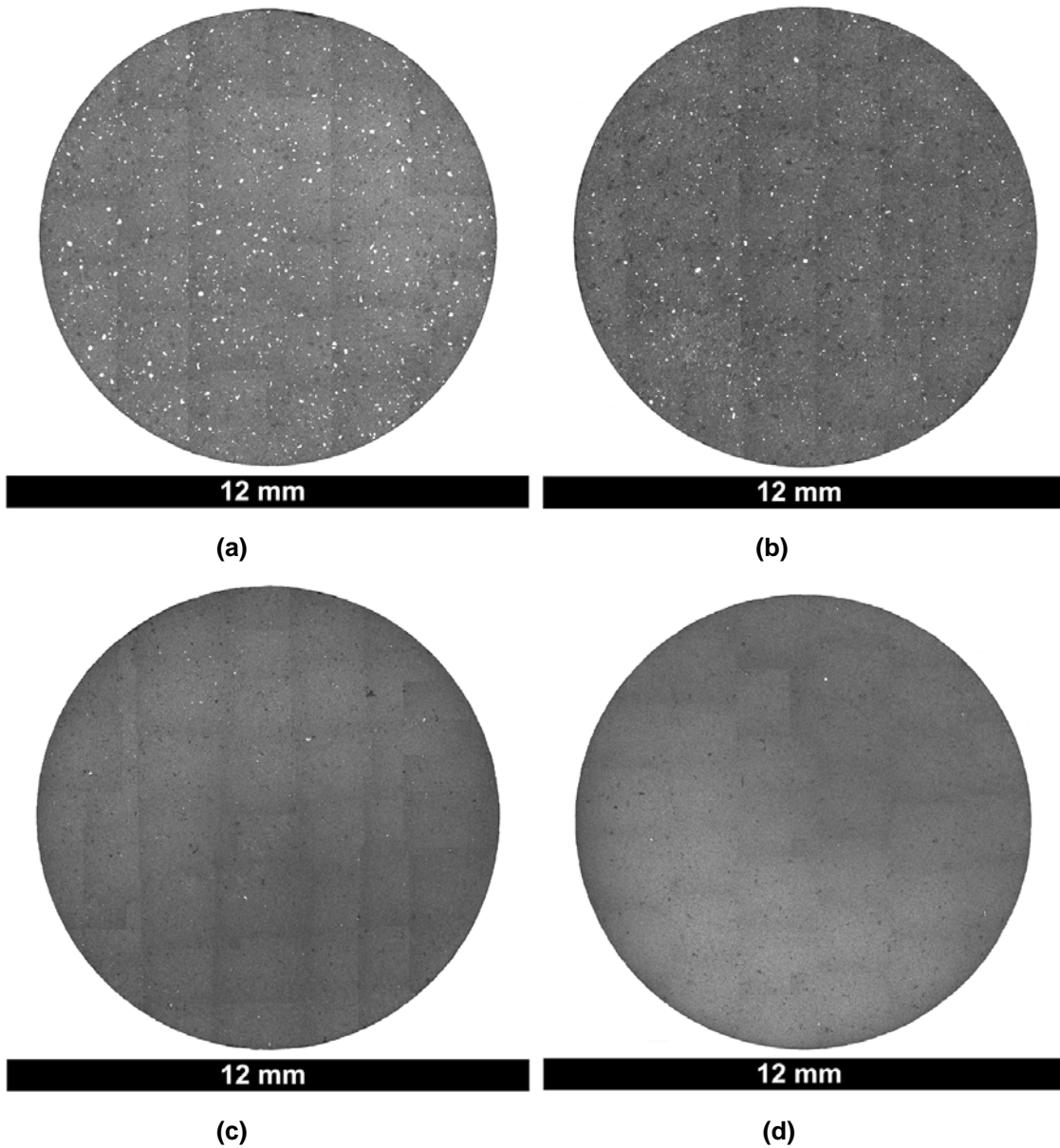


Figure 4-4: Composite of optical images from pellets processed by the four processing methods. A) mortar and pestle B) magnetic bar stirring C) Spex blending D) ball milling

The Spex blended and ball milled composites in Figures 4.4c and 4.4d are sparsely populated by heterogeneities. The density and distribution of the heterogeneities in the random optical images of the composites shown in Figure 4.3 correspond reasonably well to the density of heterogeneities observed throughout the latitudinal cross-section of the pellets in Figure 4.4. Therefore, the macrostructure can be treated as homogeneous for each processing method and the random optical images of the composite macrostructure are representative.

The technique described in Section 4.3.1 to determine the volume fraction of a second phase was used to more accurately analyze the quantity of the MgO and Nd₂Zr₂O₇ heterogeneities. The stereology results in Table 4.1 verified that there is a higher volume fraction of heterogeneities in the mortar and pestle and magnetic bar stirred composites than in the Spex blended and ball milled composites. The total volume fraction of heterogeneities is nearly the same between the mortar and pestle and magnetic bar stirred composites, but there is a larger proportion of Nd₂Zr₂O₇ heterogeneities and a smaller proportion of MgO heterogeneities in the mortar and pestle composites than in the magnetic bar stirred composites. There is a small difference in the total volume fraction of heterogeneities between the Spex blended and ball milled composites due to the slightly higher quantity of MgO heterogeneities in the ball milled composites.

Table 4-1: Quantitative stereology results for the MgO and Nd₂Zr₂O₇ heterogeneities

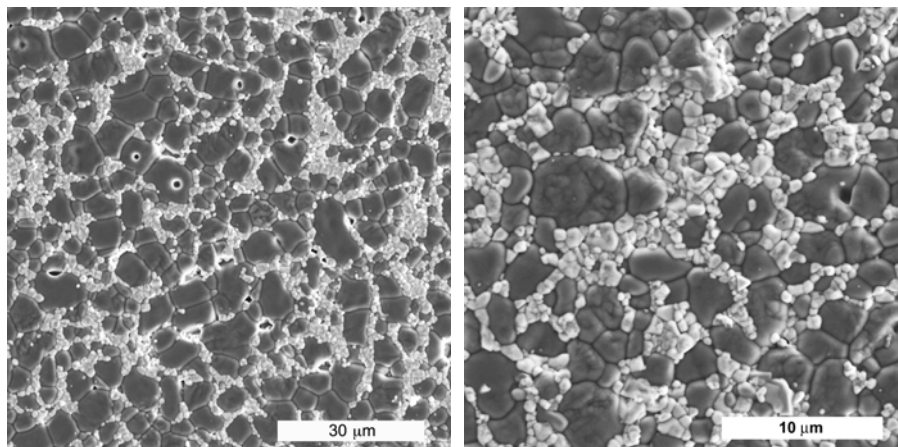
Process	MgO		Nd ₂ Zr ₂ O ₇		Total	
	Volume Fraction (%)	N _L (m ⁻¹)	Volume Fraction (%)	N _L (m ⁻¹)	Volume Fraction (%)	N _L (m ⁻¹)
Mortar and Pestle	0.29	40	1.92	424	2.21	464
Magnetic Bar Stirring	1.33	128	0.73	161	2.06	289
Spex Blending	0.13	53	0.04	22	0.17	75
Ball Milling	0.40	60	0.04	21	0.44	81

The frequency of the heterogeneities was also estimated using the technique described in Section 4.3.1. Mortar and pestle and magnetic bar stirring produce composites with much

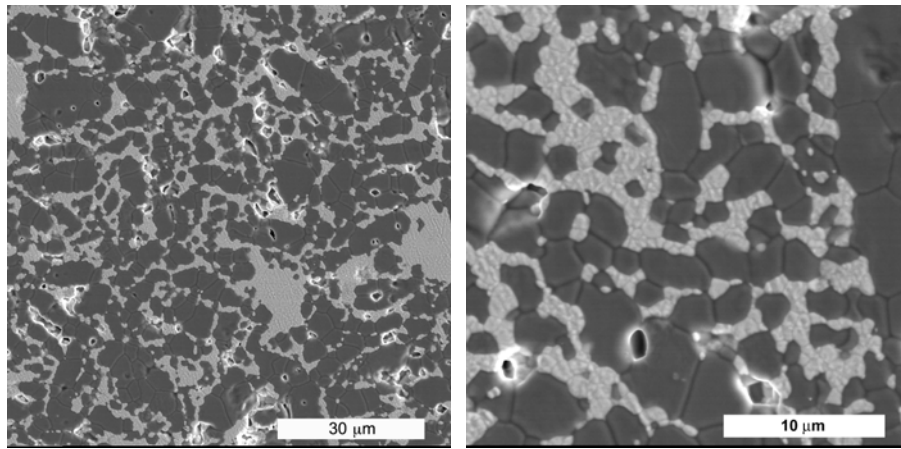
higher total frequencies of heterogeneities than Spex blending and ball milling, although the frequency of the heterogeneities is slightly lower in the magnetic bar stirred composites than in the mortar and pestle composites. Unlike the mortar and pestle and magnetic bar stirred composites, the frequency of the heterogeneities in the Spex blended and ball milled composites is essentially the same. No strong correlation between the volume fraction of heterogeneities and the frequency of the heterogeneities is observed, however. The stereology data shows that a small difference in the total volume fraction of the heterogeneities produces a large difference in the frequency of the heterogeneities in the mortar and pestle and magnetic bar stirred composites, but a larger proportional difference in volume fraction of heterogeneities produces only a slight difference in the frequency of the heterogeneities in the Spex blended and ball milled composites.

4.4.2 Characterization of the Microstructure

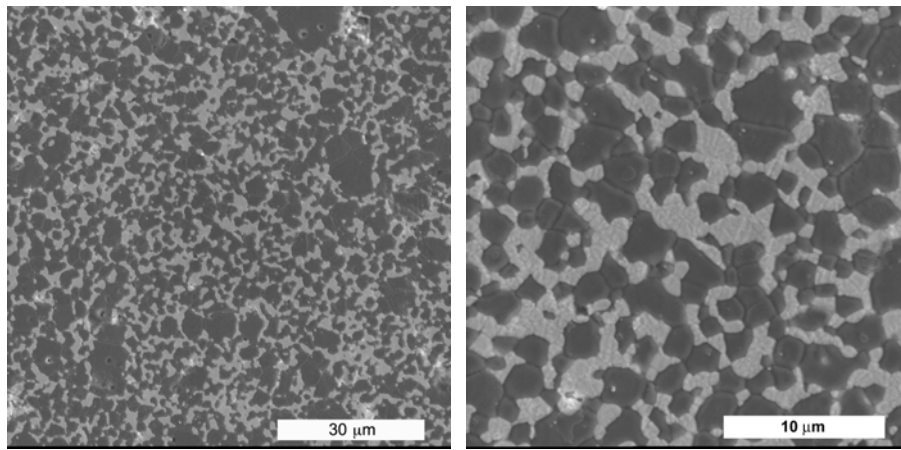
SEM images were used to analyze how the processing method affected the grain size and distribution of the MgO and Nd₂Zr₂O₇ in the interpenetrating matrix. Two SEM images of the interpenetrating matrix from each processing method are shown in Figure 4.5 below. Grain growth experiments carried out at 1450°C has shown that this temperature is not conducive to grain growth in the composites, therefore, thermal etching is not expected to significantly affect the microstructure of the composites.



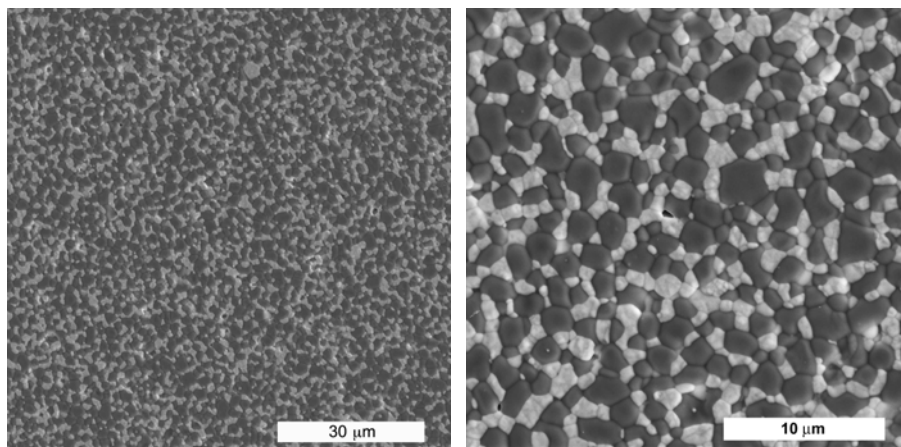
(a)



(b)



(c)



(d)

Figure 4-5: SEM images of the interpenetrating matrix for composites synthesized by the four processing methods. A) mortar and pestle B) magnetic bar stirring C) Spex blending D) ball milling

When the microstructures are compared with each other, there are visible differences in how the constituents are distributed and the average grain size of the MgO and Nd₂Zr₂O₇. The MgO and Nd₂Zr₂O₇ in the Spex blended and ball milled composites appears much more homogeneously distributed than in the mortar and pestle and magnetic bar stirred composites. The grain size of the Nd₂Zr₂O₇ looks approximately the same in all of the composites, but there is an observable variation in grain size of the MgO between the different composites. The connectivity of the thermally conductive MgO is difficult to ascertain visually, so more quantitative techniques were required to accurately characterize the composites. In the following sections the homogeneity, grain size, and contiguity of the interpenetrating matrix is analyzed to determine how processing affects the microstructure of the composite.

4.4.2.1 Homogeneity

The homogeneity of the MgO and Nd₂Zr₂O₇ was characterized using the technique described in Section 4.3.2. The results of the analysis are shown below in Table 4.2, where lower values are indicative of more homogeneous structures. The MgO is more homogeneous than the Nd₂Zr₂O₇ in all of the composites. The results also confirm the previous observation that the Spex blended and ball milled composites are more homogeneous than the mortar and pestle and magnetic bar stirred composites. The homogeneity of the MgO and Nd₂Zr₂O₇ in the mortar and pestle and magnetic bar stirred composites is essentially the same, demonstrating that the distribution of the phases in these composites is identical. The Spex blended composite is more homogeneous than the mortar and pestle and magnetic bar stirred composites. As expected, ball milling produces the most homogeneous composite.

Table 4-2: Homogeneity of the MgO and Nd₂Zr₂O₇ constituent phases in the interpenetrating matrix.

Constituent	Homogeneity			
	Mortar and Pestle	Magnetic Bar Stirring	Spex Blending	Ball Milling
MgO	0.22	0.24	0.18	0.10
Nd ₂ Zr ₂ O ₇	0.56	0.53	0.35	0.20

The homogeneity of the microstructure depends on the how the processing method mixes the MgO and $\text{Nd}_2\text{Zr}_2\text{O}_7$. The primary difference in the processing methods between the mortar and pestle and magnetic bar stirring processes and the Spex blending and ball milling processes is the presence of milling media in the Spex blending and ball milling methods. Not only does the milling media provides mechanical energy to break up the agglomerates, but it also improves the homogeneity of the microstructure. The milling media increases the surface area between which the MgO and $\text{Nd}_2\text{Zr}_2\text{O}_7$ agglomerates were broken apart and the constituents mixed together. The increase in surface area mixes the constituents more thoroughly improving the homogeneity of the microstructure. The ball milling process has more surface area than the Spex blending media since there are ten 10 mm YSZ milling media and 150 g of 3 mm YSZ milling media in the ball milling jar compared to the two 10 mm PMMA blending media in the Spex blending jar. The considerable increase in the quantity of media and the corresponding increase in surface area resulted in an improvement of the homogeneity in the ball milled composites compared to the Spex blended composites. In the case of the mortar and pestle method, the combined surface area of the 120 mm mortar and pestle is not large enough to homogeneously mix the constituents and in the magnetic bar stirring method there is no media to affect the mixing.

4.4.2.2 Grain Size

The grain size of the MgO and $\text{Nd}_2\text{Zr}_2\text{O}_7$ in the interpenetrating matrix was measured using the technique described in Section 4.3.3. In all of the composites the grain size of the $\text{Nd}_2\text{Zr}_2\text{O}_7$ was smaller than that of the MgO. The grain size of the $\text{Nd}_2\text{Zr}_2\text{O}_7$ is the same in all of the composites, but the grain size of the MgO varies across the composites. Ball milling produces composites with the smallest average MgO grain size and the smallest standard deviation. Mortar and pestle mixing produces composites with the largest MgO grain size and largest standard deviation. Magnetic bar stirring and Spex blending produce composites that are identical in MgO and $\text{Nd}_2\text{Zr}_2\text{O}_7$ grain sizes and standard deviations.

Table 4-3: Grain size of the MgO and Nd₂Zr₂O₇ constituent phases in the interpenetrating matrix.

Constituent	Grain Size (μm)			
	Mortar and Pestle	Magnetic Bar Stirring	Spex Blending	Ball Milling
MgO	3.7 \pm 1.0	2.5 \pm 0.6	2.4 \pm 0.6	2.1 \pm 0.3
Nd ₂ Zr ₂ O ₇	1.2 \pm 0.4	1.1 \pm 0.3	1.0 \pm 0.3	1.2 \pm 0.3

The similar grain size of the MgO and Nd₂Zr₂O₇ between the composites is due to the coarsening resistant nature of dual phase interpenetrating microstructures. Limited solubility is expected between MgO and Nd₂Zr₂O₇, therefore, grain growth is inhibited because long range diffusion of the phases is not favorable. The growth of the two phases is coupled, so the grain growth of both the MgO and Nd₂Zr₂O₇ is controlled by the growth of the slowest growing phase.⁴⁶ The microstructure will evolve such that the ratio of the two phases is constant. As the microstructure coarsens, the character of the microstructure should remain the same even though the scale of the microstructure increases.⁴⁴

4.4.2.3 Contiguity

The third microstructure feature of interest is the contiguity of the MgO and Nd₂Zr₂O₇. The procedure to calculate the contiguity of the phases is described in Section 4.3.4, and the results of the analysis is shown below in Table 4.4. There appears to be no discernable pattern in the contiguity of the Nd₂Zr₂O₇. The contiguity of the Nd₂Zr₂O₇ ranges from the lowest value of 0.25 for the ball milled composites to 0.61 for the mortar and pestle composites. The contiguity of the MgO is between 0.40 and 0.47 in three of the composites, but decreases to 0.29 in the Spex blended composites.

The contiguity of the microstructure is not related to the homogeneity or grain size of the interpenetrating matrix. The Spex blended and ball milled composites were more homogeneous than the mortar and pestle and magnetic bar stirred composites, yet the contiguity of the MgO in the mortar and pestle, magnetic bar stirred, and ball milled composites are approximately the

same and the contiguity of the Spex blended composites is lower than the others. The grain size of the $\text{Nd}_2\text{Zr}_2\text{O}_7$ is the same in all of the composites, but the contiguity of the $\text{Nd}_2\text{Zr}_2\text{O}_7$ is not consistent between the composites. Since the homogeneity and grain size of the microstructure cannot be correlated with the contiguity of the interpenetrating matrix, it is an independent parameter to describe the effect of processing on the microstructure of the composites.

Table 4-4: Contiguity of the MgO and $\text{Nd}_2\text{Zr}_2\text{O}_7$ constituent phases in the interpenetrating matrix.

Constituent	Contiguity			
	Mortar and Pestle	Magnetic Bar Stirring	Spex Blending	Ball Milling
MgO	0.47	0.40	0.29	0.45
$\text{Nd}_2\text{Zr}_2\text{O}_7$	0.61	0.52	0.35	0.25

4.4.3 Processing Defects

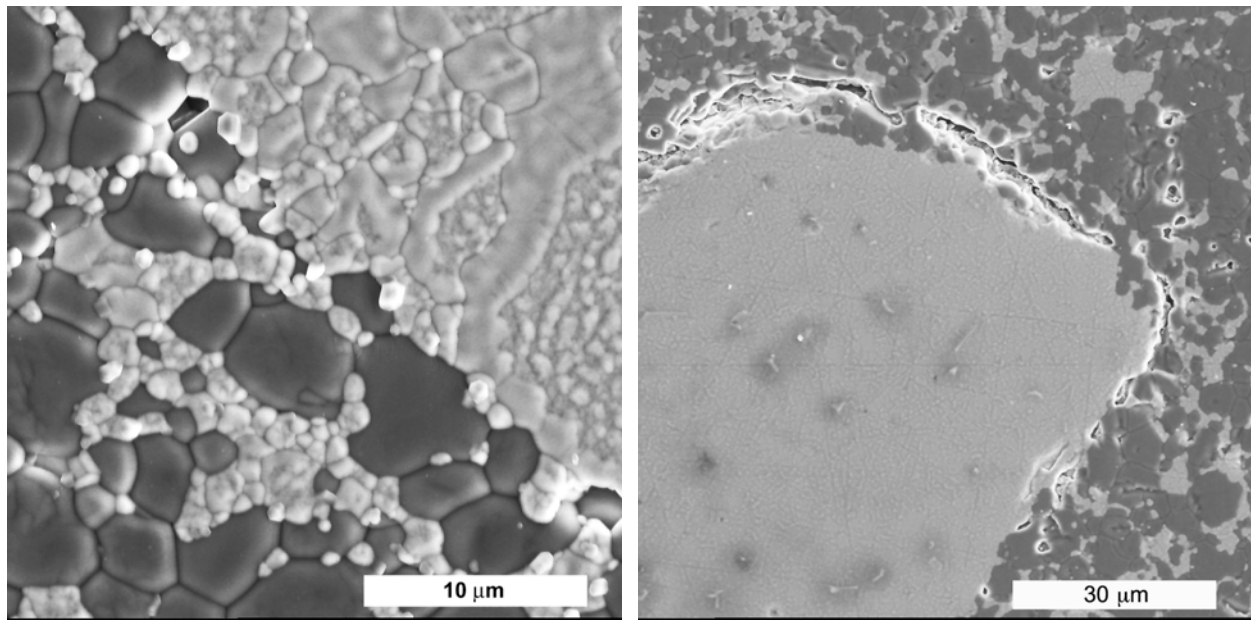
The composite microstructures were analyzed in more detail on polished and thermally etched samples to look for processing defects. Circumferential cracking was observed between $\text{Nd}_2\text{Zr}_2\text{O}_7$ heterogeneities and the interpenetrating matrix in mortar and pestle and magnetic bar stirred composites, but not in Spex blended or ball milled composites. Representative images of the heterogeneity—matrix interface in mortar and pestle and magnetic bar stirred composites are shown below in Figure 4.6. In Figure 4.6a the heterogeneity—matrix interface is intact, but in Figure 4.6b circumferential cracking has occurred between the heterogeneity and the interpenetrating matrix. The circumferential cracking observed between the heterogeneities and the interpenetrating matrix could be caused by either the difference in the coefficients of thermal expansion between the MgO and $\text{Nd}_2\text{Zr}_2\text{O}_7$, or by differential sintering.

It is unlikely that the difference in the coefficient of thermal expansion between the heterogeneities and the interpenetrating matrix could have caused the circumferential cracking. The coefficient of thermal expansion (CTE) for MgO is $13.1 \times 10^{-6} \text{ K}^{-1}$ and the CTE of $\text{Nd}_2\text{Zr}_2\text{O}_7$ is

$9.5 \times 10^{-6} \text{ K}^{-1}$.^{76;77} However, the difference in the CTEs is modulated by the morphology of the interpenetrating matrix. The effective CTE of the matrix will fall between the two values according to the equation

$$\alpha_e = \frac{V_d E_d \alpha_d + V_m E_m \alpha_m}{V_d E_d + V_m E_m} \quad (4.10)$$

where V is the volume fraction, E is the Young's modulus^{78;79}, and α is the CTE of the dispersed or matrix phase. The effective CTE of the matrix is calculated to be $12.2 \times 10^{-6} \text{ K}^{-1}$, further decreasing the difference between the CTEs of the heterogeneities and the interpenetrating matrix. In addition, MgO and $\text{Nd}_2\text{Zr}_2\text{O}_7$ are isotropic and the composites are polycrystalline. Therefore, the stresses that are created as the composites cool are homogeneously distributed throughout the microstructure and areas of high stress concentration are unlikely to develop.



(a)

(b)

Figure 4-6: SEM images of $\text{Nd}_2\text{Zr}_2\text{O}_7$ heterogeneities showing the interface between the heterogeneity and the interpenetrating matrix. A) an intact interface between the heterogeneity and the interpenetrating matrix B) circumferential cracking between the heterogeneity and the interpenetrating matrix

Chapter 3 showed that there is a significant population of both soft and hard agglomerates present in the mortar and pestle and magnetic bar stirred mixed composite powders. The hard agglomerates are composed of loosely packed particles connected by solid chemical bridges of material. The green density of the hard agglomerates is less than the green density of the matrix because the particles are more loosely packed within the hard agglomerates than in the surrounding matrix. Isostatic pressing is unlikely to provide enough pressure to break the hard bridges and improve the green density of the agglomerate when the green pellet is fabricated. Differences between the green density of the agglomerates and the matrix causes differential strain according to

$$\Delta\varepsilon = \varepsilon_m - \varepsilon_a = \left(\frac{\rho_{0a}}{\rho_a} \right)^{1/3} - \left(\frac{\rho_{0m}}{\rho_m} \right)^{1/3} \quad (4.11)$$

where ρ_{0a} and ρ_{0m} are the green densities of the agglomerate and the matrix, respectively.⁸⁰ The ratio of (ρ_a/ρ_m) determines if $\Delta\varepsilon$ is tensile or compressive. In this case, the agglomerates shrink faster than the surrounding matrix and isostatic tensile stresses arise within the agglomerate. In the surrounding matrix, the radial stresses are tensile and the tangential stresses are compressive creating a pure shear state. When the magnitude of the stresses exceeds the strength of the interfacial bond, the internal stresses are relieved through the formation of a circumferential crack between the heterogeneity and the interpenetrating matrix.

4.5 Conclusions

The macrostructure and microstructure of the composites processed by the four processing methods were characterized. The composite was composed of MgO and Nd₂Zr₂O₇ heterogeneities surrounded by an interpenetrating matrix of MgO and Nd₂Zr₂O₇ grains. The macrostructure was defined as the features identifiable with optical microscopy and the microstructure was defined as the features identifiable with SEM. The heterogeneities were characterized using established quantitative stereology techniques by treating the

heterogeneities as a second phase. Quantitative stereology was also used to characterize the homogeneity, grain size, and contiguity of the MgO and $\text{Nd}_2\text{Zr}_2\text{O}_7$ in the interpenetrating matrix.

The MgO and $\text{Nd}_2\text{Zr}_2\text{O}_7$ heterogeneities appeared in composites that possessed a large population of agglomerates in the mixed composite powders. The agglomerates also resulted in differential sintering which caused circumferential cracking between the heterogeneities and the interpenetrating matrix to occur. The heterogeneities were homogeneously distributed through the composite with no depletion regions within or near the edges of the composites. The mortar and pestle and magnetic bar stirred composites possessed a higher quantity and frequency of heterogeneities than the Spex blended and ball milled composites. A correlation between the volume fraction and the frequency of the heterogeneities could not be made since increases in the volume fraction of the heterogeneities did not result in a proportional increase in the frequency of the heterogeneities.

The interpenetrating matrix of the composite was characterized using SEM to analyze the size and distribution of the MgO and $\text{Nd}_2\text{Zr}_2\text{O}_7$. Ball milling produced the most homogeneous composites since the ball milling media provided the most surface area to mix the constituent phases. The grain size of the $\text{Nd}_2\text{Zr}_2\text{O}_7$ in the interpenetrating matrix was the same for all of the composites, but there were slight differences in the grain size of the MgO. The contiguity of the $\text{Nd}_2\text{Zr}_2\text{O}_7$ varied among the composites, but the contiguity of the MgO in the mortar and pestle, magnetic bar stirred, and ball milled composites was nearly the same. However, the contiguity of the Spex blended composites decreased slightly. No correlations could be made between the homogeneity, grain size, and contiguity of the interpenetrating matrix.

More detailed analysis of the microstructure was performed to search for processing defects. Cracks were observed between $\text{Nd}_2\text{Zr}_2\text{O}_7$ heterogeneities and the interpenetrating matrix in mortar and pestle and magnetic bar stirred composites. It was determined that these cracks were probably not caused by CTE mismatch between the heterogeneity and the matrix.

It is more likely that the circumferential cracks result from stresses that cause interfacial debonding between the heterogeneities and interpenetrating matrix when the $\text{Nd}_2\text{Zr}_2\text{O}_7$ agglomerates densify faster than the surrounding matrix.

The processing—structure relationships discussed in this chapter will be used to analyze the macrostructure—thermal diffusivity relationships in Chapter 5 and the microstructure—thermal conductivity relationships in Chapter 6 to correlate the effect of processing on the thermal diffusivity and thermal conductivity of composites.

CHAPTER 5 MACROSTRUCTURE—THERMAL DIFFUSIVITY RELATIONSHIP

5.1 Introduction

This chapter begins by describing the laser flash thermal diffusivity technique. The thermal diffusivity results for the composites synthesized in Chapter 3 and characterized in Chapter 4 are then reported. A discussion on the relationship between the macrostructure and the thermal diffusivity of the composites follows.

5.2 Laser Flash Thermal Diffusivity

A ~10 mm diameter and ~1.5 mm thick pellet was ground flat and parallel (<2% variation in thickness) using a Struers polishing wheel equipped with 320 grit SiC paper. The flat and parallel pellet was cleaned in an ultrasonic bath for 3 minutes before being dried with compressed air. The precise diameter and thickness of the flat and parallel pellet were measured using calibrated calipers and weighed on a calibrated scale. Both flat surfaces of the pellets were coated with colloidal graphite (Kontakt Chemie Graphit 33) to reduce the sample transparency to the laser before being placed into the graphite sample carrier shown in Figure 5.1 by placing the pellet on the sample support and covering the sample with the cap.



Figure 5-1: Schematic of a Netzsch LFA sample holder (courtesy of Netzsch Thermal Analysis).

The sample holder assembly was placed in the sample carousel along with sample holders containing a graphite reference and a second sample to be measured. The schematic of the Netzsch LFA 457 in Figure 5.2 shows the location of the sample carousel in the instrument along with the position of the detector and laser.

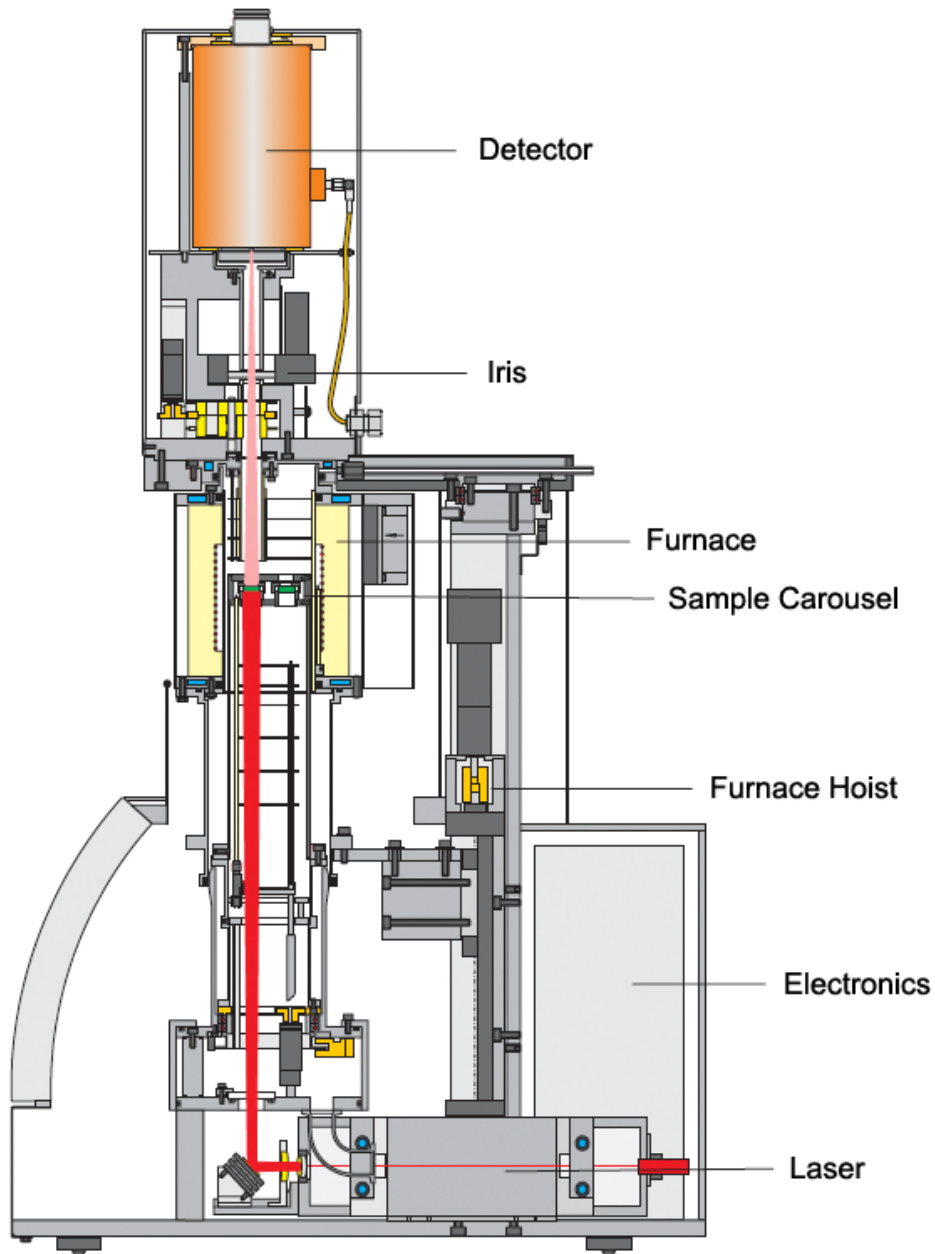


Figure 5-2: Cutaway schematic of a Netzsch LFA 457 laser flash analyzer (courtesy Netzsch Thermal Analysis).

The laser flash method was first proposed by Parker et al.⁸¹ to measure the thermal diffusivity on homogeneous and isotropic samples. The method involves a laser pulse of known energy striking the surface of the sample and a detector measuring the rise in temperature on the opposite side of the sample as a function of time. A schematic of this process is shown in Figure 5.3.

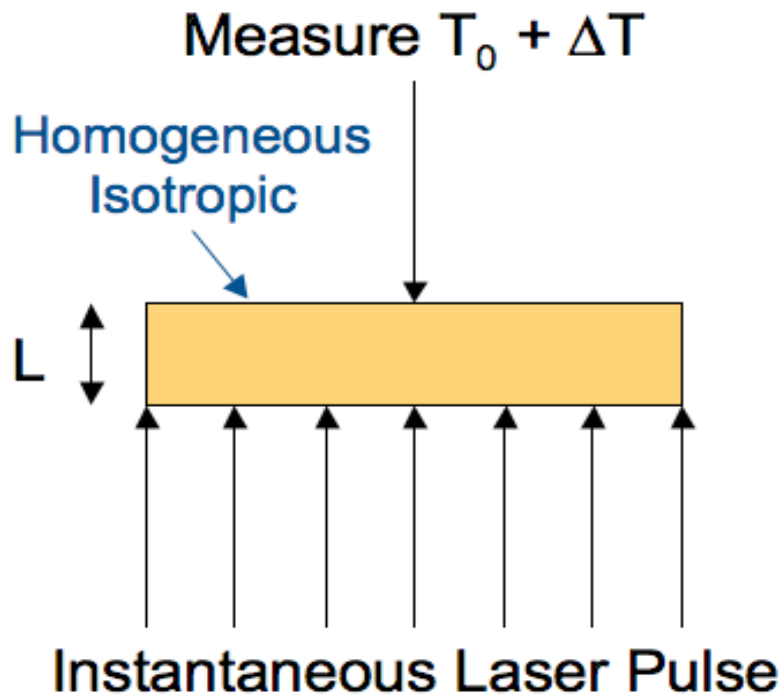


Figure 5-3: Diagram of the laser pulse and measurement in laser flash thermal diffusivity.

The detector signal outputs a thermogram of the signal vs. time, an example of which is shown below in Figure 5.4. The Netzsch Proteus software analyzes the thermogram to find the maximum signal V_{max} that determines the half time $t_{1/2}$. At this time, a Cowan⁸² correction was applied to account for the heat losses at the surface of the samples. The half time is used in the equation below to calculate the thermal diffusivity of the sample

$$\alpha = 1.38 \frac{L^2}{\pi^2 t_{1/2}} \quad (5.1)$$

where L is the thickness of the sample. Three laser shots were performed on each sample at each of the designated temperatures, resulting in three separate thermal diffusivity measurements.

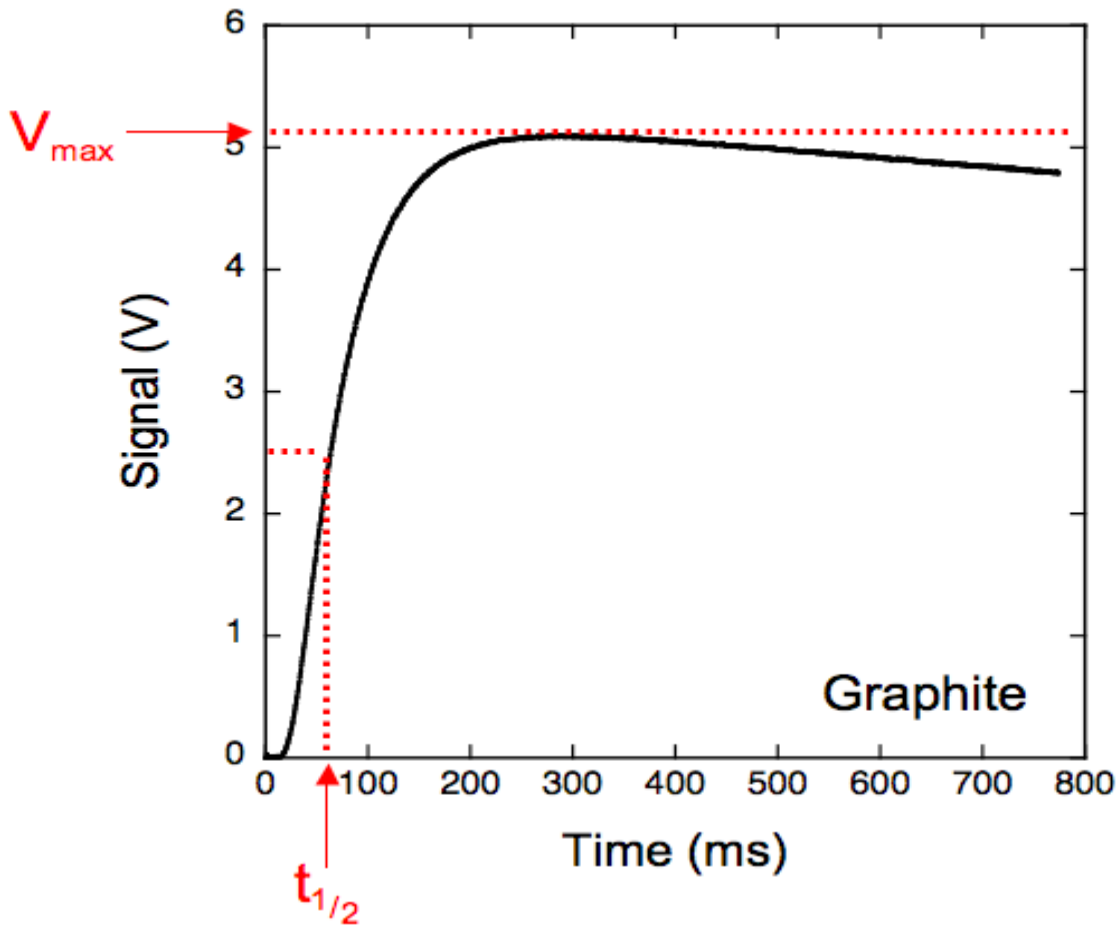


Figure 5-4: Thermogram signal from the graphite standard showing the calculation of $t_{1/2}$.

The samples were measured under flowing Argon in 100°C intervals from 100°C to 1000°C according to the furnace profile shown in Figure 5.5. The sample thermocouple was used to establish the measurement temperature, not the furnace thermocouple. Before the thermal diffusivity measurements could begin at the designated 100°C intervals, the samples were required to thermally equilibrate for 10 minutes.

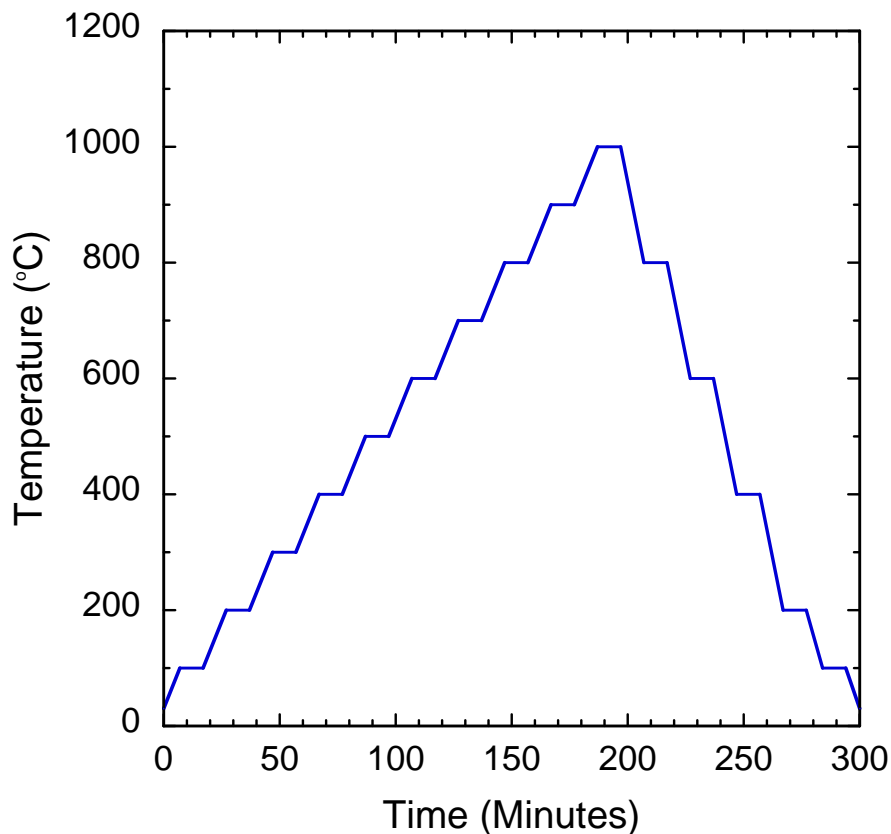
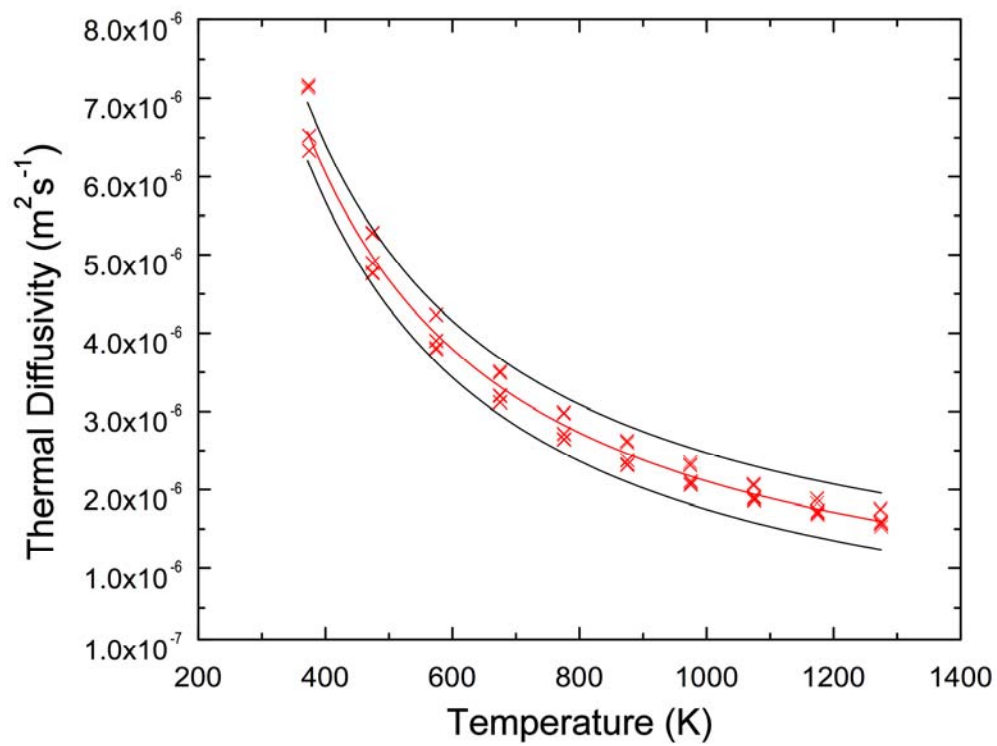


Figure 5-5: Temperature profile for laser flash thermal diffusivity measurements.

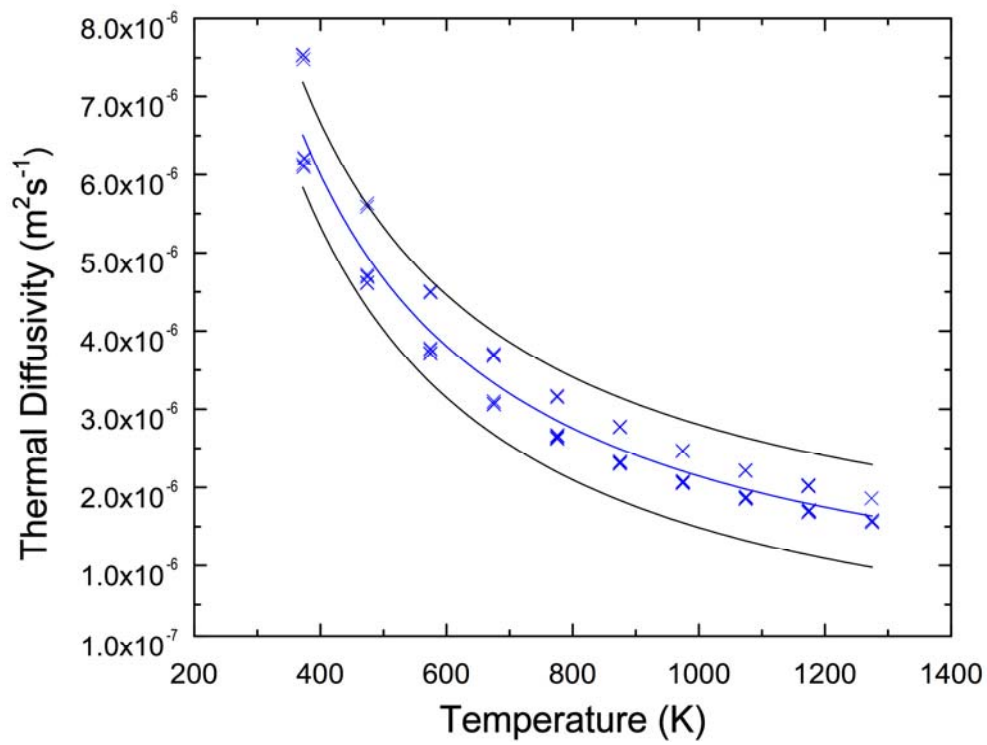
The thermal diffusivity was measured at 200°C intervals as the furnace temperature decreased. The thermal diffusivity at the 200°C intervals was compared to the thermal diffusivity at the 100°C intervals to check for if there was a thermal diffusivity hysteresis.

5.3 Results and Discussion

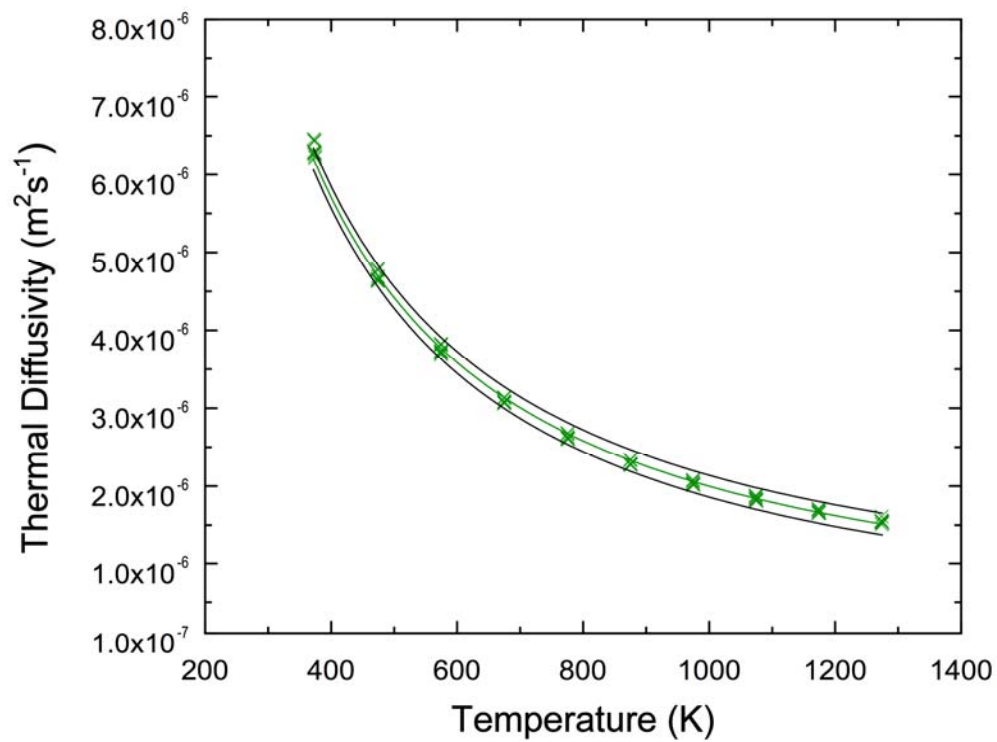
Three pellets were measured from each batch of mixed composite powder and all of the thermal diffusivity measurements are plotted in Figure 5.6. The average thermal diffusivity was calculated from the nine measurements at each temperature. The average thermal diffusivity and the 95% confidence interval bands are plotted in Figure 5.6 using solid black lines for the lower and upper bounds. The average composite porosity was shown in Section 3.6, and the variation in the porosity was only ~0.5% between the three measured samples. All of the samples were corrected to 0% porosity.



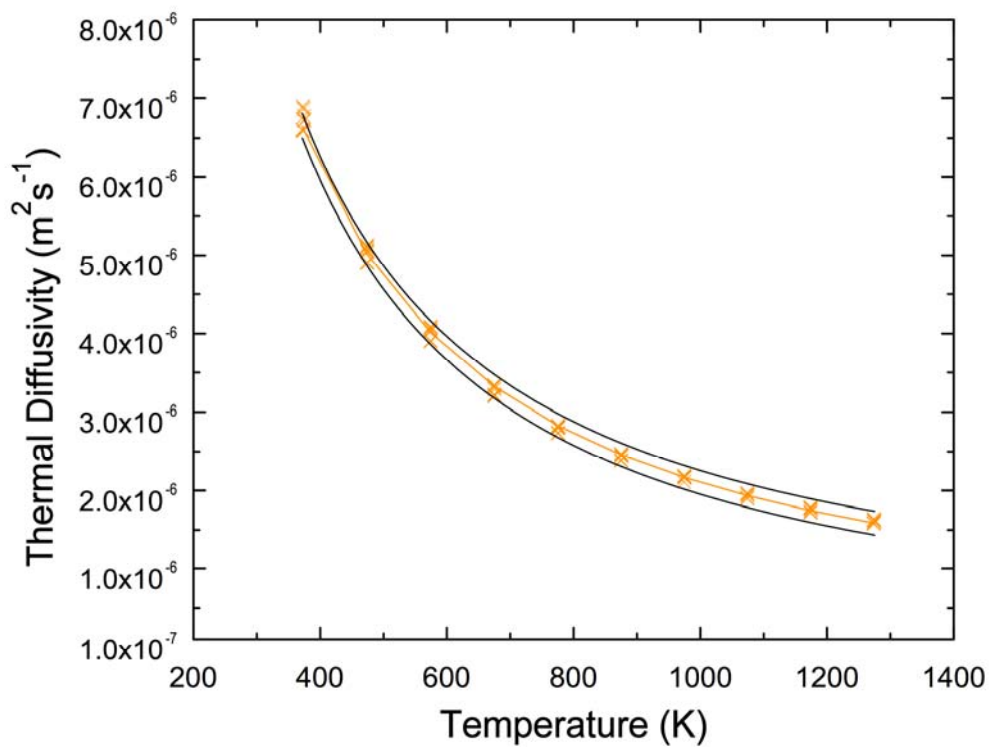
(a)



(b)



(c)



(d)

Figure 5-6: Corrected thermal diffusivity of pellets processed by the four processing methods. A) mortar and pestle B) magnetic bar stirring C) Spex blending D) ball milling.

The widths of the confidence intervals were compared to assess the amount of sample-to-sample variation in the composites synthesized from the same processing method. The confidence intervals for the mortar and pestle and magnetic bar stirred composites are much wider than the confidence intervals for Spex blended and ball milled composites. The width of the confidence interval for the Spex blended composites is ~3% of the average thermal diffusivity and the width of the confidence interval for the ball milled composites is ~6% of the average thermal diffusivity. However, the width of the confidence intervals in the mortar and pestle composites is ~12% of the average thermal diffusivity and the width of the confidence interval for the magnetic bar stirred composites is ~20% of the average thermal diffusivity. Therefore, there is much less sample-to-sample variation in the thermal diffusivity in the Spex blended and ball milled composites than in the mortar and pestle and magnetic bar stirred composites.

Chapter 3 showed the existence of hard and soft agglomerates in the mortar and pestle and magnetic bar stirred mixed composite powders and Chapter 4 established that these agglomerates led to the formation of heterogeneities in the sintered composites. Given that the confidence intervals are much wider in the mortar and pestle and magnetic bar stirred composites than in the Spex blended and ball milled composites, it is reasonable to conclude that the heterogeneities are responsible for the increase in the sample-to-sample variation.

Section 4.3.3 discussed how the presence of hard agglomerates in the mixed composite powders resulted in the formation of the circumferential cracks from differential sintering. The presence of these circumferential cracks at the heterogeneity—interpenetrating matrix interface will cause a decrease in the effective thermal diffusivity of the composite.⁸³⁻⁸⁵ There is likely to be a variation in the number of hard agglomerates pressed into green pellets because of the probability of more or less hard agglomerates in a specific sample of the composite powder. The variation in the number of hard agglomerates in the green pellets will cause more or less circumferential cracks to form in the magnetic bar stirred and mortar and pestle composites.

Hasselmann⁸³ derived an expression to describe the effect of microcracks on the effective conductivity of a material. Equation 5.2 is a simplified expression of the equation that relates the effective conductivity of the material to the density and size of the cracks present in the material

$$\kappa = \kappa_0 \left(1 + \frac{8Nb^3}{9} \right)^{-1} \quad (5.2)$$

where N is the density of cracks and b is the crack radius. Although this is an expression for the thermal conductivity of a material and not the diffusivity, it still applies in this case because the composition of the composites is constant between the processing methods. Therefore, the thermal diffusivity is the only property that would affect the thermal conductivity of the composites.

Equation 5.2 clearly shows that as the number of circumferential cracks in the composites increases, the effective conductivity of the composite decreases. Chapter 3 showed that the number of hard agglomerates is greater in the magnetic bar stirring composite powder than in the mortar and pestle composite powder. An increase in the number of hard agglomerates in the green pellet will increase the density of circumferential cracks that are formed. Therefore, it makes sense that the width of the confidence interval is larger in the magnetic bar stirred composites because the effective conductivity of the magnetic bar stirred composites will decrease more than the effective conductivity of the mortar and pestle composites.

Detailed characterization of the circumferential cracking in the composites was not performed, therefore it is not possible to calculate the actual crack density in these composites. A rough estimate of a crack density that would result in the observed sample-to-sample variation in the composites was calculated based on Equation 5.2 and an average crack width of 2 μm . In the case of the magnetic bar stirred composites, the estimated crack density is

$\sim 1.4 \times 10^{16} \text{ m}^{-3}$ and the crack density for the mortar and pestle composites is $\sim 0.7 \times 10^{16} \text{ m}^{-3}$. The density is higher than can be predicted based on the quantitative stereology of the heterogeneities, but the analysis that was performed on the circumferential cracks suggests that there is a wide variation in crack sizes and in the number of cracks that surround one particular heterogeneity. Without detailed characterization of the circumferential cracks, the estimated crack density is assumed to be reasonable.

5.4 Conclusions

The thermal diffusivity of three pellets from each batch of mixed composite powder was measured from 100°C to 1000°C at 100°C intervals using laser flash thermal diffusivity. The results show that the sample-to-sample variation in the thermal diffusivity of the Spex blended and ball milled composites is small, however, the sample-to-sample variation of the mortar and pestle and magnetic bar stirred composites is 4× and 7× that of the Spex blended composites, respectively. The heterogeneities are the likely cause of the observed sample-to-sample variation in the mortar and pestle and magnetic bar stirred composites, due to the presence of circumferential cracks between the $\text{Nd}_2\text{Zr}_2\text{O}_7$ heterogeneities and the interpenetrating matrix. The circumferential cracks will interfere with the transfer of heat across the heterogeneity—interpenetrating matrix interface, decreasing the effective thermal diffusivity of the composite. The presence of hard agglomerates in the mortar and pestle and magnetic bar stirred composite powder causes the circumferential cracking. The variation in the number of hard agglomerates in the green pellets results in the observed sample-to-sample variation in the mortar and pestle and magnetic bar stirred composites.

There are more hard agglomerates in the magnetic bar stirred composites than in the mortar and pestle composites, resulting in an increase in the number of circumferential cracks present in the magnetic bar stirred composites compared to the mortar and pestle composites. The increase in the number of circumferential cracks causes a larger decrease in the effective

thermal conductivity of the composite according to Equation 5.2. Thus, the width of the confidence interval in the magnetic bar stirred composites is larger than the width of the confidence interval in the mortar and pestle composites.

CHAPTER 6 MICROSTRUCTURE—THERMAL CONDUCTIVITY RELATIONSHIP

6.1 Introduction

This chapter begins by describing how the thermal conductivity is calculated from the thermal diffusivity measurements that were performed in Chapter 5. The thermal conductivity of the composites is then reported and discussed. The microstructure—thermal conductivity relationships are then developed.

6.2 Thermal Conductivity Calculation

The thermal conductivity was calculated from the thermal diffusivity measurements using the following equation

$$\kappa = \alpha\rho C_p \quad (6.1)$$

where α is the thermal diffusivity, ρ is the density, and C_p is the specific heat capacity of the sample. The thermal diffusivity was calculated by averaging the nine thermal diffusivity measurements on the three composites from each processing method. The specific heat capacity of the composites was measured using differential scanning calorimetry. The experimental procedure and results are described in Appendix C. The thermal expansion of the composites was also measured using dilatometry to calculate the density of the composites as a function of temperature. The thermal expansion of the composites and details of the experimental procedure are given in Appendix D.

Equation 6.2 was then applied to the calculated thermal conductivity to correct for the porosity in the composites

$$\kappa_c = \kappa_m \left(1 - \frac{4}{3} f \right) \quad (6.2)$$

where k_c and k_m are the thermal conductivities of the composite and matrix and f is the volume fraction of the pores.⁸⁶ The composites were corrected to 0% porosity. The error bars that account for the sample-to-sample variation within the processing methods were calculated by

propagating the standard deviation from the average thermal diffusivity through the calculation of the thermal conductivity.

6.3 Results and Discussion

The thermal conductivity and its corresponding error for each processing method is shown below in Figure 6.1. In Section 2.3.1 it was shown that at high temperatures ($T > \theta_D$) that the thermal conductivity can be fit to the following relationship

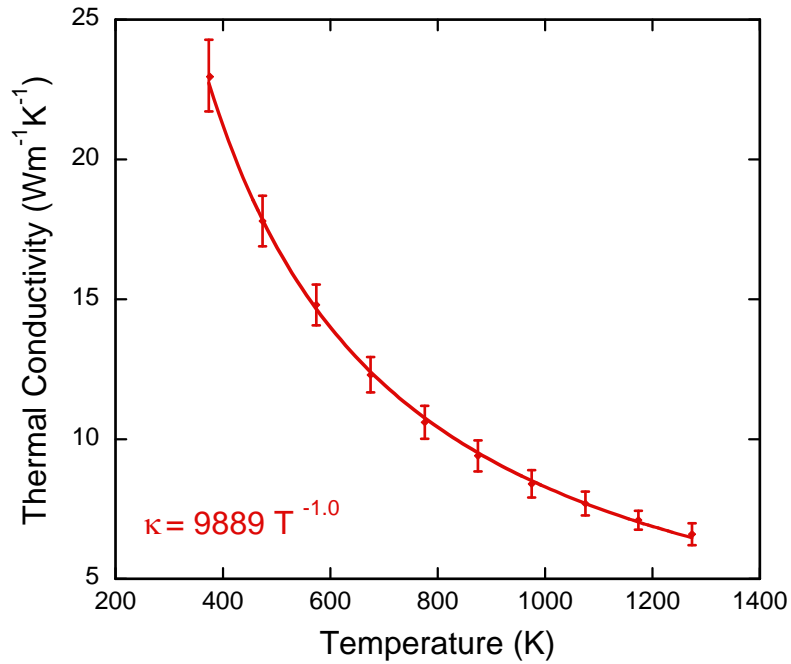
$$\kappa = cT^{-\alpha} \quad (6.3)$$

where α is between 1 and 2 depending on the type of scattering mechanism that dominates and c is a constant. The resulting equation describing the thermal conductivity for each processing method is also given in Figure 6.1. The α value for all of the composites is 1, confirming that 3-phonon Umklapp processes is the dominant scattering mechanism of the thermal energy in the composites.⁸⁷

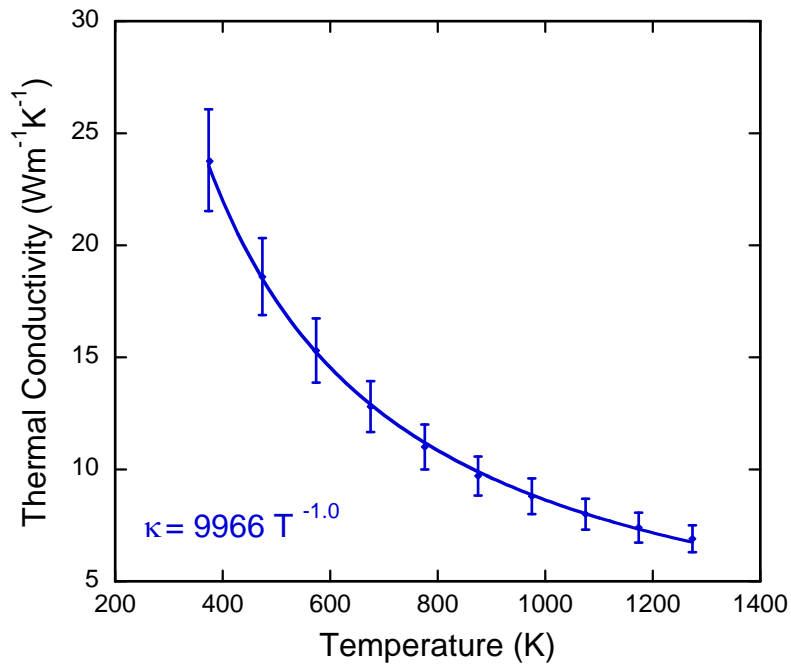
The value of the constant c can be used to compare the magnitude of the thermal conductivity between the different processing methods. The thermal conductivity of the ball milled composites is the highest of the four processing methods. The thermal conductivity of the magnetic bar stirred composites is slightly higher than the mortar and pestle composites, and the thermal conductivity of the Spex blended composites is the lowest of the four processing methods. The thermal conductivity of all of the composites from the different processing methods is compared in Figure 6.2. If the error is included in the analysis, the thermal conductivity of the mortar and pestle, magnetic bar stirred, and ball milled composites is the same. However, even when the errors are included, the thermal conductivity of the Spex blended composites is lower than the composites from the other three processing methods.

The effect of processing on the thermal conductivity of the composites began by analyzing if the macrostructure affected the thermal conductivity. As it was shown in Chapter 4, the mortar and pestle and magnetic bar stirred composites have a much higher quantity and

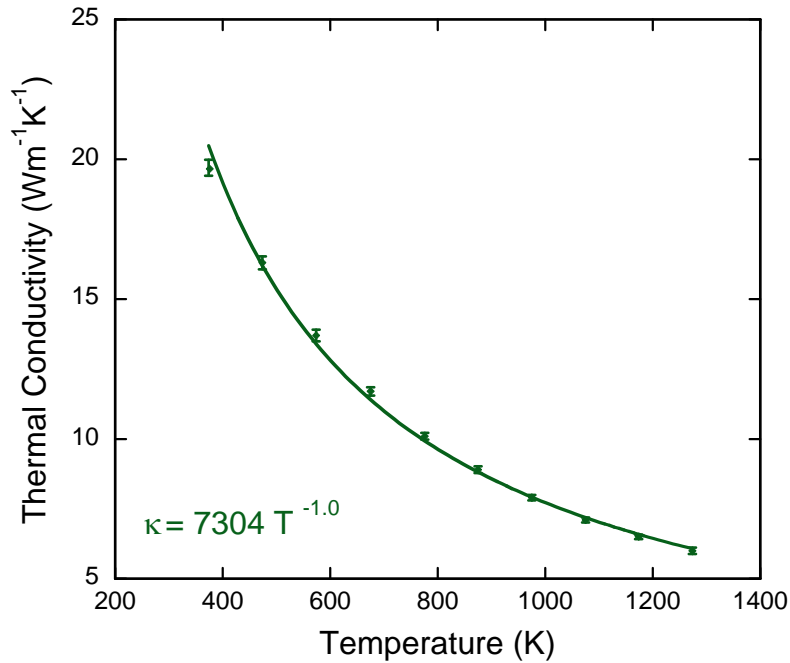
frequency of heterogeneities than the Spex blended or ball milled composites. Yet, it can be observed in Figure 6.2 that the thermal conductivity of the ball milled, mortar and pestle, and magnetic bar stirred composites have essentially the same average thermal conductivity.



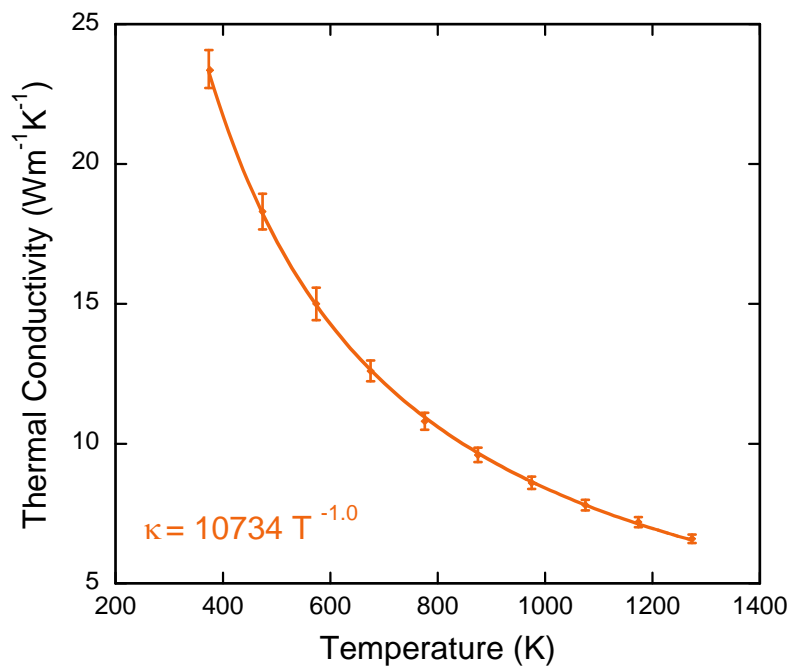
(a)



(b)



(c)



(d)

Figure 6-1: Corrected thermal conductivity and corresponding error of the composites processed by the four processing methods. A) mortar and pestle B) magnetic bar stirring C) Spex blending D) ball milling

The macrostructure of the Spex blended and ball milled composites was found to be virtually identical in Chapter 4, but the thermal conductivity of the Spex blended composites is

lower than that of the ball milled composites by $\sim 3 \text{ Wm}^{-1}\text{K}^{-1}$ at 373 K. Therefore, since composites with and without large quantities and frequencies of heterogeneities have the same average thermal conductivity and composites with virtually identical macrostructures have a different average thermal conductivities, no relationship can be observed between the heterogeneities and the overall thermal conductivity of the composites.

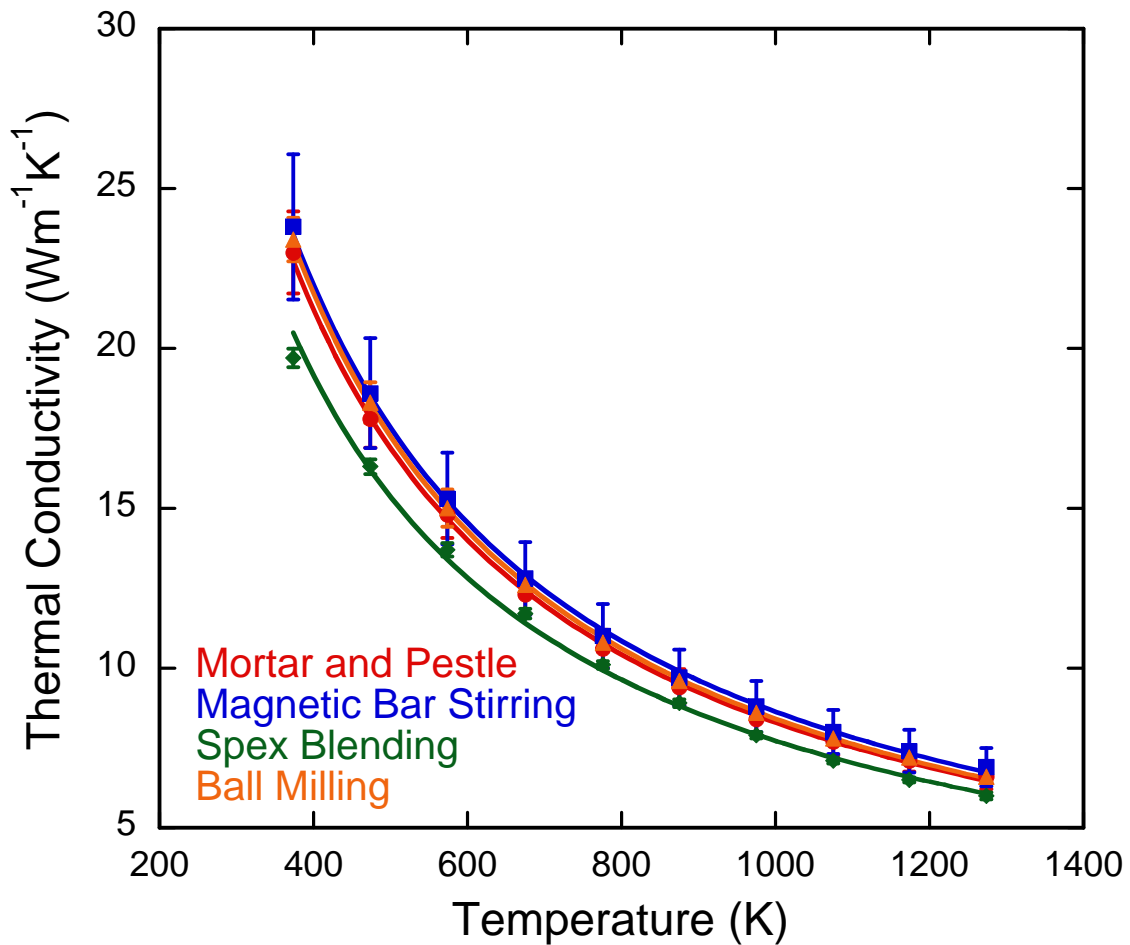


Figure 6-2: Comparison of the thermal conductivity of the composites between the different processing methods.

Since the macrostructure does not appear to affect the thermal conductivity of the composites, the microstructure was analyzed next to determine if any microstructure—thermal conductivity relationships could be observed. The homogeneity of the microstructure was first

examined to determine if it affected the thermal conductivity of the composites. As discussed above, the average thermal conductivity of the ball milled, mortar and pestle, and magnetic bar stirred composites is essentially the same when the errors are included. However, the ball milled composites are far more homogeneous than either the mortar and pestle or magnetic bar stirred composites. The Spex blended composites are more homogeneous than the mortar and pestle and magnetic bar stirred composites, but the thermal conductivity of the Spex blended composites is the lowest of the four processing methods. Therefore, based on these inconsistencies no relationship could be observed between the homogeneity of the microstructure and the thermal conductivity of the composites.

The lack of a homogeneity—thermal conductivity relationship is not unexpected. The homogeneity characterizes the consistency in how the MgO and Nd₂Zr₂O₇ is dispersed within the composite. Homogeneity does not influence the connectivity of the thermally conductive MgO. A more homogeneous distribution of MgO and Nd₂Zr₂O₇ would not increase the average thermal conductivity of the composites because the homogeneity does not correlate to an increase in thermal transport.

The next feature of the microstructure that was analyzed to determine if it affected the thermal conductivity of the composites was the grain size of the MgO and Nd₂Zr₂O₇. The grain size of the Nd₂Zr₂O₇ in the composites is between 1.0 μm and 1.2 μm for all four processing methods, therefore, it can be assumed that it has no effect on the thermal conductivity of the composites. The average grain size of the MgO in the magnetic bar stirred is 2.5 μm and the average grain size of the MgO in the Spex blended composites is 2.4 μm, but the thermal conductivity of the Spex blended composites is lower than that of the magnetic bar stirred composites. The average thermal conductivity of the magnetic bar stirred and mortar and pestle composites is nearly the same, but the grain size of the MgO in the mortar and pestle composites is 3.7 μm and the grain size of the magnetic bar stirred composites is 2.5 μm. At

2.1 μm the ball milled composites have the smallest grain size of MgO, but they have the highest thermal conductivity of the four processing methods. Since a pattern could not be extracted, it can be concluded that the grain size of the microstructure probably has no effect on the thermal conductivity of the composites. The predicted thermal conductivity of MgO and $\text{Nd}_2\text{Zr}_2\text{O}_7$ is constant in grains larger than $\sim 1 \mu\text{m}$, therefore the grain size was not expected to affect the average thermal conductivity in these composites.⁸⁸

The final feature of the microstructure that was examined to determine if there was any effect on the thermal conductivity was the contiguity of the $\text{Nd}_2\text{Zr}_2\text{O}_7$ and MgO. The thermal conductivity of the ball milled composites is the highest, but the contiguity of the $\text{Nd}_2\text{Zr}_2\text{O}_7$ is the lowest of the four processing methods. The contiguity of the $\text{Nd}_2\text{Zr}_2\text{O}_7$ in the mortar and pestle and magnetic bar stirred composites is nearly twice the contiguity of the $\text{Nd}_2\text{Zr}_2\text{O}_7$ in the Spex blended and ball milled composites, but there is little difference between the thermal conductivity of the mortar and pestle, magnetic bar stirred, and ball milled composites. The contiguity of the $\text{Nd}_2\text{Zr}_2\text{O}_7$ in the Spex blended composites is higher than the ball milled composites and lower than the contiguity of the $\text{Nd}_2\text{Zr}_2\text{O}_7$ in the mortar and pestle and magnetic bar stirred composites, yet the thermal conductivity of the Spex blended composites was the lowest of the four processing methods. Based on these inconsistencies, a pattern cannot be discerned that associates the contiguity of the $\text{Nd}_2\text{Zr}_2\text{O}_7$ with the thermal conductivity of the composites. Since thermal transport in $\text{Nd}_2\text{Zr}_2\text{O}_7$ is inefficient, increasing or decreasing the contiguity of the $\text{Nd}_2\text{Zr}_2\text{O}_7$ is not likely to affect the thermal conductivity in the composites.

The contiguity of the MgO was analyzed next. The contiguity of the MgO in the mortar and pestle, magnetic bar stirred, and ball milled composites is very similar, averaging around ~ 0.45 . In addition, the thermal conductivity of the mortar and pestle, magnetic bar stirred, and ball milled composites is essentially the same. The contiguity of the MgO in the Spex blended composites decreased to 0.29, and there was also a decrease in the thermal conductivity of the

Spex blended composites compared to the thermal conductivity of the mortar and pestle, magnetic bar stirred, and ball milled composites. These results indicate that there could be a correlation between the contiguity of the MgO and the thermal conductivity of the composites.

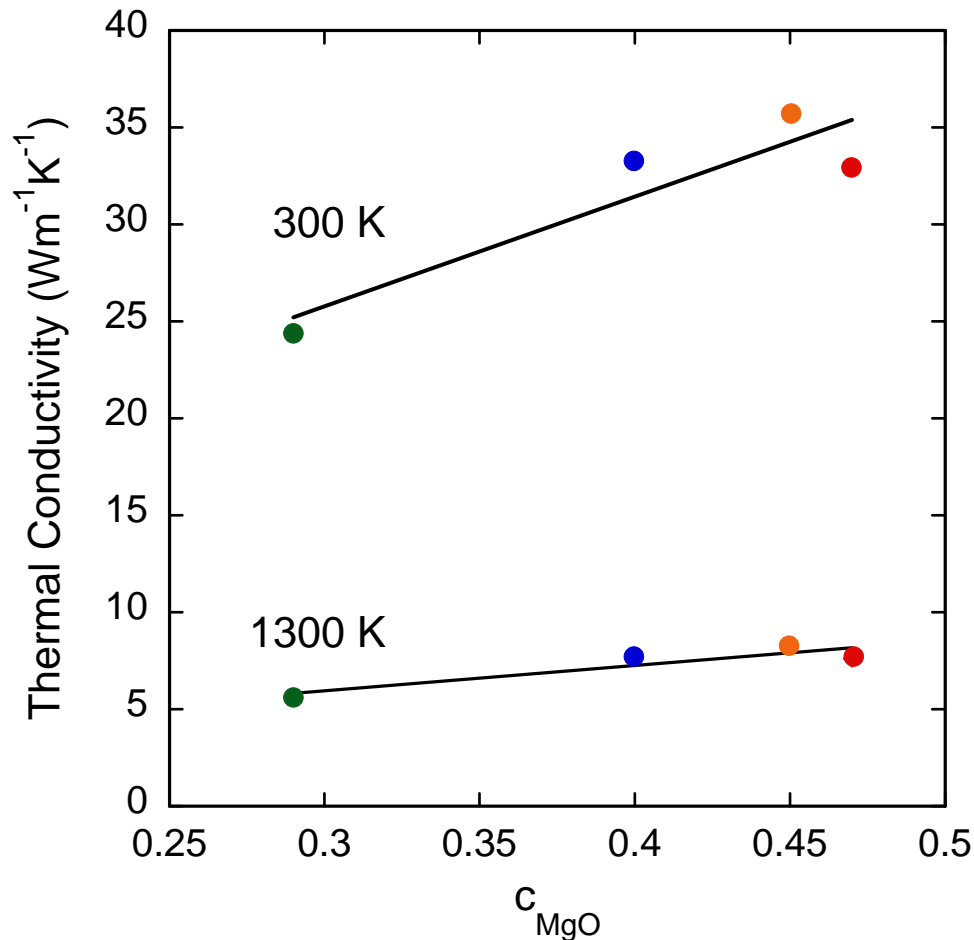


Figure 6-3: The contiguity—thermal conductivity relationship at 300 K and 1300 K.

The thermal conductivity of the composites was plotted as a function of the contiguity of MgO for each processing method at 300 K and 1300 K in Figure 6.2 to verify if a MgO contiguity—thermal conductivity relationship emerges. Figure 6.2 does indicate that there is a linear relationship between the contiguity of the MgO and the thermal conductivity of the composites at both 300 K and 1300 K. An increase in the contiguity of the MgO corresponds to an increase in the path for thermal conduction, and this results in an increase in the thermal conductivity. The steeper slope at 300 K suggests that the MgO contiguity has a greater effect

on the thermal conductivity at lower temperatures, and that the effect diminishes with increasing temperature.

Multiple researchers have correlated the conductivity of composites with the contiguity of the conducting phase. Jernot et al.⁸⁹ and Lee et al.⁹⁰ investigated the effect of the contiguity of the electrically conductive phase with the effective electrical conductivity of the composite. Tajika et al.⁹¹ and Jackson et al.⁹² correlated the contiguity of the thermally conductive phase with the thermal conductivity of the composite. In all of these cases, the conductivity of the composites increased as the contiguity of the conductive phase increased. However, all of these investigators measured the change in contiguity as a function of the increasing volume fraction of the conductive phase. Thus, the effect of the contiguity on the conductivity of the composites is muddled by the increasing the volume fraction of the conductive phase.

In this case, the volume fraction of thermally conductive MgO in the MgO—Nd₂Zr₂O₇ composites is held constant. In Chapter 4 it was observed that the processing method affected the contiguity of the MgO and Nd₂Zr₂O₇ in the composites. Since the composite composition was kept constant, the changes in contiguity were due to differences in how the processing method mixed the two phases. However, the other researchers showed that the contiguity increased as the volume fraction of the conductive phase increased. Therefore, this is the first time it has been shown that the processing method can affect the contiguity of a composite when the composite composition is held constant. Furthermore, this is the first time it has been shown that the thermal conductivity of a composite increases with increasing contiguity of the thermally conductive phase when the composite composition is held constant.

The thermal conductivity of the composites is compared with the thermal conductivity of the constituent phases and UO₂ in Figure 6.3. The thermal conductivity of the composites is closer to the thermal conductivity of the MgO than to the thermal conductivity of the Nd₂Zr₂O₇. The thermal conductivity of the composite is also much higher than the thermal conductivity of UO₂, satisfying the requirement that the candidate IM has a higher thermal conductivity than

UO₂. At temperatures greater than ~1000 K, the thermal conductivity of the composite is nearly the same as the thermal conductivity of MgO.

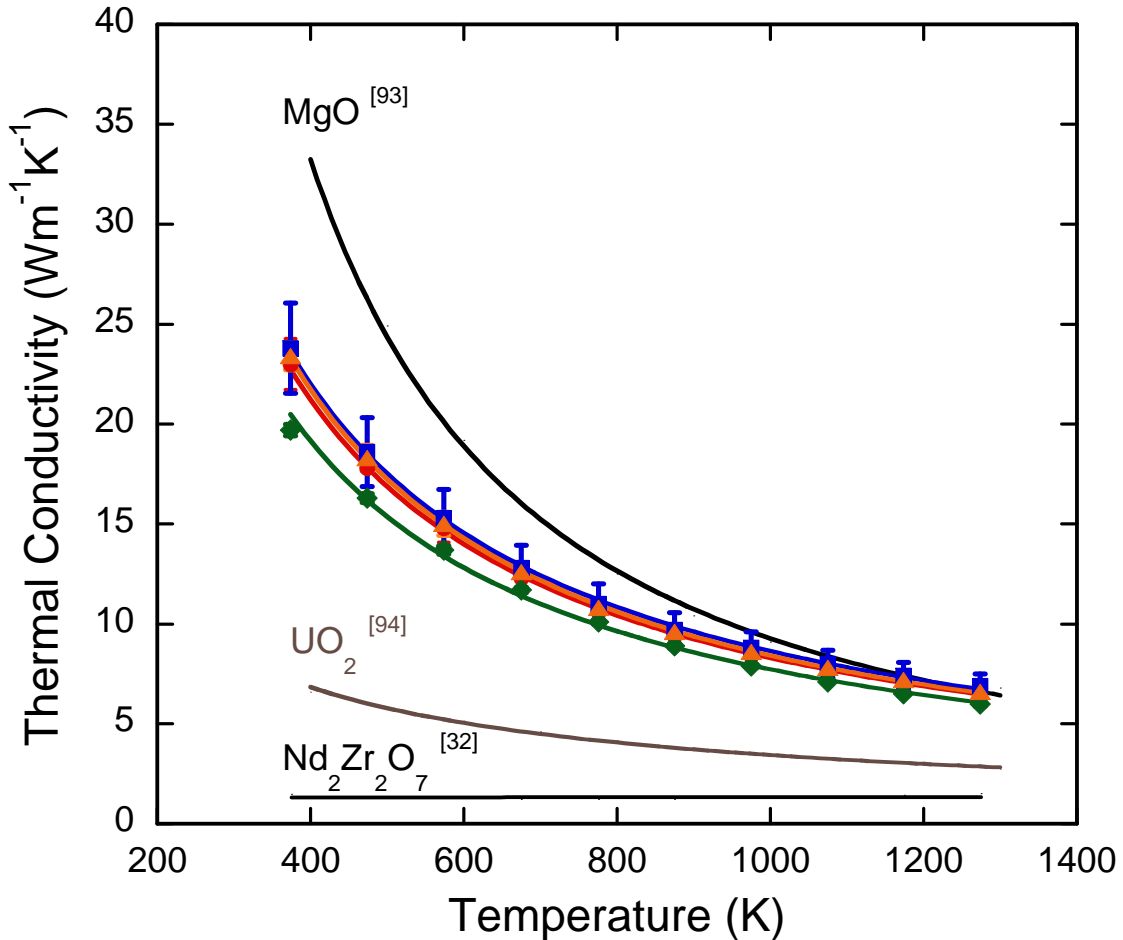


Figure 6-4: Thermal conductivity of the composites compared to the thermal conductivity of MgO⁹³, Nd₂Zr₂O₇³², and UO₂⁹⁴.

The effect of the contiguity on the thermal conductivity of the composite diminishes as the temperature increases. The thermal conductivity of all of the composites, regardless of the contiguity, is essentially the same after ~1000 K. This indicates that the thermal conductivity of the composites becomes independent of the MgO contiguity after 1000 K. Phonons transporting thermal energy propagate through the lattice in a direction defined by its wave vector \mathbf{k} , but at higher temperatures Umklapp scattering reduces the efficiency of the phonons

at transporting the thermal energy through the material. The other vibration modes that exist within the material do not possess well-defined wave vectors, so the thermal energy is spread diffusely through the material. When this occurs, the thermal conductivity of the material depends on the specific heat capacity and will become temperature independent.⁹⁵

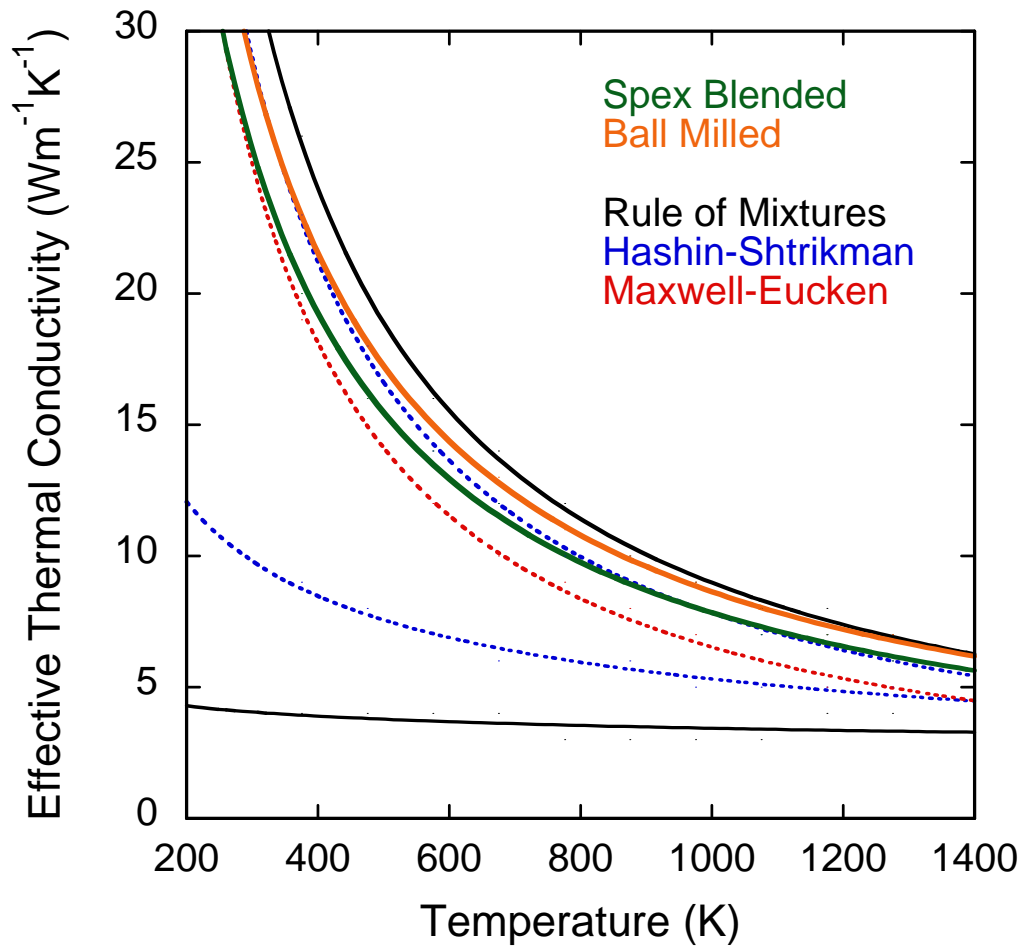


Figure 6-5: The thermal conductivity of the Spex blended and ball milled composites compared to the thermal conductivity of the composites calculated from the thermal conductivity of the constituents using Equations 2.5 through 2.9.

The thermal conductivity of the ball milled and Spex blended composites is compared to the effective thermal conductivity of the composite calculated by Equations 2.5 through 2.9 using the thermal conductivities of MgO and Nd₂Zr₂O₇ from Touloukian⁹³ and Lutique et al.³² in Figure 6.4. The thermal conductivity of the ball milled composites ranges between the upper

bound of the Hashin-Shtrikman relationship and the highest upper bound calculated using the rule of mixtures. The thermal conductivity of the Spex blended composites is slightly lower, ranging between the effective thermal conductivity given by the Maxwell-Euken relationship and the upper bound of the Hashin-Shtrikman relationship. The thermal conductivity of the composites is of the same magnitude as the highest predicted effective thermal conductivities. The ball milled composite probably closely follows the rule of mixtures because interactions between the MgO and $\text{Nd}_2\text{Zr}_2\text{O}_7$ are minimal and the thermal conductivity of each phase appears to act independently to contribute to the effective thermal conductivity of the composite.

6.4 Conclusions

The thermal conductivity of the composites was calculated from the thermal diffusivity measured in Chapter 5 and thermal conductivity curves were fit to the data. The thermal conductivity equations from the different processing methods were then compared to each other. The thermal conductivity of the mortar and pestle composites was slightly higher than the thermal conductivity of the magnetic bar stirred and ball milled composites, which had the same thermal conductivity. The thermal conductivity of the Spex blended composites was lower than the other three methods.

The average thermal conductivity was not found to be dependent on the macrostructure of the composites. Since the macrostructure did not affect the thermal conductivity, the features of the microstructure were analyzed to determine if the overall thermal conductivity of the composites was controlled by the microstructure of the composites. The homogeneity and grain size of the microstructure was found not to affect the thermal conductivity of the composites. However, when the contiguity of the $\text{Nd}_2\text{Zr}_2\text{O}_7$ and MgO was analyzed a pattern emerged to suggest that the thermal conductivity of the composites was related to the contiguity of the MgO. When the thermal conductivity of the composites was plotted as a function of the contiguity of the MgO a linear relationship was established. Therefore, the thermal conductivity of the

composites is controlled by the contiguity of the thermally conductive MgO until ~ 1000 K, after which the average thermal conductivity becomes independent of the contiguity of the MgO.

CHAPTER 7 BALL MILLING BATCH-TO-BATCH VARIATION ANALYSIS

7.1 Introduction

This chapter begins by selecting the best processing method from the four different methods that have been investigated based on the best combination of macrostructure, microstructure, and thermal conductivity compared to that of the other composites. The processing and characterization of two additional batches of composites using the selected method is then presented and it is followed by a batch-to-batch comparison and analysis. A discussion then follows on the robustness of the process to produce composites with consistent macrostructures and microstructures that result in predictable and consistent thermal properties.

7.2 Process Selection

The macrostructure and microstructure of the composites was characterized in Chapter 4 and the thermal diffusivity of the composites was measured in Chapter 5. The characterization and thermal diffusivity of the composites was compared among the different processing methods to determine which method synthesized the most ideal IM candidate composite. When the best processing method is selected, two more batches will be synthesized using the processing method to analyze the batch-to-batch variation in the candidate composites.

The selection began with comparing the macrostructures of the composites. As shown in Chapter 4, the mortar and pestle and magnetic bar stirred composites contained a population of both MgO and Nd₂Zr₂O₇ heterogeneities that was much larger than the quantity and frequency of heterogeneities present in the Spex blended and ball milled composites. The Spex blended and ball milled mixed composite powders did not contain agglomerates which were the source of the heterogeneities in the mortar and pestle and magnetic bar stirred composites. The lack of hard agglomerates in the Spex blended and ball milled composite powders resulted in composites that did not contain the circumferential cracks which caused sample-to-sample

variations in the thermal diffusivity of the composites. Therefore, mortar and pestle and magnetic bar stirred were eliminated from the four processing methods as possible candidate IMF composite processing methods. Further analysis then focused on comparing the Spex blending or ball milling processes to determine which process produced the best composites.

The microstructure of the Spex blended and ball milled composites was compared next to determine which of the two methods produced better microstructures. As shown in Section 4.4.2.1, the microstructure of the ball milled composites was more homogeneous than the Spex blended composites. Section 4.4.2.2 showed that the grain size of the MgO and $\text{Nd}_2\text{Zr}_2\text{O}_7$ in the Spex blended and ball milled composites was nearly the same. The contiguity of the $\text{Nd}_2\text{Zr}_2\text{O}_7$ was 0.10 higher in the Spex blended composites, but the contiguity of the MgO in the ball milled composites was 0.45 and the contiguity of the MgO in the Spex blended composites was 0.29.

Since it was not clear which composite process was best based solely on the characterization of the microstructures, the microstructure—thermal conductivity relationships analyzed in Chapter 6 had to be considered before selecting the best composite processing method. The homogeneity of the microstructure did not affect the thermal conductivity of the composites. The grain size of the constituents also was not found to have an effect on the thermal conductivity of the composites in the temperature range at which the thermal diffusivity was measured. The contiguity of the $\text{Nd}_2\text{Zr}_2\text{O}_7$ was not found to affect the thermal conductivity of the composites, so the difference between the contiguities of the $\text{Nd}_2\text{Zr}_2\text{O}_7$ in the Spex blended and ball milled composites was ignored. However, a direct correlation between the contiguity of the MgO and the thermal conductivity of the composites was established. The increase in the MgO contiguity in the ball milled composites resulted in an increase in the thermal conductivity of the ball milled composites compared to that of the Spex blended composites. Therefore, ball milling was selected as the best composite processing method since it had a higher thermal conductivity compared to the Spex blended composites.

7.3 Batch Processing

The robustness of ball milling process was tested by investigating the batch-to-batch variation in the composites. The ball milling batches were differentiated as ball milling Batch A, Batch B, and Batch C. The synthesis and characterization of the Batch A composites was discussed in the preceding chapters. Batch B and Batch C of ball milled composite powder were synthesized according to the experimental procedure described in Section 3.5.2.4 using the same ball milling apparatus as Batch A. Pellets were fabricated from Batch B and Batch C of the composite powder for macrostructure and microstructure characterization as well as for thermal diffusivity measurements.

Optical microscopy was performed on one pellet from each batch, and the optical composite images of the pellets are shown below in Figure 7.1. There is not a clear difference in the macrostructure between the composites in Figure 7.1A-C, indicating that ball milling does produce a consistent macrostructure between batches. In all three batches, MgO and Nd₂Zr₂O₇ heterogeneities are visible within the composites. The few heterogeneities that are present are small and appear to be fairly well distributed throughout the microstructure.

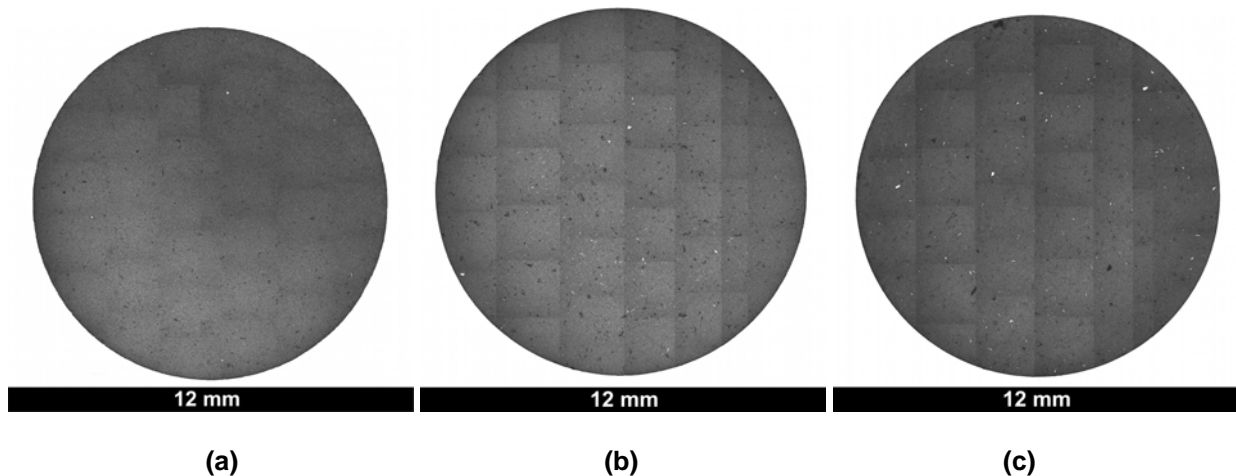


Figure 7-1: Composite optical images of pellets processed from the three batches of ball milled composite powder. A) Batch A B) Batch B C) Batch C

7.4 Composite Characterization

In this section, the results of the macrostructure and microstructure characterization for the composites synthesized from Batch A, Batch B, and Batch C will be presented.

7.4.1 Macrostructure Characterization

The ball milled composite macrostructures were characterized to more accurately compare the quantity and frequency of heterogeneities between the batches. The macrostructure of the composites was analyzed according to the procedure described in Section 4.3.1. Since the heterogeneities are homogeneously distributed throughout the pellet, random optical images of the composite are treated as representative of the macrostructure. Examples of the random optical images used to characterize the macrostructure of the ball milled composites are shown in Figure 7.2.

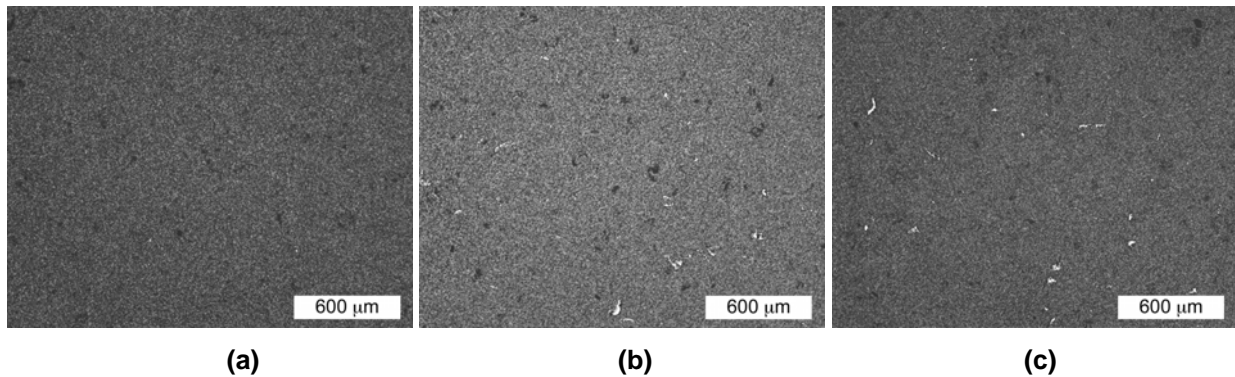


Figure 7-2: Optical images of the composites from the three batches of ball milled composite powder. A) Batch A B) Batch B C) Batch C.

The results of the macrostructure analysis are shown below in Table 7.1. The quantity and frequency of both MgO and Nd₂Zr₂O₇ heterogeneities is identical for Batch A and Batch B. The volume fraction of the MgO in Batch C is the same as the volume fraction of MgO in Batches A and B, but the frequency of the MgO heterogeneities is slightly lower in Batch C than in Batches A and B. The volume fraction and frequency of Nd₂Zr₂O₇ heterogeneities increased in Batch C. These increases resulted in doubling the total volume fraction and a slightly increasing the total frequency of the heterogeneities present in the Batch C composites. Even

though the total volume fraction of the heterogeneities doubled in Batch C compared to Batch A and B, the total volume fraction of heterogeneities in the Batch C composites is still less than 1%. These results show that there is relatively little variation in the quantity and frequency of the heterogeneities between the different ball milling batches, and the macrostructure of the composites synthesized from the three batches of composite powder is consistent.

Table 7-1: Quantitative stereology results for the heterogeneities in the ball milled composites.

Ball Milling Batch	MgO		Nd ₂ Zr ₂ O ₇		Total	
	Volume Fraction (%)	N _L (m ⁻¹)	Volume Fraction (%)	N _L (m ⁻¹)	Volume Fraction (%)	N _L (m ⁻¹)
A	0.40	60	0.04	21	0.44	81
B	0.40	60	0.04	21	0.44	81
C	0.40	50	0.40	41	0.80	91

7.4.2 Microstructure Characterization

The microstructure of the composites was analyzed to determine if the contiguity of the MgO differed between the different ball milling batches. Only the contiguity of the microstructures was measured because it was determined in Chapter 6 that the homogeneity and grain size of the microstructure did not affect the thermal conductivity of the composites. An SEM image of one pellet from each batch is shown below in Figure 7.3. Comparing the images, there is no distinguishable difference that can be observed between the batches. The microstructures of the composites from Batch A, B, and C appear to be on the same scale and have identical distributions of the MgO and Nd₂Zr₂O₇.

The results of the microstructure analysis for the contiguity of the constituent phases is shown below in Table 7.2. The contiguity of the Nd₂Zr₂O₇ varies more than the contiguity of the MgO between the batches. The contiguity values for the Nd₂Zr₂O₇ are similar in Batches A and C, but does increase slightly in Batch B. The contiguity of the MgO in Batches A and C is the same, and the contiguity of the MgO in Batch B is slightly higher.

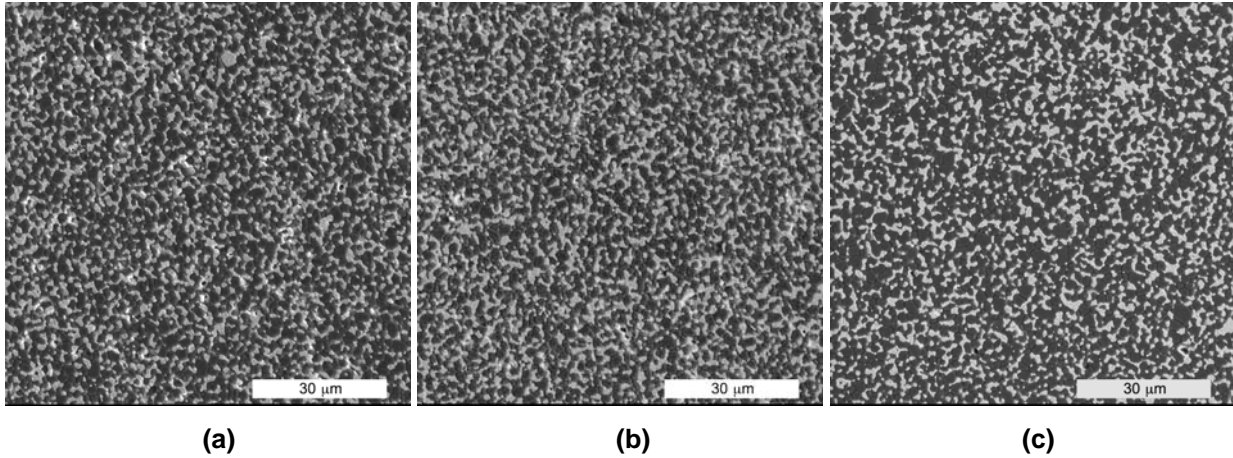


Figure 7-3: SEM images of the composites from the three batches of ball milled composite powder. A) Batch A B) Batch B C) Batch C.

Although the differences in the contiguity of the composites is slight, further analysis was performed to estimate the range of error in the contiguity measurement to allow for a better comparison between the batches. In order to estimate the error, the contiguity of the same Batch A sample was measured twice using different sets of SEM images. When the second contiguity measurement was performed, the contiguity of the MgO increased from 0.43 to 0.45 and the contiguity of the $\text{Nd}_2\text{Zr}_2\text{O}_7$ increased from 0.25 to 0.28. This result indicates that there is approximately a ± 0.02 error in the contiguity when the same person measures the contiguity. When the contiguity is measured by a different individual, the error in the measurement increases to ± 0.04 . Based on these errors, it can be concluded that the contiguity of the MgO in all of the batches is identical, and the contiguity of the $\text{Nd}_2\text{Zr}_2\text{O}_7$ slightly increased only in Batch B.

Table 7-2: Contiguity results for the microstructure in the ball milled composites.

Constituent	Contiguity		
	Batch A	Batch B	Batch C
MgO	0.43	0.45	0.43
$\text{Nd}_2\text{Zr}_2\text{O}_7$	0.25	0.29	0.23

7.5 Composite Thermal Diffusivity and Thermal Conductivity

This section will discuss the results of the thermal diffusivity measurements and the thermal conductivity calculation. A discussion on the effect of the composite macrostructure on the thermal diffusivity and the effect of the composite microstructures on the thermal conductivity of the composites will follow.

7.5.1 Thermal Diffusivity

The thermal diffusivity was measured on three pellets from each batch of ball milled powder. The measurements for the nine pellets from Batches A, B, and C are compiled in Figure 7.4 and bounded by a 95% confidence interval. At ~6% of the thermal diffusivity, the confidence interval for all three batches of ball milled composites is no wider than the confidence interval for Batch A of the ball milled composites. This indicates that there is no difference in the sample-to-sample variation in the thermal diffusivity between Batches A, B, and C. Furthermore, these results also indicate that there is no batch-to-batch variation in the thermal diffusivity of the composites.

It is important to remember that the ball milling process was selected from the four candidate processing methods because minimal sample-to-sample variation was expected. Chapter 3 and Chapter 4 proved ball milling does not produce composites that possess circumferential cracks arising from the differential sintering of hard agglomerates. Provided the processing was consistent from batch-to-batch, a similar result was expected in Batch B and Batch C of the ball milled composites. Indeed, the characterization of the Batch B and Batch C composites in Section 7.4.1 indicated that the composite macrostructures from the different ball milling batches were consistent. The composites in all three batches lacked both the large volume fraction and high frequency of heterogeneities and the circumferential cracks associated with the sample-to-sample variation in the thermal diffusivity. Therefore, the thermal diffusivity of the composites confirmed that ball milling can synthesize composites with consistent thermal diffusivities.

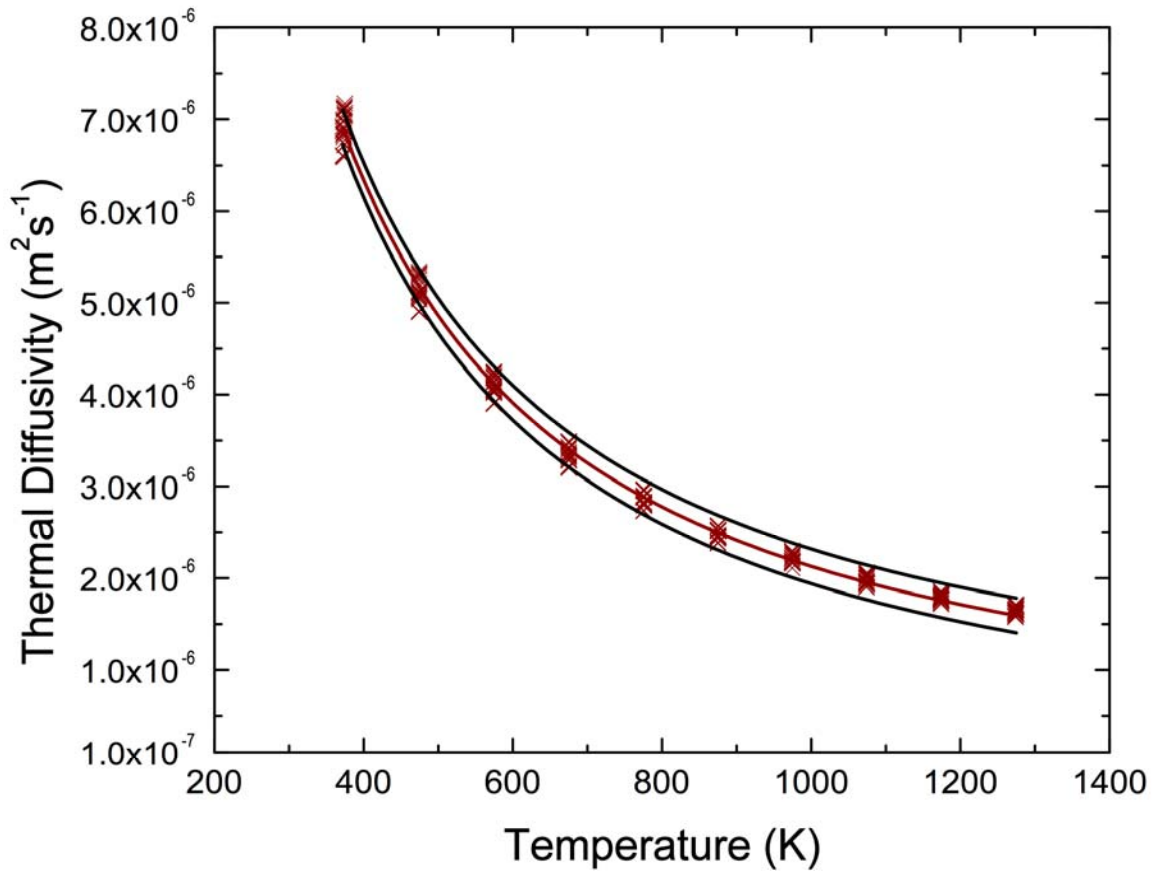


Figure 7-4: Compiled thermal diffusivity measurements of the ball milled composites from Batches A, B, and C plotted with the average thermal diffusivity and corresponding confidence interval.

7.5.2 Thermal Conductivity

The thermal conductivity of each batch of ball milled composites was calculated from the thermal diffusivity measurements in Section 7.5.1 using the procedure described in Section 6.2. The thermal conductivity and its corresponding standard deviation of Batches A, B, and C are compiled below in Figure 7.5. The average thermal conductivity values are listed in Table B.4. The average thermal conductivity of the composites in the three batches of ball milled composites are very similar to each other. As shown in Chapter 6, the error in the thermal diffusivity is ~6% of the thermal conductivity at 373 K in the Batch A composites. The error in the Batch B composites is ~3% and the error in the Batch C composites is ~4% of the average

thermal conductivity. This indicates that there is a batch-to-batch variation in the sample-to-sample variation in the composites.

If the overlapping of the thermal conductivity errors are included in the analysis, the thermal conductivity of the composites between the batches is essentially the same. Section 6.3 discussed how the thermal conductivity of the composites is related to the contiguity of the MgO in the interpenetrating matrix. In Section 7.4.2 it was shown that the contiguity of the MgO in Batches A, B, and C of the ball milled composites was the same. Therefore, the average thermal conductivity of the ball milled batches was expected to be very close to one another. The miniscule differences in the thermal conductivity between the batches will be absorbed into the sample-to-sample error of ball milled composites when the average thermal conductivity is calculated for the process from the thermal diffusivity measurements of the Batch A, B, and C composites.

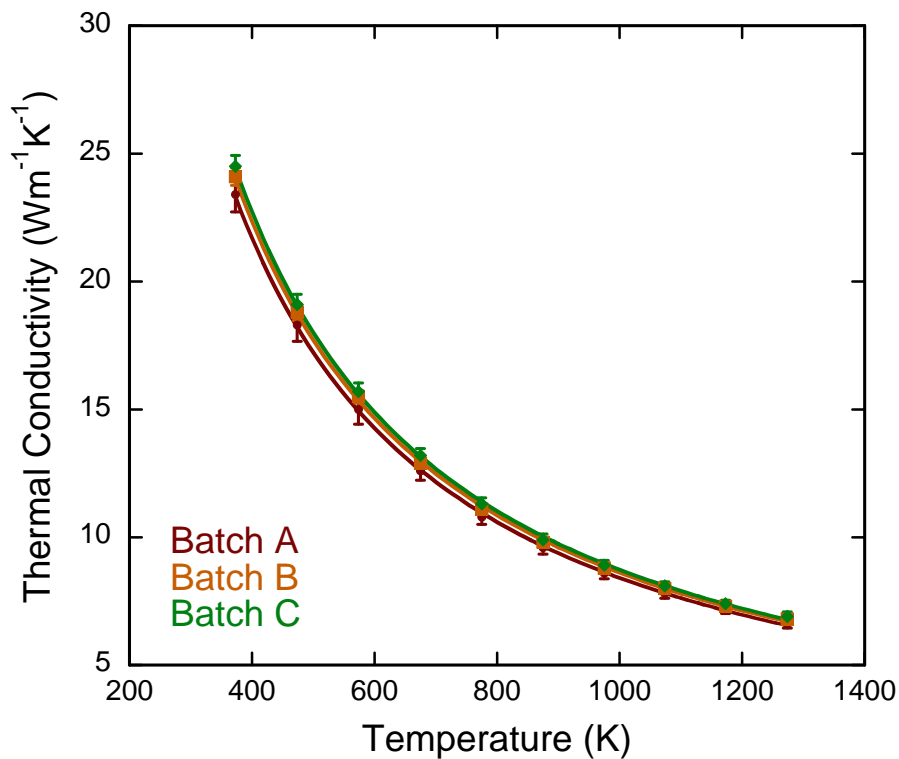


Figure 7-5: Thermal conductivity compilation for the three ball milling batches.

The thermal diffusivity measurements from all three batches were compiled and averaged. The thermal conductivity was calculated and the resulting thermal conductivity curve is shown below in Figure 7.6 with its corresponding error. The thermal conductivity of the ball milled composites is in the same range of the thermal conductivity values Medvedev et. al.²⁵ reported on ZrO₂—MgO composites. The error at 373 K in the compiled thermal conductivity of the composites is ~5%, lower than the ~6% error in the Batch A composites and slightly higher than the ~3% and ~4% error in the Batch B and Batch C composites, respectively. The error in the thermal conductivity produces a variation of 0.6 Wm⁻¹K⁻¹ at 373 K, and this error reduces to 0.2 Wm⁻¹K⁻¹ at 1273 K. Considering the average thermal conductivity and error in Figure 7.6 was computed from the measurements on 9 pellets from 3 different batches of composite powder, ball milling has been shown to produce a consistent and replicable thermal conductivity both within the same batch of composites and between different batches of composites.

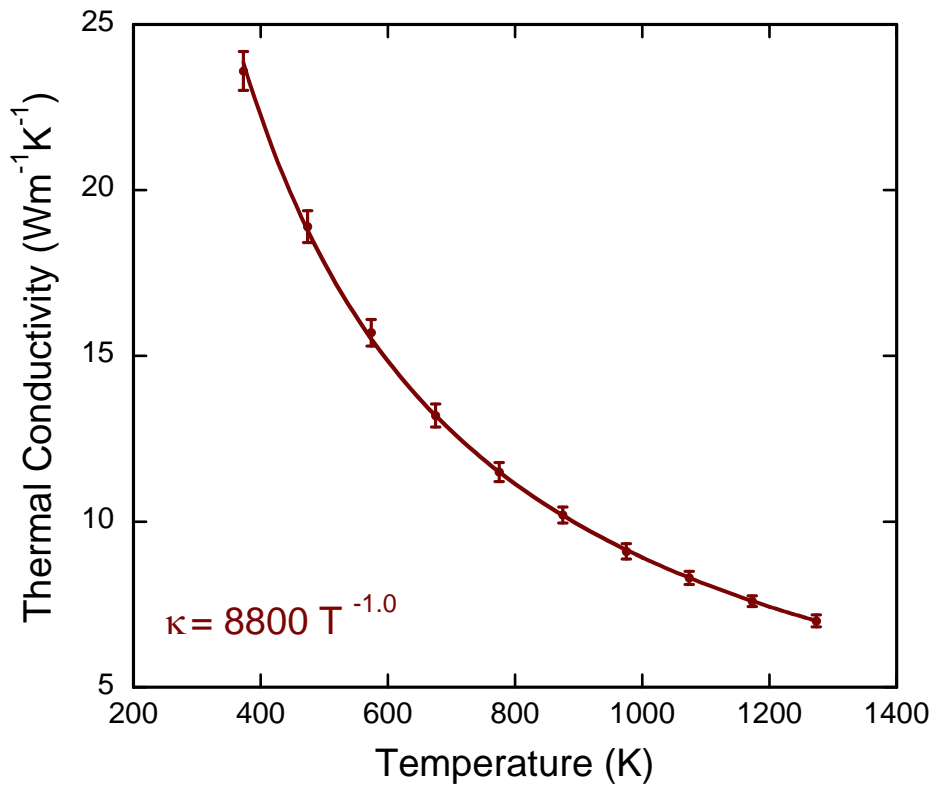


Figure 7-6: The thermal conductivity and corresponding error of ball milled composites.

7.6 Conclusions

Ball milling was selected as the best of the four different processing methods used to synthesize the 70 vol% MgO—30 vol% $\text{Nd}_2\text{Zr}_2\text{O}_7$ composites because the test batch had the best combination of microstructure, microstructure, and thermal conductivity. Two additional batches of composites were synthesized using the same procedure as the test batch, and the resulting composites were compared to the composites in the first batch. The characterization of the macrostructure showed that the three batches of composites had similar quantities and frequencies of heterogeneities. Characterization of the microstructure proved that the contiguity of the MgO between the batches was essentially the same. The thermal diffusivity was measured on three pellets per batch, and the width of resulting confidence interval for all of the pellets was ~6% of the thermal diffusivity. The thermal conductivity was calculated from the thermal diffusivity measurements for each batch, and the resulting thermal conductivities were very close to each other. The sample-to-sample variation did differ between the batches, however. The average thermal conductivity for the ball milling process was calculated using the thermal diffusivity measurements for all of the pellets from all of the batches. The resulting thermal conductivity has an error of ~5% at 373 K. Therefore, it was concluded that ball milling can produce composites with a predictable and consistent thermal conductivity.

CHAPTER 8 SUMMARY AND FUTURE WORK

8.1 Summary

Excess plutonium from dismantled nuclear weapons and spent nuclear fuel is a threat to national and international security. Current strategies to reduce the stockpile include fabricating inert matrix fuels and targets to burn the plutonium and other minor actinides in nuclear reactors or accelerator driven systems. The potential inert matrices must possess a variety of properties that include high temperature stability, high thermal conductivity, good irradiation behavior, and reactor coolant compatibility. Oxides have attracted a lot of attention as potential IM candidates, however, the effect of composite processing on the microstructure of the composites has not been well addressed and has led to an imperfect understanding of the processing—microstructure—thermal conductivity interrelationships of candidate IMF.

MgO is a promising IM candidate due to its high melting point, good irradiation behavior, and high thermal conductivity, but its hot water corrosion resistance is poor limiting its use in light water reactors. MgO—pyrochlore composites are proposed as a potential IM. The MgO will provide a thermally conductive path and the pyrochlore will act as a hydration barrier. The specific zirconate pyrochlore composition $\text{Nd}_2\text{Zr}_2\text{O}_7$ was chosen based on the neutronics, predicted radiation tolerance, and the simulated thermal conductivity. A single composition of the composite was selected using neutronics and used throughout this investigation. In this work, the 70 vol% MgO—30 vol% $\text{Nd}_2\text{Zr}_2\text{O}_7$ composites were synthesized using multiple processing methods, the composite microstructures were characterized, and the thermal diffusivity was measured. The processing—microstructure—property interrelationships were then analyzed.

Processing of IM composites is inconsistent among different researchers, resulting in a variety of microstructures. The processing—microstructure—property relationships were also not developed. To begin to remedy the lack of information on these relationships in IM

composites, the MgO—pyrochlore composites were synthesized using different processing methods. Two methods, mortar and pestle and magnetic bar stirring, relied on the mixing of the constituent powders. The other two methods, Spex blending and ball milling relied on the presence of milling media to blend or mill the constituents together. The characterization of the mixed composite powders showed that the processing methods that relied on mixing the constituents produced agglomerated powders, while the methods that involved blending or milling of the constituents using media did not produce agglomerated composite powder. There was also a larger fraction of hard agglomerates in the magnetic bar stirring composite powder than in the mortar and pestle composite powder.

Detailed characterization of the microstructures in potential IM composites is also lacking in the literature, therefore the synthesized composites were analyzed using quantitative stereology techniques. The macrostructures of the composites synthesized from the agglomerated powders were populated by both MgO and $\text{Nd}_2\text{Zr}_2\text{O}_7$ heterogeneities, however the composites fabricated from powders that were not agglomerated had comparatively fewer heterogeneities. Thus, synthesizing composites from agglomerated powders was shown to produce heterogeneities of the constituent phases within the macrostructure of the composites.

The thermal diffusivity of the composites was measured to establish a processing—macrostructure—thermal diffusivity relationship. Three samples from each composite processing method were measured. When the data was analyzed, the composite processing methods that mixed the constituents had more sample-to-sample variation in the thermal diffusivity than the composite processing methods that blended or milled the constituents. Since the composite processing methods that mixed the constituents led to the formation of agglomerated powders and the agglomerates were the source of the heterogeneities in the composite macrostructure, the sample-to-sample variation in the thermal diffusivity can be correlated with the presence of heterogeneities in the composite macrostructure.

The sample-to-sample variation in the thermal diffusivity of the composites will affect the performance of the IMF. Considering the composition of the MgO—Nd₂Zr₂O₇ composite is constant, the variation in the thermal diffusivity will translate to a variation in the thermal conductivity of the composites. Therefore, the thermal conductivity of the composites synthesized from processing methods that mix, rather than blend or mill the constituent phases, can be predicted less reliably. If the thermal conductivity can be predicted less reliably, it becomes more difficult to license the IMF for use in a nuclear reactor.

A second processing—microstructure—thermal conductivity relationship was extracted from the work in this investigation. The processing method not only affected the formation of agglomerates that were the source of the heterogeneities, but it also affected the distribution of the MgO and Nd₂Zr₂O₇ in the interpenetrating matrix that surrounded the heterogeneities. The microstructure of the composites was characterized using quantitative stereology techniques. The first feature that was characterized was the homogeneity of the constituent phases in the matrix. The homogeneity of the matrix was better in the composites fabricated from composite powders synthesized by methods that blended or milled the constituents, rather than mixing them. The average grain size of the MgO and Nd₂Zr₂O₇ in the matrix did not differ significantly among the processing methods, however. The contiguity was used to characterize the amount of connectivity of each phase in the matrix. The contiguity of the MgO in the mortar and pestle, magnetic bar stirred, and ball milled composites was essentially the same at ~0.45, but the contiguity of the Spex blended composites was significantly lower at 0.29 than the other methods. Therefore, the contiguity of the MgO in the matrix does not depend on if the processing method mixed, blended, or milled the constituents together.

Development of the microstructure—thermal conductivity relationship begins with calculating the thermal conductivity of the composites from specific heat capacity and thermal diffusivity measurements. The change in density as a function of temperature was calculated from the coefficients of thermal expansion determined from the thermal expansion

measurements on the composites. The average thermal conductivity of the mortar and pestle, magnetic bar stirred, and ball milled composites are within $\sim 1 \text{ W}^{-1}\text{K}^{-1}$ of each other at 373 K, but the thermal conductivity of the Spex blended composites is $\sim 3 \text{ Wm}^{-1}\text{K}^{-1}$ lower than the other three methods at 373 K. The thermal conductivity of the composites is between $\sim 6\text{-}7 \text{ Wm}^{-1}\text{K}^{-1}$ at 1273 K, which is within the range of values that Medvedev et. al.²⁵, Ronchi et. al.³⁹, and Lutique et. al.³² observed on MgO composites.

When the thermal conductivity of the composites is plotted as a function of the contiguity of the MgO in the composites, a linear relationship emerges between the thermal conductivity and the contiguity of the composites. Therefore, it is likely that the thermal conductivity of the composites is controlled by the contiguity of the MgO. However, at $\sim 1000 \text{ K}$ there is no longer any discernable difference between the thermal conductivity of the composites and the thermal conductivity of the pure MgO. Thus, the thermal conductivity of the composites appears to become independent of microstructure above 1000 K.

The macrostructures, microstructures, thermal diffusivity, and thermal conductivity of the composites was compared to determine which of the four processes produced the best IM composite. The ball milled and Spex blended composites had consistent macrostructures that resulted in a small sample-to-sample variations in the thermal diffusivity, unlike the mortar and pestle and magnetic bar stirred composites which had large sample-to-sample variations in the thermal diffusivity. However, the contiguity of the MgO in the ball milled composites was higher than the contiguity of the MgO in the Spex blended composites. The increase in the contiguity of the MgO in the ball milled composites produced composites that possessed a higher thermal conductivity. Although the thermal conductivity is independent of microstructure above 1000 K, it will be easier to scale up a ball milling process to accommodate larger batches of materials and it is more likely to be more tolerant of potential variations in the particle size of the feedstocks than Spex blending. Therefore, ball milling was selected to analyze the batch-to-

batch variation to assess the ability of the process to produce consistent microstructures and a predictable thermal conductivity.

Two more batches of ball milled composite powder was synthesized using the same experimental procedure as the first batch of ball milled composite powder. Pellets were then fabricated from the composite powder, the composites were characterized, the thermal diffusivity was measured, and the thermal conductivity was calculated. Characterization of the macrostructure showed that there was minimal variation in the quantity and frequency of heterogeneities between the batches of the ball milled composites. The characterization of the microstructure also confirmed that the contiguity of the MgO was essentially the same between the batches. The sample-to-sample variation in the thermal diffusivity of the composites from all of the samples in the three different batches was less than the sample-to-sample variation in the thermal diffusivity of only the first batch of ball milled composites, indicating that the consistent microstructures between batches translated into a consistent thermal diffusivity for the ball milled composites. The thermal conductivity of the composites was virtually the same between the batches of ball milled composites, verifying the existence of the contiguity—thermal conductivity relationship, in this case as well. Therefore, ball milling showed in this limited laboratory test consisting of three batches of composites that it can synthesize composites with a consistent and predictable thermal conductivity.

Ball milled composites were isothermally held for 1, 4, 8, 24, and 100 hours at 1550°C to measure the grain growth and analyze the grain growth kinetics. Grain size measurements of the composite microstructures shows that the ball milled composites display normal grain growth. The grain growth of the MgO and $\text{Nd}_2\text{Zr}_2\text{O}_7$ is coupled, and controlled by the growth of the slowest growing phase. The grain growth kinetics were analyzed and it was determined that the ball milled composites grow by grain boundary diffusion. SEM images of the composite supplemented the grain growth kinetics by showing that the grain growth was controlled by the diffusion of the $\text{Nd}_2\text{Zr}_2\text{O}_7$ through the MgO—MgO grain boundaries.

8.2 Future Work

8.2.1 Controlling the Agglomerates

Processing composites from reprocessed fuel is complicated by the possibility of unpredictable, inconsistent, and undesirable particle size distributions of the feedstock. However, it is necessary to design a process that can synthesize composites with consistent microstructures from this variable feedstock. In order to design a robust process, the range of acceptable particle sizes that can be accommodated in the composites must be determined. This range of acceptable particle sizes is process specific. The size and distribution of particles that can be incorporated into the composites will vary depending on the processing method, with milling processes being more tolerant than other processes that do not have the ability to reduce the size of large particles.

To determine the range of particle sizes that ball milling can accommodate and still produce consistent microstructures, the effectiveness of the process at ball milling different particle size distributions needs to be assessed. Particle size distributions collected before and after the composite powder synthesis would measure the efficiency of ball milling at accommodating irregular feedstock. The result will be a range of particle sizes that can be ball milled into a particle size distribution that will produce consistent microstructures when synthesized into composites.

Modifying the feedstock of the MgO may also provide an avenue to increase the robustness of composite processing without having to use a milling-based method. Bi-modal and multi-modal particle size distributions of MgO can mitigate the effect of unpredictable and undesirable particle sizes of the recycled fuel by improving the particle packing within the green ceramic.⁹⁶ The bi-modal and multi-modal distributions of MgO must be synthesized and tested in both mixing and milling processes. Composite characterization will demonstrate if the bi-modal and multi-modal distributions of MgO produced more consistent microstructures than the relatively monodisperse distribution of MgO that was used in this work. Thermal diffusivity

measurements can assess if better particle packing in the green ceramic translates into less sample-to-sample variation.

8.2.2 Sintering Kinetics

The sintering kinetics of the ball milled composites should be investigated to complete the discussion on the sintering and grain growth of the MgO—Nd₂Zr₂O₇ composites. The sintering kinetics of the ball milled composites can be investigated using the dilatometer. The composites will be sintered in the dilatometer using different constant heating rates. The densification of the composites at the different shrinkage rates will be compared and the sintering kinetics of the ball milled composites can be extracted. Furthermore, a master sintering curve can be constructed from the data. A master sintering curve will dictate the sintering schedule of the composite based on the density that is desired.

Agglomerates present in the composite powder will affect the densification of the composites. To complete the discussion on the effect of agglomerates on the composite densification, green ceramics pressed from agglomerated powders can be inserted into a dilatometer and sintered. The dilatometer will measure the densification of the composites as a function of constant heating rate. Constant heating rate and isothermal sintering schedules can both be tested to determine which type of schedule is more tolerant to the presence of agglomerates in the green ceramic. In addition, master sintering curves can be constructed from different particle size distributions of agglomerated feedstock. If these master sintering curves are compiled together a master sintering surface can be constructed that will compute a sintering schedule for a range of particle size distributions in the composite powder feedstock for a selected composite density. This will allow sintering schedules for mixed composite powders with unpredictable particle size distributions to be reliably chosen to sinter the composite powder to a predetermined density.

8.2.3 Circumferential Crack Characterization

In order to determine the size and distribution of agglomerates that the composite microstructure can accommodate without exceeding the tolerances for the sample-to-sample variation in the thermal diffusivity, further characterization of the circumferential cracks is needed on the composites. Equation 5.2 is for randomly oriented cracks with an extreme ellipsoidal shape. Slight variations of the equation can account for cracks of varying sizes and shapes of oblate ellipsoids. However, since the size and density of the circumferential cracks has not been quantitatively characterized in this work it is not possible to use Equation 5.2 to calculate the effective conductivity of the composites based on the actual size and density of the circumferential cracks present in the composites. The size and density of the circumferential cracks will be characterized to determine the relationship between the quantity and frequency of heterogeneities and the density of circumferential cracks.

**APPENDIX A
DETAILS OF QUANTITATIVE STEREOLOGY**

A.1 Details on the Characterization of the Macrostructure

The image below in Figure A.1 shows an optical image with the 10×8 grid of vertical and horizontal lines applied by the Image J software that was used during the composite characterization. Examples of the locations where the vertical and horizontal lines meet to form the points P and what constituted a P_p are shown in the figure. If there was a P lying on the heterogeneity—interpenetrating matrix interface it was counted as 0.5 instead of 1. An examples of N_i for 3 of the 18 lines that were used in the analysis is also shown.

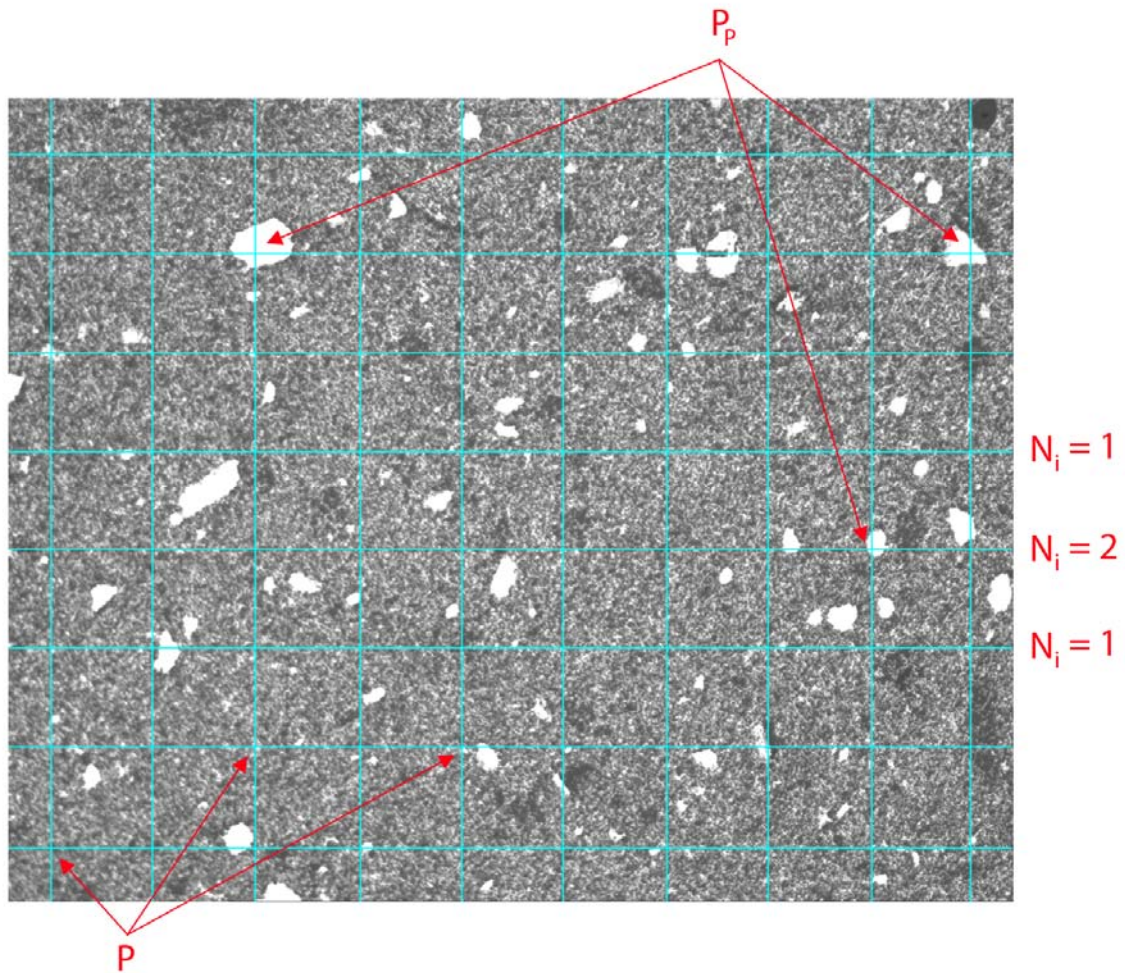


Figure A-2: Example of an optical image showing how N_i and P, and P_p were counted.

In the composite characterization 30 of these images were used in the analysis for each process, 10 images on 3 different pellets from the same batch. The statistics for every image were compiled and N_L and V_V calculating in an Excel spreadsheet as shown in Table A.1.

Table A-1: Example of the Excel spreadsheet used to calculate the V_V and N_L for the composite constituents. This particular spreadsheet is for the magnetic bar stirred composites.

Sample Number	Agglomerate Volume Fraction		Agglomerate Interceptions	
	P_{MgO}	P_{NdZrO}	N_{MgO}	N_{NdZrO}
87	1	1.5	6	8
	0.5	1	3	9
	2	0	5	5
	1	0	3	2
	2	2	5	10
	0	2	4	9
	1.5	0	7	3.5
	0	0	6	9
	2	2	8	7
	2	0	5	2
88	3	2	8	5
	3	0.5	12	8
	5	0	5	4
	1	0	5	2
	0	1	5	8
	2	0	7	9
	1	1	6	7
	0	0	5	5
	0	0	7	3
89	0	0	2	6
	0	1	2	8
	0	0	2	2
	2	0	4	4
	0	0	1	2
	1	2.5	4	9
	0	0	1	9
	0	0	1	8
	1	1	3	6
	1	0	3	2
Quantitative Stereology Results	$(V_V)_{MgO}$	$(V_V)_{NdZrO}$	$(N_L)_{MgO}$	$(N_L)_{NdZrO}$
	0.0133	0.0073	128	161

A.2 Details on the Characterization of the Microstructure

Figure A.2 shows a SEM image with the 8×8 grid of horizontal and vertical lines applied by the Image J software. Examples of the $N_{\alpha\alpha}$ and $N_{\alpha\beta}$ intercepts for MgO are shown on the image for 2 of the 16 horizontal and vertical lines. The $N_{\alpha\alpha}$ and $N_{\alpha\beta}$ were counted manually for all 16 lines on 3 different SEM images for each processing method to calculate the grain size and contiguity of the microstructure. The $N_{\alpha\alpha}$ and $N_{\alpha\beta}$ for each line was recorded into an Excel spreadsheet and the grain size and contiguity calculations were performed.

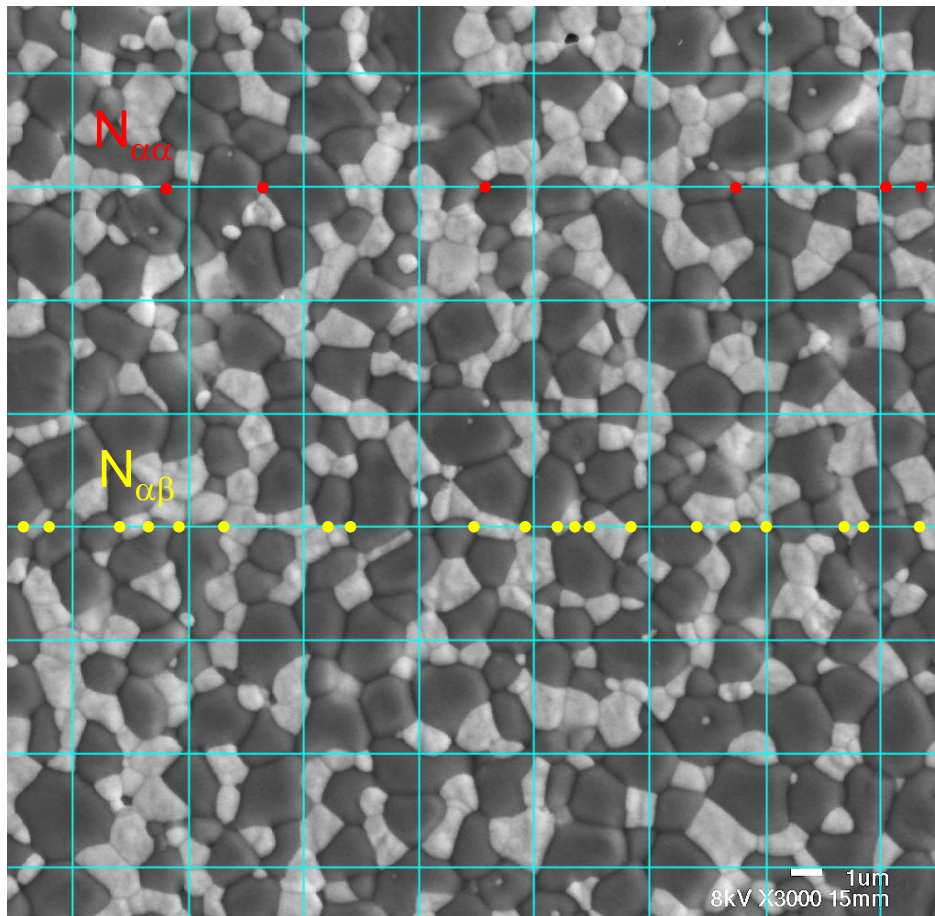


Figure A-3: Example of a SEM image with examples of both $N_{\alpha\alpha}$ and $N_{\alpha\beta}$ intercepts.

An example of the Excel spreadsheet used in the analysis is shown in Table A.2. The calculations for the grain size of the MgO and $\text{Nd}_2\text{Zr}_2\text{O}_7$ is shown in the right columns and the calculation for the contiguity of the MgO and $\text{Nd}_2\text{Zr}_2\text{O}_7$ is shown in the bottom of the

spreadsheet after all of the intercept data has been summed. The average grain size and its standard deviation was calculated from the grain sizes calculated in each row.

Table A-2: Example of an Excel spreadsheet with the intercept data and the grain size and contiguity calculations. This spreadsheet is for the Spex blended composites.

Sample Number	Grain Interceptions				Grain Size Calculation MgO			Grain Size Calculation Nd ₂ Zr ₂ O ₇		
	N _{MgO-MgO}	N _{MgO-NdZrO}	N _{NdZrO-NdZrO}	L _i (m)	N _{eff}	C _{eff}	D (m)	N _{eff}	C _{eff}	D (m)
042a	6	20	8	4.08E-05	16	2.86E-05	2.78E-06	18.00	1.22E-05	1.06E-06
	3	21	5.5	4.08E-05	13.5	2.86E-05	3.30E-06	16.00	1.22E-05	1.19E-06
	3	29	8	4.08E-05	17.5	2.86E-05	2.55E-06	22.50	1.22E-05	8.49E-07
	4	20	4	4.08E-05	14	2.86E-05	3.18E-06	14.00	1.22E-05	1.36E-06
	5	26	7.5	4.08E-05	18	2.86E-05	2.48E-06	20.50	1.22E-05	9.31E-07
	4	20	3.5	4.08E-05	14	2.86E-05	3.18E-06	13.50	1.22E-05	1.41E-06
	3	22	9.5	4.08E-05	14	2.86E-05	3.18E-06	20.50	1.22E-05	9.31E-07
	6	18	4.5	4.08E-05	15	2.86E-05	2.97E-06	13.50	1.22E-05	1.41E-06
	3	21	8	4.08E-05	13.5	2.86E-05	3.30E-06	18.50	1.22E-05	1.03E-06
	5	25	5	4.08E-05	17.5	2.86E-05	2.55E-06	17.50	1.22E-05	1.09E-06
	0	23	9	4.08E-05	11.5	2.86E-05	3.87E-06	20.50	1.22E-05	9.31E-07
	6	20	9	4.08E-05	16	2.86E-05	2.78E-06	19.00	1.22E-05	1.00E-06
	5	27	9	4.08E-05	18.5	2.86E-05	2.41E-06	22.50	1.22E-05	8.49E-07
	3	21	8	4.08E-05	13.5	2.86E-05	3.30E-06	18.50	1.22E-05	1.03E-06
	8	21	5	4.08E-05	18.5	2.86E-05	2.41E-06	15.50	1.22E-05	1.23E-06
	1	23	5	4.08E-05	12.5	2.86E-05	3.56E-06	16.50	1.22E-05	1.16E-06
7	13	7	4.08E-05	13.5	2.86E-05	3.30E-06	13.50	1.22E-05	1.41E-06	
042k	3	20	10	2.91E-05	13	2.04E-05	2.44E-06	20.00	8.73E-06	6.81E-07
	7	20	2	2.91E-05	17	2.04E-05	1.87E-06	12.00	8.73E-06	1.13E-06
	2	26	6	2.91E-05	15	2.04E-05	2.12E-06	19.00	8.73E-06	7.17E-07
	6	26	10	2.91E-05	19	2.04E-05	1.67E-06	23.00	8.73E-06	5.92E-07
	3	22	6	2.91E-05	14	2.04E-05	2.27E-06	17.00	8.73E-06	8.01E-07
	8	24	6	2.91E-05	20	2.04E-05	1.59E-06	18.00	8.73E-06	7.57E-07
	9	21	1	2.91E-05	19.5	2.04E-05	1.63E-06	11.50	8.73E-06	1.18E-06
	8	20	4	2.91E-05	18	2.04E-05	1.77E-06	14.00	8.73E-06	9.73E-07
	7	20	5	2.91E-05	17	2.04E-05	1.87E-06	15.00	8.73E-06	9.08E-07
	5	24	2	2.91E-05	17	2.04E-05	1.87E-06	14.00	8.73E-06	9.73E-07
	7	21	4	2.91E-05	17.5	2.04E-05	1.82E-06	14.50	8.73E-06	9.39E-07
	3	23	7	2.91E-05	14.5	2.04E-05	2.19E-06	18.50	8.73E-06	7.36E-07
4	26	8	2.91E-05	17	2.04E-05	1.87E-06	21.00	8.73E-06	6.49E-07	

Table A-2. Continued

Sample Number	Grain Interceptions				Grain Size Calculation MgO			Grain Size Calculation Nd ₂ Zr ₂ O ₇		
	N _{MgO-MgO}	N _{MgO-NdZrO}	N _{NdZrO-NdZrO}	L _i (m)	N _{eff}	C _{eff}	D (m)	N _{eff}	C _{eff}	D (m)
042q	5	27	3	2.91E-05	18.5	2.04E-05	1.72E-06	16.50	8.73E-06	8.25E-07
	2	17	10	2.91E-05	10.5	2.04E-05	3.03E-06	18.50	8.73E-06	7.36E-07
	3	25	5	2.91E-05	15.5	2.04E-05	2.05E-06	17.50	8.73E-06	7.78E-07
	1	23	12	2.91E-05	12.5	2.04E-05	2.54E-06	23.50	8.73E-06	5.80E-07
	4	16.5	6.5	2.91E-05	12.25	2.04E-05	2.59E-06	14.75	8.73E-06	9.23E-07
	5	19.5	3	2.91E-05	14.75	2.04E-05	2.15E-06	12.75	8.73E-06	1.07E-06
	2	22	4	2.91E-05	13	2.04E-05	2.44E-06	15.00	8.73E-06	9.08E-07
	8	21.5	4	2.91E-05	18.75	2.04E-05	1.69E-06	14.75	8.73E-06	9.23E-07
	2.5	21	4	2.91E-05	13	2.04E-05	2.44E-06	14.50	8.73E-06	9.39E-07
	7	21	3	2.91E-05	17.5	2.04E-05	1.82E-06	13.50	8.73E-06	1.01E-06
	4	18	3	2.91E-05	13	2.04E-05	2.44E-06	12.00	8.73E-06	1.13E-06
	4	26.5	6	2.91E-05	17.25	2.04E-05	1.84E-06	19.25	8.73E-06	7.07E-07
	1	25	10	2.91E-05	13.5	2.04E-05	2.35E-06	22.50	8.73E-06	6.05E-07
	6	31.5	4.5	2.91E-05	21.75	2.04E-05	1.46E-06	20.25	8.73E-06	6.73E-07
	5	21	6	2.91E-05	15.5	2.04E-05	2.05E-06	16.50	8.73E-06	8.25E-07
	4	22	7	2.91E-05	15	2.04E-05	2.12E-06	18.00	8.73E-06	7.57E-07
	4	27	3	2.91E-05	17.5	2.04E-05	1.82E-06	16.50	8.73E-06	8.25E-07
	7	14	0	2.91E-05	14	2.04E-05	2.27E-06	7.00	8.73E-06	1.95E-06
Sum	219	1062	281	1.60E-03	Average		2.39E-06	Average		9.61E-06
Contiguity (MgO)	0.29	Contiguity (NdZrO)	0.35	Std. Dev		5.97E-07	Std. Dev		2.61E-07	

APPENDIX B
TABLES OF THERMAL CONDUCTIVITY VALUES

This appendix lists the thermal conductivity values for the composites that were plotted in Chapter 6, Chapter 7, and Chapter 8.

Table B-1: Thermal conductivity and corresponding error for composites processed by the four processing methods. The data was corrected to 0% porosity using Equation 6.2.

Temperature (K)	Thermal Conductivity ($\text{Wm}^{-1}\text{K}^{-1}$)			
	Mortar and Pestle	Magnetic Bar Stirring	Spex Blending	Ball Milling
373	23.0 ± 1.3	23.8 ± 2.3	19.7 ± 0.3	23.4 ± 0.7
473	17.8 ± 0.9	18.6 ± 1.7	16.3 ± 0.2	18.3 ± 0.6
573	14.8 ± 0.7	15.3 ± 1.4	13.7 ± 0.2	15.0 ± 0.6
673	12.3 ± 0.6	12.8 ± 1.1	11.7 ± 0.2	12.6 ± 0.4
773	10.6 ± 0.6	11.0 ± 1.0	10.1 ± 0.1	10.8 ± 0.3
873	9.4 ± 0.6	9.7 ± 0.9	8.9 ± 0.1	9.6 ± 0.3
973	8.4 ± 0.5	8.8 ± 0.8	7.9 ± 0.1	8.6 ± 0.2
1073	7.7 ± 0.4	8.0 ± 0.7	7.1 ± 0.1	7.8 ± 0.2
1173	7.1 ± 0.3	7.4 ± 0.7	6.5 ± 0.1	7.2 ± 0.2
1273	6.6 ± 0.4	6.9 ± 0.6	6.0 ± 0.1	6.6 ± 0.2

Table B-2: Thermal conductivity and corresponding error for the ball milled composites. The data was corrected to 0% porosity using Equation 6.2.

Temperature (K)	Thermal Conductivity ($\text{Wm}^{-1}\text{K}^{-1}$)			
	Batch A	Batch B	Batch C	Average
373	23.4 ± 0.7	24.1 ± 0.3	24.5 ± 0.4	24.0 ± 0.6
473	18.3 ± 0.6	18.8 ± 0.3	19.1 ± 0.4	18.7 ± 0.5
573	15.0 ± 0.6	15.5 ± 0.3	15.7 ± 0.3	15.4 ± 0.4
673	12.6 ± 0.4	12.9 ± 0.2	13.2 ± 0.3	12.9 ± 0.3
773	10.8 ± 0.3	11.1 ± 0.2	11.3 ± 0.2	11.1 ± 0.3
873	9.6 ± 0.3	9.8 ± 0.2	9.9 ± 0.2	9.8 ± 0.3
973	8.6 ± 0.2	8.8 ± 0.1	8.9 ± 0.2	8.8 ± 0.2
1073	7.8 ± 0.2	8.0 ± 0.1	8.1 ± 0.2	7.9 ± 0.2
1173	7.2 ± 0.2	7.3 ± 0.1	7.4 ± 0.1	7.3 ± 0.2
1273	6.6 ± 0.2	6.8 ± 0.1	6.9 ± 0.2	6.8 ± 0.2

Table B-3: Thermal conductivity and corresponding error for the ball milled composites isothermally soaked at 1550 °C. The data was corrected to 0% porosity using Equation 6.2.

Temperature (K)	Thermal Conductivity ($\text{Wm}^{-1}\text{K}^{-1}$)				
	1 hr	4 hr	8 hr	24 hr	100 hr
373	24.1 ± 0.6	24.6 ± 0.6	24.3 ± 0.6	25.2 ± 0.6	24.3 ± 0.6
473	19.1 ± 0.5	19.1 ± 0.5	19.0 ± 0.5	19.5 ± 0.5	19.0 ± 0.5
573	15.8 ± 0.4	15.7 ± 0.4	15.6 ± 0.4	16.0 ± 0.4	15.6 ± 0.4
673	13.3 ± 0.4	13.2 ± 0.4	13.1 ± 0.3	13.3 ± 0.3	13.0 ± 0.3
773	11.5 ± 0.3	11.3 ± 0.3	11.3 ± 0.3	11.4 ± 0.3	11.2 ± 0.3
873	10.2 ± 0.2	10.0 ± 0.2	10.0 ± 0.2	10.0 ± 0.2	9.8 ± 0.2
973	9.1 ± 0.2	8.9 ± 0.2	9.0 ± 0.2	8.9 ± 0.2	8.8 ± 0.2
1073	8.3 ± 0.2	8.1 ± 0.2	8.1 ± 0.2	8.1 ± 0.2	8.0 ± 0.2
1173	7.6 ± 0.2	7.5 ± 0.2	7.5 ± 0.1	7.5 ± 0.2	7.4 ± 0.2
1273	7.1 ± 0.2	6.9 ± 0.2	7.0 ± 0.2	6.9 ± 0.2	6.8 ± 0.2

Table B-4: Thermal conductivity and corresponding error for the ball milled composites isothermally soaked at 1650 °C. The data was corrected to 0% porosity using Equation 6.2.

Temperature (K)	Thermal Conductivity ($\text{Wm}^{-1}\text{K}^{-1}$)				
	1 hr	4 hr	8 hr	24 hr	100 hr
373	23.5 ± 0.6	24.5 ± 0.6	24.0 ± 0.6	23.0 ± 0.6	29.9 ± 0.5
473	18.3 ± 0.5	19.1 ± 0.5	18.7 ± 0.5	17.8 ± 0.5	15.7 ± 0.4
573	15.0 ± 0.4	15.7 ± 0.4	15.2 ± 0.4	14.6 ± 0.4	13.0 ± 0.3
673	12.5 ± 0.3	13.1 ± 0.3	12.8 ± 0.3	12.4 ± 0.3	11.0 ± 0.3
773	10.7 ± 0.3	11.2 ± 0.3	11.0 ± 0.3	10.6 ± 0.3	9.6 ± 0.2
873	9.5 ± 0.2	9.8 ± 0.2	9.7 ± 0.2	9.4 ± 0.2	8.5 ± 0.2
973	8.5 ± 0.2	8.8 ± 0.2	8.6 ± 0.2	8.4 ± 0.2	7.7 ± 0.2
1073	7.7 ± 0.2	8.0 ± 0.2	7.8 ± 0.2	7.6 ± 0.2	7.1 ± 0.2
1173	7.1 ± 0.2	7.3 ± 0.2	7.2 ± 0.2	7.0 ± 0.2	6.6 ± 0.1
1273	6.6 ± 0.2	6.8 ± 0.2	6.7 ± 0.2	6.7 ± 0.2	6.2 ± 0.2

APPENDIX C SPECIFIC HEAT CAPACITY

C.1 Introduction

This appendix begins by describing the experimental procedure to measure the specific heat capacity of a sample using differential scanning calorimetry (DSC).⁹⁷ The specific heat capacity of the composites is then reported.

C.2 Differential Scanning Calorimetry

Instrument setup begins by positioning the Pt alloy pans and lids in the DSC using a set of scratches on the pans and dimples on the lids to be able to consistently line up the pans and lids between measurement runs.

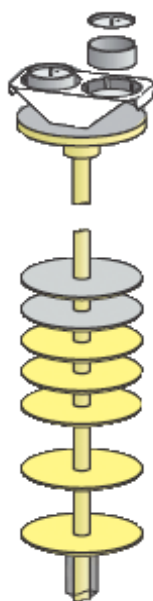


Figure C-1: Sample holder for the DSC 404C showing the two Pt alloy pans on the sample head. (courtesy of Netzsch Thermal Analysis)

The furnace was closed and the vacuum and turbo pumps turned on. The sample chamber was evacuated to 8.9×10^{-5} mbar before UHP Ar was bled into the sample chamber from the mass flow controller (MFC) to equilibrate the sample chamber to atmospheric pressure.

The MFC was then set to flow Ar into the DSC at 50 ml/min. The instrument was then programmed with the temperature profile shown below in Figure C.3.

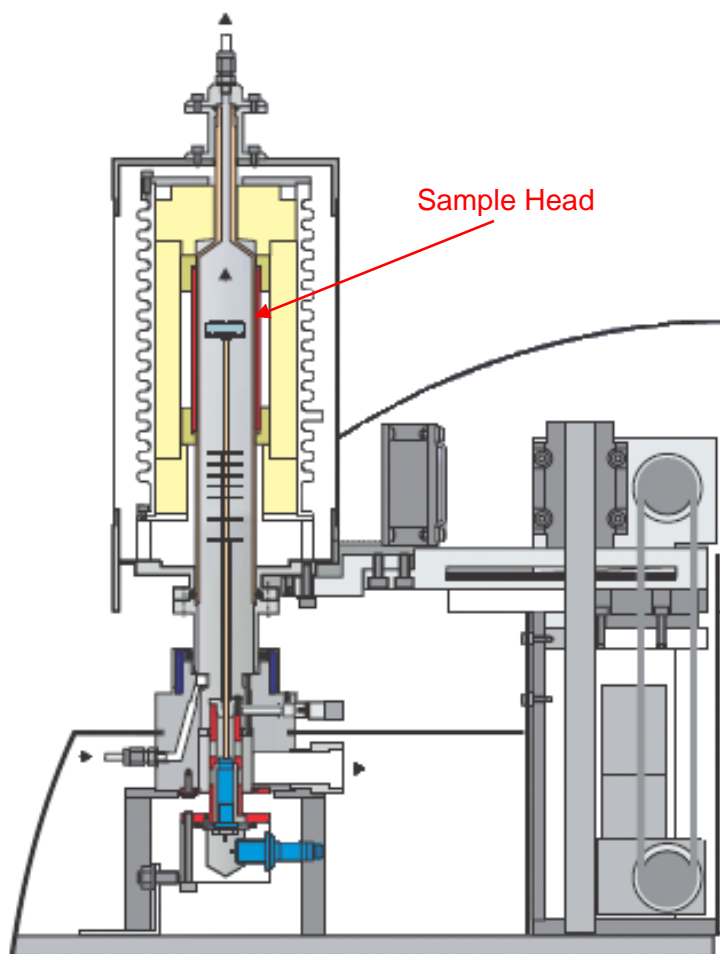


Figure C-2: Cross-section of the Netzsch DSC 404C. (courtesy of Netzsch Thermal Analysis)

A ball milled composite disk 6 mm in diameter and ~1.5 mm thick was fabricated according to the procedure described in Section 3.6. One side of the composite was polished flat so the thickness of the pellet was ~1 mm and weighed ~90 mg.

The specific heat capacity measurement began by running a baseline with empty Pt alloy pans in the front and back position of the DSC according to the temperature profile shown in Figure C.3. If the total variation of the signal was within 2 mV, the run was accepted as a good baseline. A 6 mm diameter sapphire standard was placed in the center of the front pan

and the DSC was run again using the accepted baseline and corresponding temperature profile. A third DSC run with the composite pellet centered in the front Pt alloy pan was then performed. All three measurements were performed back-to-back with minimal down-time between the measurements.

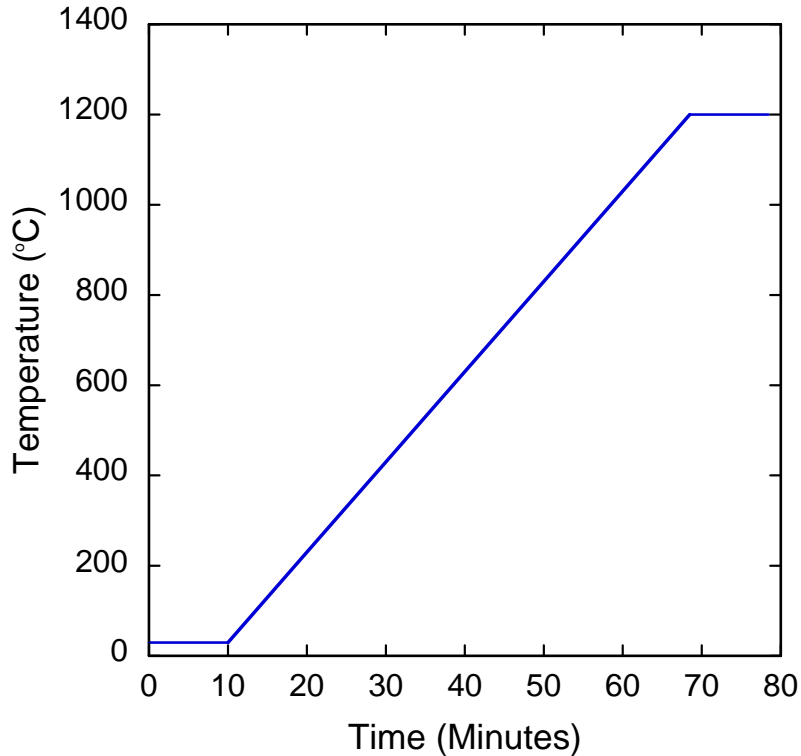


Figure C-3: Furnace temperature profile for specific heat capacity measurements with a ramp rate of 20 °C/min.

The sapphire standard and composite sample run were opened in the Netzsch Proteus Analysis software. The specific heat capacity of the composite was extracted using calculations based on ASTM Standard E1269-05.

C.3 Results

The specific heat capacity of the composite was calculated as a function of temperature using the rule of mixtures and heat capacity data from Touloukian⁹⁸ and Lutique et al.⁹⁹ according to the following equation.

$$C_p = 0.7C_p^{MgO} + 0.3C_p^{Nd_2Zr_2O_7} \quad (C.1)$$

The calculated specific heat capacity is plotted with the measured specific heat capacity of the composite in Figure C.4.

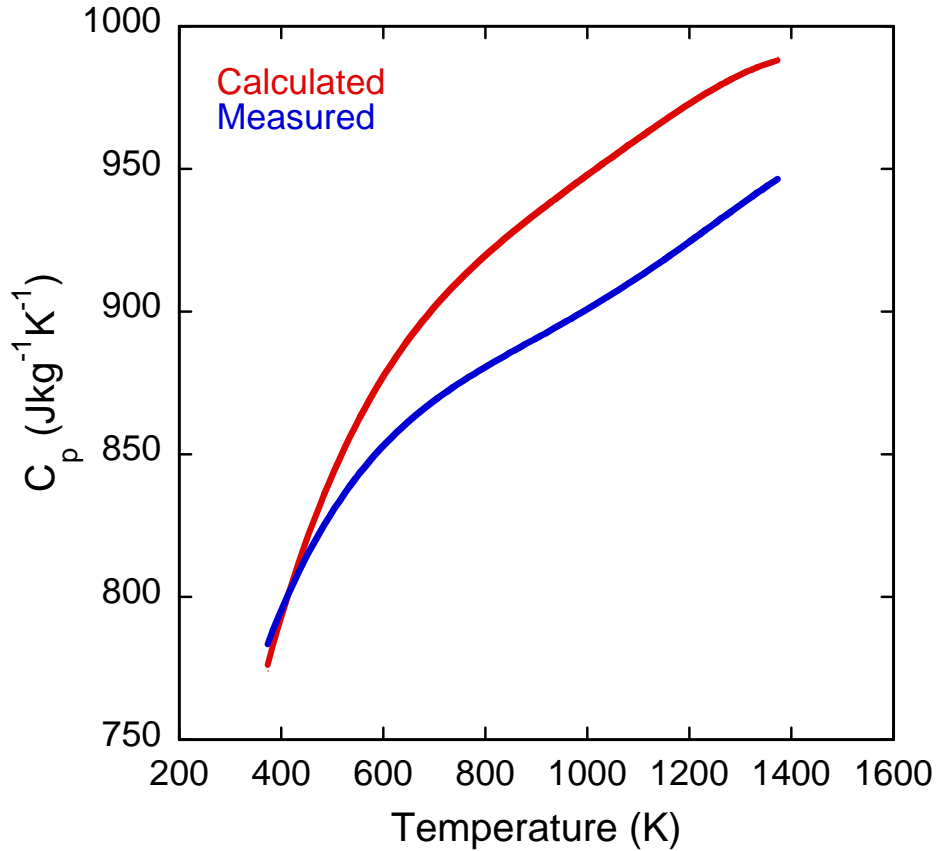


Figure C-4: The measured specific heat capacity of the 70 vol% MgO—30 vol% $Nd_2Zr_2O_7$ composite and the specific heat capacity of the composite calculated from the rule of mixtures and specific heat capacity data from Touloukian⁹⁸ and Lutique⁹⁹.

The calculated and measured specific heat capacity are in reasonably good agreement, with only a ~5% difference in values at 1373 K. Therefore, the specific heat capacity measurement was accepted and fit to a polynomial equation. The specific heat capacity of the composite as a function of temperature is shown in Equation C.2.

$$C_p = 437.7 + 1.55T - 2.1 \times 10^{-3}T^2 + 1.4 \times 10^{-6}T^3 - 3.2 \times 10^{-10}T^4 \left(\frac{J}{kg \cdot K} \right) \quad (C.2)$$

Since the heat capacity of a material depends only on the lattice and electronic properties, the specific heat capacity is independent of microstructure. Therefore, the specific heat capacity measured on the ball milled composite can be used for all of the composites since the composition of the composites is the same. The specific heat capacity was re-measured on the same sample to check for consistency. The two measured specific heat capacity curves were essentially identical.

APPENDIX D THERMAL EXPANSION MEASUREMENTS

D.1 Introduction

This appendix describes the experimental procedure to measure the thermal expansion of a sample and presents the thermal expansion results on the composites processed by the four processing methods. The coefficients of thermal expansion extracted from the thermal expansion measurements on the composites are used in the thermal conductivity calculation in Chapter 6.

D.2 Dilatometry

Figure D.1 shows the Netzsch DIL402C dilatometer used to perform the thermal expansion measurements. The furnace slides to the right exposing the sample tube to load the sample for measurement. A schematic of the sample tube is shown below in Figure D.2.

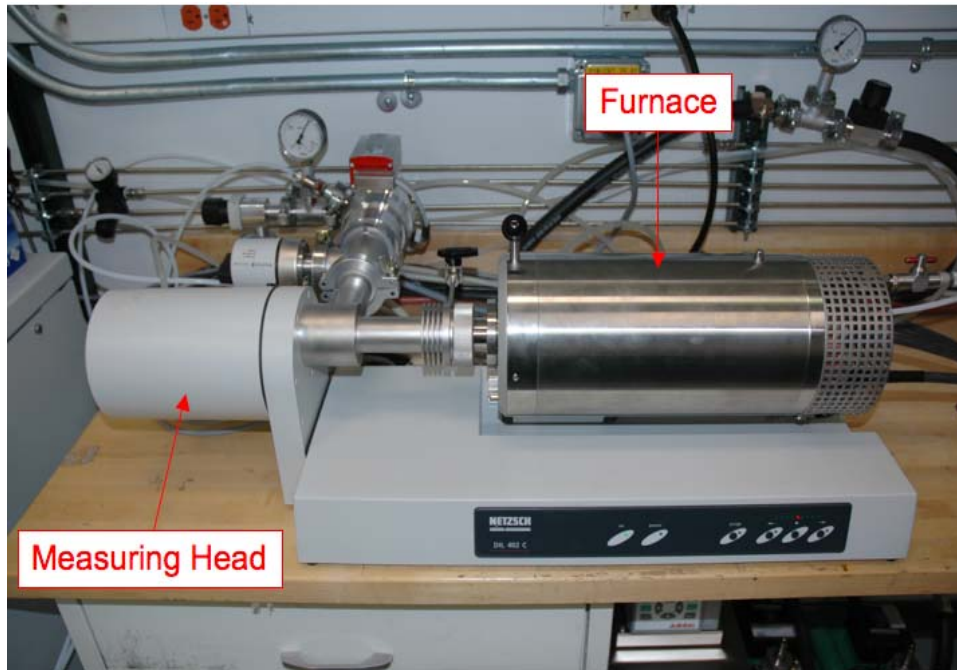


Figure D-1: Netzsch DIL 402C dilatometer showing the measuring head and the sample furnace.

A flat and parallel alumina rod spacer 6 mm in diameter and 20 mm long was used to center a 5-7 mm long sample beneath the sample thermocouple and to prevent material

interactions with the push rod. The thin alumina spacer disk in the back of the sample tube prevented any material reactions between the sample and the back of the sample tube. Although not pictured in the schematic, the spacers and samples are sitting on alumina cradles that stabilize the samples and center them laterally with the push rod. The sample is located parallel to the push rod, spacers, and the end is centered over the sample. The push rod is moved back and forth to settle the series of spacers and samples until there is no vertical bowing of the push rod, spacers, and sample when the push rod is engaged.

The furnace was then moved back to the left and closed. The vacuum and turbo pumps are started and the sample tube was evacuated to 8.9×10^{-5} mbar. The pressure in the sample tube was equilibrated using UHP Ar bled in from the mass flow controller (MFC) and then set to 25 ml/min. The dilatometer was programmed according to the profile in Figure D.3 and the test is started.

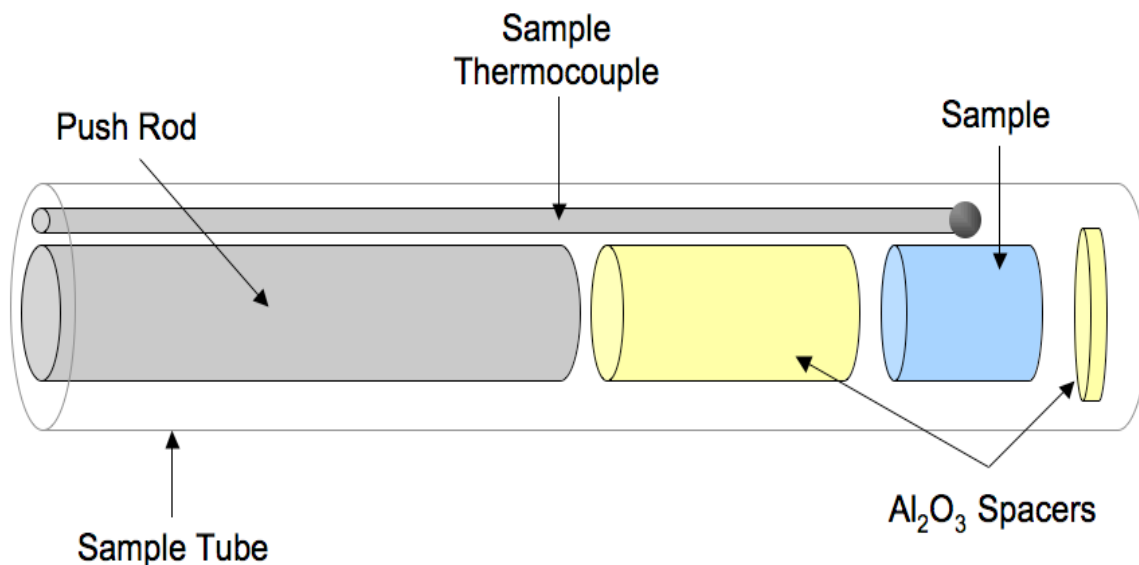


Figure D-2: Sample and spacer setup in the sample tube for thermal expansion measurements.

A baseline was measured using an alumina standard placed in the sample position to correct for the expansion of the fixture. A new baseline must be measured for every temperature profile used to measure the thermal expansion of samples. In this case, the

temperature profile used to measure the thermal expansion of the composites is shown below in Figure D.3.

Thermal expansion measurements were then performed on a 6 mm diameter by ~7 mm long pellet fabricated from the mixed composite powders according the procedure described in Section 3.6. The sample was setup using the procedure described above and programmed with the temperature profile of the alumina baseline. When the test was complete on the composite sample, the Netzsch Proteus software extracts the coefficient of thermal expansion from the data using the temperature range of 300 °C to 1000 °C.

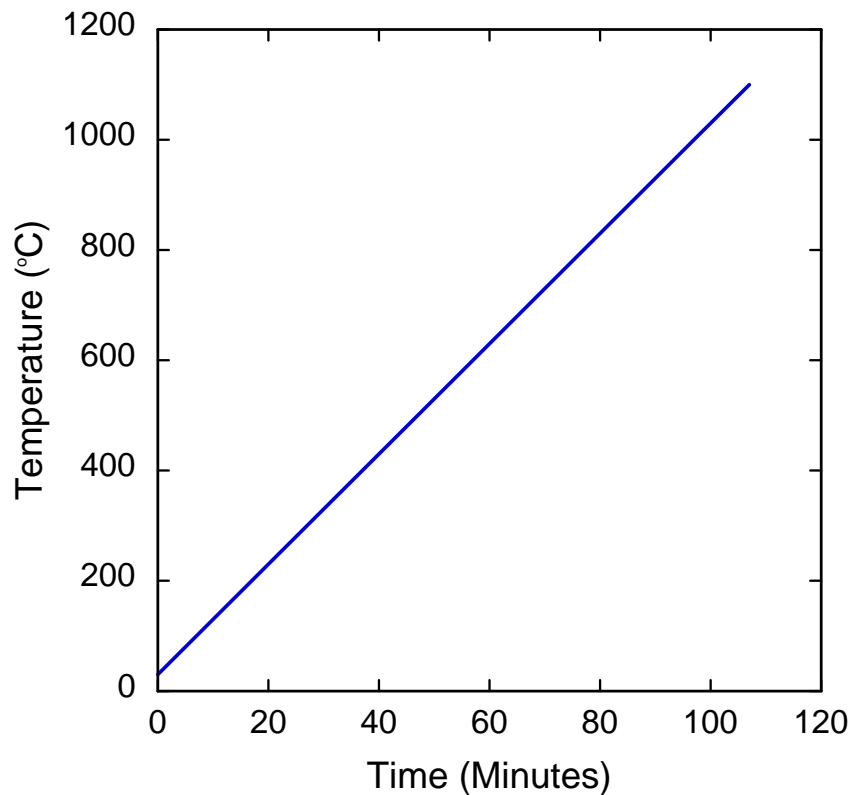


Figure D-3: Furnace profile for thermal expansion measurements with a ramp rate of 10 °C/min.

D.3 Results.

One composite pellet from each processing method was measured. The thermal expansion of the composites from 600 K to 1273 K is shown below in Figures D.4—D.7 along with the extracted coefficients of thermal expansion.

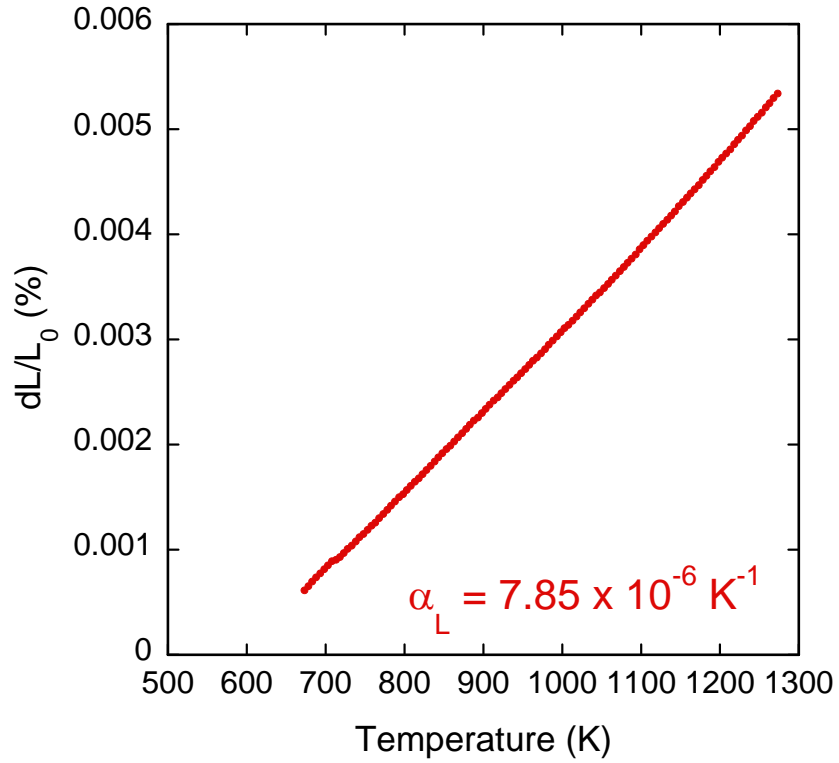


Figure D-4: Thermal expansion of a mortar and pestle composite.

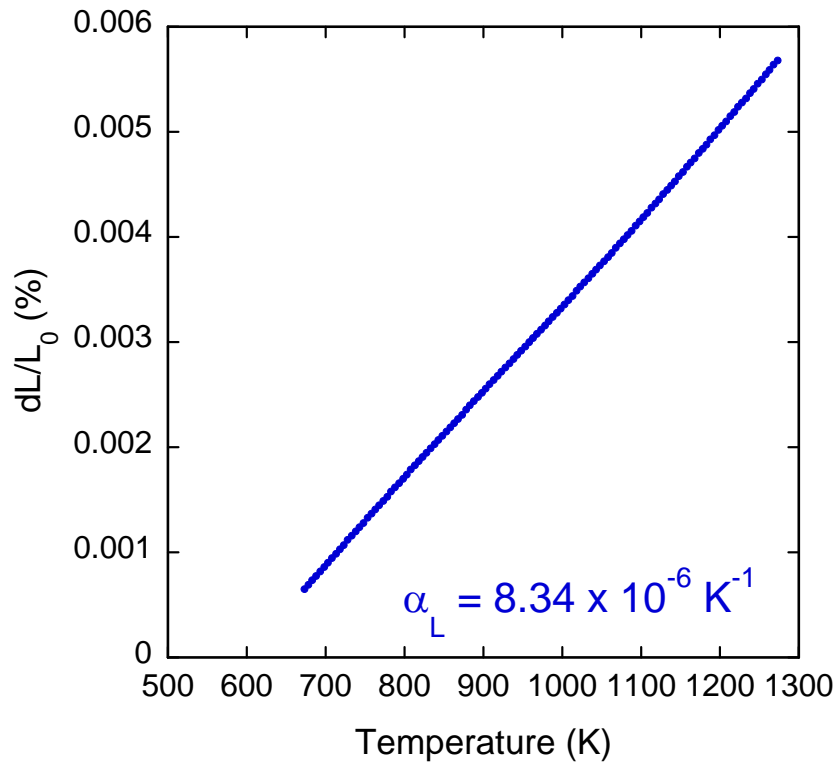


Figure D-5: Thermal expansion of a magnetic bar stirred composite.

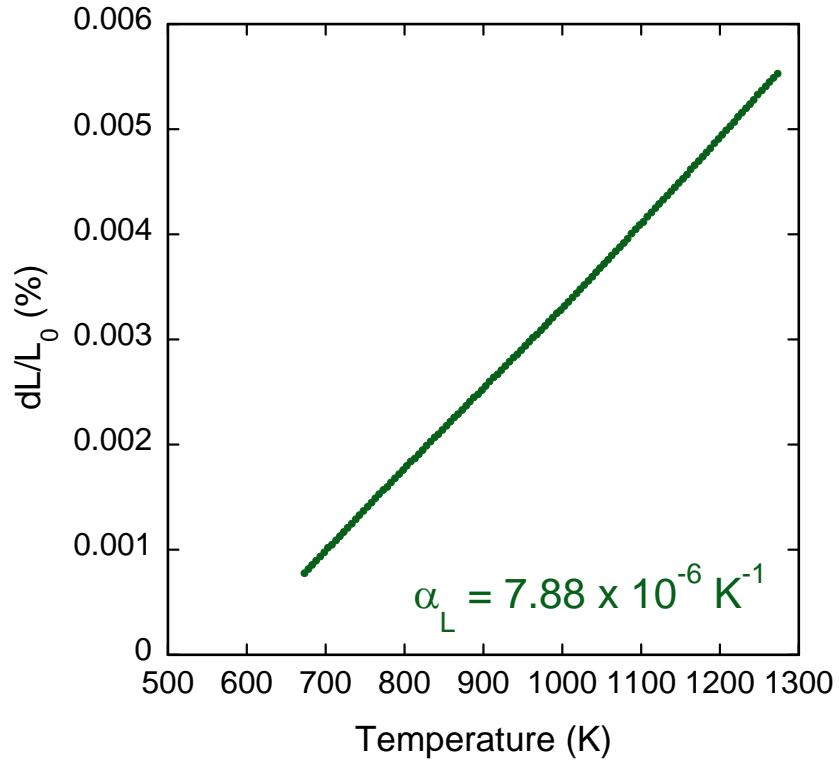


Figure D-6: The thermal expansion of a Spex blended composite.

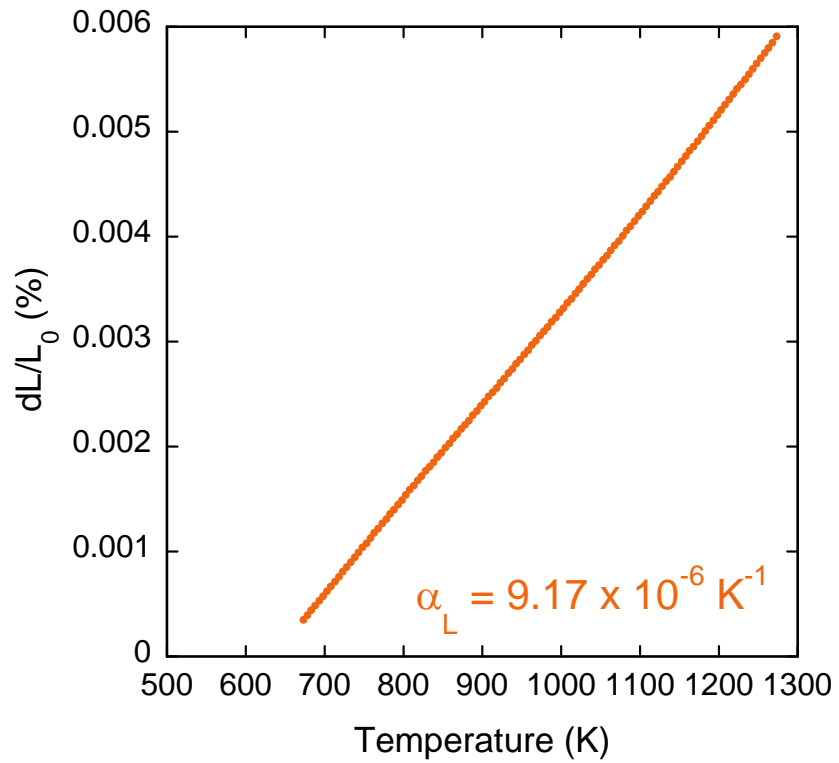


Figure D-7: Thermal expansion of a ball milled composite.

The change in density of the composites as a function of temperature was calculated from the coefficients of thermal expansion. In isotropic samples, the volumetric coefficient of thermal expansion α_V is related to the linear coefficient of thermal expansion α_L given in Figures D.4—D.7 by the following relationship

$$\alpha_V \approx 3\alpha_L \quad (\text{D.1})$$

The volumetric coefficient of thermal expansion is related to the change in the sample density according to Equation D.2.

$$\alpha_V = -\frac{1}{\rho} \left(\frac{\partial \rho}{\partial T} \right) \quad (\text{D.2})$$

Therefore, the change in density of the composites can be calculated as function of temperature using Equation D.3.

$$\Delta\rho = -\alpha_V \rho_0 \Delta T \quad (\text{D.3})$$

The density of the composite at any temperature T_i can then be calculated using Equation D.4

$$\rho_i = \rho_0 - \alpha_V \rho_0 (T - T_i) \quad (\text{D.4})$$

where ρ_0 is the density of the composite at room temperature measured by Archimedes.

APPENDIX E COMPOSITE GRAIN GROWTH AT 1550°C

E.1 Introduction

The following appendix describes the grain growth and grain growth kinetics of the ball milled composites isothermally soaked at 1550°C. The results of the microstructure characterization on the composites is also shown and thermal conductivity is reported.

E.2 Experimental Procedure

Pellets were fabricated from the ball milled mixed composite powder according to the procedure in Section 3.6. During sintering, the furnace temperature reached the isothermal hold time at 1550°C according to the furnace profile in Section 3.21, but the isothermal hold time was varied. Composites were isothermally held at 1550°C for 1, 4, 8, 24, and 100 hours. In addition, composites were sintered at 1450°C and 1650°C for 4 hours to the data to calculate the activation energy for grain growth.

The composites were prepared and analyzed with the SEM using the experimental procedure described in Section 3.3.2. The grain size of the composites was calculated using the procedure described in Section 4.3.3 and the contiguity was calculated using the procedure described in Section 4.3.4.

E.3 Results

In the following section the grain size and contiguity of the composites is characterized. The analysis of the grain growth kinetics of the composites then follows.

E.3.1 Microstructure Characterization

SEM images of the composites are shown below in Figure E.1. As expected, as the isothermal hold time increases the grain size of both the MgO and Nd₂Zr₂O₇ increases. Since the microstructure in Figure E.1a was not soaked at 1550°C to allow grain growth, it can be used to measure the minimum grain size D_0 for the MgO and Nd₂Zr₂O₇.

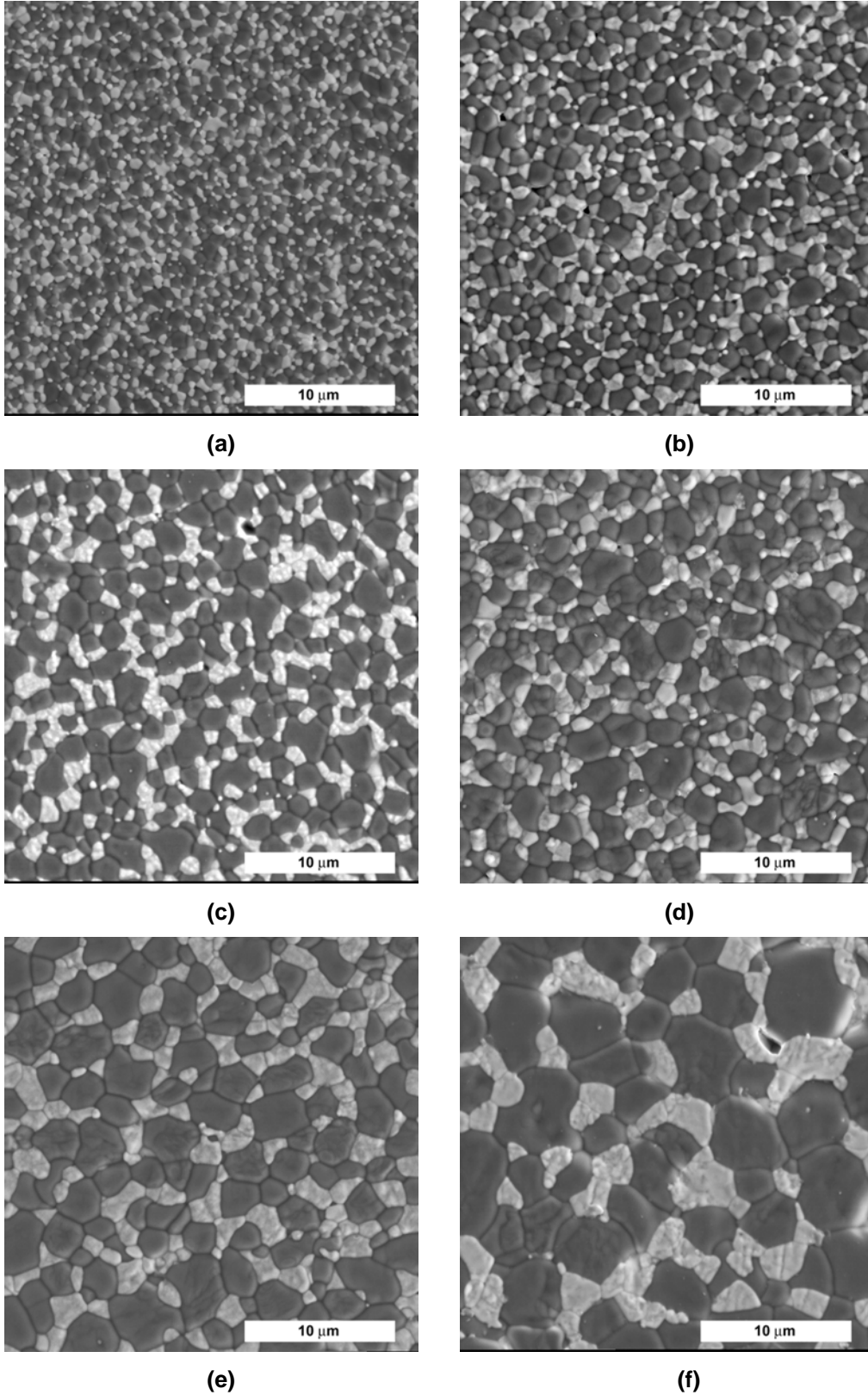


Figure E-1: Microstructures of ball milled composites isothermally held at 1550°C. A) 0 hours B) 1 hour C) 4 hours D) 8 hours E) 24 hours F) 100 hours

The grain size of the MgO and Nd₂Zr₂O₇ was measured using the technique described in Section 4.3.3 and the results are shown below in Table E.1. The grain size of both phases increases with increasing isothermal soaking time at 1550°C.

Table E-1: Grain sizes of the MgO and Nd₂Zr₂O₇ in the microstructure of the ball milled composites isothermally held for the given amount of time.

Phase	Grain Size (μm)					
	0 hr	1 hr	4 hr	8 hr	24 hr	100 hr
MgO	1.1 \pm 0.1	1.6 \pm 0.2	2.1 \pm 0.3	2.2 \pm 0.3	2.9 \pm 0.5	5.0 \pm 0.8
Nd ₂ Zr ₂ O ₇	0.7 \pm 0.2	1.1 \pm 0.2	1.2 \pm 0.3	1.4 \pm 0.3	2.0 \pm 0.5	2.7 \pm 0.8

The contiguity of the MgO and Nd₂Zr₂O₇ was measured using the technique described in Section 4.3.4. The contiguity of the Nd₂Zr₂O₇ varied between 0.22 and 0.32 in the composites, and the contiguity of the MgO varied between 0.45 and 0.50. These results indicate that while the microstructure of the composites increased in scale, the character of the microstructures remained essentially constant.

Table E-2: Contiguity of the MgO and Nd₂Zr₂O₇ in the microstructure of the ball milled composites isothermally held for the given amount of time.

Phase	Contiguity					
	0 hr	1 hr	4 hr	8 hr	24 hr	100 hr
MgO	0.46	0.48	0.45	0.51	0.50	0.46
Nd ₂ Zr ₂ O ₇	0.22	0.24	0.29	0.28	0.23	0.32

E.3.2 Grain Growth Kinetics

The grain growth behavior is shown in Figure E.2 for both the MgO and Nd₂Zr₂O₇ phases. The ratio of the MgO and Nd₂Zr₂O₇ grain sizes is constant, as shown in Figure E.3. Figure E.2 confirms the grain growth of the MgO and Nd₂Zr₂O₇ in the composites appear regular, and the constant ratio of MgO to Nd₂Zr₂O₇ grain sizes indicates that grain growth in the composites is coupled.

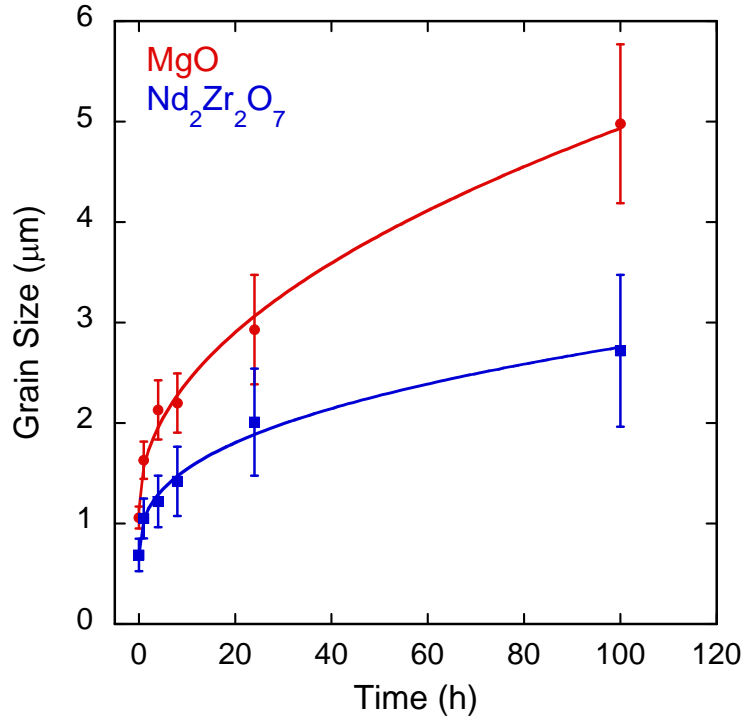


Figure E-2: Grain growth of MgO and Nd₂Zr₂O₇ in ball milled composites.

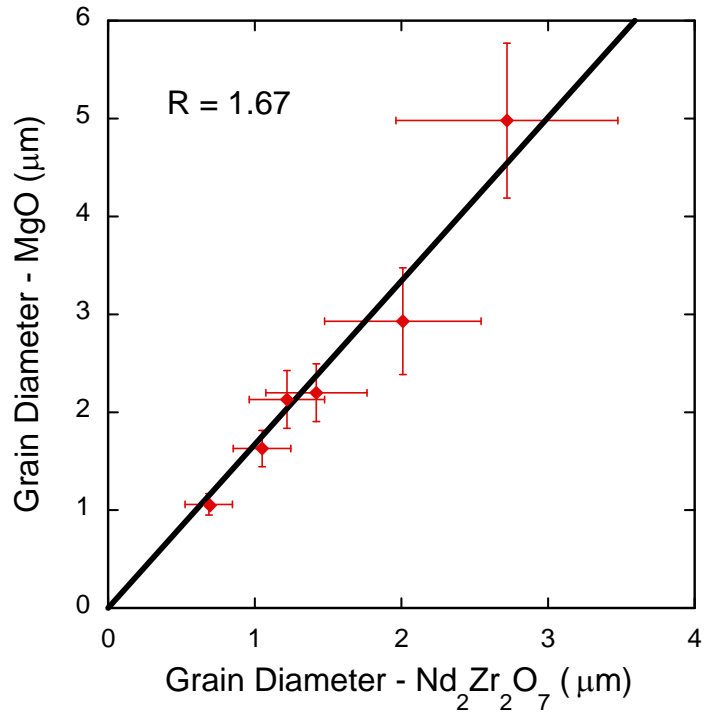


Figure E-3: The grain size of the MgO compared to the grain size of the Nd₂Zr₂O₇ showing a constant grain size ratio during grain growth.

According to Equation 2.1 there is an independent D_0 , K , and n for each phase in the composite. The D_0 was measured from the composites sintered for 0 hours at 1550°C, the minimum sintering conditions for the composite. Figure E.4 shows a log-log plot of $D^n - D_0^n$ as a function of time using values of n that correspond to interface controlled growth ($n = 2$), lattice controlled growth ($n = 3$), and grain boundary diffusion controlled growth ($n = 4$). Since the slope of the line in the $\log(D^n - D_0^n)$ vs. $\log(t)$ is equal to $1/n$ according to Equation 2.1, the correct grain growth mechanism will have a slope that equals one. From Figure E.4, it can be observed that the best fit is for n is 4, indicating that grain growth in these composites was controlled by grain boundary diffusion.

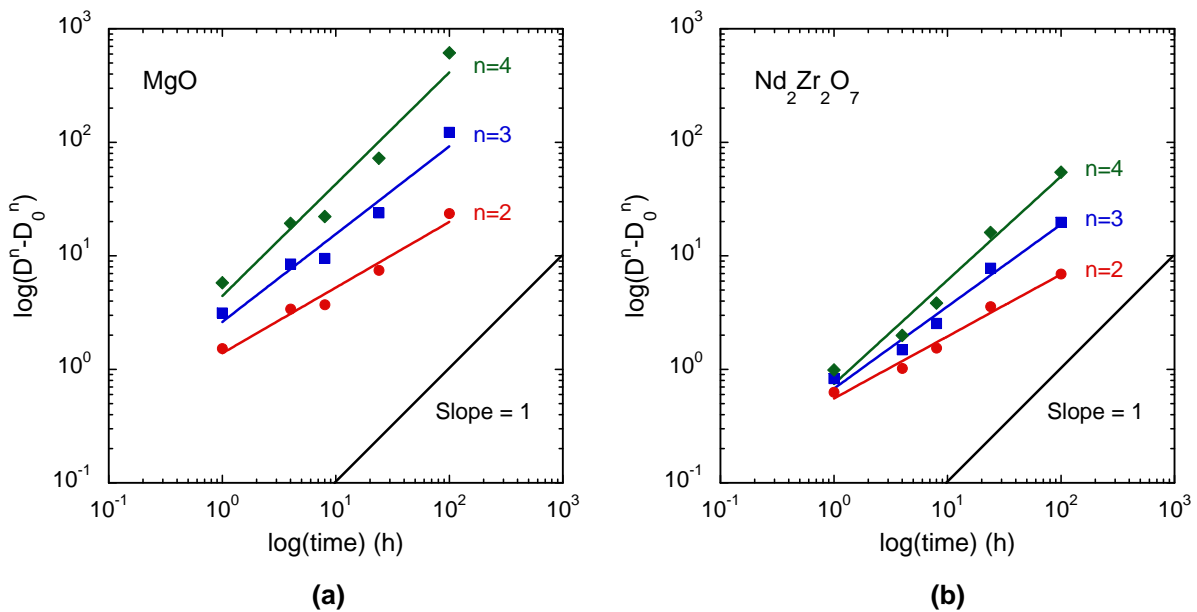


Figure E-4: Determination of the grain growth exponent by calculating K for $n = 2$, $n = 3$, and $n = 4$. The line with the correct grain growth exponent has a slope that equals 1. A) MgO
B) $\text{Nd}_2\text{Zr}_2\text{O}_7$

Additional evidence can be found in the microstructures of the composites to support the claim that grain growth in the MgO— $\text{Nd}_2\text{Zr}_2\text{O}_7$ composites is controlled by grain boundary diffusion. In Figure E.5 there is an example of a $\text{Nd}_2\text{Zr}_2\text{O}_7$ grain diffusing through a MgO—MgO grain boundary. This image shows a process that is similar to an Ostwald ripening type of

process where the large second phase particles grow at the expense of the smaller second phase particles. The driving force for the diffusion of the $\text{Nd}_2\text{Zr}_2\text{O}_7$ through the MgO — MgO grain boundaries is the difference in the concentration gradient between the grains. Based on the fact that the grain growth in the composites is coupled, it is likely that the grain growth of both phases is controlled by the kinetics of the grain boundary diffusion of the $\text{Nd}_2\text{Zr}_2\text{O}_7$.

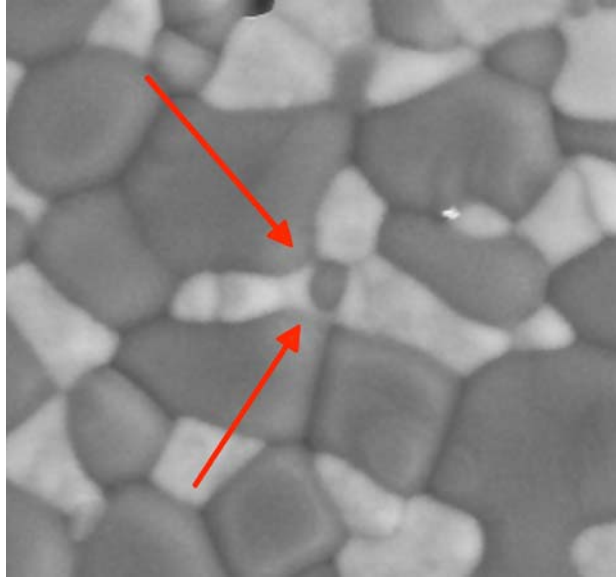


Figure E-5: Composite showing grain boundary diffusion of the $\text{Nd}_2\text{Zr}_2\text{O}_7$ between the MgO — MgO grain boundary.

The grain boundary diffusion of the $\text{Nd}_2\text{Zr}_2\text{O}_7$ will result in a rearrangement of the MgO and $\text{Nd}_2\text{Zr}_2\text{O}_7$ grains, theoretically effecting not only the scale, but also the character of the microstructure. However, the contiguity of the MgO and $\text{Nd}_2\text{Zr}_2\text{O}_7$ is relatively constant between the composites. This indicates that although the grains rearranged during grain growth, they did so in such a way as to not drastically affect the character of the microstructure.

A 4 hour isochronal series of composites was fabricated and characterized in order to determine the activation energy of the grain growth of the MgO and $\text{Nd}_2\text{Zr}_2\text{O}_7$ in the composites. The slope of an Arrhenius plot of $\log\left(\frac{D^n - D_0^n}{t}\right)$ as a function of the inverse temperature ($1/T$) should yield a curve where the activation energy for grain growth can be extracted from

the slope. This plot for the MgO—Nd₂Zr₂O₇ composites is shown below in Figure E.6. The *n* values used in the calculation are shown and were determined from the best fit of the data in Figure E.4a and Figure E.4b to a slope of one. The values for *D*₀, *K*, *n*, and the resulting activation energy *Q* for each phase in the composite is compiled in Table E.3.

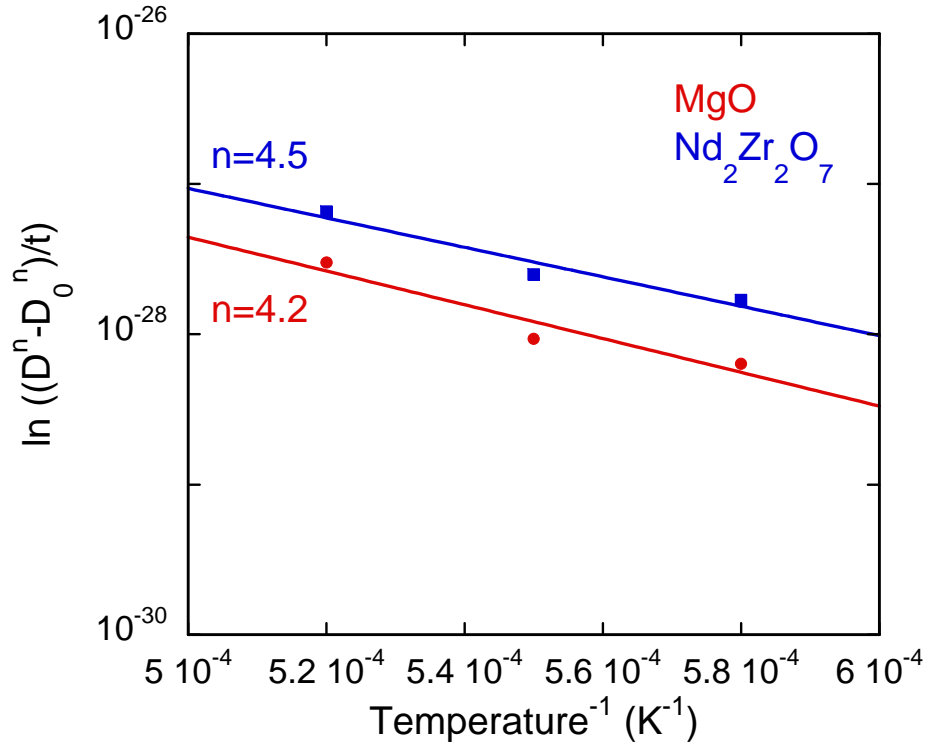


Figure E-6: Calculation of the activation energy for grain growth in the ball milled composites for the given grain growth exponents.

The activation energies of the MgO and Nd₂Zr₂O₇ are similar, but the activation energy for the Nd₂Zr₂O₇ is slightly higher.

Table E-3: Grain growth exponents, constants, and the correlation coefficient from the best fit to the grain growth equation. The activation energy of the grain growth is also included.

Phase	$D^n - D_0^n = Kt$				Q (kJ/mol)
	D ₀ (μm)	n	K (m ² /s)	R ²	
MgO	1.1 ± 0.1	4.2	8.5 × 10 ⁻²²	0.96	225 ± 45
Nd ₂ Zr ₂ O ₇	0.7 ± 0.2	4.5	9.1 × 10 ⁻²¹	0.97	276 ± 62

E.3.3 Thermal Conductivity

The thermal diffusivity of the MgO—Nd₂Zr₂O₇ composites isothermally soaked at 1550°C was measured to determine the effect of the grain growth on the thermal conductivity. Figure E.7 shows that the thermal conductivity of the composites is virtually the same, indicating that the grain size does not effect the thermal conductivity of the composites. This is expected, since it is believed that the mean free path is less than the grain size of the MgO or Nd₂Zr₂O₇. Therefore, the phonons would have been scattered before the thermal energy reached the grain boundary. Furthermore, this also provides additional evidence that the contiguity of the MgO is related to the thermal conductivity of the composites since the contiguity of the MgO did not differ drastically between the composites as a function of the isothermal holding time.

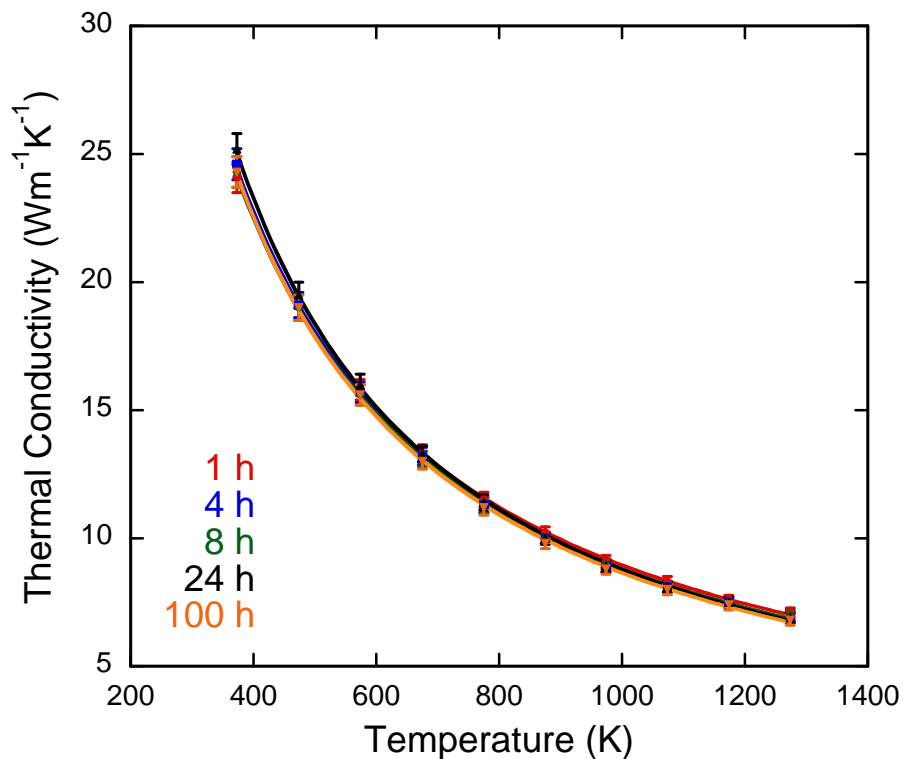


Figure E-7: Thermal conductivity of the composites isothermally held for the given time at 1550°C.

APPENDIX F COMPOSITE GRAIN GROWTH AT 1650°C

F.1 Introduction

A series of composites was also isothermally held at 1650°C for 1, 4, 8, 24, and 100 hours. The results of the microstructure characterization and preliminary work on the grain growth kinetics is shown in this appendix. The thermal conductivity of these composites is also reported.

F.2 Experimental Procedure

Pellets were fabricated from the ball milled mixed composite powder according to the procedure in Section 3.6. During sintering, the furnace temperature reached the isothermal hold time at 1650°C according to the furnace profile in Section 3.21, but the isothermal hold time was varied. Composites were sintered at 1650°C for 1, 4, 8, 24, and 100 hours.

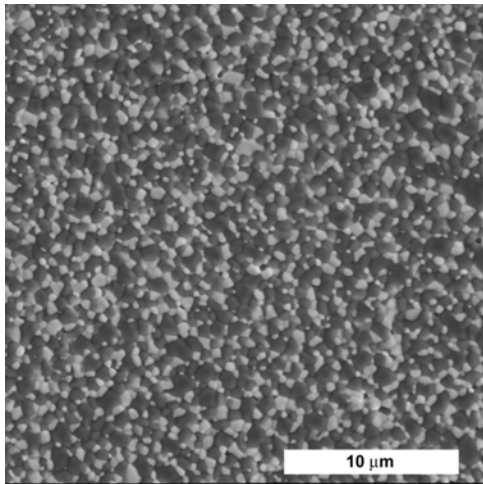
The composites were prepared and analyzed with the SEM using the experimental procedure described in Section 3.3.2. The grain size of the composites was calculated using the procedure described in Section 4.3.3 and the contiguity was calculated using the procedure described in Section 4.3.4.

F.3 Results

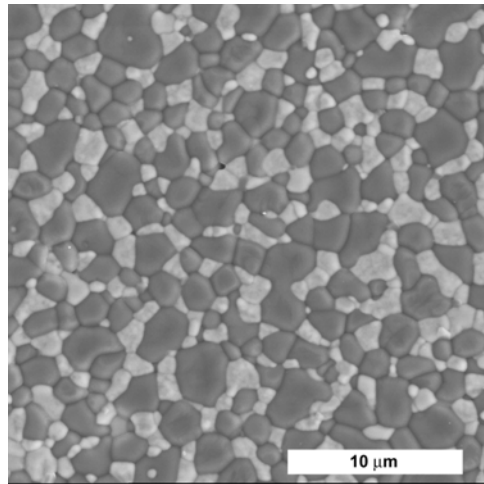
The microstructure characterization, grain growth kinetics, and the thermal conductivity of the composites is presented in the following section.

F.3.1 Microstructure Characterization

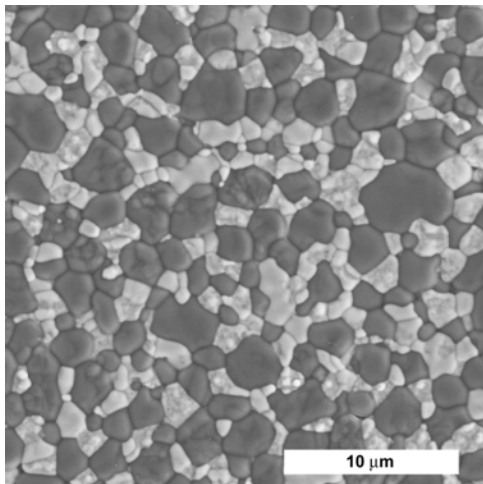
The microstructures are shown in Figure E.1 for the composites isothermally held at 1650°C. The grain size of both phases increased with increasing hold time. The grains of both the MgO and Nd₂Zr₂O₇ grew faster at 1650°C than at 1550°C, and the final grain size of the MgO and Nd₂Zr₂O₇ was much larger in the composites isothermally held at 1650°C. This is expected because at higher temperatures diffusion increases, accelerating the grain growth kinetics in the composites.



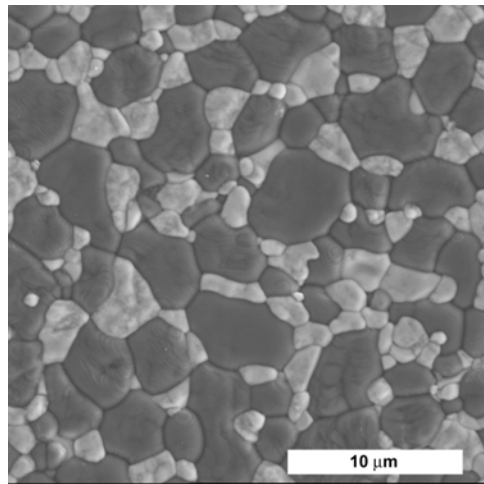
(a)



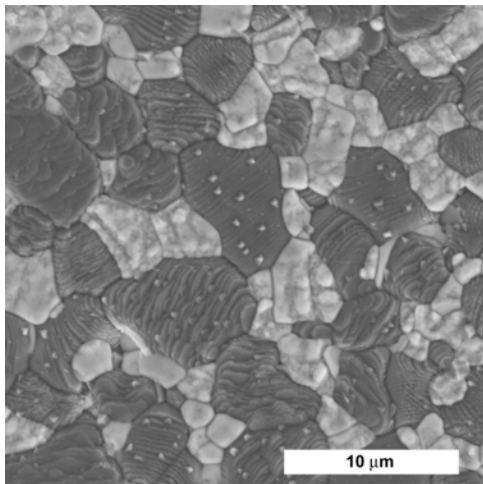
(b)



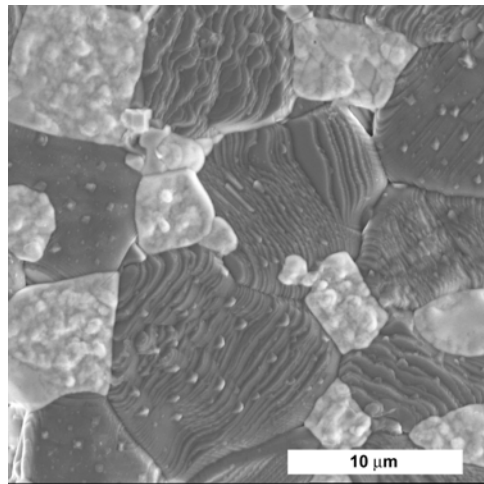
(c)



(d)



(e)



(f)

Figure F-1: Microstructures of ball milled composites isothermally held at 1650°C. A) 0 hours B) 1 hour C) 4 hours D) 8 hours E) 24 hours and F) 100 hours

The grain size measurements for the composites is shown below in Table F.1. The grain size of the MgO at 100 hours is nearly 3× larger than the grain size of the MgO at 100 hours in the samples isothermally held at 1550°C, confirming that the increase in temperature accelerated the grain growth of the phases in the composites.

Table F-1: Grain sizes of the MgO and Nd₂Zr₂O₇ in the microstructure of the ball milled composites isothermally held for the given amount of time.

Phase	Grain Size (μm)					
	0 hr	1 hr	4 hr	8 hr	24 hr	100 hr
MgO	1.1 ± 0.1	2.3 ± 0.2	2.8 ± 0.3	3.7 ± 0.6	6.2 ± 0.8	15.5 ± 2.3
Nd ₂ Zr ₂ O ₇	0.7 ± 0.2	1.5 ± 0.3	1.5 ± 0.3	1.9 ± 0.4	3.3 ± 0.6	7.4 ± 1.5

The contiguity of the composites is shown below in Table F.2. The contiguity of the MgO is essentially constant in all of the composites except the sample sintered for 100 hours. There is a significant drop in the average contiguity values from ~0.45 to 0.34.

Table F-2: Contiguity of the MgO and Nd₂Zr₂O₇ in the microstructure of the ball milled composites isothermally held for the given amount of time.

Phase	Contiguity					
	0 hr	1 hr	4 hr	8 hr	24 hr	100 hr
MgO	0.46	0.50	0.41	0.43	0.46	0.34
Nd ₂ Zr ₂ O ₇	0.22	0.25	0.28	0.33	0.34	0.29

F.3.2 Grain Growth Kinetics

Figure E.2 shows the grain growth of the MgO and Nd₂Zr₂O₇ as a function of time. Figure F.3 shows the ratio of MgO and Nd₂Zr₂O₇ grain sizes. The composites isothermally held at 1650°C display a constant grain size ratio of 2.06, which is larger than the grain size ratio of the phases in the composites isothermally held at 1550°C. This indicates that although the grain growth kinetics are different than the kinetics at 1550°C, grain growth in the composites appears to still be coupled at 1650°C.

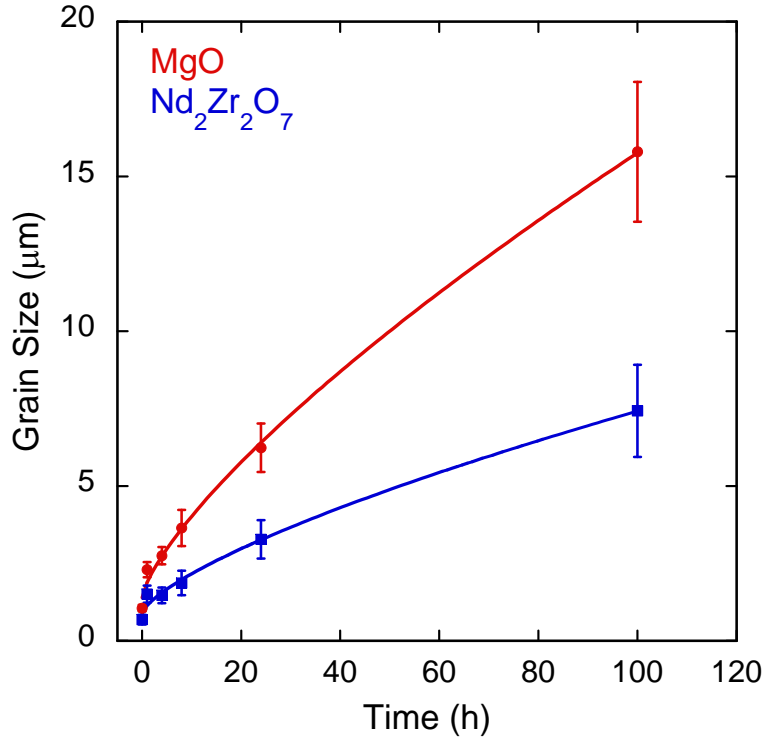


Figure F-2: Grain size of ball milled composites isothermally held at 1650°C .

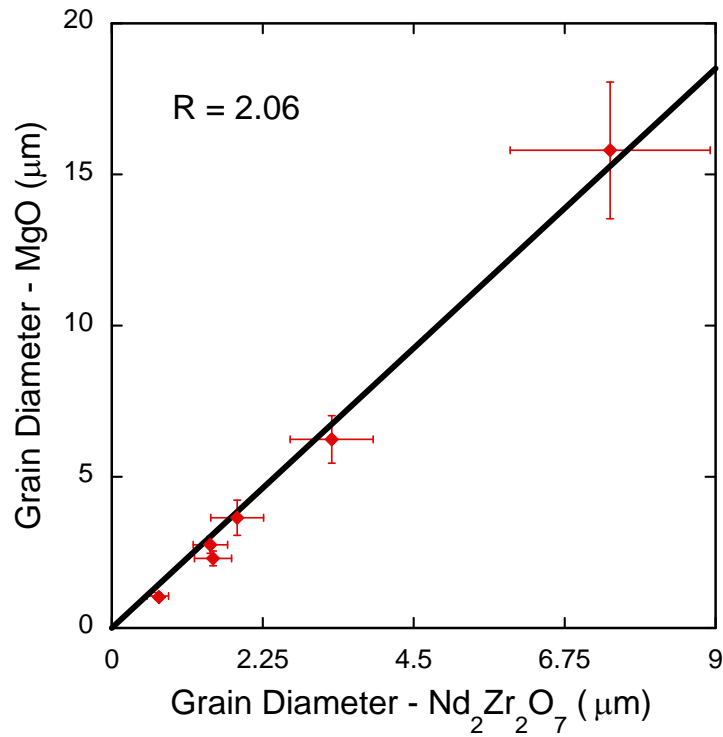


Figure F-3: The grain diameter of the MgO vs. the grain diameter of the $\text{Nd}_2\text{Zr}_2\text{O}_7$ showing the constant grain size ratio as the isothermal time increases.

A log-log plot of the grain size vs. time is shown below in Figure F.4. An interesting observation in this plot is that it appears as if the grain growth mechanism changes from one mechanism to another during the grain growth of the composite. The dashed line is for the grain growth from 0-8 hours and the solid line is the grain growth from 4-100 hours in the composites.

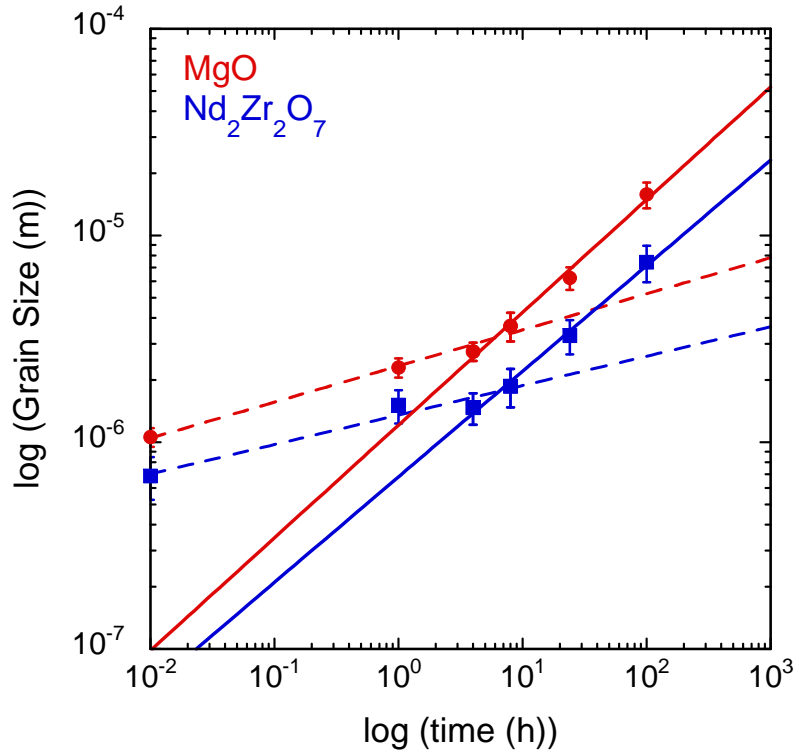


Figure F-4: A log-log plot of the grain size vs. time showing the change in slope. The change in slope indicates that there is a change in the grain growth mechanism. The dashed line is for grain growth through 8 hours and the solid line is for grain growth from 4-8 hours.

Figure F.5 and Figure F.6 show the log-log plot of $D^n - D_0^n$ as a function of time using values of n that correspond to interface controlled growth ($n = 2$), lattice controlled growth ($n = 3$), and grain boundary diffusion controlled growth ($n = 4$). Since the slope of the line in the $\log(D^n - D_0^n)$ vs. $\log(t)$ is equal to $1/n$ according to Equation 2.1, the correct grain growth mechanism will have a slope that equals one. The mechanism appears to change from a grain

boundary diffusion controlled process to an interface controlled diffusion process between 4 and 8 hours.

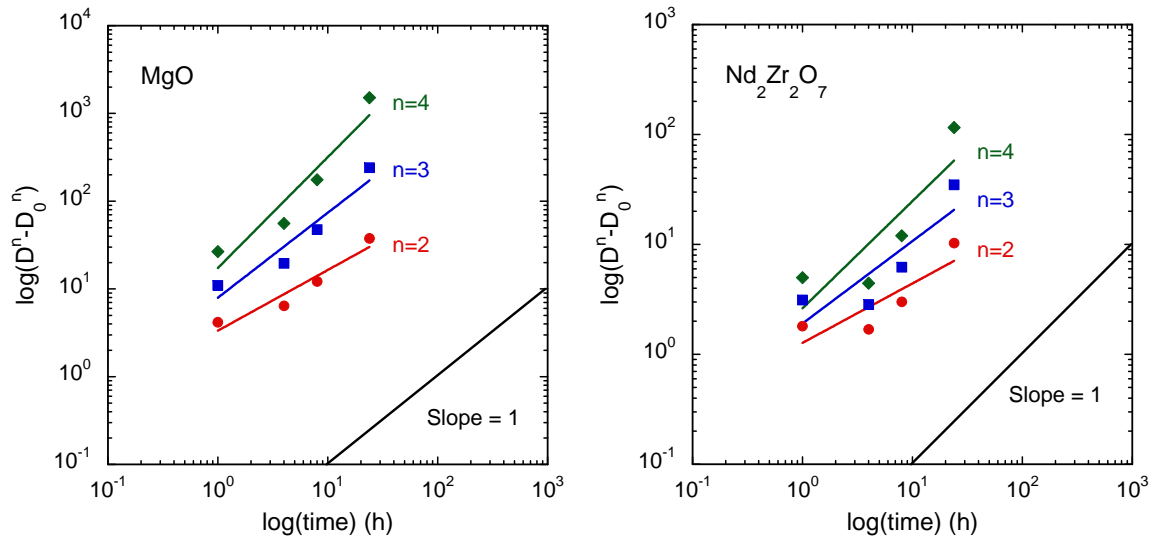


Figure E-5: Calculation of the grain growth exponent for the initial stage of grain growth in the composites isothermally held at 1650°C. The correct grain growth exponent will have a slope that equals 1.

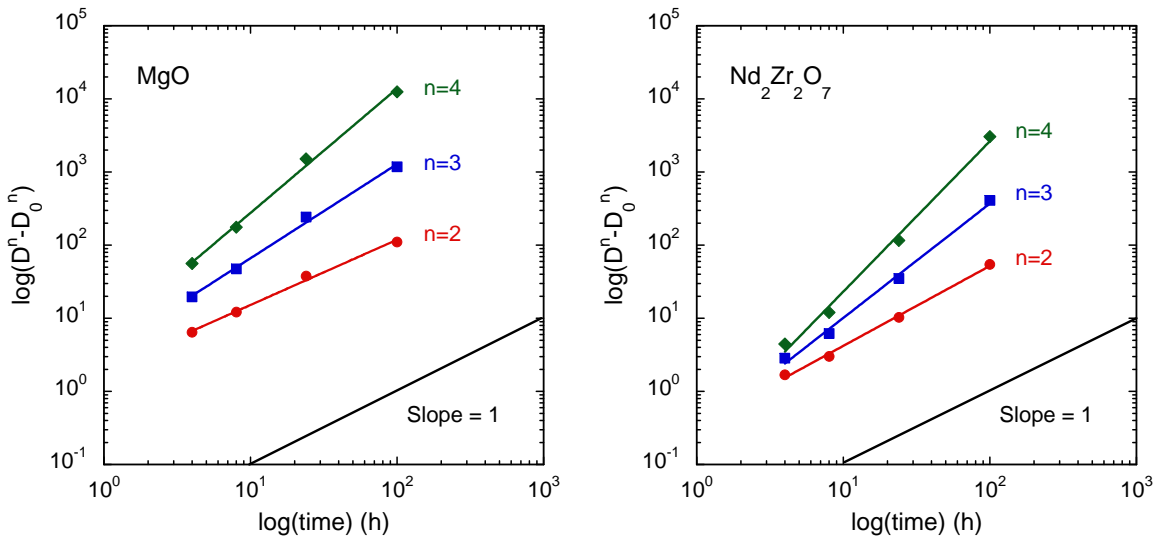


Figure F-6: Calculation of the grain growth exponent for the second stage of grain growth in the composites isothermally held at 1650°C. The correct grain growth exponent will have a slope that equals 1.

The activation energy was calculated for both stages separately since it appears as if there were two different grain growth mechanisms. Figure F.7 calculates the activation energy

for grain growth in the initial stage and Figure F.8 calculates to activation energy for grain growth in the second stage.

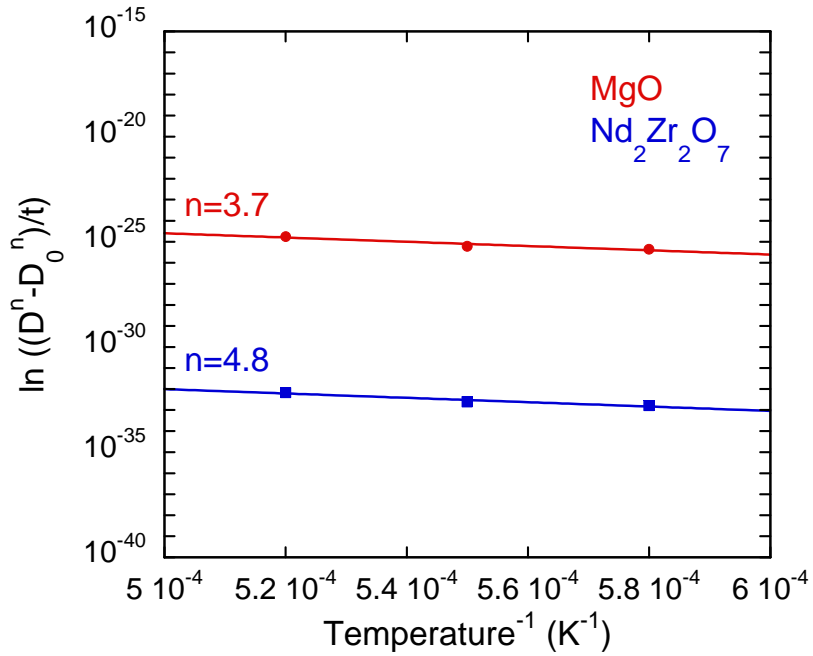


Figure F-7: The calculation of the activation energy for the initial stage of grain growth in the ball milled composites isothermally held at 1650°C.

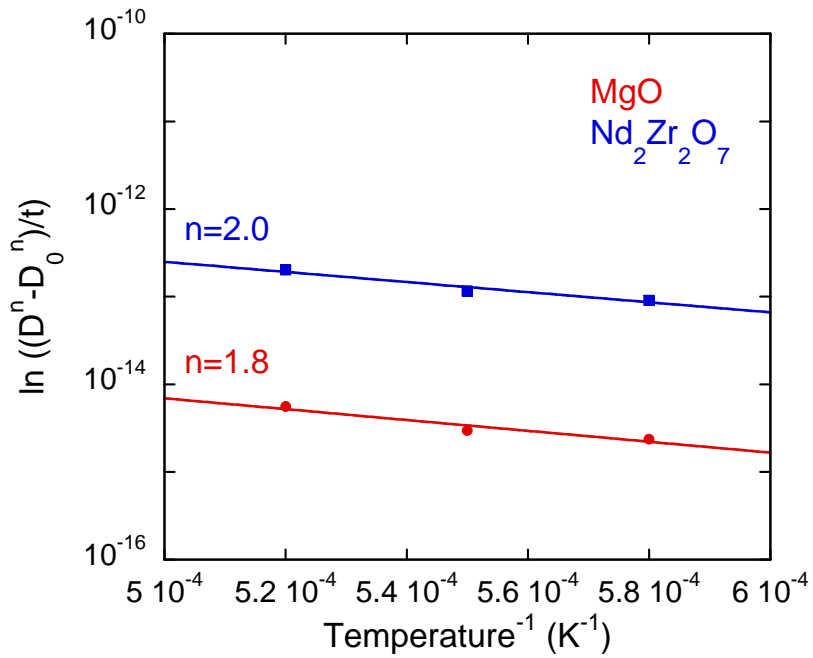


Figure F-8: The calculation of the activation energy for the second stage of grain growth in the ball milled composites isothermally held at 1650°C.

The values for the grain growth exponents, grain growth constants, correlation coefficients, and the activation energy for the initial stage is given in Table E.3 and for the second stage in Table F.4. The activation energy for the initial stage of the grain growth is similar to the activation energy observed in the composites isothermally held at 1550 °C. The difference between the activation energy of the MgO and the Nd₂Zr₂O₇ is smaller in the composites isothermally held at 1650 °C, however. The activation energy for the second stage of the grain growth decreased compared to the activation energy calculated in the initial stage. This is expected because the activation energy for bulk or interface diffusion is less than the activation energy required for grain boundary diffusion.

Table F-3: Grain growth exponents, constants, and the correlation coefficient from the best fit to the grain growth equation for the initial stage. The activation energy of grain growth is also included.

Phase	$D^n - D_0^n = Kt$				Q (kJ/mol)
	D ₀ (μm)	n	K (m ² /s)	R ²	
MgO	1.1 ± 0.1	3.7	6.7 × 10 ⁻¹⁹	0.96	242 ± 56
Nd ₂ Zr ₂ O ₇	0.7 ± 0.2	4.8	2.2 × 10 ⁻²⁶	0.97	240 ± 47

Table F-4: Grain growth exponents, constants, and the correlation coefficient from the best fit to the grain growth equation for the second stage. The activation energy of grain growth is also included.

Phase	$D^n - D_0^n = Kt$				Q (kJ/mol)
	D ₀ (μm)	n	K (m ² /s)	R ²	
MgO	1.1 ± 0.1	1.8	2.6 × 10 ⁻¹¹	0.95	136 ± 32
Nd ₂ Zr ₂ O ₇	0.7 ± 0.2	2.0	4.2 × 10 ⁻¹⁰	0.96	122 ± 25

F.3.3 Thermal Conductivity

The thermal conductivity of the composites isothermally held at 1650°C is shown below in Figure F.9. The thermal conductivity of the composites isothermally held at 1, 4, 8, and 24 hours is similar, although not as consistent as the composites isothermally held at 1550°C. The composite isothermally held at 100 hours is much lower than the other composites. There was

a corresponding decrease in the contiguity of the MgO to 0.34, much lower than the average of ~0.45 that the rest of the composites exhibited. However, there is evidence that the composite isothermally held for 100 hours possesses microcracks, which muddles the contiguity—thermal conductivity relationship. In addition, there are $\text{Nd}_2\text{Zr}_2\text{O}_7$ grains trapped in the larger MgO grains in the composites. Therefore, further characterization of the composites is required before the microstructure—thermal conductivity relationships can be analyzed.

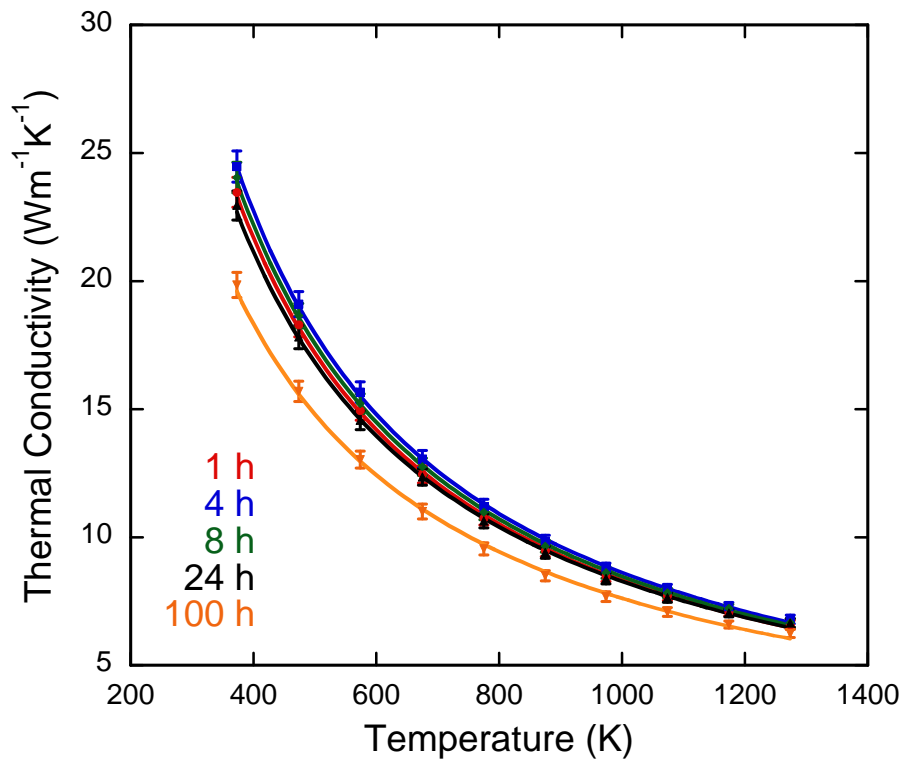


Figure F-9: Thermal conductivity of composites isothermally held at 1650°C for the given time.

LIST OF REFERENCES

1. I. A. E. Agency, "Viability of inert matrix fuel in reducing plutonium amounts in reactors." 2006.
2. I. E. Agency, "Nuclear Power Plants Information. Number of Reactors Operation Worldwide." 2007.
3. T. Yamashita, K. Kuramoto, H. Akie, Y. Nakano, N. Nitani, T. Nakamura, K. Kusagaya, and T. Ohmichi, "Rock-like oxide fuels and their burning in LWRs," *Journal of Nuclear Science and Technology*, **39**[8] 865-871 (2002).
4. N. Chauvin, R. J. M. Konings, and H. Matzke, "Optimisation of inert matrix fuel concepts for americium transmutation," *Journal of Nuclear Materials*, **274**[1-2] 105-111 (1999).
5. C. Degueldre and J. M. Paratte, "Concepts for an inert matrix fuel, an overview," *Journal of Nuclear Materials*, **274**[1-2] 1-6 (1999).
6. K. E. Sickafus, R. J. Hanrahan, K. J. McClellan, J. N. Mitchell, C. J. Wetteland, D. P. Butt, P. Chodak, K. B. Ramsey, T. H. Blair, K. Chidester, H. Matzke, K. Yasuda, R. A. Verrall, and N. Yu, "Burn and bury option for plutonium," *American Ceramic Society Bulletin*, **78**[1] 69-74 (1999).
7. R. J. M. Konings and D. Haas, "Fuels and targets for transmutation," *Comptes Rendus Physique*, **3**[7-8] 1013-1022 (2002).
8. G. Ledergerber, C. Degueldre, P. Heimgartner, M. A. Pouchon, and U. Kasemeyer, "Inert matrix fuel for the utilisation of plutonium," *Progress in Nuclear Energy*, **38**[3-4] 301-308 (2001).
9. K. Pasamehmetoglu, "GNEP Technology Demonstration Program." IMF-11. Park City, UT, 2006.
10. H. Matzke, V. V. Rondinella, and T. Wiss, "Materials research on inert matrices: a screening study," *Journal of Nuclear Materials*, **274**[1-2] 47-53 (1999).
11. H. R. Trellue, "Safety and neutronics: A comparison of MOX vs UO₂ fuel," *Progress in Nuclear Energy*, **48**[2] 135-145 (2006).
12. L. C. Walters, D. L. Porter, and D. C. Crawford, "Nuclear fuel considerations for the 21st century," *Progress in Nuclear Energy*, **40**[3-4] 513-521 (2002).
13. R. A. Verrall, M. D. Vlajic, and V. D. Krstic, "Silicon carbide as an inert-matrix for a thermal reactor fuel," *Journal of Nuclear Materials*, **274**[1-2] 54-60 (1999).
14. K. H. Sarma, J. Fourcade, S. G. Lee, and A. A. Solomon, "New processing methods to produce silicon carbide and beryllium oxide inert matrix and enhanced thermal conductivity oxide fuels," *Journal of Nuclear Materials*, **352**[1-3] 324-333 (2006).
15. M. Streit and F. Ingold, "Nitrides as a nuclear fuel option," *Journal of the European Ceramic Society*, **25**[12] 2687-2692 (2005).

16. V. V. Rondinella, T. Wiss, H. Matzke, R. Mele, F. Bocci, and P. G. Lucuta, "Radiation damage and simulated fission product effects on the properties of inert matrix materials," *Progress in Nuclear Energy*, **38**[3-4] 291-294 (2001).
17. V. Sobolev, S. Lemehov, N. Messaoudi, P. Van Uffelen, and H. A. Abderrahim, "Modelling the behaviour of oxide fuels containing minor actinides with urania, thoria and zirconia matrices in an accelerator-driven system," *Journal of Nuclear Materials*, **319** 131-141 (2003).
18. R. P. C. Schram, R. R. van der Laan, F. C. Klaassen, K. Bakker, T. Yamashita, and F. Ingold, "The fabrication and irradiation of plutonium-containing inert matrix fuels for the 'Once Through Then Out' experiment," *Journal of Nuclear Materials*, **319** 118-125 (2003).
19. M. Osaka, S. Miwa, and Y. Tachi, "Simple fabrication process for CeO₂-MgO composite as surrogate for actinide-containing target for use in nuclear fuel," *Ceramics International*, **32**[6] 659-663 (2006).
20. S. Pillon, J. Somers, S. Grandjean, and J. Lacquement, "Aspects of fabrication of curium-based fuels and targets," *Journal of Nuclear Materials*, **320**[1-2] 36-43 (2003).
21. Y. W. Lee, H. S. Kim, S. H. Kim, C. Y. Joung, S. H. Na, G. Ledergerber, P. Heimgartner, M. Pouchon, and M. Burghartz, "Preparation of simulated inert matrix fuel with different powders by dry milling method," *Journal of Nuclear Materials*, **274**[1-2] 7-14 (1999).
22. K. Bakker and R. J. M. Konings, "On the thermal conductivity of inert-matrix fuels containing americium oxide," *Journal of Nuclear Materials*, **254**[2-3] 129-134 (1998).
23. C. Degueldre, T. Arima, and Y. W. Lee, "Thermal conductivity of zirconia based inert matrix fuel: use and abuse of the formal models for testing new experimental data," *Journal of Nuclear Materials*, **319** 6-14 (2003).
24. G. Szenes, "Ion-induced amorphization in ceramic materials," *Journal of Nuclear Materials*, **336** 81-89 (2005).
25. P. G. Medvedev, M. J. Lambregts, and M. K. Meyer, "Thermal conductivity and acid dissolution behavior of MgO-ZrO₂ ceramics for use in LWR inert matrix fuel," *Journal of Nuclear Materials*, **349**[1/2] 167-177 (2006).
26. P. K. Schelling, S. R. Phillpot, and R. W. Grimes, "Optimum pyrochlore compositions for low thermal conductivity," *Philosophical Magazine Letters*, **84**[2] 127-137 (2004).
27. K. E. Sickafus, L. Minervini, R. W. Grimes, J. A. Valdez, M. Ishimaru, F. Li, K. J. McClellan, and T. Hartmann, "Radiation tolerance of complex oxides," *Science*, **289**[5480] 748-751 (2000).
28. K. Shimamura, T. Arima, K. Idemitsu, and Y. Inagaki, "Thermophysical properties of rare-earth-stabilized zirconia and zirconate pyrochlores as surrogates for actinide-doped zirconia," *International Journal of Thermophysics*, **28**[3] 1074-1084 (2007).
29. A. Cleave, R. W. Grimes, and K. Sickafus, "Plutonium and uranium accommodation in pyrochlore oxides," *Philosophical Magazine*, **85**[9] 967-980 (2005).

30. M. A. Subramanian, G. Aravamudan, and G. V. S. Rao, "Oxide pyrochlores-a review," *Progress in Solid State Chemistry*, **15**[2] 55-143 (1983).
31. R. C. Ewing, W. J. Weber, and J. Lian, "Nuclear waste disposal-pyrochlore ($A_2B_2O_7$): Nuclear waste form for the immobilization of plutonium and "minor" actinides," *Journal of Applied Physics*, **95**[11 I] 5949-5971 (2004).
32. S. Lutique, R. J. M. Konings, W. Rondinella, J. Somers, and T. Wiss, "The thermal conductivity of $Nd_2Zr_2O_7$ pyrochlore and the thermal behaviour of pyrochlore-based inert matrix fuel," *Journal of Alloys and Compounds*, **352**[1-2] 1-5 (2003).
33. M. C. Flemings and S. Suresh, "Materials education for the new century," *Mrs Bulletin*, **26**[11] 918-924 (2001).
34. K. Bakker and R. J. M. Konings, "The influence of americium oxide inclusions on the thermal conductivity of inert-matrix fuel," *Journal of Alloys and Compounds*, **271-273** 632-635 (1998).
35. A. Fernandez, K. Richter, and J. Somers, "Fabrication of transmutation and incineration targets by infiltration of porous pellets by radioactive solutions," *Journal of Alloys and Compounds*, **271-273**[0] 616-619 (1998).
36. A. Jankowiak, F. Jorion, C. Maillard, and L. Donnet, "Preparation and Characterization of $Pu_{0.5}Am_{0.5}O_{2-x}$ -MgO Ceramic/Ceramic Composites," *Nuclear Science and Engineering*, **160**[3] 378-384 (2008).
37. P. G. Medvedev, J. F. Jue, S. M. Frank, and M. K. Meyer, "Fabrication and characterization of dual phase magnesia-zirconia ceramics doped with plutonia," *Journal of Nuclear Materials*, **352**[1/3] 318-323 (2006).
38. F. D. J.M. Bonnerot, M.P. Ferroud-Plattet, G. Gaillard-Groleas, F. Sudreau, D. Warin, "Development of oxide fuels and targets for the transmutation of minor actinides." *IMF-11*. Park City, UT, October 10, 2006.
39. C. Ronchi, J. P. Ottaviani, C. Degueldre, and R. Calabrese, "Thermophysical properties of inert matrix fuels for actinide transmutation," *Journal of Nuclear Materials*, **320**[1-2] 54-65 (2003).
40. N. Chauvin, T. Albiol, R. Mazoyer, J. Noirot, D. Lespiaux, J. C. Dumas, C. Weinberg, J. C. Menard, and J. P. Ottaviani, "In-pile studies of inert matrices with emphasis on magnesia and magnesium aluminate spinel," *Journal of Nuclear Materials*, **274**[1-2] 91-97 (1999).
41. P. G. Medvedev, S. M. Frank, T. P. O'Holleran, and M. K. Meyer, "Dual phase MgO-ZrO₂ ceramics for use in LWR inert matrix fuel," *Journal of Nuclear Materials*, **342**[1/3] 48-62 (2005).
42. F. S. Galasso, "Structure and Properties of Inorganic Solids," Vol. 7. Oxford, England, Pergamon Press Inc. (1970).

43. M. N. Rahaman, "Ceramic Processing and Sintering." New York, NY, Marcel Dekker, Inc. (2003).
44. G. T. Higgins, S. Wiryolukito, and P. Nash, "The kinetics of coupled phase coarsening in 2 phase structures," pp. 671-676 *Proceedings of the 1st International Conf on Grain Growth in Polycrystalline Materials; June 18-21, 1991; Rome, Italy*. Edited by G. Abbruzzese and P. Brozzo. Rome, Italy, 1992.
45. B. Kibbel and A. H. Heuer, "Exaggerated grain growth in ZrO₂ toughened Al₂O₃," *Journal of the American Ceramic Society*, **69**[3] 231-236 (1986).
46. J. D. French, M. P. Harmer, H. M. Chan, and G. A. Miller, "Coarsening-resistant dual-phase interpenetrating microstructures," *Journal of the American Ceramic Society*, **73**[8] 2508-2510 (1990).
47. K. B. Alexander, P. F. Becher, S. B. Waters, and A. Bleier, "Grain growth kinetics in alumina-zirconia (CeZTA) composites," *Journal of the American Ceramic Society*, **77**[4] 939-946 (1994).
48. G. Grewal and S. Ankem, "Isothermal particle growth in two phase titanium alloys," *Metallurgical Transactions A-Physical Metallurgy and Materials Science*, **20**[1] 39-54 (1989).
49. G. Grewal and S. Ankem, "Particle coarsening behavior of alpha-beta titanium alloys," *Metallurgical Transactions A-Physical Metallurgy and Materials Science*, **21**[6] 1645-1654 (1990).
50. M. V. Speight, "Growth kinetics of grain boundary precipitates," *Acta Metallurgica*, **16**[1] 133-135 (1968).
51. V. V. Srdic and D. I. Savic, "Grain growth in sol-gel derived alumina-zirconia composites," *Journal of Materials Science*, **33**[9] 2391-2396 (1998).
52. R. E. Newnham, D. P. Skinner, and L. E. Cross, "Connectivity and piezoelectric-pyroelectric composites," *Materials Research Bulletin*, **13**[5] 525-536 (1978).
53. E. E. Underwood, "Quantitative Stereology," pp. 274. Reading, MA, Addison-Wesley. (1970).
54. F. N. R. R.T. DeHoff, "Quantitative Stereology." New York, NY, McGraw-Hill Book Company. (1968).
55. J. Gurland, "Measurement of grain continuity in two-phase alloys," *Metallurgical Society of American Institute of Mining, Metallurgical and Petroleum Engineers -- Transactions*, **212**[4] 452-455 (1958).
56. J. Gurland, "Spatial Distribution of Discrete Particles." In *Quantitative Microscopy*. Edited by F. N. R. Robert T. DeHoff. McGraw-Hill Book Company, New York, NY, 1968.
57. G. Grimvall, "Thermophysical Properties of Materials," pp. 348 Vol. 18. Amsterdam, North-Holland Physics Publishing. (1986).

58. C. Kittel, "Introduction to Solid State Physics," in 8th ed. Hoboken, NJ, Wiley. (2005).
59. Z. Hashin and S. Shtrikman, "A variational approach to the theory of the elastic behaviour of polycrystals," *Journal of the Mechanics and Physics of Solids*, **10** 343-352 (1962).
60. J. C. Maxwell, "A Treatise on Electricity and Magnetism," in 3rd Ed. ed. New York, Dover Publications Inc. (1954).
61. A. Eucken, "Allgemeine Gesetzmässigkeiten für das Wärmeleitvermögen verschiedener Stoffarten und Aggregatzustände," *Forschung Gebiete Ingenieur*, **11**[1] 6-20 (1940).
62. C. Degueldre, "Zirconia inert matrix for plutonium utilisation and minor actinides disposition in reactors," *Journal of Alloys and Compounds*, **444-445** 36-41 (2007).
63. V. Sears, "Neutron scattering lengths and cross sections," *Neutron News*, **3**[3] 26-37 (1992).
64. J. Tulenko, *Nuclear Science and Engineering Committee Member, May 12, 2005*.
65. R. Vassen, X. Q. Cao, F. Tietz, D. Basu, and D. Stover, "Zirconates as new materials for thermal barrier coatings," *Journal of the American Ceramic Society*, **83**[8] 2023-2028 (2000).
66. G. Suresh, G. Seenivasan, M. V. Krishnaiah, and P. S. Murti, "Investigation of the thermal conductivity of selected compounds of gadolinium and lanthanum," *Journal of Nuclear Materials*, **249**[2-3] 259-261 (1997).
67. J. Wu, X. Z. Wei, N. P. Padture, P. G. Klemens, M. Gell, E. Garcia, P. Miranzo, and M. I. Osendi, "Low-thermal-conductivity rare-earth zirconates for potential thermal-barrier-coating applications," pp. 3031-3035.
68. MONTEBURNS Burnup Code System,
69. MCNP Burnup Code System,
70. V. K. S. Shante and S. Kirkpatrick, "Introduction to percolation theory," *Advances in Physics*, **20**[85] 325 (1971).
71. S. R. S. B.D. Cullity, "Elements of X-Ray Diffraction," in 3rd ed. New Jersey, Prentice Hall. (2001).
72. L. O. A. Kitamura, K. Tanaka, "Hydration characteristics of magnesia," *Taikabutsu Overseas*, **16**[3] 3-11 (1995).
73. F. F. Lange, "Sinterability of agglomerated powders," *Journal of the American Ceramic Society*, **67**[2] 83-89 (1984).
74. M. J. G. W. Heijman, N. E. Benes, J. E. ten Elshof, and H. Verweij, "Quantitative analysis of the microstructural homogeneity of zirconia-toughened alumina composites," *Materials Research Bulletin*, **37**[1] 141-149 (2002).

75. J. C. Wurst and J. A. Nelson, "Lineal intercept technique for measuring grain size in two-phase polycrystalline ceramics," *Journal of the American Ceramic Society*, **55**[2] 109 (1972).
76. L. S. Dubrovinsky and S. K. Saxena, "Thermal expansion of periclase (MgO) and tungsten (W) to melting temperatures," *Physics and Chemistry of Minerals*, **24**[8] 547-550 (1997).
77. K. V. G. Kutty, S. Rajagopalan, C. K. Mathews, and U. V. Varadaraju, "Thermal expansion behaviour of some rare earth oxide pyrochlores," *Materials Research Bulletin*, **29**[7] 759-766 (1994).
78. R. G. Munro, "Elastic Moduli Data for Polycrystalline Ceramics," *NISTIR*, **6853** (2002).
79. M. P. van Dijk, K. J. de Vries, and A. J. Burggraaf, "Oxygen ion and mixed conductivity in compounds with the fluorite and pyrochlore structure," *Solid State Ionics*, **9-10**[Part 2] 913-919 (1983).
80. F. F. Lange and M. Metcalf, "Processing-related fracture origins. II. Agglomerate motion and cracklike internal surfaces caused by differential sintering," *Journal of the American Ceramic Society*, **66**[6] 398-406 (1983).
81. W. J. Parker, R. J. Jenkins, G. L. Abbott, and C. P. Butler, "Flash method of determining thermal diffusivity, heat capacity and thermal conductivity," *Journal of Applied Physics*, **32**[9] 1679-1684 (1961).
82. R. D. Cowan, "Pulse method of measuring thermal diffusivity at high temperatures," *Journal of Applied Physics*, **34**[4 (I)] 926-927 (1963).
83. D. P. H. Hasselman, "Effect of cracks on thermal conductivity," *Journal of Composite Materials*, **12** 403-407 (1978).
84. A. Hoenig, "Thermal conductivities of a cracked solid," *Journal of Composite Materials*, **17**[3] 231-237 (1983).
85. P. G. Klemens, "Thermal conductivity of inhomogeneous materials," *International Journal of Thermophysics*, **10**[6] 1213-1219 (1989).
86. P. G. Klemens, "Thermal conductivity of inhomogeneous media," *High Temperatures - High Pressures*, **23**[3] 241-248 (1991).
87. P. G. Klemens, "Thermal Conductivity and Lattice Vibrational Modes." In *Solid State Physics*, **Vol. 7**. Edited by F. S. a. D. Turnbull. Academic Press Inc., New York, 1958.
88. P. Shukla, T. Watanabe, J. C. Nino, J. S. Tulenko, and S. R. Phillpot, "Thermal transport properties of MgO and Nd₂Zr₂O₇ pyrochlore by molecular dynamics simulation," *Journal of Nuclear Materials*, **380**[1-3] 1-7 (2008).
89. J. P. Jernot and J. L. Chermant, "On the importance of the contiguity and electrical conductivity for sintered materials," *Scripta Metallurgica*, **16**[8] 943-946 (1982).

90. J. H. Lee, H. Moon, H. W. Lee, J. Kim, J. D. Kim, and K. H. Yoon, "Quantitative analysis of microstructure and its related electrical property of SOFC anode, Ni-YSZ cermet," *Solid State Ionics*, **148**[1-2] PII S0167-2738(0102)00050-00054 (2002).
91. M. Tajika, H. Matsubara, and W. Rafaniello, "Effect of grain contiguity on the thermal diffusivity of aluminum nitride," *Journal of the American Ceramic Society*, **82**[6] 1573-1575 (1999).
92. T. B. Jackson, A. V. Virkar, K. L. More, R. B. Dinwiddie, and R. A. Cutler, "High-thermal-conductivity aluminum nitride ceramics: The effect of thermodynamic, kinetic, and microstructural factors," *Journal of the American Ceramic Society*, **80**[6] 1421-1435 (1997).
93. Y. S. Touloukian and E. H. Buyco, "Thermal Conductivity: Nonmetallic Solids," Vol. 5. New York, Plenum. (1970).
94. J. K. Fink, "Thermophysical properties of uranium dioxide," *Journal of Nuclear Materials*, **279**[1] 1-18 (2000).
95. P. B. Allen, J. L. Feldman, J. Fabian, and F. Wooten, "Diffusons, locons and propagons: character of atomic vibrations in amorphous Si," *Philosophical Magazine B-Physics of Condensed Matter Statistical Mechanics Electronic Optical and Magnetic Properties*, **79**[11-12] 1715-1731 (1999).
96. G. L. Messing and G. Y. Onoda, "Sintering of inhomogeneous binary powder mixtures," *Journal of the American Ceramic Society*, **64**[8] 468-472 (1981).
97. W. F. H. G. W. H. Hohne, H.-J. Flammersheim, "Differential Scanning Calorimetry," pp. 298 in 2nd ed. New York, Springer-Verlag Berlin Heidelberg. (2003).
98. Y. S. Touloukian and E. H. Buyco, "Specific Heat: Nonmetallic Solids," Vol. 5. New York, Plenum. (1970).
99. S. Lutique, P. Javorsky, R. J. M. Konings, A. C. G. van Genderen, J. C. van Miltenburg, and F. Wastin, "Low temperature heat capacity of Nd₂Zr₂O₇ pyrochlore," *Journal of Chemical Thermodynamics*, **35**[6] 955-965 (2003).

BIOGRAPHICAL SKETCH

Samantha Yates was born in Dunedin, FL in 1979. She slogged her way through the Pinellas County Public School System and began her undergraduate studies at the University of Florida in August of 1997. In 1999 she found her best friend, confidant, and partner of the last 9 years. After 3.5 years of sampling many of the majors UF offered, she stumbled on materials science and engineering. Half-way through her Junior year and 2 semesters away from graduating with dual liberal arts degrees she found herself sitting in Martha McDonald's office asking to switch her major. Martha made a leap of faith and petitioned the College of Engineering to allow her to join the Department of Materials Science and Engineering as an undergraduate student. Two and a half years later she graduated the University of Florida with a bachelor's degree in materials science and engineering with a metals specialty, and minors in sociology and women's studies in August of 2002.

After taking a semester off to toil in the US Postal Service, she returned to the University of Florida Department of Materials Science and Engineering to pursue her master's in January of 2003. She decided to join Dr. Fereshteh Ebrahimi's group and began designing her own curriculum focusing on biometallics. She graduated with her master's degree in materials science and engineering in December of 2003. She left Randy in Gainesville and began an internship with Abbott Vascular Devices the next month working on the chemical descale and electropolishing of coronary stents under the guidance of Sanjay Shrivastava. Her internship ended 11 months later and she returned to Gainesville, FL to pursue her doctorate at the University of Florida.

She met Dr. Juan C. Nino in January of 2005 after receiving 4 emails within 2 days from different people requesting a meeting to discuss a potential research opportunity. There wasn't much of a discussion in the meeting, instead, she was essentially drafted to work on nuclear fuels. Amused, intrigued, and without any other definite plans while she waited for funding to become available in Dr. Ebrahimi group, she decided to give Dr. Nino's offer a chance for the

semester. After spending the next 6 months learning ceramics did not behave like metals, she found her footing and started applying her will to help shape the policies and procedures for Dr. Nino's growing group. Meanwhile, she abandoned Randy again to spend 6 months at Idaho National Laboratory and 1.5 years at Los Alamos National Laboratory researching nuclear fuels and exploring Idaho and New Mexico on the back of a horse. She received her Ph.D. from the University of Florida in the Spring of 2009. Samantha is now working at Intel as a Process Technology Development Engineer.